X-RAY STUDIES OF ORDERED INTERMETALLIC PHASES FOR FUEL CELL APPLICATIONS

A Dissertation

Presented to the Faculty of the Graduate School

of Cornell University

In Partial Fulfillment of the Requirements for the Degree of

Doctor of Philosophy

by

Yi Liu

August 2009

X-RAY STUDIES OF ORDERED INTERMETALLIC PHASES FOR FUEL CELL APPLICATIONS

Yi Liu, Ph. D.

Cornell University 2009

Synchrotron based X-ray techniques in combination with electrochemical methods have been employed to characterize the composition and structure of ordered intermetallic materials in bulk polycrystalline, single crystal and nanoscale forms as electrocatalysts for fuel cell applications. The major objective of this research project is to thoroughly understand the structure/composition/property/activity relationships of these materials and obtain valuable information to guide the design of new electrocatalysts. It is of great importance to characterize ordered intermetallic phases as electrocatalysts since they exhibit excellent electrocatalytic activity towards the oxidation of small organic molecules. In addition, intermetallic phases can serve as model system for the electrocatalyst resaerch, complementing alloy materials and modified single crystal surfaces.

In-situ gazing incidence diffraction was applied to characterize polycrystalline PtBi and PtPb intermetallic electrodes in the absence or presence of active fuel molecules in supporting electrolyte. While absence of active fuel molecules, the surface composition and structure of these electrodes were significantly altered as a function of applied upper limit potential (E_{ulp}) while cycling to increasingly positive values. Less noble metals (Bi and Pb) leached out from the matrix. The process resulted that Pt nanocrystal domains were formed on the surface. Instead of cycling the potential, the electrochemical pretreatment of holding the potential reproducibly generated

bismuth oxide domains with the diameter of ca. 50 nm on PtBi electrodes. It is surprising that the electrocatalytic activities of different terminations of PtBi electrodes after different electrochemical pretreatments were very similar. This suggests that the activity of PtBi comes from the boundary lines of bismuth oxide and PtBi domains. On the other hand, for PtPb electrodes, no oxidized lead species were formed after similar electrochemical pretreatment.

PtBi and PtPb single crystal (100) and (001) facets were prepared by orienting the crystals via back Laue reflection method (BRL). Well-defined Pt domains with 6 fold symmetry but offsetting 23 deg to the (001) directions were produced while cycling the potential to +0.80 V. On the other hand, highly oriented polycrystalline Pt domains with no offset angle to the substrates were formed after similar treatment. Anisotropic activity properties were only observed for PtPb (100) and (001) electrodes towards the formic acid oxidation.

X-ray fluorescence (XRF) and X-ray absorption spectroscopic (XAS) methods were utilized to characterize intermetallic nanoparticles. A multi-functional general method was developed to simultaneously obtain XRF and EXAFS data in an *in-situ* measuring fashion. EXAFS data suggest that bismuth atoms had been essentially oxidized for initial modified electrodes, but the nanoparticles still had the intermetallic crystal structure. Quantitative XRF data suggest the leaching out of bismuth occurred at relatively negative potentials when compared to bulk electrodes.

BIOGRAPHICAL SKETCH

Yi Liu was born in Wuhan (武汉), China on October 11th, 1979. He finished his first “degree” in Tangjiadun Elementary School (唐家墩小学) in 1991. His interest in science was initially inspired by the trip of nature and biology groups to the Natural Museum at Wuhan University (武汉大学) when he was less than 10 years old. He went to Xianfeng Middle School (先锋中学) for three years and then moved to No.1 High School in Wuhan (武汉市第一中学) for three years high school life. His interest in science had never faded out for his six years middle school life.

Since his mom could not afford being away from him over 100 miles, he had to choose one of the colleges in the city for his higher education. Wuhan University is one of the best universities in China and offers top undergraduate programs in all scientific majors. It was lucky for him to obtain the best college education in China without hurting mom’s heart. He was enrolled in the special program, so-called National Chemistry Talent Class, at Wuhan University without taking National College Entrance Examination (NCEE), which is the most top honor to less than 2% high school students in China. He worked as undergraduate research assistant in Prof. Wang’s group on the project to design and fabricate new type of sensitive thermo device to monitor the heat change from biological reactions when he was sophomore. He then joined Prof. Pang’s group and worked on the project to study the interaction between biomolecules (such as protein and DNA) and small inorganic ions via electrochemical methods when he started his senior year in 2000. This was the first time he was introduced to the world of electrochemistry.

His thesis for Bachelor degree was awarded as First-Class Award of the Most Outstanding Senior Thesis of the College of Chemistry and Molecular Sciences. He had also annually earned *Renmin* Scholarship Award for the undergraduate students. He obtained his Bachelor of Science degree in Chemistry in July 2001, that same year

he joined the chemistry graduate program at Wuhan University and worked in Prof. Pang's group on the project of quantum dots and their application in biochemistry. This was first time for him to be introduced to the research world of nanotechnology. He obtained *Renmin* Scholarship Award for graduate students in two consecutive years and earned Wuhan University Outstanding Graduate Student Award in 2003.

Yi met Prof. Héctor D. Abruña sometime in October 2003 at Wuhan University while Prof. Abruña was invited to give a series of lectures on the topics of molecular electronics and fuel cells. Prof. Abruña made him an offer to join the Ph.D. program in Chemistry Department at Cornell University, he accepted it with pleasure. Yi finished his Master program and graduated from Wuhan University in June 2004, then earned his first Master of Science degree in chemistry.

In the summer of 2004, Yi left his mom and dad, Chengyu and other family members, and left his hometown, Wuhan, where he had never been away for more than a month until he was 24 years old. He headed to the gorgeous summer days in Ithaca and started his foreign study life alone. He joined Prof. Abruña's research group and initially felt interesting on the projects of biosensor and molecular electronics, then Prof. Abruña persuaded him to make efforts on the surface characterization of catalysts for energy issues. It showed that Prof. Abruña had sharp insight and excellent sense of future research directions, and Yi devoted himself to the research projects of X-ray studies for electrocatalysts. He thought that there are many fantastic opportunities in this research field and planned to focus on this area for his short-term academia goals. After he passed his A-exam in June 2006, he earned his second Master of Science degree in chemistry. He went back to China in the summer of 2006 and had the fabulous wedding with his lovely wife, Chengyu. Chengyu and Yi came back to Ithaca together in August 2006.

He was one of the four recipients all over the world to receive Annual Student

Award from International Precious Metal Institute (IPMI) in June 2007 and also earned Liu Memorial Award as the only recipient of Chemistry Department from Graduate School at Cornell University in May 2008. At the beginning of the last semester at Cornell, his son, Henry X. Liu, was born on January 19th, 2009. As first time dad, he could not be happier and thought his son as the most magic thing in his life so far.

He received his degree of Doctor of Philosophy in August 2009.

谨以此文献给爸爸、妈妈和妻子，感谢你们一直以来的鼓励、支持、帮助、无条件的付出和无私的爱！

也献给子恒，你是我生命中的奇迹！

“Where there is a will, there is a way.”

ACKNOWLEDGMENTS

I would never have been able to finish my dissertation without the guidance of my Ph.D. advisor and committee members, help of the friends and colleagues, and support from my wife and family members.

I would like to express the deepest appreciation and gratitude to my advisor, Professor Héctor D. Abruña, for the opportunity to work in his research group, his guidance and support throughout my graduate career. His attitude of the flexibility and allowance towards the experiments and research projects is truly appreciated. I always felt strongly about his trust, patience and unconditional support, even when things were not working out. He continually and convincingly conveyed a spirit of adventure in regard to research and scholarship and an excitement in regard to teaching. His sharp insight and powerful positive attitude inspired me in many aspects. I will always be grateful of his mentorship, wisdom, friendship and his advice, which sometimes were beyond scientific problems. It has been a great pleasure and honor working with him.

I am also great thankful to Professor Francis J. DiSalvo and Professor Joel D. Brock for being my committee members and their time for revising my research work, and their advices. I would like thank to them for generous support and recommendation while I need it. I will like to also acknowledge the faculties and professors who introduced me to various scientific research fields and gave me support and help at different stages: Prof. Dai-Wen Pang, who introduced me to electrochemistry and nanotechnology; Prof. Lin Zhuang, who inspired me in many ways for the research of electrocatalysts; Prof. Cui-Xin Wang, who accepted me as a research undergraduate student in his group and let me have a first taste of independent research; Prof. Mei-Yun Xi, who was my undergraduate study advisor. I would like to acknowledge

financial support for my research and living stipend throughout the Cornell Center for Materials Research (CCMR) and the Cornell Fuel Cell Institute (CFCI).

Throughout my graduate career I had great pleasure to collaborate with talent graduate students, post-doctoral associates, staff scientist, technicians and professors, from my group, chemistry department, other departments and elsewhere. I would like thank to Dr. Daniel R. Blasini, who technically taught me experimental skills of X-ray gazing incidence diffraction and useful survival tips at CHESS. We had so many exhausting but full of fun working nights at G2 stations over three beam runs. Thanks for all the discussions and advices in either research work or personal life. I wish him the best for future. I would like to also acknowledge Professor Francis J. DiSalvo, Drs Hideki Abe, Laif R. Alden, Chandrani Roychowdhury and Heather Edvenson, Tanusheree Ghosh collaborations to offer excellent solid state and nanoscale intermetallic samples for the research projects in this dissertation. Another collaborator I would like to thank is Michael A. Lowe; I wish him and his family the best in the future. Thanks for all the great discussions in the scientific problems and beyond we had. I would like to also acknowledge all the faculty members and staff scientists at CHESS and G-line for their invaluable support and help, especially Professor Joel D. Brock, Drs Detlef M. Smilgies, Ken D. Finkelstein, Arthur Woll and Darren Dale. I will like to thanks for the state-of-art facilities offered by CCMR too.

It was great honor and pleasure working with all the present and past members in the Abruña research group. I thank you all for creating and maintaining such a great working environment, and also for your indeed friendship. My special thanks go to Drs Jing Jing, Hongseng Wang and Yu-Wu Zhong for useful and interesting discussions on different research topics and also for offering familiar gathering events to colorize my daily life in Ithaca. My thanks go to Drs Emerilis Casado, Samuel Flores Torres, Geoffrey Hutchison, Jamie Cohen, Burak Ülgüt, Yasuyaki Kiya, Jay

Henderson and Suddhasattwa Nad for their friendship and help. My thanks also go to Dr. Mitk'El B. Santiago-Berrios, Michele Tague, Eric Rus, David Finkelstein, Stephen Burkhardt, Prof. Longzhen Zheng, Dr. Jie Gao, Dr. Mao Li, Cen Tan, Jimmy John, Sean Conte and Anna Legard.

Now I would like to acknowledge my family members who supported and encourage me on a personal level. I would not survive from the winters in Ithaca and graduate student life at Cornell without the lovely and unconditional support from my wife Chengyu Xiong. You cannot even image how you have intensively influence my life in positive ways and make it lovely than even. To my son, Henry X. Liu, you are definitely the most magic thing in my life ever and the source of my happiness and inspirations. Lastly, thanks to my mom, dad, parents-in-law and all other family members for their continuous and lovely support for those years I was not even around. Thanks to all of you for helping me to achieve my personal goal.

TABLE OF CONTENTS

LIST OF FIGURES

LIST OF TABLE

CHAPTER ONE

INTRODUCTION

Global energy consumption and demand dramatically and continuously increase, even in the face of the critical issue of substantial declines in energy source, due to population growth and increase in economic utinity.[1-3] The estimated world energy consumption will increase from 13.5 TW (terawatt) in 2001 to 43.0 TW in 2100 which is almost tripled while the global population will be doubled and will be close to 10.4 B (billion).[1] Without developing and switching to renewable and sustainable energy sources, this demand will be principally supplied by fossil based energy sources, such as petroleum and coal. It is clear that the health living of the planet and humans will require improvement, supplement and/or replacement for energy techniques and sources in two main ways. Firstly, it is of great importance to significantly improve the energy consumption efficiencies for traditional techniques utilizing fossil based fuels. This is intimately connected with the emission of carbon dioxide (CO_2) which is a major cause for the green house effect and global warming. The estimated equivalent CO_2 emission rate will be at least doubled from 2001 to 2100 even if the energy demand is not heavily based on fossil fuels.[4] Secondly, or more importantly, alternative energy sources and techniques should be discovered and developed to supplement traditional source. A sustainable energy policy is one that meets present needs without compromising the ability of future generations to meet theirs. Sustainable energy sources are most often regarded as including all renewable sources, such as biomass energy, solar power, hydropower, wind power, geothermal power and ocean energy (including wave and tide power). On the other hand, the sustainable energy concept also includes the technologies which dramatically improve energy efficiency, such as fuel cell

Figure 1.1 In this 1970 picture, an average American family was surrounded by the barrels of oil they consumed annually. This consumption was about 40% higher in 2007.

technologies.

A fuel cell is an electrochemical energy conversion device. It produces electricity directly from fuel (at the anode side) and an oxidant (at the cathode side), which react at suitable electrodes in the presence of an electrolyte. The reactants flow into the cell, and the reaction products flow out of it, while the electrolyte remains within it. Fuel cells can operate virtually continuously as long as the necessary flows are maintained. The principle of the fuel cell was discovered by the German scientist Christian Friedrich Schönbein in 1838 and published in one of the scientific magazines of the time. Based on this work, the first fuel cell was demonstrated by the Welsh scientist and barrister Sir William Robert Grove, who is considered to be the "Father of the Fuel Cell", in the February 1839 by using platinum as electrode materials. The first practical fuel cell was developed by Francis Thomas Bacon in 1959.[5] Many combinations of fuel and oxidant are possible. A hydrogen cell uses hydrogen as fuel and oxygen (usually from air) as oxidant. Other fuels include hydrocarbons and alcohols. Other oxidants include chlorine and chlorine dioxide. There are six generic types of fuel cells in various stages of development, namely, phosphoric acid fuel cells (PAFCs), alkaline fuel cells (AFCs), polymer electrolyte membrane fuel cells (PEM-FCs), molten electrolyte fuel cells (MCFCs), solid oxide fuel cells (SOFCs) and direct alcohol fuel cells (DAFCs). Figure 1.2 shows the fuel sources of all these types of fuel cells and their potential applications.

Due to increasing demands of power sources for small portable electronic devices, the development and utilization of DAFCs has attracted great interest in recent time.[6-8] Figure 1.3 demonstrates the operating mode of a direct methanol fuel cell (DMFC). Methanol in acidic solution is continuously flowed into the anode when it is electrooxidized on the surface of an electrocatalyst to produce electrons, protons and CO_2. Each methanol molecule gives six electrons if completely oxidized to CO_2. The generated protons travel through the proton-conductive membrane which separates the

Figure 1.2 Demonstration of six types of fuel cells with the fuel sources and their potential applications.

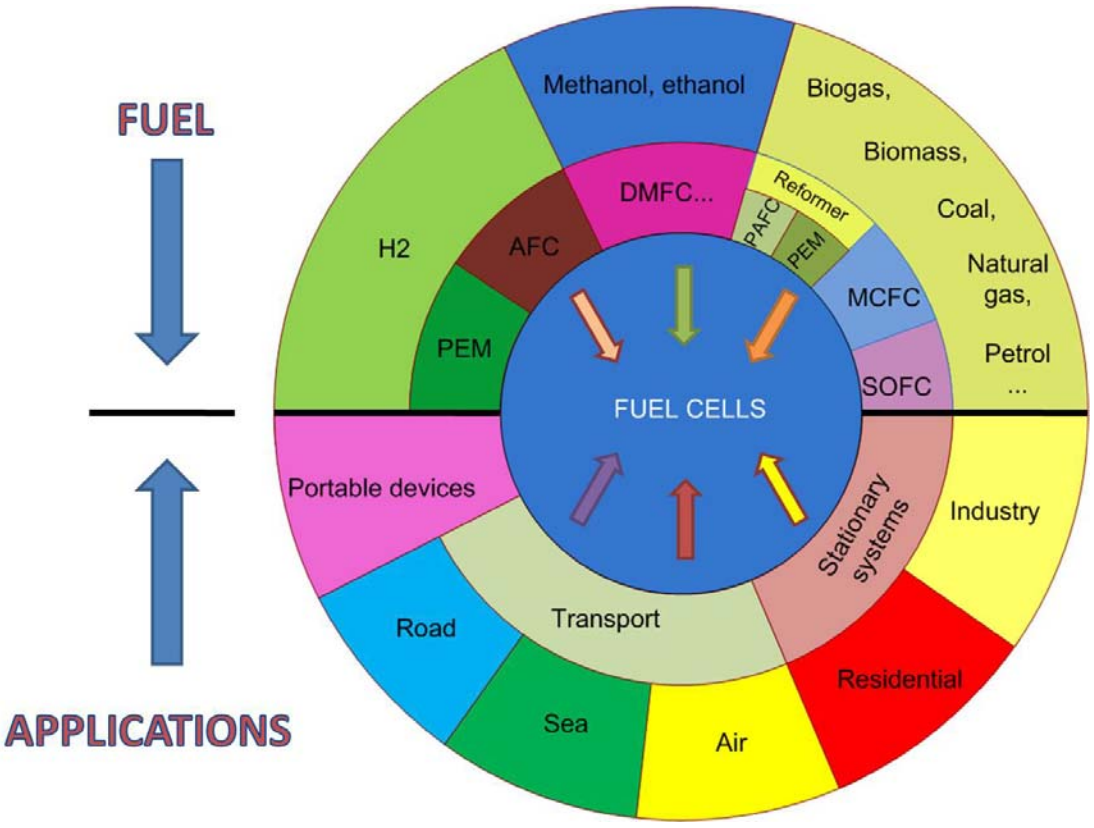
FUEL
APPLICATIONS
Methanol, ethanol
Biogas,
Biomass,
Coal,
Natural gas,
Petrol ...
H2
DMFC...
Reformer
PAFC
PEM
AFC
MCFC
PEM
SOFC
FUEL CELLS
Portable devices
Stationary systems
Industry
Transport
Road
Residential
Sea
Air

Figure 1.3 The working mechanism of direct methanol fuel cells (DMFCs). Methanol is directly used as a fuel source in DMFCs and oxidized at the anode. Oxygen from air is used as oxidant at the cathode. The theoretical voltage of DMFCs is ~1.2 V.

Direct Methanol Fuel Cell (DMFC)

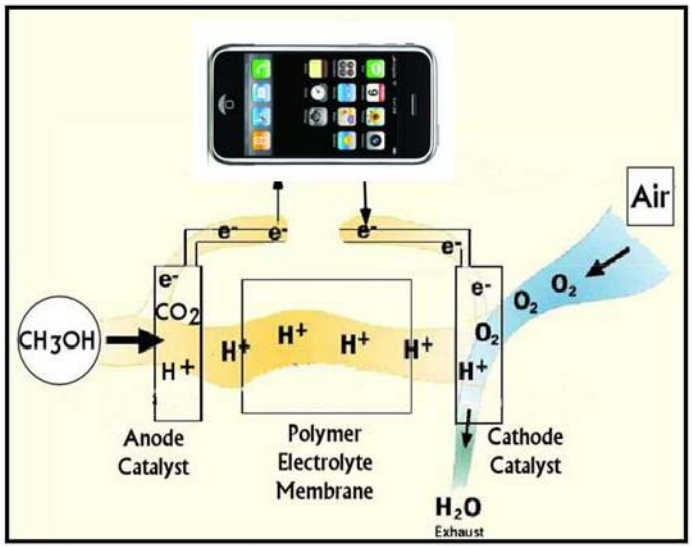

Anode Reaction: $CH_3OH + H_2O \rightarrow CO_2 + 6H^+ + 6e^-$

$E_{anode} = -0.20V$

Cathode Reaction: $3/2O_2 + 6H^+ + 6e^- \rightarrow 3H_2O$

$E_{cathode} = 1.00V$

$$E_{theo} = 1.2V$$

anode and cathode materials and react with oxygen molecules directly from air on the surface of the cathode to produce water as final by-product. Energy conversion efficiencies of DMFCs can reach values as high as 80% in different calculation methods, which is much higher than direct combustion. The free energy change for the overall reaction of a DMFC is -702 $kJ \cdot mol^{-1}$ with the enthalpy being -726 $kJ \cdot mol^{-1}$. The theoretical standard electromotive force (emf) of this reaction is 1.20V. Unfortunately this value is never reached due to the significant overpotentials for the anodic and cathodic reactions at the electrode surfaces. It is clear that the development of advanced functional materials as electrocatalysts plays a key role to the commercialization of fuel cell technologies.[9-13] For the case of methanol oxidation shown in Figure 1.3, its mechanism can be summarized in two steps; namely the electroadsorption of methanol to on the electrode surface followed by further oxidation of adsorbed carbon-containing intermediates to CO_2. Platinum[14] exhibits some activity towards this reaction but is easily poisoned by carbon monoxide (CO) which is the most common intermediate in methanol oxidation. Platinum-based bimetallic[15-17] catalysts have been introduced and widely studied for two reasons: 1) the secondary element lowers the cost of catalyst itself by decreasing platinum usage; 2) the additive promoters (the secondary metals) can mitigate poisoning opportunities of the catalysts and decrease the overpotentials. So far, PtRu has been the most successful electrocatalyst towards methanol oxidation for industrial applications and has been extensively studied.[18-20] Recently, ordered metallic phases, a new category of electrocatalyst, was demonstrated by DiSalvo and Abruña [21-22] as promising candidates towards the electrooxidation of small organic molecules (SOMs). Even with intensive studies and research efforts, the electrocatalyst is still the major obstacle for the wide deployment of fuel cell technologies. One may be surprised that the electrode materials were remained largely. For example, platinum, used like 170 years ago, is still the most widely used electrode material.

In order to guide the design of new electrocatalysts in a rational fashion, it is of great importance to explore and reveal the structure/composition/property relationships and reaction activity of the materials.[23-24] The catalytic activity of a material is determined by its physical and electronic structures which are, in turn, related to their composition and structure. It is clear that both physical and electronic properties may be altered when the electrocatalyst is under active electrochemical control, or in other words, in the active working state. Thus, the ideal characterization of a catalyst involves measurement of its properties during the catalytic reaction. If these properties are measured, and their relationships with catalytic activity are understood in-depth, such knowledge will allow the design of higher performance catalysts.

Electrochemical reactions occur at the interface of an electrolytic solution and an electrode surface. In principle, surface spectroscopic methods, which have no requirement for experimental conditions of ultra high vacuum (UHV), could be used in combination with electrochemical methods to investigate electrocatalysts under reaction conditions, namely, *in-situ*. Even techniques requiring UHV, such as X-ray photoelectron spectroscopy (XPS),[25] high-resolution transmission electron microscopy (HR-TEM),[26] Auger spectroscopy[27] and low energy electron diffraction (LEED),[28] will offer invaluable information while supplementing electrochemical characterization. For *in-situ* measurements, the surface/interface characteristic techniques can be categorized in two ways based on the objective probed. One category of methods probes the electrode surface itself, focusing on the alteration in composition and structure and/or chemical oxidation states, coordinating atoms, and neighbors and bonding distances. X-ray techniques belong to this category and will be discussed in details later. The other category of methods probes adsorbed species on the electrode surface, focusing on the identification and chemical structure of intermediates. These include techniques differential electrochemical mass spectroscopy (DEMS),[29] infrared

spectroscopy (IR)[30] and Raman spectroscopy.[31]

X-ray techniques have been widely utilized to characterize surfaces/interfaces of electrocatalysts in combination with electrochemical performance.[32-33] X-ray diffraction (XRD) is a powerful technique to investigate crystalline structures of solid state materials.[34] Grazing incidence diffraction (GID), (i.e using the incidence angles below the critical angle of the electrode surface), has great surface sensitivity, and is especially well-suited for *in-situ* measurements of bulk electrodes.[35] The crystal truncation rod (CTR) method can probe change in the outmost atomic layer if a significant flat single crystal sample can be obtained.[36] X-ray reflectivity (XRR) can be used to investigate the adsorbed layers such as layer-by-layer polymer structures.[37] X-ray absorption spectroscopy (XAS), also known as extended X-ray absorption fine structure (EXAFS) and X-ray absorption near edge structure (XANES), offer invaluable information on local chemical environment, such as chemical oxidation states, coordination numbers, local geometry, and closest distance to the neighboring atoms.[38-40]

From the foregoing, it is clear that it is of great importance to be able to measure and characterize catalysts under active electrochemical control and obtain an in-depth understanding of structure/composition/property/activity relationships so as to guide the improvement of current catalysts and/or the design of new generations of materials. The work presented in this dissertation was geared towards the in-situ characterization of novel ordered intermetallic phases as fuel cell electrodes. The ultimate goal of this research project is to achieve the objectives described above. Both investigation techniques and materials are important concepts in the research. Ordered intermetallic phases are very promising materials towards the electrooxidations of SOMs. The materials themselves are very interesting for electrocatalytic research. It is of great importance and interest to characterize these kinds of materials under electrochemical

control. Moreover, they also serve as model systems for company to alloy materials or modified single crystal and polycrystalline materials. Single crystal facets of ordered intermetallic phases with well-defined and controlled surface terminations can serve as catalytic model systems.

In chapter two, the theory and experimental background of synchrotron radiation, XRD/GID, X-ray fluorescence (XRF) and EXAFS are briefly described and discussed. In chapter three, *in-situ* GID experiments were employed to investigate the surface composition and structure changes of a polycrystalline PtBi electrode as a function of applied potentials in supporting electrolyte only. In chapter four, the effects of active fuel molecules on the stability of these intermetallic phases were characterized *via in-situ* GID. A kinetic stabilization process was observed for different intermetallic phases. Reproducible and controlled surface terminations could be obtained by different electrochemical treatments – oxidized species termination by holding the applied potential and platinum rich skin termination by potential cycling. Chapter five presents experiments related to single crystal intermetallic facets. High quality PtBi and PtPb single crystal facets were fabricated and studied *in-situ* via GID methods. Well-defined external Pt domains, with six-fold hexagonal symmetry, were formed on the single crystal (001) facets which also had a hexagonal pattern but rotated 23 deg relative to the substrate. Polycrystalline Pt domains with high preferential orientation were generated on single crystal (100) facets without any offset angle. In chapter six, a multi-functional X-ray fluorescence experiment was designed and developed to characterize intermetallic nanoparticles. By recording the fluorescence signals from different elements in the matrix and extracting the individual element data via post-experimental data analysis, both quantitative XRF and normal EXAFS data could be obtained at same time. This was also the first attempt to combine XRF with electrochemistry for electrocatalysts characterization under active electrochemical control based on our

knowledge. Chapter seven presents EXAFS investigation of PtBi nanoparticles. Bismuth oxidized species were substantially present in the nanoparticle matrix even for freshly prepared electrodes, but the PtBi intermetallic crystal structure was still maintained even after surface bismuth atoms were aggressively changed via the applied potentials. Chapter eight presents brief closing remarks and future work related to these X-ray techniques and energy issues.

REFERENCES

1. N.S. Lewis and D.G. Nocera, *Proceeding of the National Academy of Sciences* 103, 15729, **2006**
2. D.G. Nocera, *Chem. Rev. Soc.* 38, 13, **2009**
3. N. Armaroli and V. Balzani, *Angew. Chem. Int. Ed.* 46, 52, **2007**
4. M.I. Hoffert, K. Caldeira, A.K. Jain, E.F. Haites, L.D. Harvey, S.D. Potter, M.E. Schlesinger, T.M.L. Wigley, D.J. Wuebbles, *Nature* 395, 881, **1998**
5. Information sources: wikipedia encyclopedia and other internet websites.
6. C.L. Lamy, J.-M. Leger and S. Srinivasan, *Direct Methanol Fuel Cell: From a Twentieth Century Electrochemist's Dream to a Twenty-First Century Emerging Technology,* Kluwer Academic/Plenum Publishers, New York, Vol.24, **2001**
7. E. Reddington, A. Sapienza, B. Gurau, R. Viswanathan, S. Sarangapani, E.S. Smotkin and T.E. Mallouk, *Science* 280, 1735, **1998**
8. K. Scott and A. Shukla, *Direct Methanol Fuel Cells: Fundamentals, Problems, and Perspectives* in *Modern Aspects of Electrochemistry*, Springer, New York, Vol.40, **2007**
9. H.D. Abruña *et al.*, *Bulletin of Chemical Society of Japan* 80, 1843, **2007**
10. J. Zhang, K. Sasaki, E. Sutter and R.R. Adzic, *Science* 315, 220, **2007**
11. V.R. Stamenkovic, B. Fowler, B.S. Mun, G. Wang, P.N. Ross, C.A. Lucas and N.M. Markovic *Science* 315, 493, **2007**
12. R. Narayanan and M.A. El-Sayed, *Nano Letters* 4, 1343, **2004**
13. N. Tian, Z. Zhou, S. Sun, Y. Ding and Z. Wang *Science* 316, 732, **2007**
14. P.S. Kauranen, E. Skou and J. Munk, *J. of Electroanal. Chem.* 404, 1, **1996**
15. V.S. Bagotzky and Y.B. Vassilyer, *Electrochim. Acta* 12, 1323, **1967**
16. W.H. Lizcano-Valbuena, V.A. Paganin and E.R. Gonzalez, *Electrochim. Acta* 47,

3715, **2002**

17. K.L. Ley, R. Liu, C. Pu, Q. Fan, N. Leyarovska, C. Serge and E.S. Smotkin, *J. Electrochem. Soc.* 144, 1543, **1997**
18. M. Watanabe and S. Motoo, *J. of Electroanal. Chem.* 60, 267, **1975**
19. V. Radmilovic, H.A. Gasteiger and P.N. Ross, *J. Catal.* 154, 98, **1995**
20. J.S. Spendelow and A. Wieckowski, *Phys. Chem. Chem. Phys.* 21, 2654, **2007**
21. E. Casado-Rivera, Z. Gál, A.C.D. Angelo, C. Lind, F.J. DiSalvo and H.D. Abruña, *Chem. Phys. Chem.* 4, 193, **2003**
22. E. Casado-Rivera, D.J. Volpe, L. Alden, C. Lind, C. Downie, T. Vázquez-Alvarez, A.C.D. Angelo, F.J. DiSalvo and H.D. Abruña, *J. Am. Chem. Soc.* 126, 4043, **2004**
23. G. Rupprechter and C. Weilach, *Nnao Today* 2, 20, **2007**
24. N.M. Markovic and P.N. Ross, *Surface Science Reports* 45, 117, **2002**
25. S.S.C. Yu, E.S.Q. Tan, R.T. Jane and A.J. Downard, *Langmuir* 23, 11074, **2007**
26. J. Hu, Y. Zhang, B. Liu, J. Liu, H. Zhou, Y. Xu, Y. Jiang, Z. Yang and Z.-Q. Tian, *J. Am. Chem. Soc.* 126, 9470, **2004**
27. S. Thomas, Y.-E. Sung, H. S. Kim and A. Wieckowski, *J. Phys. Chem.* 100, 11726, **1996**
28. J. Sanabria-Chinchilla, H. Abe, F.J. DiSalvo and H.D. Abruña, *Surface Science* 602, 1830, **2008**
29. H. Wang and H. Baltruschat, *J. Phys. Chem. C* 111,7038, **2007**
30. P.J. Kulesza, M.A. Malik, A. Denca and J. Strojek, *Anal. Chem.* 68, 2442, **1996**
31. H.W. Abernathy, E. Koep, C. Compson, Z. Cheng and M. Liu, *J. Phys. Chem. C* 112, 13299, **2008**
32. R. Schlögl, *Advances in Catalysis (Chapter 5)* 52, 273, **2009**
33. S.R. Bare and T. Ressler, *Advances in Catalysis (Chapter 6)* 52, 339, **2009**

34. J.M. Ziegelbauer, D. Gatewood, A. F. Gullá, M.J.-F. Guinel, F. Ernst, D.E. Ramaker and S. Mukerjee, *J. Phys. Chem. C* 113, 6955, **2009**
35. L. Xiao, L. Zhuang, Y. Liu, J. Lu and H.D. Abruña, *J. Am. Chem. Soc.* 131, 602, **2009**
36. N.M. Marković, C.A. Lucas, B.N. Grgur and P.N. Ross, *J. Phys. Chem. B* 103, 9616, **1999**
37. H. Imai, K. Izumi, M. Matsumoto, Y. Kubo, K. Kato and Y. Imai, *J. Am. Chem. Soc.* 131, 6293, **2009**
38. S. Maniguet, R.J. Mathew and A.E. Russell, *J. Phys. Chem. B* 104, 1998, **2000**
39. F.J. Scott, C. Roth and D.E. Ramaker, *J. Phys. Chem. C* 111, 11403, **2007**
40. V.S. Murthi, R.C. Urian and S. Mukerjee, *J. Phys. Chem. B* 108, 11011, **2004**

CHAPTER TWO

EXPERIMENTAL OVERVIEW

The main objective of this research project is to reveal the structure-composition-property-activity relationships of catalysts and offer invaluable information to guide the design of new advanced materials for fuel cell applications. The work is based on the utilization of synchrotron radiation X-ray based characteristic techniques to perform surface/interface investigations of the specific electrode materials in bulk or nanoscale phases under active electrochemical control. Novel ordered intermetallic phases were studied as they represent a new category of model catalytic system in comparison to alloys and modified single crystal surfaces. In this chapter, all the experimental aspects of the X-ray techniques used in the following chapters will be extensively discussed, focusing on the specific experimental set up and design for the combination of surface characteristic techniques and electrochemical methods. Also included is brief discussion of the background and theory of the various techniques. Additional detailed experimental information will be discussed in the materials and experimental sections of each of the following chapters.

2.1 Synchrotron Radiation Basics[1-2]

X-rays were discovered by W.C. Röntgern in 1895 in Wüzburg and are a type of electromagnetic wave. The relationship between the wavelength and energy is given by:

$$\lambda\left[\text{Å}\right] = \frac{12.398}{\varepsilon[\text{keV}]} \qquad \text{Eq. 2.1}$$

Since the time they were discovered, X-rays have become an invaluable tool to probe the structure of matter. There have been 23 Nobel Prize Laureates related to the X-ray research community, who worked on theoretical and experimental X-ray techniques or expanded the impact of X-rays to other interdisciplinary research fields. Steady progress in both theoretical understanding of the interaction of X-rays with matter, and the knowledge of how to exploit this interaction experimentally, continued from the period covering their discovery through to the mid 1970s. The main limitation was the source, which had remained essentially unchanged from about 1912. In those early days, laboratory X-ray sources were X-ray tubes and the rotating anode. Both of these two methods produce X-rays from an electron beam impinging on a metal anode, although the latter one, which offers 2~3 orders higher flux, only became available on a commercial basis in the 1960's.

There are two distinct components in the spectrum of X-rays generated from all laboratory X-ray instruments. The broad continuous part, so-called *bremsstrahlung* radiation, is due to electrons being decelerated and eventually stopped by the metal and its maximum energy corresponds to the high voltage applied to the tube. The characteristic sharp line spectrum, also known as fluorescence radiation, is superimposed on the top of the broad continuous part and is the consequence of the interaction between X-ray photons and electrons in specific enery levels in the atoms.

In the 1970s, it was realized that synchrotron radiation could potentially be a much more intense and versatile source of X-rays. Synchrotron radiation is produced when charged particles, electrons and positrons, moving at relativistic speeds, are put through magnetic fields which force them to travel along curved trajectories with the cone of radiation being tangential to the direction of motion. In a storage ring, synchrotron radiation is produced either in the bending magnets, needed to keep the electrons in a closed orbit, or in insertion devices such as wigglers or undulators

placed in the straight sections of the storage ring. In these devices an alternating magnetic field forces the electrons to follow oscillating paths rather than moving in a straight line.

Brilliance, which is a combined quantity to determine the quality of an X-ray beam, is given by:

$$\text{Brilliance} = \frac{\text{photons/second}}{(\text{mrad})^2\,(\text{mm}^2\text{source area})(0.1\%\ \text{bandwidth})} \qquad \text{Eq. 2.2}$$

This unit, also known as spectral brightness, can be used to compare the quality of X-ray beams from different sources. Brilliance is also a function of the photon energy.

Figure 2.1 shows the spectral brightness for several synchrotron radiation sources and conventional laboratory X-ray sources. The maximum brilliance for undulators is about 10 orders of magnitude higher than that from a rotating anode source, but for different synchrotron radiation X-ray sources, they exhibit the distinct emission photon energy/characteristic energy curves. The radiation from a bending magnet can be likened to a sweeping search light. The radiation power is particularly intense at the moment when the instantaneous electron velocity points directly towards the observer, but it dies away when the angle between the direction to the observer and the electron velocity is of order γ^{-1}, where γ is the ratio of the electron energy in storage ring to the rest mass energy. The characteristic photon energy of bending magnet is given by:

$$\hbar\omega_c\,[\text{keV}] = 0.665\,\varepsilon_e^2\,[\text{GeV}]\,\text{B}[\text{T}] \qquad \text{Eq. 2.3}$$

where ε_e is the electron energy in the storage ring and B is the magnetic field. From Figure 2.1, the maximum flux from a bending magnetic source at a characteristic energy (critical energy) is ~10^{15} in brilliance units. A wiggler can be viewed as a series of bending magnets, turning successively to the left and to the right. This leads to an enhancement in the intensity of the observed radiation by a factor of 2*N*, where *N* is the number of periods. As shown in Figure 2.1, the spectrum from a wiggler is quite

Figure 2.1 Spectral brightness for several synchrotron radiation sources and conventional laboratory X-ray sources. The data for conventional X-ray tubes should be taken as rough estimates only, since brightness depends strongly on such parameters as operating voltage and take-off angle.[2]

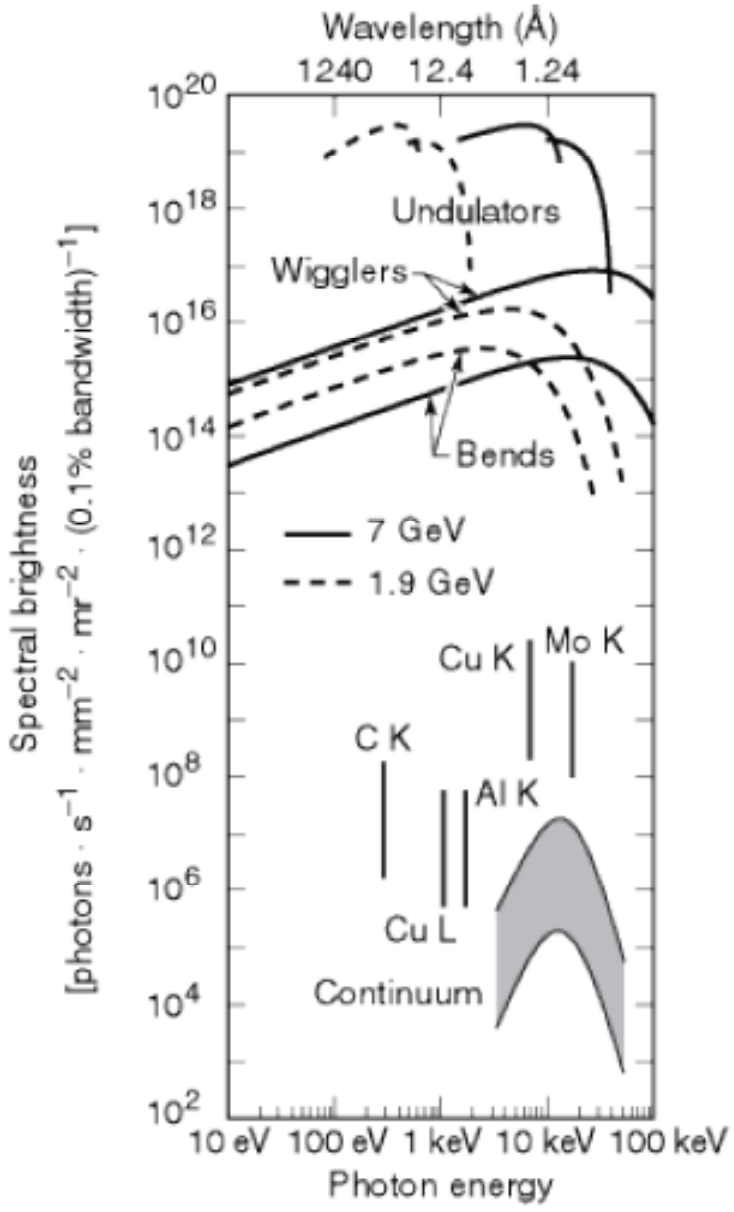
Wavelength (Å)
1240
12.4
1.24
10^{20}
10^{18}
10^{16}
10^{14}
10^{12}
10^{10}
10^{8}
10^{6}
10^{4}
10^{2}
Undulators
Wigglers
Bends
7 GeV
1.9 GeV
Cu K
Mo K
C K
Al K
Cu L
Continuum
Spectral brightness
[photons · s^{-1} · mm^{-2} · mr^{-2} · (0.1% bandwidth)$^{-1}$]
10 eV
100 eV
1 keV
10 keV
100 keV
Photon energy

similar to that from a bending magnet. The maximum flux from a wiggler at the critical energy is ~10^{17} in brilliance units. Unlike a wiggler, where the intensities of the radiation from each wiggle are incoherently added up to give the resulting intensity, in an undulator, the radiation from different periods interferes coherently, thus producing sharp radiation peaks at harmonics of the fundamental when N is equal to 1.

To meet the normal requirements of most end users, the ideal X-ray source should be monochromatic with tunable energy. The angular divergence of the beam should be small, preferably in all directions. The main power of the source beam should be in a quasi-monochromatic band. The beam from an undulator in a third-generation synchrotron storage ring has all of these desired properties. The maximum flux from the undulator shown in Figure 2.1 at the critical energy is over 10^{19} in brilliance units.

Figure 2.2 presents a schematic of a typical synchrotron radiation source. The charged particles (electrons and/or positrons) are injected into the storage ring and circulate at constant energy after achieving relativistic speeds via the small booster ring. Intense X-ray beams are generated while these charged particles are accelerated or decelerated by bending magnets or insertion devices (wigglers and undulators). These raw beams usually have wide energy and angular dispersions which are not ideally suited for well-established experimental techniques. Up-stream optics devices are required to optimize and deliver high quality monochromatic X-ray beams with tunable energy into the experimental hutch of the individual beam stations. Moving mechanical components and data acquisition are achieved via remote, computer controlling software at the end-user experimental interface. All X-ray studies in this dissertation, except for chapter seven (EXAFS investigations), were carried out at the Cornell High Energy Synchrotron Source (CHESS), which is one of the earliest operated synchrotron centers in the world. Table 2.1 provides the information of the operation energies of several major leading synchrotron facilities dedicated to

Figure 2.2 Schematic of a typical synchrotron radiation source which includes an injector (booster ring), a storage ring with different insertion devices (such as bending magnets, wigglers and undulators) and several individual beamlines for end users.

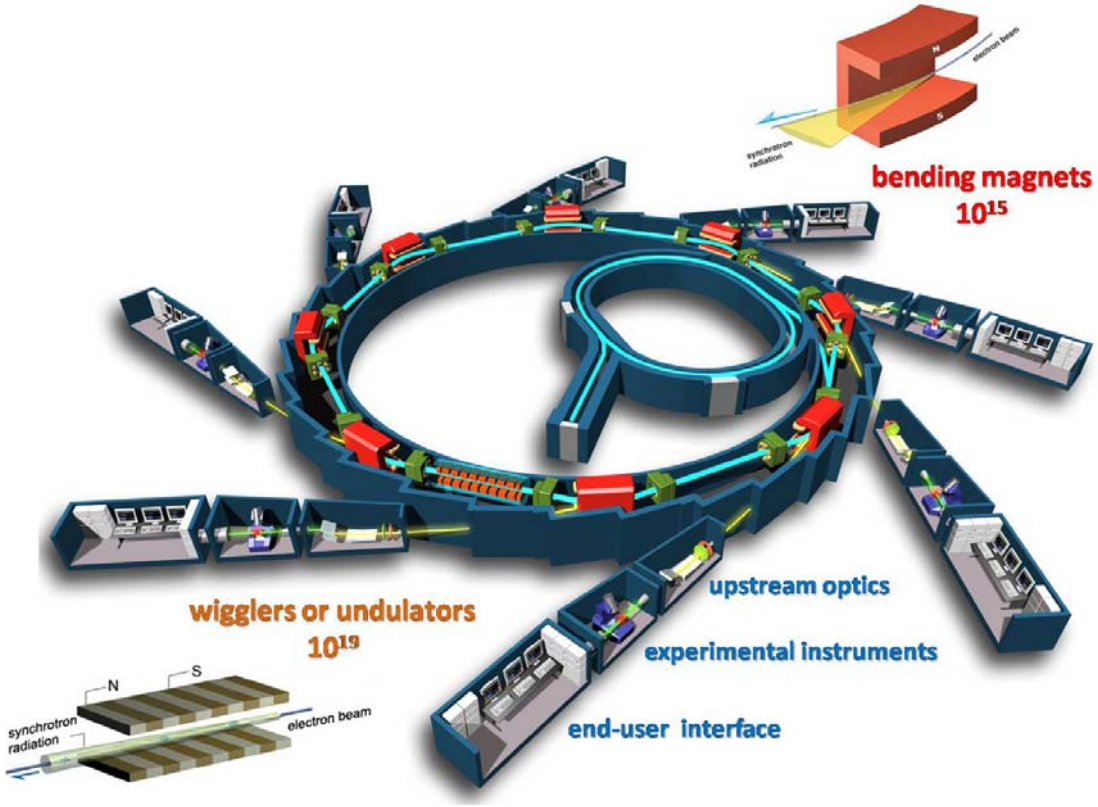
bending magnets
10^{15}
wigglers or undulators
10^{19}
upstream optics
experimental instruments
end-user interface
N
S
synchrotron radiation
electron beam

Table 2.1 Selected synchrotron radiation centers all over the world which are dedicated to X-rays generation and material research applications (the information is adapted from internet sources).

LOCATION	FACILITY	ENERGY (GeV)
Argonne, IL	Advanced Photon Source	7
Berkeley, CA	Advanced Light Source	1.5-1.9
Ithaca, NY	Cornell High Energy Synchrotron Source	5.5
Stanford, CA	Stanford Synchrotron Radiation Lightsource	3
Upton, NY	National Synchrotron Light Source	2.5-2.8
Nishi Harima, Japan	Super Photon Ring – 8 GeV	8
Grenoble, France	European Synchrotron Radiation Facility	6
Hamburg, Germany	Deutsches Elektronen-Synhcrotron	4.5-5.3
Shanghai, China	Shanghai Synchrotron Radiation Facility	3.5

materials research.[3] The typical operating energy for CHESS is ~5.5 GeV, although it can operate over the energy range of 4-8 GeV. Table 2.2 shows the various well-established X-ray techniques for materials research that are available at different CHESS beam stations.[4] The experiments for our research projects have been performed at G2, C1 and F3 beam stations. *In-situ* high resolution grazing incidence diffraction characterization in combination with electrochemistry for bulk electrodes (polycrystalline and single crystal facets) have been carried out via a home-made six-circle *kappa* diffractometer at the G2 station, and X-ray fluorescence characterization of nanoparticles was carried out at C1 and G2 stations.

2.2 Grazing Incidence Diffraction[1,5]

X-ray photons interact with a crystalline material in two ways: they can be scattered or absorbed. The scattering behavior follows the principle of Bragg's law:

$$2d\sin\theta = n\lambda \qquad \text{Eq. 2.4}$$

This is the condition for constructive interference of an X-ray beam of wavelength λ which has an angle of incidence θ relative to a set of lattice planes a distance d apart. While this is a useful relationship, it does have its limitations, principal among there is the fact that it does not enable us to calculate the intensity of this constructive interference scattering phenomenon. The scattering amplitude factors can be derived from classical electromagnetism and expressed as:

$$F^{\text{crystal}}(\mathbf{Q}) = \sum_{\mathrm{r}_j} f_j(\mathbf{Q})\, e^{i\mathbf{Q}\cdot\mathrm{r}_j} \sum_{\mathrm{R}_n} e^{i\mathbf{Q}\cdot\mathrm{R}_n} \qquad \text{Eq. 2.5}$$

where $\mathbf{R}_n$ is the lattice vector that defines the lattice, and $\mathbf{r}_j$ are the position vectors of the atoms with respect to any one particular lattice site. The above expression has two terms: the first term is the unit cell structure facto and the second term is a sum over

Table 2.2 Brief descriptions of major beam stations at the Cornell High Energy Synchrotron Source (CHESS). The data are adapted from http://www.chess.cornell.edu website. HR-XRD: high resolution – X-ray diffraction; HP-XRD: high pressure – X-ray diffraction; XAS: X-ray absorption spectroscopy; GIWAXS: Grazing incidence wide angle X-ray scattering; XRF: X-ray fluorescence; HR-GID: high resolution – grazing incidence diffraction.

	A2	**B2**	**C1**	**D1**	**F3**	**G2**	**G3**
Source	49 pole wiggler	hard-bending magnet	hard-bending magnet	hard-bending magnet	hard-bending magnet	49 pole wiggler	49 pole wiggler
Energy	7-60 keV	5-35 keV	5-35 keV	6-30 keV	6-20 keV	7-12 keV	7-12 keV
Techniques	HR-XRD	HP-XRD	XAS, XRD	GIWAXS	XAS, XRF	HR-GID	thin film

lattice sites.

Since X-rays are electromagnetic waves, refraction should be expected at the interface between media with different refractive indices. In general for X-rays, the refractive index can be expressed as:

$$n = 1 - \delta + i\beta \qquad \text{Eq. 2.6}$$

where δ is of order 10^{-5} in solid materials and only around 10^{-8} in air. The imaginary part, β, is usually much smaller than δ. Unlike the visible light, for X-rays, n is smaller than unity. The refraction behavior follows the principle of Snell's law:

$$\cos\alpha = n\cos\alpha' \qquad \text{Eq. 2.7}$$

Since the index of refraction for X-ray is less than unity, it implies that below a certain incident grazing angle, so called the critical angle, α_c, X-rays undergo total external reflection. For this case, $\alpha = \alpha_c$ and $\alpha' = 0$ and using Eq. 2.7 allows us to relate δ to the critical angle α_c:

$$\alpha_c = \sqrt{2\delta} \qquad \text{Eq. 2.8}$$

Where, for simplicity, the imaginary part is neglected. With δ being typically around 10^{-5}, α_c is of the order of a milli-radian. The value of the critical angle is actually dependent on the wavelength of the X-ray beam, the electron density of the material and the scattering amplitude per electron.[1] As shown in Figure 2.3, while total external reflection occurs for incidence angles below α_c, there is a so-called evanescent wave within the refracting medium. It propagates parallel to the flat interface, and its amplitude decays rapidly in the materials – typically with a penetration depth of only a few nano-meters. This should be compared with a penetration depth of several micrometers at a glancing angle of several times α_c. The much-reduced penetration depth of X-ray for angles below α_c increases their surface sensitivity. This allows the scattering from the surface and near surface regions to be studied. Grazing incidence

Figure 2.3 Schematic for X-ray total external reflection and an evanescent wave within the medium. At glancing angles, below the critical angle, the reflectivity is almost 100%, and the X-ray only penetrates into the material as an evanescent wave with a typical penetration depth of ~10 Å. In this way X-rays request a surface sensitive probe.

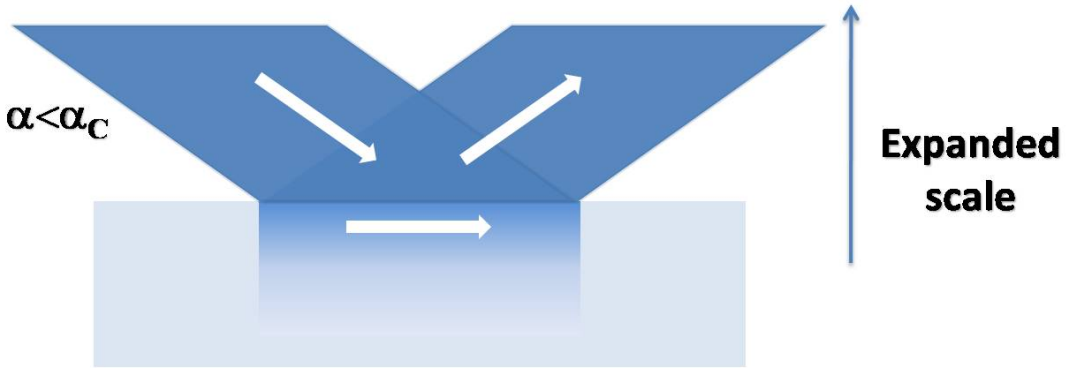
$\alpha<\alpha_C$
Expanded scale

diffraction (GID) is based on this principle and takes advantage of this phenomenon to be a very powerful surface/interface characterization method. Other aspects have been extensively discussed elsewhere.[6]

All GID experiments in this dissertation were conducted at the G2 station of CHESS, which was deliberately built for surface/interface investigations for materials applications. Figure 2.4 shows the home-made six-circle *kappa* diffractormeter employed.[7] Unlike a normal commercial four-circle diffractometer, this *kappa* diffractometer has six circles with the capability of six different degrees of freedoms to control either the sample or the detector. In principle any diffraction spot in reciprocal space can be captured by controlling the movement of these circles (motors). Circle *Mu* is used to select one of the two different experimental geometries, labeled as *psic* and *psicL*. Circles *Phi*, *Eta* and *kappa*, are used to control the degrees of freedom of the samples. *Phi* makes the sample rotate within a plane that is perpendicular to the surface normal of the sample. This circle makes powder and azimuthal scans available. The powder scan method allows averaging of the non-uniform texture of the non-perfect polycrystalline materials and was extensively used for polycrystalline ordered intermetallic samples. The azimuthal scan method allows exploration of the surface texture of single crystal surfaces, especially the crystalline domain structure of the outmost layer of single crystal surfaces. Circles *Nu* and *Del* are used to control the degrees of freedom of the detector. In an in-plane diffraction geometry, (Figure 2.5 (a)), circle *Nu* is scanned within the plane almost parallel to the sample surface. This would be a GID scan if the incidence angle is below the critical angle and has been extensively used to determine surface composition and structure in the following chapters. In an out-of-plane diffraction geometry, (Figure 2.5 (b)), circle *Del* is scanned within the plane almost perpendicular to the sample surface. The scan is utilized to determine the layer-by-layer structure from thin films.

Figure 2.4 Home-made six-circle *kappa* diffractometer. All six circles are labeled here as NU, MU, PHI, KAPPA, DEL and ETA.

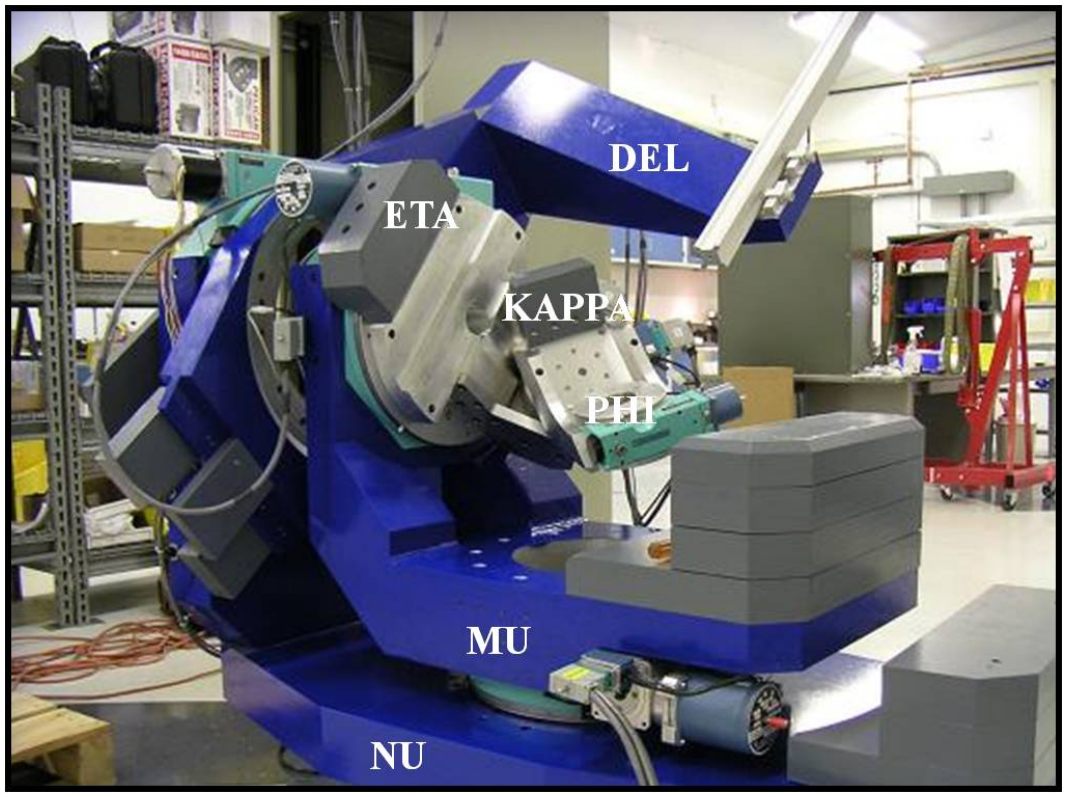
DEL
ETA
KAPPA
PHI
MU
NU

Figure 2.5 Schematics for in-plane diffraction and out-of-plane diffraction geometries. K_i and K_o represent wavevectors of incident and outgoing beams, respectively. Lines here stand for crystal lattice planes. The red part is the outmost layer of the sample surface.

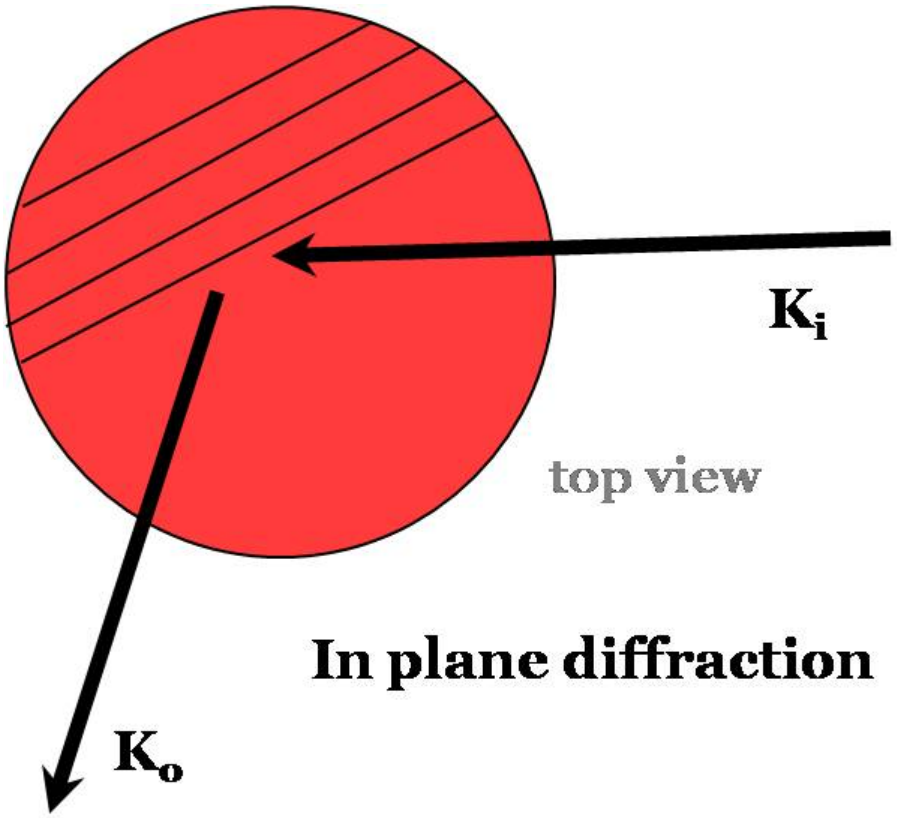
K_i
top view
In plane diffraction
K_o

(a)

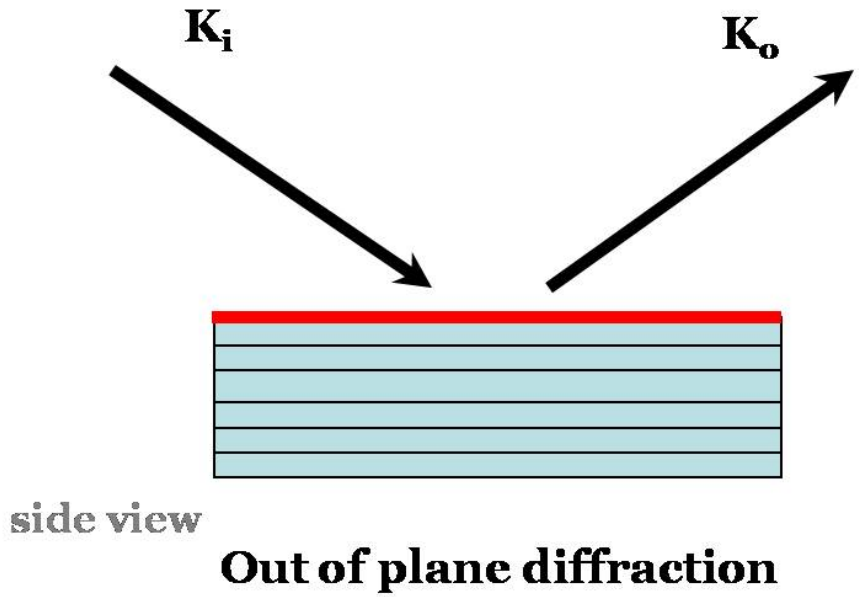
K_i
K_o
side view
Out of plane diffraction

(b)

X-ray diffraction or GID methods are powerful techniques to determine the crystalline structure and composition in qualitative or semi-quantitative approaches. They also can be used to accurately determine the size of small crystalline domains based on the width of X-ray diffraction peaks. The relationship is expressed by the Scherrer equation:

$$B(2\theta) = \frac{0.94\lambda}{L\cos\theta} \qquad \text{Eq. 2.9}$$

where $B(2\theta)$ is the full width, in radians, subtended by the half maximum intensity width of the powder pattern peak; L is the average crystal dimension perpendicular to the reflection planes. Although the Scherrer equation was derived for a sample of cubic crystals, it is often applied to the peak width of noncubic materials and the approximation is acceptable.

A simplified universal procedure is described in the following part while more detailed information will be discussed in chapters three and four. After a complex alignment procedure, an asymmetric beam, 2 mm in horizontal and 200 μm in vertical, was purposely obtained and went through the center of rotation (COR) of the diffractometer. Single crystal surfaces or commercial polycrystalline samples could be used to do energy calibrations. In Figure 2.6 (a), a commercial Pt disc was used to calibrate the energy for GID experiments. A partial survey scan over the 2θ range of 30~40 deg was employed to cover Pt(111) and Pt(002) diffraction peaks. The known *d* spacing values of Pt(111) and Pt(002) and the measured 2θ value could be used to determine the wavelength of the X-ray beam based on Bragg's law. The beam energy could be derived from Eq. 2.1. Figure 2.6 (b) is the pseudo 2D-mapping image of the same scan in which the uniform powder rings suggested a perfect polycrystalline structure. Figure 2.5 shows the real experimental and geometric set up of the GID method employed at the G2 station of CHESS. A rocking scan, also known as a θ-2θ scan, was employed to obtain the X-ray reflectivity (XRR) profile from a commercial

Figure 2.6 Commercial Pt disc used to do energy calibration for GID experiment. (a) is normal partial survey scan; (b) is pseudo 2D-mapping image of the same scan.

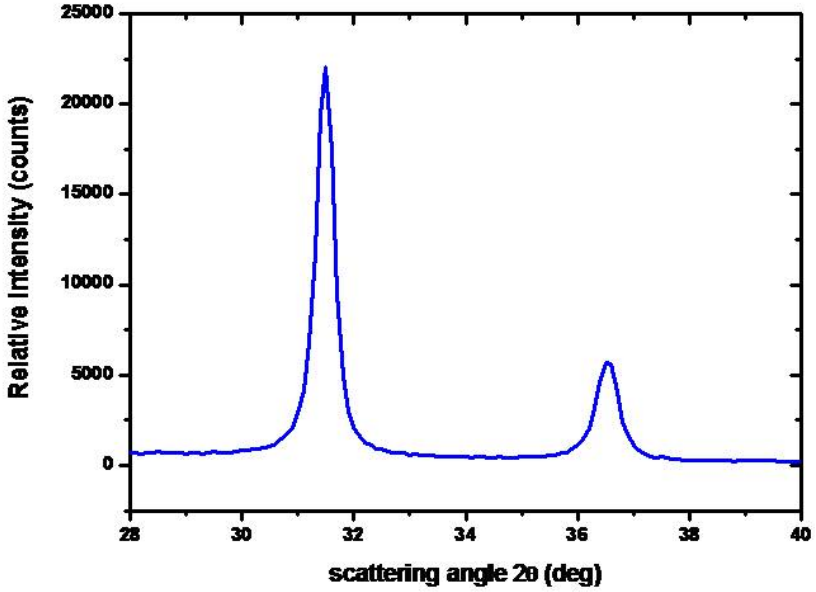
Relative Intensity (counts)
25000
20000
15000
10000
5000
0
28
30
32
34
36
38
40
scattering angle 2θ (deg)

(a)

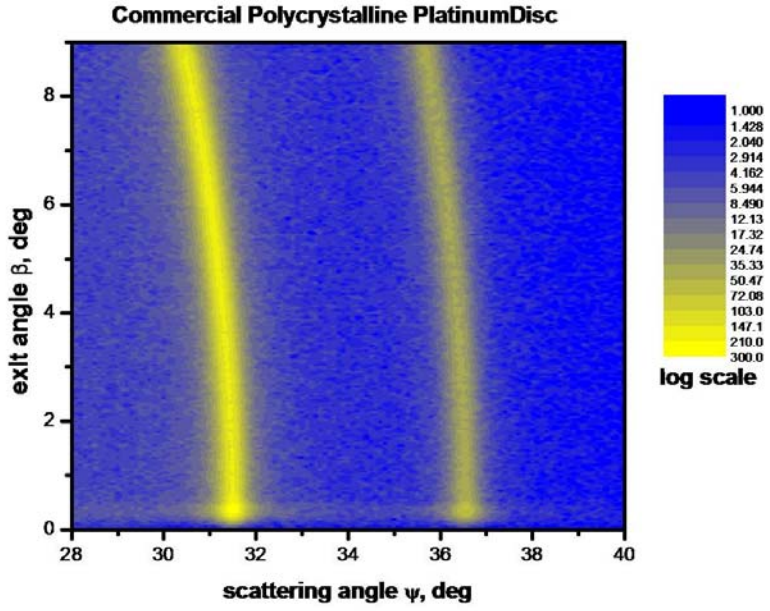
Commercial Polycrystalline PlatinumDisc
exit angle β, deg
8
6
4
2
0
28
30
32
34
36
38
40
scattering angle ψ, deg
1.000
1.428
2.040
2.914
4.162
5.944
8.490
12.13
17.32
24.74
35.33
50.47
72.08
103.0
147.1
210.0
300.0
log scale

(b)

Pt disc sample for energy calibration. The rocking scan was carried out for two reasons: 1) as part of sample alignment, to make the X-ray beam impinge on the surface; and 2) to obtain information about the surface roughness of the sample. The full width at half maximum (FWHM) of the XRR data in Figure 2.7 (a) was ~ 0.18 deg which is quite small and indicates a flat sample surface. The pseudo 2D-mapping image in Figure 2.7 (b) showed the characteristic features below the critical angle. The incidence angle employed for the experiment was ~ 0.2 deg which is well below the critical angle of Pt which is ~ 0.55 deg. Similar rocking scans were also used to check the surface roughness and critical angle features for PtBi and PtPb intermetallic polycrystalline electrodes. As seen in Figure 2.8, the surface roughness of both intermetallic electrodes was much higher than that of commercial Pt disc but they still presented critical angle features from XRR data. Actually, even with a relatively high surface roughness, surface sensitivity was still obtained by comparison with a normal XRD experiment. More detailed information about this will be discussed in chapter three. Figure 2.9 shows the real experimental and geometric set-up of GID method at the G2 station of CHESS. The *in-situ* electrochemical cell was placed at the COR of the diffractometer. A position sensitive detector (PSD), also known as a linear or gas detector, was utilized to record the scattering signals. Soller slits placed after the downstream Huber slits, were set to increase the angular resolution in the horizontal direction.

GID techniques have been widely used in surface/interface characterization for many different research fields, such as polymers,[8-10] biomaterials,[11-12] fuel cells[13-17] and solar cells.[18-20]

Figure 2.7 X-ray reflectivity (XRR) from a commercial Pt disc for energy calibration. (a) Rocking scan for XRR; (b) pseudo 2D-mapping image of the same scan.

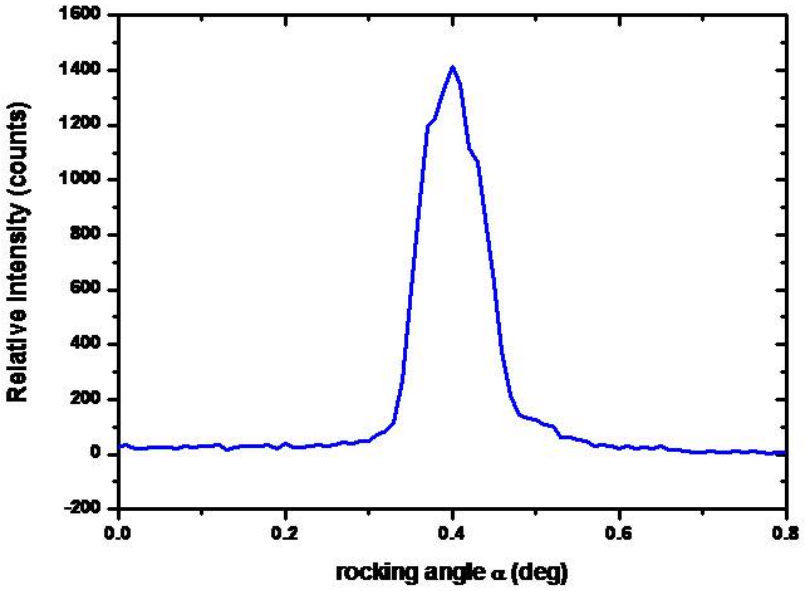
Relative Intensity (counts)
1600
1400
1200
1000
800
600
400
200
0
-200
0.0
0.2
0.4
0.6
0.8
rocking angle α (deg)

(a)

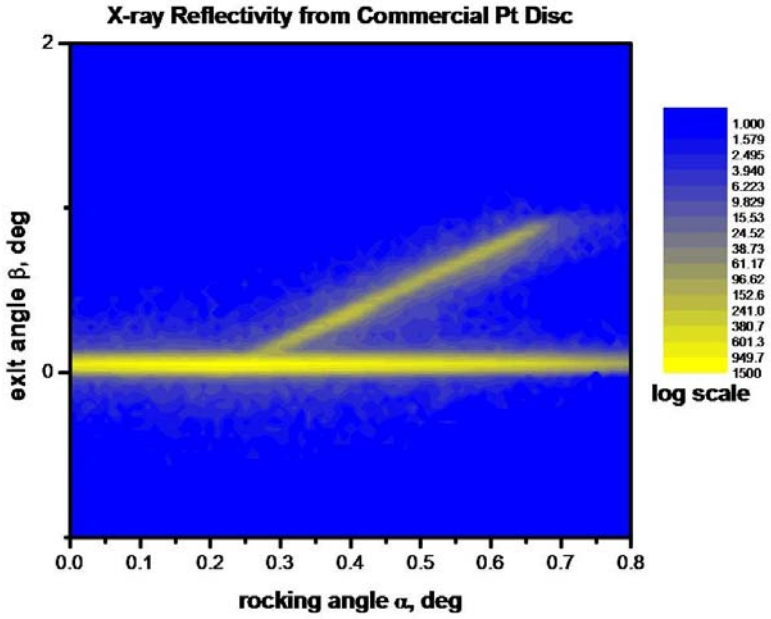
X-ray Reflectivity from Commercial Pt Disc
exit angle β, deg
2
0
0.0
0.1
0.2
0.3
0.4
0.5
0.6
0.7
0.8
rocking angle α, deg
1.000
1.579
2.495
3.940
6.223
9.829
15.53
24.52
38.73
61.17
96.62
152.6
241.0
380.7
601.3
949.7
1500
log scale

(b)

Figure 2.8 Pseudo 2D-mapping images of XRR rocking scans for PtBi (a) and PtPb electrodes (b).

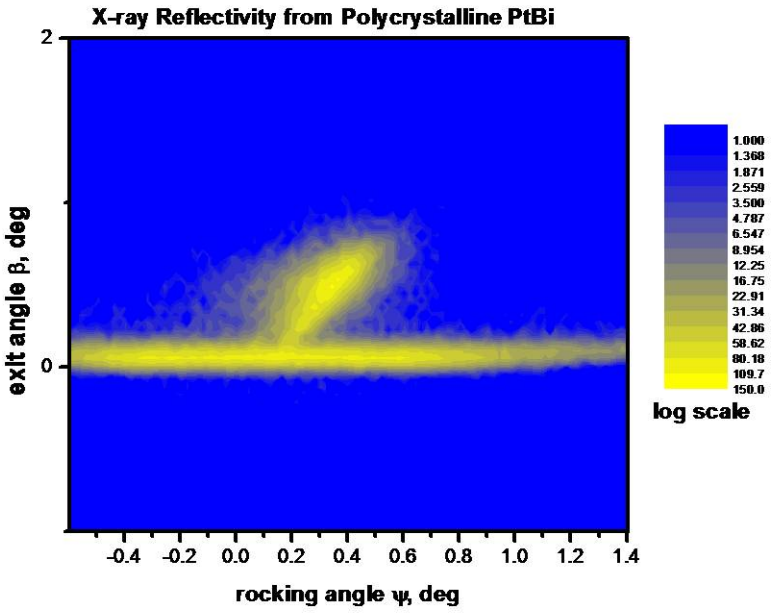
X-ray Reflectivity from Polycrystalline PtBi
exit angle β, deg
rocking angle ψ, deg
log scale
1.000
1.368
1.871
2.559
3.500
4.787
6.547
8.954
12.25
16.75
22.91
31.34
42.86
58.62
80.18
109.7
150.0

(a)

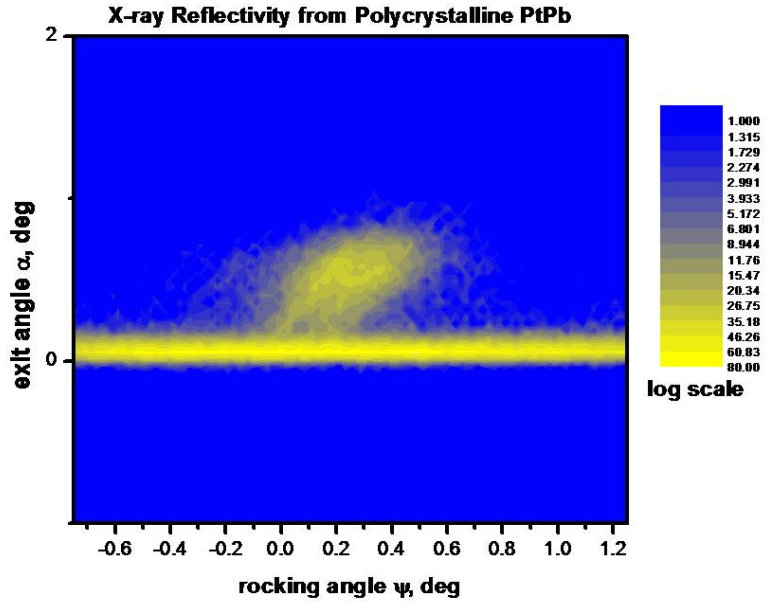
X-ray Reflectivity from Polycrystalline PtPb
exit angle α, deg
rocking angle ψ, deg
log scale
1.000
1.315
1.729
2.274
2.991
3.933
5.172
6.801
8.944
11.76
15.47
20.34
26.75
35.18
46.26
60.83
80.00

(b)

Figure 2.9 GID experimental set-up at the G2 station of CHESS. *In-situ* electrochemical cell is placed at the center of rotation of the diffractometer.

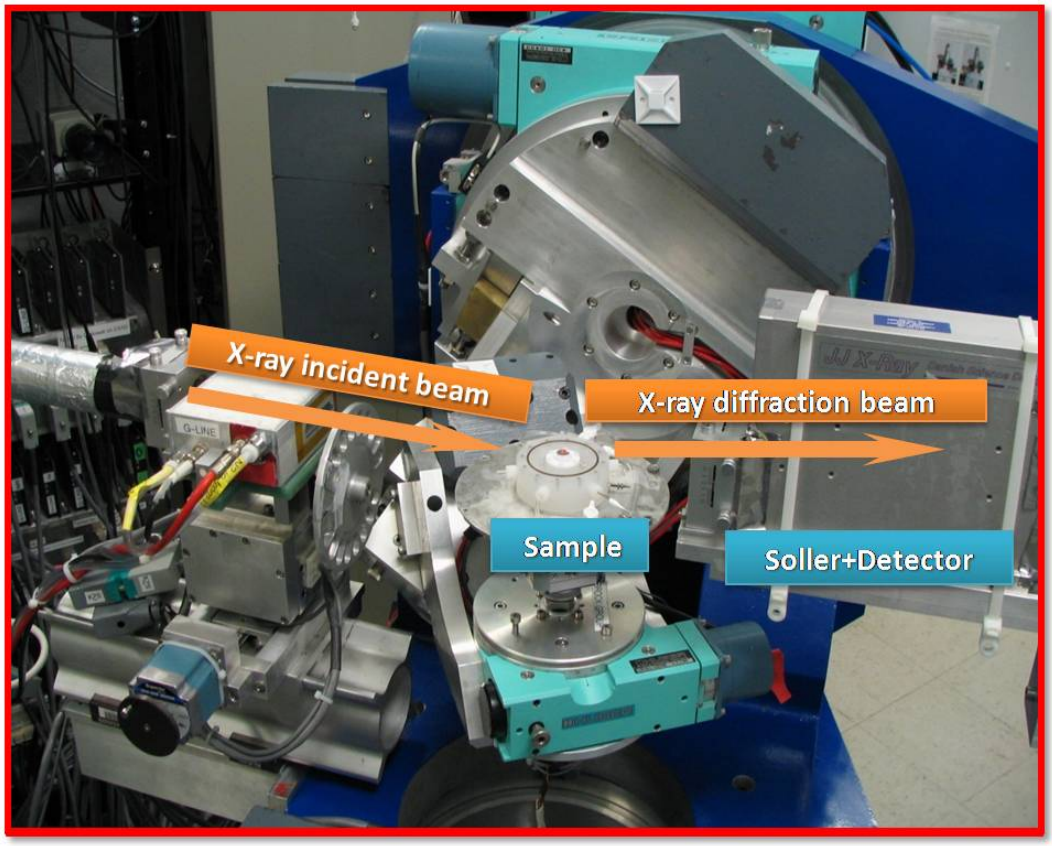
X-ray incident beam
X-ray diffraction beam
Sample
Soller+Detector

2.3 X-ray Fluorescence Characterization[21, 2]

X-ray fluorescence spectroscopy is one of many techniques used for the determination of elemental composition. It falls under the general category of spectrometric techniques because elements are identified and their concentration determined by generating spectra from specimens submitted for analysis. More specifically, X-ray fluorescence is classified under atomic spectrochemical techniques because the characteristic X-radiation is generated in atoms.

If a specimen is irradiated with a beam of photons of energy E_0, where E_0 exceeds the critical excitation energy (so-called binding energy) of electrons in a giving atom, some electrons will be ejected from that atom. Atoms in this excited or ionized state are unstable and nearly instantly an electronic transition takes place in order to refill the vacancies left by the ejected electrons. Thus, if a *K* level electron is ejected, the vacancy may be filled by a *L*, *M*,… level electron. Similarly, an *L* level vacancy may be filled by an *M*, *N*,… level electron. Each transition constitutes an energy loss resulting in the emission of an X-ray photon, its energy being equal to the difference between the two energy levels involved. Figure 2.10 shows a schematic of the process of specific X-ray fluorescence emission. The transition can be expressed by labels of two energy levels involved. For example, the transition of an L_3 level electron to the *K* level vacancy results in the emission of a photon labeled K-L_3 (or K_α, in Siegbahn notation):

$$E_{K-L_3}\left[E_{K_\alpha}\right] = E_K - E_L \qquad \text{Eq. 2.10}$$

Instead of the X-ray fluorescence emission process described above, there is another process, similar to the Auger process for photoelectron emission, involving three different energy levels. An electron from an inner shell energy level is ejected by an incident X-ray photon and leaves a vacancy at this level. An electron from a middle

Figure 2.10 Schematic of the X-ray fluorescence emission process. An electron from an inner shell level is ejected by an incident X-ray photon and a vacancy is left behind. An electron from an upper shell may fill this vacancy and energy difference between the two energy levels involved is dissipated via X-ray fluorescent radiation.

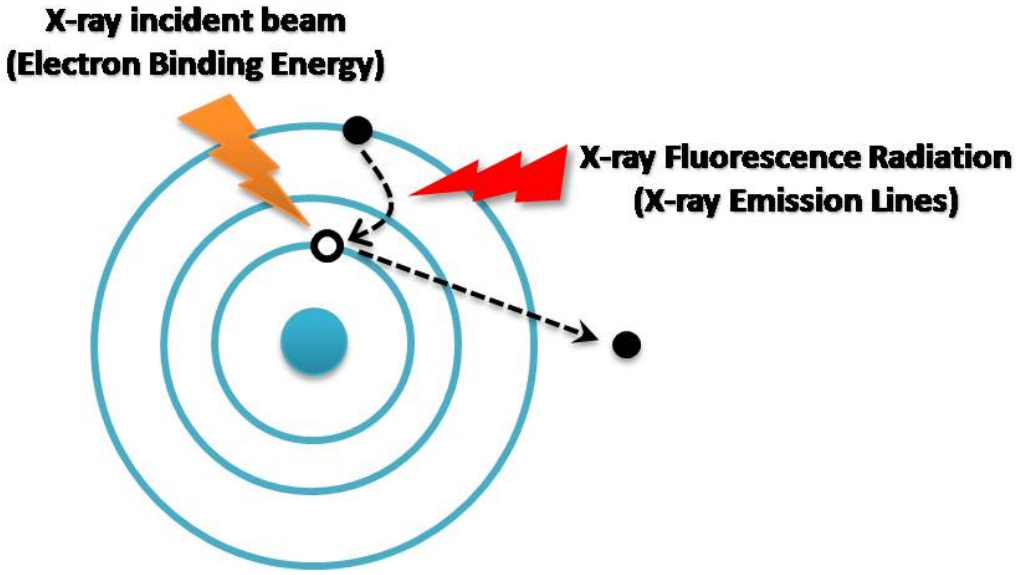
X-ray incident beam
(Electron Binding Energy)
X-ray Fluorescence Radiation
(X-ray Emission Lines)

shell energy level may fill this vacancy with the extra energy being dissipated via a non-radiative process instead of the emission of specific X-ray photons, and a new vacancy is left on the middle shell energy level. The atom is still in an excited and/or ionized state and unstable. An electron from an outer shell energy level may transfer to the middle shell energy level, filling that vacancy with the energy difference between the middle and outer shell energy levels being emitted as characteristic X-ray radiation. For example, an L_2 level electron transfers to fill the initial vacancy on the L_1 level and extra energy is dissipated via non-radiation and at same time there is a new vacancy left on L_2 level. Then an L_3 level electron fills the generated vacancy on the L_2 level and the transition results in the emission of a photon labeled as L_1-L_2-L_3. The characteristic photon energy generated by the process involving three different energy levels could be designated as the latter two energy levels because the initial vacancy energy level has no relationship to the energy of the X-ray fluorescent photons.

When X-rays interact with a specimen, the emission intensities of the different characteristic lines depend on three major factors inclduing: 1) the absorption jump ratio; 2) the relative intensity f of a characteristic line within its series; 3) the fluorescence yield ω. Figure 2.11 shows the transitions which give rise to the emission lines in relation to the experiments in chapter six. For example, $L\alpha_1 = L_3$-M_5; $L\alpha_2 = L_3$-M_4; $L\beta_1 = L_2$-M_4; $L\beta_2 = L_3$-N_5; $Ll = L_3$-M_1 and $L\gamma_1 = L_2$-N_4. Among these transitions, $L\alpha_1$ has the highest relative intensity, 100, and $L\beta_1$ has the second highest relative intensity, 67. All the other transitions have quite low relative intensities. The relative intensities of the different characteristic emission lines vary with different elements.

All XRF experiments to investigate intermetallic nanoparticles in this dissertation were carried out at the C1 station of CHESS. It is of great importance to characterize intermetallic nanoparticles because catalysts in nanomaterial form are utilized as final products in industrial applications. The well-established GID method for surface/

Figure 2.11 Schematic of the transitions that give rise to partial X-ray emission lines.

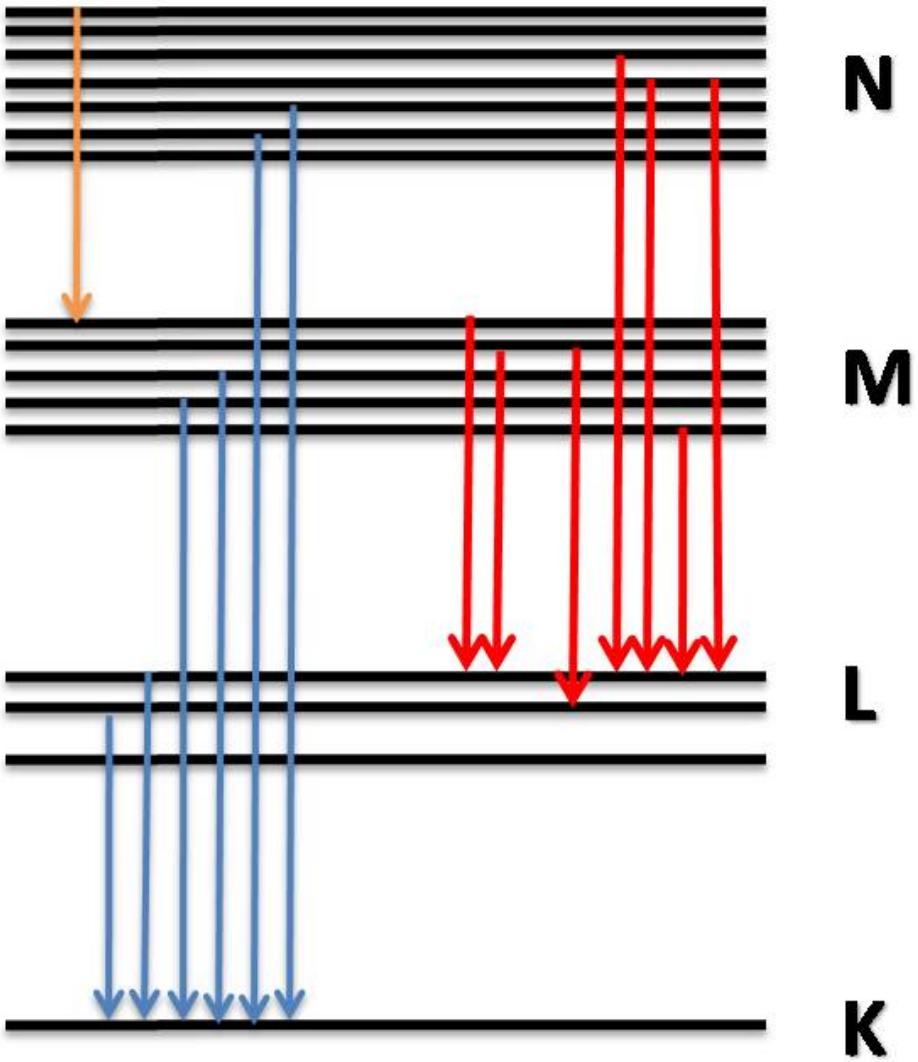

Partial X-ray Emission Lines

interface characterization is unable to probe nanoparticle samples for the following reasons: 1) Diffraction techniques are qualitative or semi-quantitative approaches; 2) for an *in-situ* measurement of a nanoparticle modified electrode, the fairly small amount of nanoparticles cannot give intense diffraction signals and the measurement also fails due to the backscattering interference from the substrate electrode; 3) most importantly, diffraction techniques offer information on the long-range ordered crystalline structures, but for the nanoparticles, the atoms of the outmost surfaces often do not have the same crystalline structure as the core material. The diffraction method is not sensitive to probe the change in structure and/or composition for this part of atoms. Although XRF has wide applications in many interdisciplinary research fields,[22-26] few literature has reported this method to characterize electrocatalysts under electrochemical active control.

In principle, the geometric and experimental set up for XRF characterization is quite straightforward. XRF, in combination with electrochemistry for PtBi and PtPb nanoparticle electrodes, has some special requirements to obtain high quality XRF data. The incidence angle was ~ 1 deg to probe the entire thin film layer of the nanoparticles on the glassy carbon substrate electrode. For the case of PtBi intermetallics, the major emission lines from Bi and Pt elements are very close to each other and cannot be completely resolved by the detectors. To solve this problem and obtain accurate fluorescence signals from each element, two detectors were deliberately set up for recording: 1) Bi fluorescence was mainly recorded by an X-Flash detector with a single channel analyzer (SCA) to only cover the bismuth fluorescence peak. This detector minimized the interference of Pt fluorescence signals but could not get rid of the tail effects. 2) At the same time, all fluorescence signals were recorded by a VORTEX detector with a multi channel analyzer (MCA). The simulation and fitting of each individual emission peak was achieved by

post-experimental data analysis and accurate fluorescence signals, without any interference, could be easily extracted. More detailed information of XRF characterization will be discussed in chapter six.

2.4 Extended X-ray Absorption Fine Structure (EXAFS)[1,27]

An X-ray absorption spectrum of free atoms has no oscillatory structure well above the X-ray absorption edge and monotomically decreases with increasing incidence photon energies. X-ray absorption spectra of molecules, solids and any other material, other than free atoms, exhibit a fine oscillation structure, so called EXAFS. This oscillatory structure is produced by the interference between the outgoing and backscattered waves as shown in Figure 2.12. In other words, the basic origin of EXAFS can be ascribed to the modulation of the final-state wave function of outgoing photoelectrons due to the presence of neighboring atoms which scatter the photoelectrons. In 1971, Sayer, Stern and Lytle pointed out[28], based on the short-range order theory, that a Fourier transform of EXAFS with respect to the photoelectron wave number should peak at distances corresponding to nearest-neighbor coordination shells of atoms.

When an incident X-ray beam passes through a material of thickness *t*, the intensity of the transmitted beam is expressed as:

$$I_t = I_0 e^{-\mu(E)t} \qquad \text{Eq. 2.11}$$

where I_0 is the intensity of incidence beam and $\mu(E)$ is absorption coefficient. This expression is equal to:

$$\mu(E) = \frac{1}{t} \ln \frac{I_t}{I_0} \qquad \text{Eq. 2.12}$$

The absorption coefficient $\mu(E)$ is approximately determined by:

Figure 2.12 Schematic of the EXAFS process. An electron of the targeted atom (blue) is ejected by an X-ray photon. This photoelectron can be treated as spherical outgoing wave which propagates in all directions in space. This outgoing wave can interact and be scattered by the near neighboring atoms (orange) around the targeted atom. The oscillatory structure in the EXAFS spectrum is due to the constructive and destructive interference between the outgoing and scattered waves.

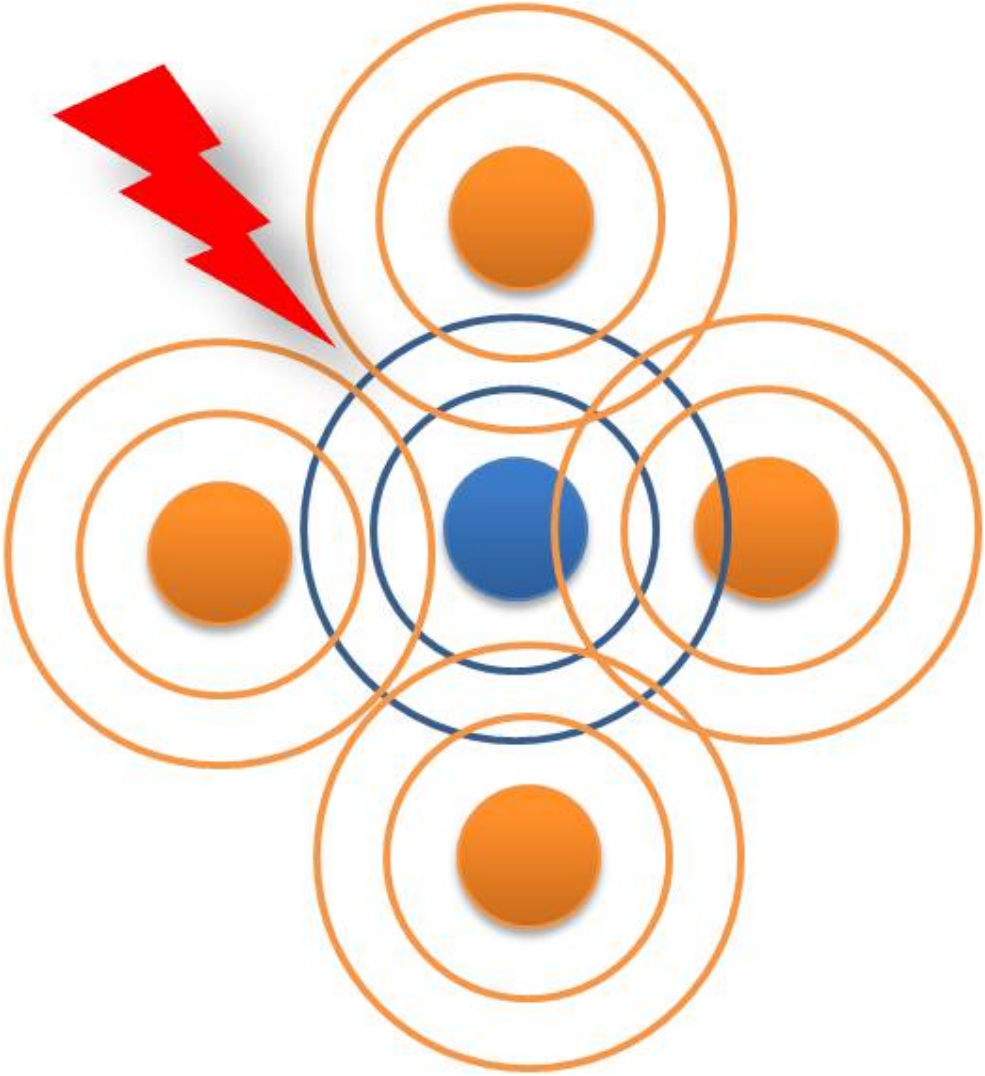

$$\mu(E) \approx \frac{\rho Z^4}{AE^3} \qquad \text{Eq. 2.13}$$

where ρ is the density of the material, Z is the atomic number, A is the atomic mass and E is the incident beam energy.

The EXAFS is elucidated from the measured absorption coefficient $\mu(E)$ by the following equation:

$$\chi(E) = \frac{\mu(E) - \mu_0(E)}{\mu_0(E)} \qquad \text{Eq. 2.14}$$

where $\mu_0(E)$ is the absorption coefficient of the isolated atom, and $\mu(E)$ is the absorption coefficient of the atom in the material of interest. Since EXAFS is an interference effect, which depends on the wave nature of the photoelectron, it is convenient to think of EXAFS in terms of the photoelectron wavenumber, k, rather than energy:

$$\mathrm{k} = \sqrt{\frac{2m(E - E_0)}{\hbar^2}} \qquad \text{Eq. 2.15}$$

where E_0 is the energy of photoelectron, and E is the energy of incident X-ray beam.

To determine the structure surrounding the absorbing atom, the experimental EXAFS data can be fitted using the EXAFS equation as follows:

$$\chi(\mathrm{k}) = \sum_j \frac{N_j f_j(\mathrm{k}) e^{-2\mathrm{k}^2\sigma_j^2}}{\mathrm{kR}_j^2} \sin\left[2\mathrm{kR}_j + \delta_j(\mathrm{k})\right] \qquad \text{Eq. 2.16}$$

where f(k) and δ(k) are photoelectron scattering properties of the neighboring atoms. This equation can be used to determine various parameters: 1) R, distance to neighboring atoms; 2) N, coordination number or neighboring atoms; 3) σ^2, mean square disorder of the neighbor distance. Only a simplified theory of EXAFS is described above. There are some excellent reviews on this topic.[29-31]

All EXAFS experiments in this dissertation were carried out at at the Materials

Research Collaborative Access Team (MRCAT) beamline, Sector 10-ID, of the Advanced Photon Source (APS) at Argonne National Laboratory (ANL), IL. EXAFS data were obtained in fluorescence mode for Pt and Bi L_3 edges of PtBi nanoparticles. EXAFS data of reference materials, such as Bi_2O_3, Bi powder and Pt foil were obtained in transmission mode. For both of experimental geometries, multiple scans obtained for each experimental condition were rebinned, summed, deglitched, and normalized using Athena software.[32] Athena employs the AUTOBK algorithm for background minimization below the *R*bkg value, which in our case was set to 1.0. More detailed information about EXAFS experiments will be discussed in chapter 7.

2.5 Combination of electrochemistry and X-ray techniques

The electrocatalytic activity of a material is determined by its composition and structure which together define the physical and electronic structure of a material. It is clear that both physical and electronic properties may be altered when an electrocatalyst is under active electrochemical control. One goal of catalyst characterization is to measure these properties *in-situ* (as the catalyst works) and to relate these properties to the catalytic activity and selectivity. If these properties are measured, and their relationships with catalytic activity is understood, then the knowledge obtained will allow the research to design these properties into the catalyst.[33-35] There are many methods, such as laser spectroscopy, polarization-modulated infrared (IR) spectroscopy, and high pressure photoelectron spectroscopy, can be used to probe the structure of a catalyst under reaction conditions.

X-ray techniques are powerful methods for the surface/interface characterization of nanomaterials. To take advantage of synchrotron radiation, X-ray techniques, in

combination with electrochemical characterization, offer invaluable information about the composition and structure of electrocatalysts under active electrochemical control. More importantly, different X-ray characterization methods can complement each other to offer information for crystalline and non-crystalline/amorphous species at the same time from well-established experimental designs. X-ray diffraction technique in combination with electrochemistry, is a powerful method to explore the crystal structure of surfaces (at grazing incidence condition) or for bulk structures (for incident angles several times the critical angle.) Unfortunately, diffraction techniques are not suitable to investigate amorphous species or nanoparticles for the reasons described in section 2.3. On the other hand, X-ray absorption spectroscopy is a powerful technique to characterize species with short-range order.

In order to conduct *in-situ* X-ray studies for different phases of intermetallic electrocatalysts, a special *in-situ* electrochemical cell was purposely designed. Figure 2.13 presents the pictures of this *in-situ* electrochemical cell in assembled (a) or disassembled (b) conditions. The cell body was machined from Kel-F and had 12 threaded holes evenly spread out on the top of the cell. An aluminum flange holding a thin (5 μm) polypropylene film was placed on the top. An exchangeable sample holder designed for accommodating different diameters of working electrodes was at the center of the cell. An internal platinum wire served to make electrical contact to the ordered intermetallic working electrode. There were two O-rings (internal/external) to provide leak-proof liquid seals. There were four threaded holes around the side wall of the cell. Two of them were used as solution inlet and outlet, respectively. One was used for Ag/AgCl (sat. NaCl) reference electrode and the final one was for connecting to a coiled platinum wire serving as an auxiliary electrode. There were six screw holes on the bottom of the cell which were used to attach the cell to an aluminum cell holder (not shown here). The whole design was intended to: 1) prevent the leakage of the

Figure 2.13 *In-situ* electrochemical cell in assembled (a) and disassembled (b) conditions.

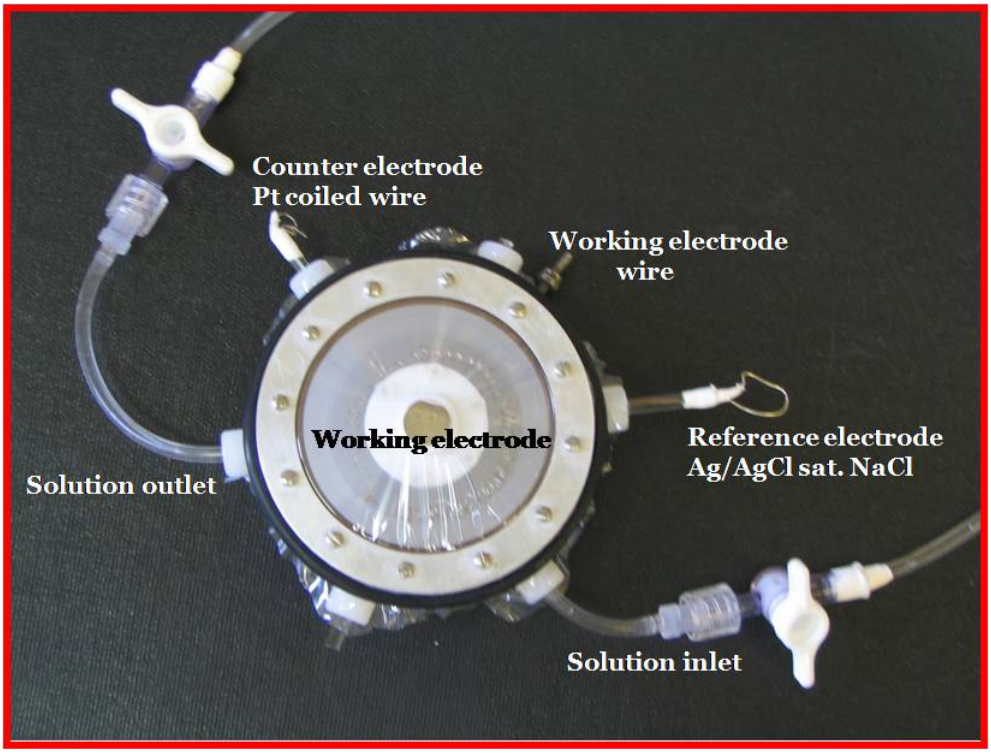
Counter electrode
Pt coiled wire
Working electrode
wire
Working electrode
Reference electrode
Ag/AgCl sat. NaCl
Solution outlet
Solution inlet

(a)

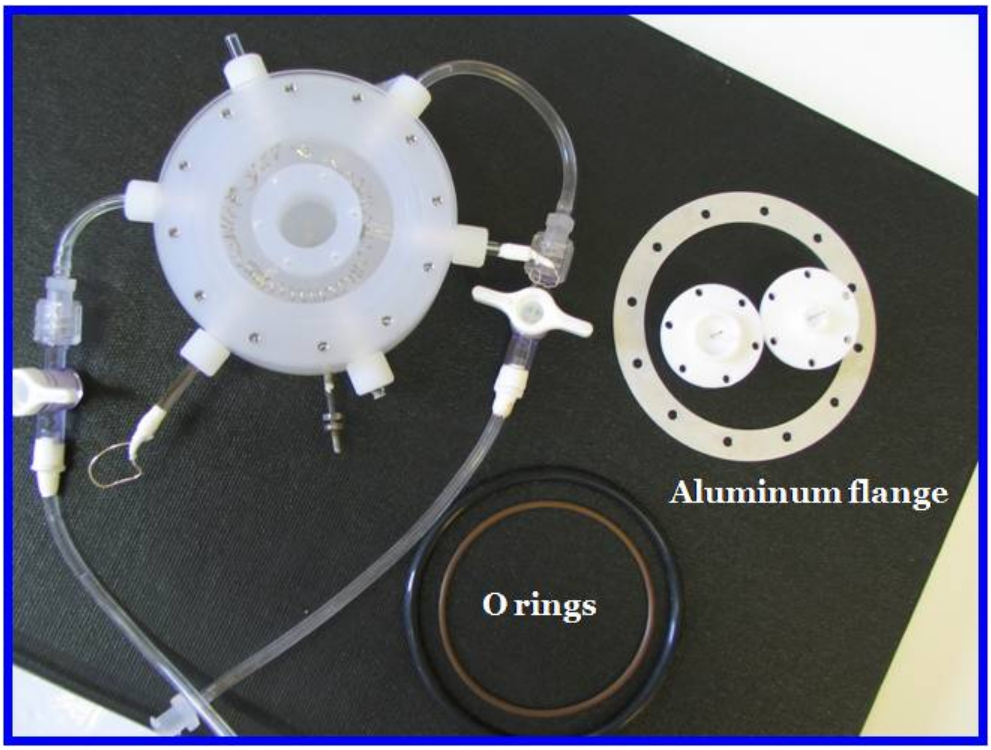
Aluminum flange
O rings

(b)

electrolyte solution from the cell on to the diffractometer and/or other instrumental parts; 2) attach the cell onto a goniometer and placing it at the center of rotation of the diffractometer. This cell can be utilized for Surface X-ray GID experiment for polycrystalline and single crystal intermetallic electrodes and EXAFS/XRF investigations for nanoparticles or solid state samples via fluorescence mode. There is no special requirement for the polymer films used to seal the whole cell for EXAFS/XRF experiments, but the film should be as thin as possible to minimize interferences raising from absorption and scattering phenomena. For surface GID investigation of PtBi and PtPb intermetallic phases, polypropylene (PP) film was selected over other conventional films (such as mylar and kapton) for normal X-ray studies because only PP had no diffraction signals interfering with the diffraction peaks of Pt and the intermetallics. More detailed information will be discussed in chapter three for *in-situ* electrochemical set up in combination with the X-ray diffraction techniques.

REFERENCES

1. J. Als-Nielsen and D. McMorrow, *Elements of Modern X-ray Physics*, Wiley, England, **2001**
2. A. Thompson *et al.*, *X-ray Data Booklet*, Lawrence Berkeley National Laboratory, **2001**
3. Website source: http://www.lightsources.org
4. Website source: http://www.chess.cornell.edu
5. B.E. Warren, *X-ray diffraction*, Dover, New York, **1969**
6. D.R. Blasini, *Characterization of thin films and the thin film phenomena in electrochemically active systems via X-ray methods*, dissertation, **2006**
7. D.E. Nowak, D.R. Blasini, A.M. Vodnick, B. Blank, M.W. Tate, A. Deyhim, D.-M. Smilgies, H.D. Abruña, S.M. Gruner and S.P. Baker, *Rev. Sci. Instrum.* 77, 113301, **2006**
8. D.W. Breiby, O. Bunk, W. Pisula, T.I. Sølling, A. Tracz, T. Pakula, K. Müllen and M. M. Nielsen, *J. Am. Chem. Soc.* 127, 11288, **2005**
9. J. Bolze, M. Takahasi, J. Mizuki, T. Baumgart and W. Knoll, *J. Am. Chem. Soc.* 124, 9412, **2002**
10. G. Kim, J. Yoon, J.-S. Kim, H. Kim and M. Ree, *J. Phys. Chem. B* 112, 8868, **2008**
11. A. Mihranyan, J. Forsgren, M. Strømme and H. Engqvist, *Langmuir* 25, 1292, **2009**
12. H. Isenberg, K. Kjaer and H. Rapaport, *J. Am. Chem. Soc.* 128, 12468, **2006**
13. T.-W. Kim, S.-J. ParkLindsay, E. Jones, M.F. Toney, K.-W. Park and Y.-E. Sung, *J. Phys. Chem. B* 109, 12845, **2005**
14. Y. Ding, M. Chen and J. Erlebacher, *J. Am. Chem. Soc.* 126, 6876, **2004**

15. V.R. Koganti, D. Dunphy, V. Gowrishankar, M.D. McGehee, X. Li, J. Wang and S.E. Rankin, *Nano Lett.*6, 2567, **2006**
16. G. Wang, M.A. Van Hove, P.N. Ross and M.I. Baskes, *J. Phys. Chem. B* 109, 11683, **2005**
17. P.J. Chupas, K.W. Chapman, G. Jennings, P.L. Lee and C.P. Grey, *J. Am. Chem. Soc.* 129, 13822, **2007**
18. E.J.W. Crossland, M. Kamperman, M. Nedelcu, C. Ducati, U. Wiesner, D.-M. Smilgies, G.E.S. Toombes, M.A. Hillmyer, S. Ludwigs, U. Steiner and H.J. Snaith, *Nano Lett.* **ASAP**, doi: 10.1021/nl803174p
19. T.A. Bull, L.S.C. Pingree, S.A. Jenekhe, D.S. Ginger and C.K. Luscombe, *ACS Nano* 3, 627, **2009**
20. B. Ingham, B.N. Illy, M.F. Toney, M.L. Howdyshell and M.P. Ryan, *J. Phys. Chem. C* 112, 14863, **2008**
21. G.R. Lachance and F. Claisse, *Quantitative X-ray Fluorescence Analysis – Theory and Application*, John Wiley & Sons, England, **1995**
22. K. Tsuji, K. Nakano, H. Hayashi, K. Hayashi and C. Ro, *Anal. Chem.* 80, 4421, **2008**
23. P. Wobrauschek, *X-ray Spectrom.* 36, 289, **2007**
24. C. Streli, *Appl. Spectro. Rev.* 41, 473, **2006**
25. A. Ide-Ektessabi, *Applications of Synchrotron Radiation*, Springer, Berlin, **2007**
26. M. West, A.T. Ellis, P. Kregsamer, P.J. Potts, C. Streli, C. Vanhoof and P. Wobrauschek, *J. Anal. At. Spectrom.* 10, 1304, **2007**
27. Y. Iwasawa, *X-ray Absorption Fine Structure for Catalysts and Surfaces* World Scientific, Singapore, **1996**
28. D.E. Sayers, E.A. Stern, and F.W. Lytle, *Phys. Rev. Lett.* 27, 1204, **1971**
29. J.J. Rehr and R.C. Albers, *Rev. Mod. Phys.* 72, 621, **2000**

30. P.A. Lee and J.B. Pendry, *Phys. Rev. B* 11, 2795, **1975**
31. D.C. Kongingsberger and R. Prins, *X-ray Absorption: Principles, Applications, Techniques of EXAFS, SEXAFS and XANES*, Wiley, New York, **1988**
32. B. Ravel and M. Newville, *Phys. Scr.* T115, 1007, **2005**
33. G. Rupprechter and C. Weilach, *Nnao Today* 2, 20, **2007**
34. R. Schlögl, *Advances in Catalysis (Chapter 5)* 52, 273, **2009**
35. S.R. Bare and T. Ressler, *Advances in Catalysis (Chapter 6)* 52, 339, **2009**

CHAPTER THREE

IN-SITU X-RAY GRAZING INCIDENCE DIFFRACTION CHARACTERIZATION OF ORDERED INTERMETALLIC PHASES FOR FUEL CELL APPLICATIONS*

3.1 Introduction

With the ever increasing need for environmentally friendly power sources and high efficiency energy conversion, fuel cells, which directly convert chemical energy to electric energy via electrochemical reactions, have attracted a great deal of interest, especially in the last 2~3 decades.[1-5] In its most general form, hydrogen gas, used as fuel, is oxidized at the anode to produce protons and release electrons into an external circuit to power an electric device. The protons travel through a membrane to the cathode side, where oxygen molecules (pure oxygen gas or directly from air) are reduced by the previously released electrons to form water and heat as the only by-products.

In recent years, so called "direct" fuel cells operated on the use of small organic molecules (SOMs), such as formic acid and methanol as fuels, have generated a great deal of attention and work.[6-7] However, the use of Pt as an anode for these systems is greatly hindered by large overpotentials and the fact that Pt is readily poisoned by carbon monoxide (CO), which is the most common intermediate product during electrooxidation process of these SOMs. Alloys such PtRu have been shown to mitigate this poisoning by providing oxygenated sites at low potentials facilitating the oxidation of CO to CO_2.[8-10] While these alloys have shown enhanced performance in certain cases, they have some inherent shortcomings such as the fact that they have a

*Reproduced with permission from the manuscript in preparation, ready to be submitted.

random distribution of the constituent elements and tend to surface segregate under high current operation, resulting in significant performance degradation. DiSalvo and Abruña recently introduced ordered intermetallic phases as promising candidates for fuel cell anode materials for SOMs electrooxidation.[11-12] These materials are crystalline, ordered and exhibit high electrocatalytic activity. For example, PtPb is the most active catalyst known for the oxidation of formic acid. Moreover, they exhibit great resistance to poisoning by CO.

The long term stability and durability of electrodes is of great importance in fuel cell application, especially when one considers the delicate interplay of the different components of the membrane electrode assembly (MEA).[13-14] It is the investigation of such stability of ordered intermetallic phases as a function of applied potentials, which serves as a main objective in the studies presented here. Alloys, such as PtRu, have a very small enthalpy of formation/mixing for the stabilization of the constituent elements. Ordered intermetallic phases, on the other hand, can have large enthalpies of formation which, in turn, can give rise to significant stabilization.

Table 3.1 presents thermodynamic data for PtBi, PtPb and PtRu where the differences in stabilization (expressed as a potential difference) can be significant for both PtBi (220mV) and PtPb(260mV) but essentially negligible (10mV) for PtRu. Such differences in stabilization can have significant consequences in fuel cell performance. In the specific cases of PtBi and PtPb ordered intermetallic phases, the fact that the dissolution and leaching of the less noble metals (Bi, Pb) can be significantly altered, and can extend the potential window of stability of these materials.

When an electrode material is exposed to different electrolytes and applied external potentials, the electrode surface can exhibit different stability and durability in relation to thermodynamic data. Previous research in our group has shown that amorphous

Table 3.1 Thermodynamic data for ordered intermetallic phases and alloys.

Materials	ΔG^0 (kJ/mole)	Electron Numbers (z)	$\Delta E = -\Delta G^0/zF$ (V)
PtBi	-63	3	**+0.22V**
PtPb	-51	2	**+0.26V**
PtRu (alloy)	-2	2	**+0.01V**

oxides, Bi_2O_3 for PtBi and $PbCO_3$ or $Pb(OH)_2$ for PtPb, are formed on the electrode surfaces after exposure to air or when subjected to different E_{ulp} values.[15] In addition, these oxides could dissolve into the supporting electrolyte with the less noble element being depleted. All of these results were based on *ex-situ* X-ray photoelectron spectroscopy (XPS) studies which, although are of value, do not provide information under real electrochemical conditions. Being able to carry out *in-situ* surface characterization is of great importance since it provides unique information about potential-dependent changes in structure and composition.

X-ray diffraction (XRD) is a very powerful technique to investigate a material's crystalline composition and structure. The major limitation of conventional XRD is a lack of surface sensitivity due to its large sampling depth which is also dependent on the experimental incidence angle. Grazing incidence diffraction (GID) has great surface sensitivity.[16] In essence, when the incidence angle is below the critical angle, total external reflection will occur at the interface of a solid surface and another material with a lower optical index of refraction *n*. In such a case, there is an evanescent wave within refracting medium. This wave propagates parallel to the flat interface, and its amplitude decays rapidly in the material - typically with a penetration depth of only a few nanometers. The short decay length of the evanescent wave greatly improves surface sensitivity. This is therefore a powerful analytical method for surface and interface characterization, which benefits greatly from the high brilliance of synchrotron X-ray sources. The critical angle for ordered intemetallic phases (PtBi for this case) is ~0.55 deg. The incidence angle in our GID experiments was 0.25 deg, fully qualified for experimental requirement.

We report here, series of experiments on *in-situ* synchrotron based grazing incidence X-ray diffraction combined cyclic voltammetry (CV) to determine changes in electrode surface crystalline composition and structure of PtBi ordered intermetallic

phases as a function of applied potentials. Initially, we designed and built up a general purpose *in-situ* electrochemical cell which could be used for most *in-situ* X-ray/electrochemical measurements, including diffraction, fluorescence and absorption. We developed precise polishing procedures, so as to generate reproducible surface crystalline composition and structure for these ordered interemetallic phases. In these studies we paid particular attention to the formation of Pt crystalline domains, the leaching out/dissolution process of the less noble metal (Bi) and the influence of electrochemical pretreatment procedure. We also investigated the effects of long term exposure of the PtBi electrode to acidic supporting electrolyte. In our studies we carried out conventional X-ray diffraction as well as surface sensitive grazing incidence diffraction since they provide different sampling depths. The freshly polished ordered intermetallic electrode surfaces were submitted to potential sweeps to increasingly positive upper limit potentials (E_{ulp}) to deliberately dissolve the less noble element from the surface and monitor the changes in surface crystalline structures. Atomic force microscopy was utilized to obtain surface roughness and morphology information to support the X-ray diffraction measurements.

3.2 Experimental Section

3.2.1 Synthesis of ordered intermetallic phases

The synthesis procedure for the polycrystalline ordered intermetallic phase PtBi is briefly described here. Platinum powder (Johnson Matthey, 99.999%) and bismuth powder (Alfa Aesar, 99.9999%) from pellets were thoroughly mixed in the appropriate molar ratios in an agate mortar. Pellets (6 mm OD, 4 mm length) were pressed in a hydraulic press. The pellets were sealed in evacuated fused silica tubes (10 mm ID, 100 mm length) and heated, oriented vertically, in a box furnace to 800 ℃ for 24 hours

and annealed at 650 ℃ for 48 hours. The pellets were ground and the above procedure was repeated twice. More detailed information on the synthesis and characterization of the material have been previously reported.[11]

3.2.2 Optimization of polishing procedure for ordered intermetallic electrodes

Proceeding to electrochemical testing, the electrode surface was initially polished starting from 600 Grit sandpaper (Buehler) for 10 min and then step by step down to 800 Grit sandpaper for 10 min and 1200 Grit sandpaper for 15 min. To optimize the polishing procedure, intended to yield a reproducible surface crystalline composition and structure, the final polishing was carried out with either 1 μm diamond paste suspended in a suitable extender (Metadi-Buehler) or 300 nm alumina / 50 nm alumina suspensions for 15 min to get the final mirror-like electrode surface. Electrodes were rinsed thoroughly with Millipore water and acetone respectively and sonicated for 10 min in both high purity water and acetone. X-ray diffraction and/or GID experiments were employed to check the surface composition and structure after each polishing procedure.

3.2.3 In-situ electrochemical cell

The *in-situ* electrochemical cell was designed and built for combining X-ray surface scattering techniques and electrochemical characterization. Figure 3.1 presents both top and cross-sectional views to better illustrate the design details. The cell body was machined from Kel-F and had 12 threaded holes evenly spread out on the top of the cell. An aluminum flange, holding a thin (5μm) polypropylene film, was placed on the top. An exchangeable sample holder designed for accommodating different diameters

Figure 3.1 Schematic of *in-situ* electrochemical cell: (a) top view; (b) cross-sectional view.

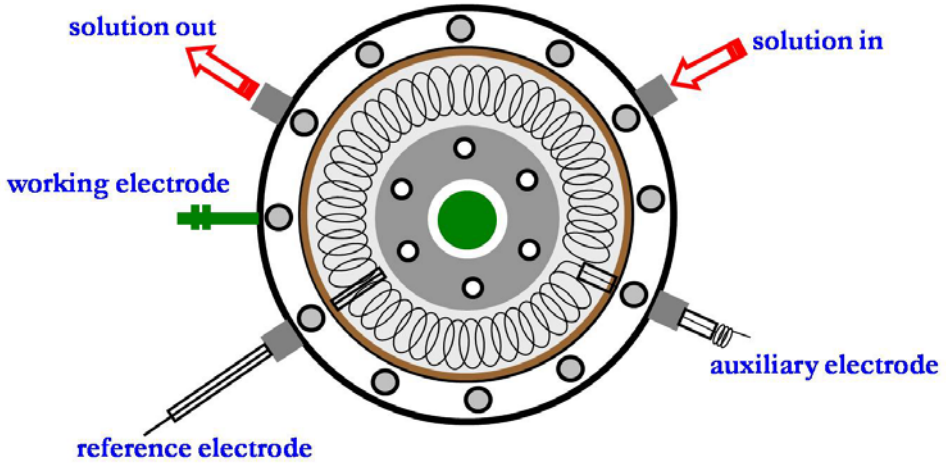
solution out
solution in
working electrode
auxiliary electrode
reference electrode

(a)

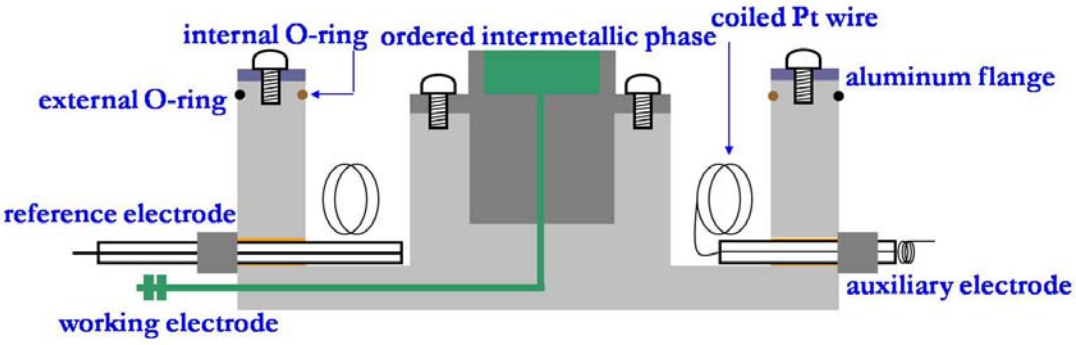
internal O-ring
ordered intermetallic phase
coiled Pt wire
aluminum flange
external O-ring
reference electrode
auxiliary electrode
working electrode

(b)

of working electrodes was at the center of the cell. An internal platinum wire served to make electrical contact to the ordered intermetallic working electrode. There were two O-rings (internal/external) to provide leak-proof liquid seal. There were four threaded holes around the side wall of the cell. Two of them were used as solution inlet and outlet, respectively. One was used for a Ag/AgCl (sat. NaCl) reference electrode and the final one was for connecting to a coiled platinum wire serving as an auxiliary electrode. There were six screw holes on the bottom of the cell which were used to attach the cell to an aluminum cell holder (not shown here). The overall design was intended to: 1) prevent leakage of the electrolyte solution from the cell on to the diffractometer and/or other instrumental parts; 2) attach the cell onto a goniometer and place it at the center of rotation of the diffractometer.

3.2.4 In-situ X-ray grazing incidence diffraction measurements

After a freshly polished working electrode was placed in the cell, a 5 μm polypropylene film was placed on top to seal the whole cell. The polypropylene film was selected for this application after a series of experiments were conducted so as to: 1) minimize the X-ray absorption from the film itself at energies employed; 2) minimize diffraction peaks and background scattering interference within the appropriate angular range under study case; 3) provide a robust and reliable window. The electrolyte solution consisted of 0.1M sulfuric acid in Millipore water. Dissolved oxygen was displaced from the solution by bubbling pre-purified nitrogen for at least 15 min. The supporting electrolyte solution was flowed into the cell via solution inlet and outlet using a syringe and taking great care to eliminate bubbles. For electrochemical studies, additional electrolyte was employed (by expanding the polypropylene film). For XRD/GID investigations, the additional electrolyte was

withdrawn to generate thin film geometry as shown in Figure 3.2. Cyclic voltammetry was carried out on a BAS CV-27 potentiostat/galvanostat (Bioanalytical Systems) and recorded on a computer through a PCI-DAQ card (National Instruments). All potentials are referenced to a Ag/AgCl (saturated NaCl) electrode without regard for the liquid junction potential. The electrochemical pretreatments consisted of cycling the potential at 10mV/s from -0.2V to different E_{ulp}, ranging from +0.4V to +1.2V. After each pretreatment, part of the supporting electrolyte solution was withdrawn so that the polypropylene film was recessed, generating a thin film of electrolyte as described above. The electrolyte film, however, was sufficiently thick to ensure good potential control at all cases. Surface X-ray grazing incidence diffraction was carried out over the range of 30~40 deg which covered Pt(111), Pt(002), PtBi(010), and PtBi(-110) reflections. Particular attention was given to changes in the appearance and intensity of the platinum diffraction peaks as a function of applied E_{ulp}. The critical angle for these Pt-based ordered intermetallic phases is ~0.55 deg. The typical incidence angle employed in our GID experiments was ~0.25 deg, well below the critical angle. We also carried out, for comparison, experiments above the critical angle with an incidence angle of 5.25 deg. All X-ray experiments were carried out at the G-line Station of the Cornell High Energy Synchrotron Source (CHESS). All diffraction experiments were carried out on a home-made six-circle *kappa* diffractometer. The experimental X-ray incidence energy was 9.374 keV (1.323 Å). The beam size was 2 mm horizontal × 200 μm vertical. This asymmetric beam shape was deliberately chosen so as to optimize surface sensitivity. The typical photon flux intensity at the center of rotation (COR) of the diffractometer was ca.10^{13} photons/sec/mm^2. A position sensitive detector (PSD) (also known as one-dimensional linear detector), was utilized for collecting the diffracted beam. The detector's angular resolution was ca. 0.18 deg. A horizontal in-plane X-ray scattering geometry was

Figure 3.2 Schematic of *in-situ* X-ray grazing incidence diffraction measurement.

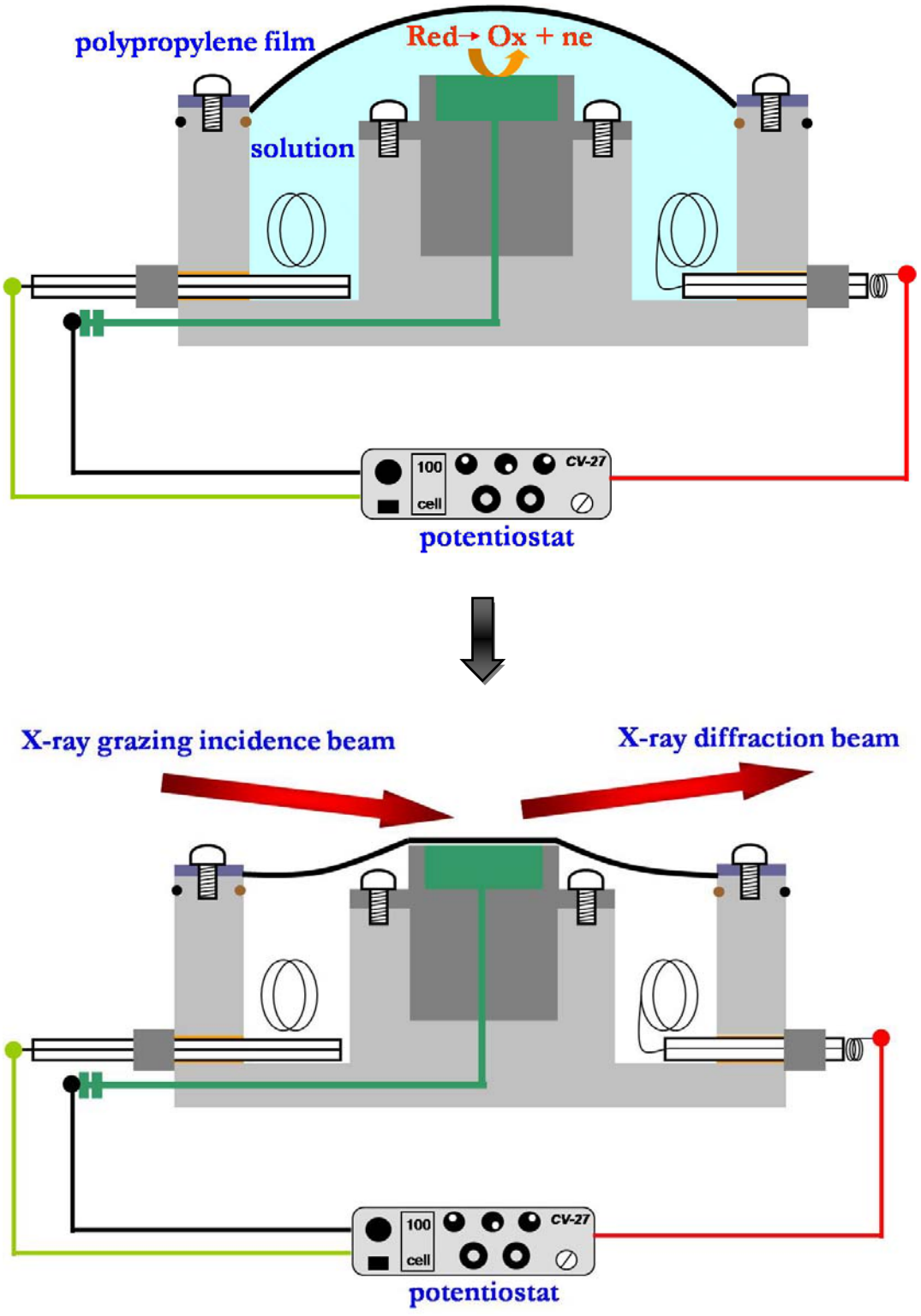
polypropylene film
Red→ Ox + ne
solution
100
cell
CV-27
potentiostat
X-ray grazing incidence beam
X-ray diffraction beam
100
cell
CV-27
potentiostat

employed. In this geometry, the electrode surface normal is perpendicular to the ground, and the detector moves within the plane which is parallel to the electrode surface. More detailed information about the diffractometer and the experimental geometry can be found elsewhere.[17]

3.2.5 Ex-situ atomic force microscopy

In order to complement *in-situ* GID measurements, and to obtain a general idea about surface roughness and morphology, a series of *ex-situ* atomic force microscopy (AFM) experiments were conducted on a Veeco Dimension 3100 SPM/AFM system. The freshly polished PtBi ordered intermetallic phases were prepared as the working electrode. Cyclic voltammetry experiments were carried out in a conventional three-electrode electrochemical cell under identical conditions as described above. The hanging meniscus method was utilized for working electrode and double-side copper tape was used for affixing the working electrode to a holder. After each pretreatment, the working electrode was removed and carefully rinsed by Millipore water for at least 5 min. After drying in air or under a nitrogen stream, the working electrode was transferred to the AFM instrument for investigations. The typical scan range was 10 μm × 10 μm.

3.3 Results and discussions

3.3.1 Optimization of polishing procedure for ordered intermetallic phases

3.3.1.1 Comparison of XRD and GID

We carried out XRD and GID experiments on a freshly polished polycrystalline PtBi electrode. The intent was to demonstrate the difference between these two diffraction

techniques and show the high surface sensitivity of GID. Employing a special polishing procedure to deliberately generate a platinum rich intermetallic electrode surface (more detailed information about polishing effects will be discussed in the next section), the less noble element, bismuth, was leached out from the surface during polishing and Pt nanoscale crystalline domains were formed at the outermost surface. As shown in Figure 3.3, Pt(111) and Pt(002) diffraction peaks were clearly present in the GID pattern, but absent in the XRD pattern. These results clearly demonstrate the specific surface sensitivity of GID vs. XRD. The remaining peaks in both diffraction patterns arose from PtBi diffraction. The different peak intensities for similar 2θ values were due to the internal crystalline asymmetry in this polycrystalline PtBi electrode. This PtBi electrode sample was not a perfect powder polycrystalline material and had some large single crystalline domains in the matrix. As shown in Figure 3.4, pseudo-2D diffraction patterns were integrated using a linear detector and mapped to yield partial powder rings. A perfect-power polycrystalline sample would yield concentric constant diffraction rings and not segmented sections. For the PtBi electrode, the partial powder rings consisted of discontinuous rings (for powder polycrystalline parts) and bright sparkling spots (for large single crystal domains). From an experimental point of view, this "non-perfect" powder polycrystalline situation could be accounted for by survey scans with the azimuth rotating for the sample (average azimuth angle is 200 deg). However, this uneven crystalline composition did not in any way affect our experimental objective, since our aim was to detect the changes in surface crystalline structure and composition as a function of applied potentials. In fact high reproducible GID diffraction patterns could be readily obtained.

Figure 3.3 Comparison of GID and XRD experiments. On a freshly prepared polycrystalline PtBi electrode, survey scans were from 18 deg to 60 deg. The incidence angles were 0.25 deg and 5.25 deg for GID and XRD, respectively. The two red lines in both patterns mark the angular positions of two Pt diffraction peaks.

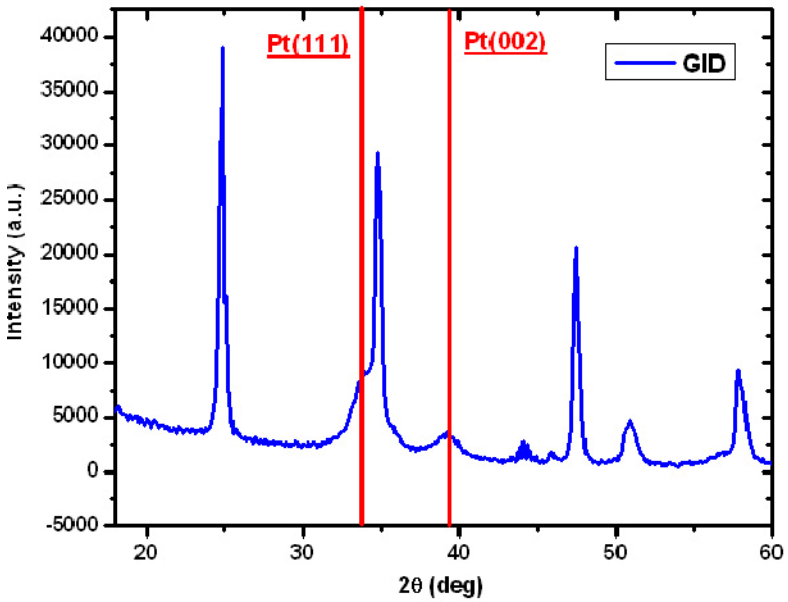
Pt(111)
Pt(002)
GID
Intensity (a.u.)
2θ (deg)
40000
35000
30000
25000
20000
15000
10000
5000
0
-5000
20
30
40
50
60

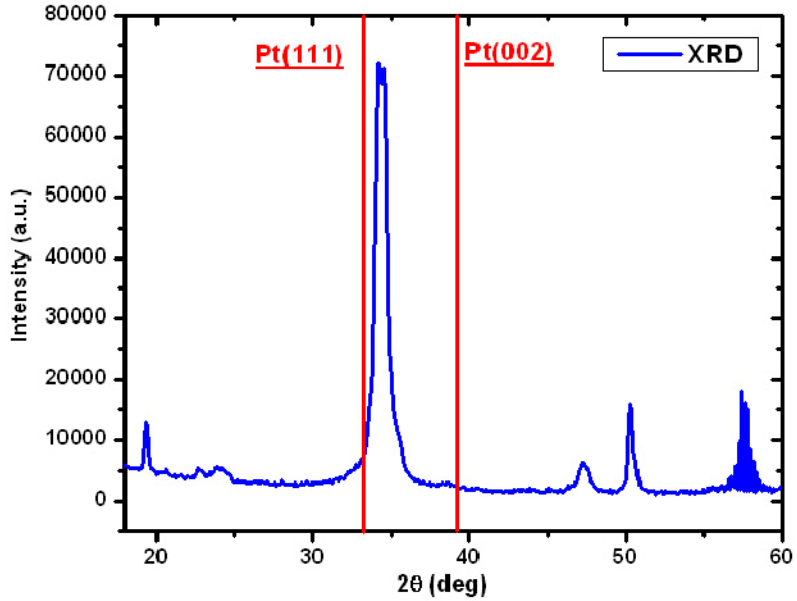
Pt(111)
Pt(002)
XRD
Intensity (a.u.)
2θ (deg)
80000
70000
60000
50000
40000
30000
20000
10000
0
20
30
40
50
60

Figure 3.4 Pseudo-2D-Mapping images of GID (upper) and XRD (lower). These 2D-Mapping images showed partial diffraction rings for the polycrystalline PtBi electrode. Mapping patterns were integrated from the linear detector.

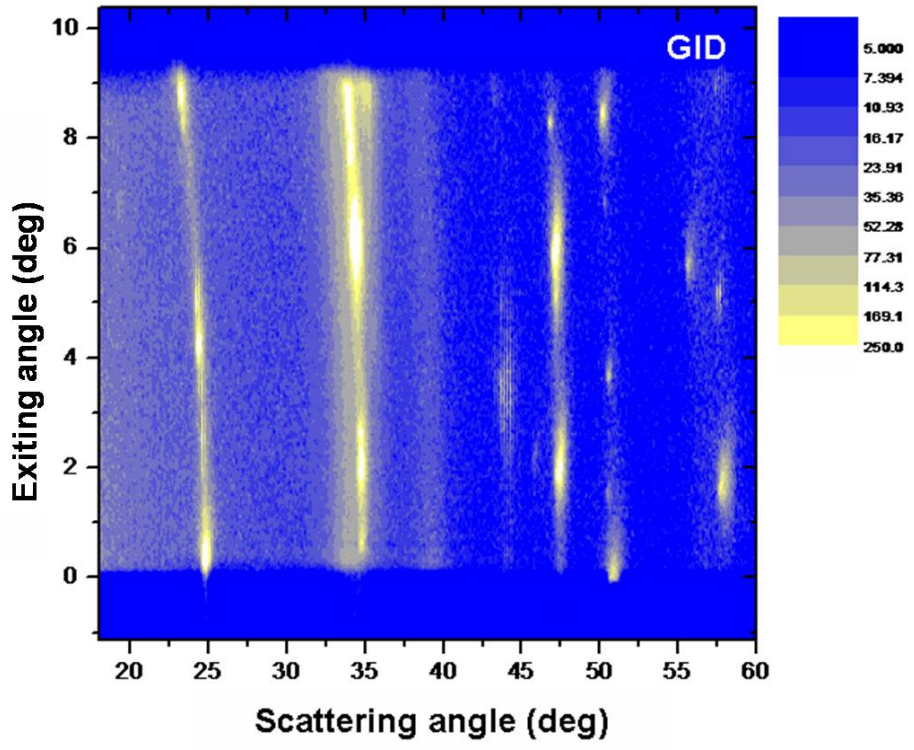
GID
Exiting angle (deg)
Scattering angle (deg)
0
2
4
6
8
10
20
25
30
35
40
45
50
55
60
5.000
7.394
10.93
16.17
23.91
35.36
52.28
77.31
114.3
169.1
250.0

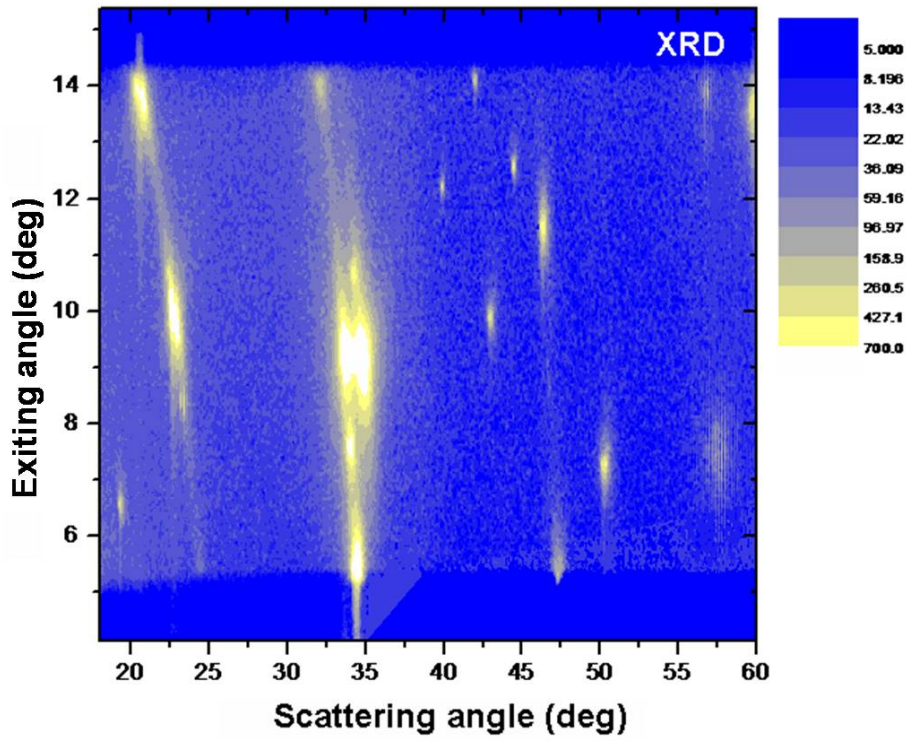
XRD
Exiting angle (deg)
Scattering angle (deg)
6
8
10
12
14
20
25
30
35
40
45
50
55
60
5.000
8.196
13.43
22.02
36.09
59.16
96.97
158.9
260.5
427.1
700.0

3.3.1.2 Optimization of polishing procedure

Polishing procedures can have a substantial influence, not only on the electrode's surface roughness and morphology, but also on surface structure and composition which can, in turn, dramatically affect electrochemical reactivity. The ordered intermetallic electrode surface degraded due to the leaching out of the less noble elements, bismuth, from the intermetallic matrix during some polishing procedures. The major objective of polishing optimization was to reproducibly obtain an intact, stoichiometric intermetallic surface. The initial polishing material employed was very important for an existing Pt-rich intermetallic electrode surface labeled as Pt_{surf}/PtBi. Detectable Pt(111) and Pt(002) diffraction peaks in the GID pattern showed that initial polishing starting with 800 Grit sandpaper or finer ones could not remove the Pt nanoscale crystalline domains from the Pt_{surf}/PtBi electrode. In order to yield intact an interemtallic surface and eliminate the existing Pt nanosize domains, the initial polishing sandpaper had to be 600 Grit or coarser. Taking into account surface roughness, composition and structure, and polishing time, the optimized starting sandpaper was 600 Grit. The final polishing materials were equally or even more important than the initial ones because they had a direct influence on the leaching-out process of the less noble elements. When the final polishing step was done with 300 or 50 nm alumina suspensions, the GID data showed that Pt crystalline domains were formed on the PtBi surface. The use of a 50 nm silica suspension as the final polishing material gave rise to a similar Pt_{surf}/PtBi terminated surface. The formation of this Pt-rich surface was relative to a Bi deficiency on the surface as the less noble element was selectively eroded way due to the "corrosive" effect of specific polishing materials and methods. Finally, the use of 1 μm diamond paste suspended in Metadi-Buehler extender as the final polishing material reproducibly yielded an

essentially stoichiometric mirror-like intermetallic surface. In summary, in order to reproducibly obtain a stoichiometric, mirror-like surface, polishing should start from 600 Grit sandpaper, then step by step down to finer sandpaper, and finalize with 1 μm diamond paste.

3.3.2 Influence of long-term exposure to acidic supporting electrolyte

Ex-situ GID results combined with electrochemical pretreatments showed that a Pt_{surf}/PtBi electrode surface was generated when E_{ulp} was as low as +0.40 V, although the Pt(111) diffraction peak intensity was quite low and the Pt(002) peak was even hardly observed (this is not surprising, since the theoretical intensity ratio of Pt(111)/Pt(002) is 100/14). Another important parameter was the exposure time for PtBi electrode to 0.1M sulfuric acid served as supporting electrolyte solution, since the PtBi electrode was exposure to the acidic supporting electrolyte for at least 50 min before a typical survey scan was completed. In this case, the formation of a Pt_{surf}/PtBi surface was due to the influence of the applied potential and/or long term exposure to sulfuric acid solutions. To discriminate between these two effects, a freshly polished PtBi electrode surface without Pt nanoscale domains was deliberately exposed to 0.1 M sulfuric acid solution for over 4 hours. After the electrode was removed from the electrochemical cell and rinsed thoroughly with Millipore water, surface GID experiments were carried out to focus on the Pt diffraction regions. Neither Pt(111) nor Pt(002) diffraction peaks were evident and no detectable Pt signals were obtained especially when compared to the situation induced by an applied E_{ulp} of +0.4 V or higher. In a summary, long-term exposure to acidic supporting electrolyte solutions did not lead to the formation of Pt crystalline domains on the PtBi substrate.

3.3.3 In-situ X-ray GID measurement

Cyclic voltammetric characterization of the polycrystalline PtBi electrode was carried out in the *in-situ* electrochemical cell. These cyclic voltammograms were consistent with profiles obtained in a conventional three-electrode electrochemical cell via the hanging meniscus method. As shown in Figure 3.5 (a), the electrochemical pretreatments for ordered intermetallic PtBi electrodes consisted of a series of potential cycles at 10 mV/s from -0.2 V to different E_{ulp} in 0.1 M sulfuric acid supporting electrolyte solution, sampling potentials of +0.2 V, +0.4 V, +0.6 V, +0.8 V, +1.0 V and +1.2 V respectively. For each E_{ulp} value, the PtBi electrode was subjected to 10 cycles between -0.2 V and E_{ulp}. After each potential cycling process, the electrode surface was investigated via X-ray grazing incidence diffraction while in the *in-situ* electrochemical cell and under active potential control. The first cyclic voltammetric profile at each E_{ulp} was recorded and presented in Figure 3.5 (a). It should be mentioned, but not shown here, that steady-state voltammograms were not achieved even after 10 cycles, especially for high positive E_{ulp} values (like +1.0 V and +1.2 V), indicative of significant changes in surface composition and structure. The cathodic waves around -0.15 V were ascribed to the reduction of bismuth ions in solution. One significant characteristic property of this series of cyclic voltammograms was the continuous increase of the double-layer charge, suggesting that the electrochemically active area continuously increased. This phenomenon was further supported by *ex-situ* AFM images and diffraction data. Another important feature in Figure 3.5 (a) was the continuous increase of the amplitudes of the anodic waves around +0.70V and cathodic waves around +40V, characteristic of platinum oxide formation and reduction, respectively, in fact the cyclic voltammetric profile for an E_{ulp} of +1.20V was quite similar to that of a polycrystalline Pt surface except for

Figure 3.5 (a) Cyclic voltammograms of PtBi electrode recorded in a nitrogen-purged 0.1 M sulfuric acid supporting electrolytic solution as E_{ulp} was varied. (b) *In-situ* X-ray GID investigation focusing on the region including Pt(111) and Pt(002) diffraction peaks as a function of E_{ulp}.

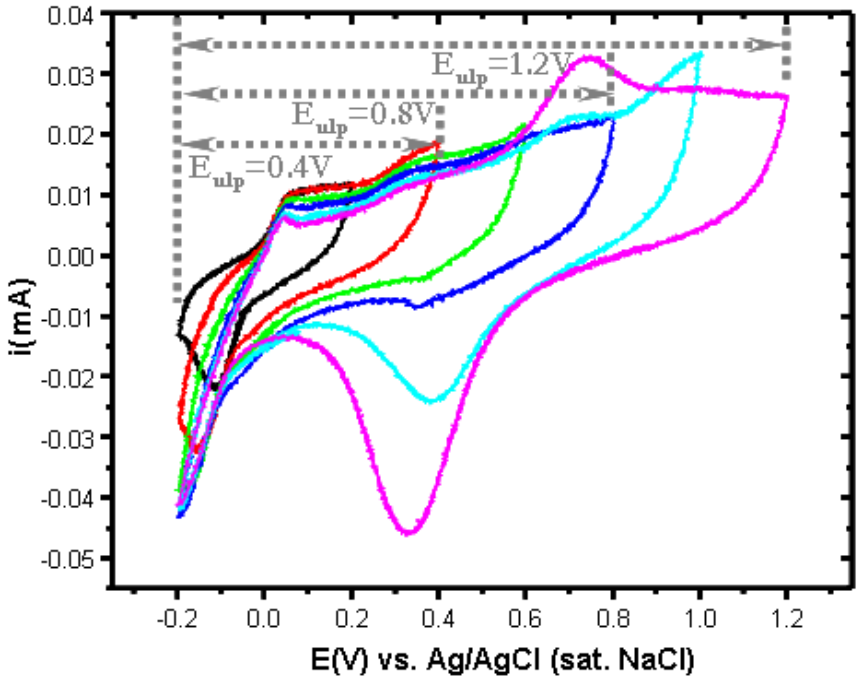
E_ulp=1.2V
E_ulp=0.8V
E_ulp=0.4V
i(mA)
E(V) vs. Ag/AgCl (sat. NaCl)

(a)

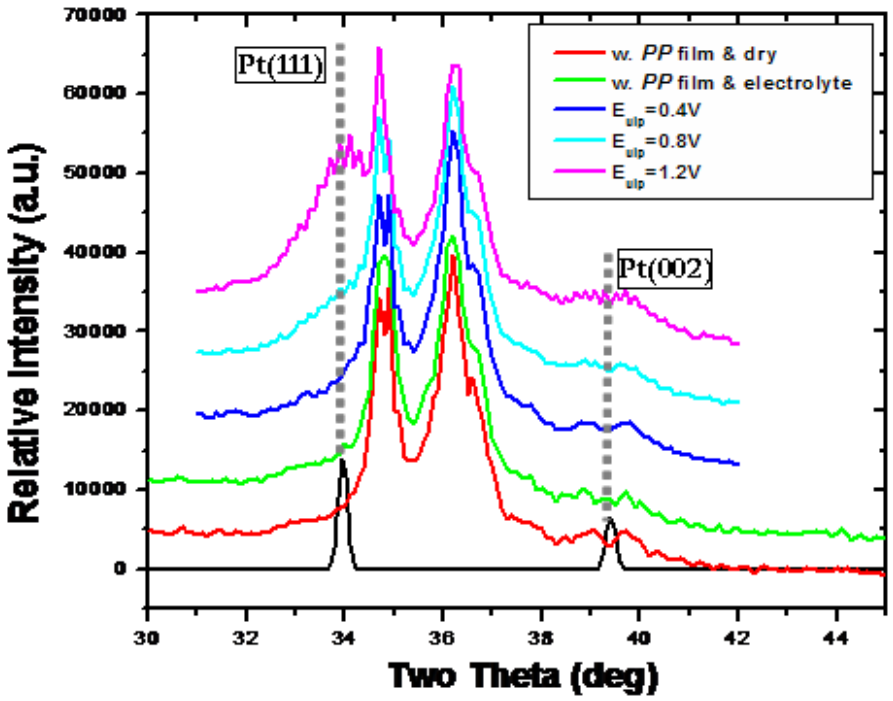
Pt(111)
Pt(002)
w. PP film & dry
w. PP film & electrolyte
E_ulp=0.4V
E_ulp=0.8V
E_ulp=1.2V
Relative Intensity (a.u.)
Two Theta (deg)

(b)

hydrogen adsorption/desorption. It appears that the electrochemical pretreatment procedure, especially to high E_{ulp} values, gave rise to a leaching-out of bismuth and the concomitant generation of Pt-rich surface.

In-situ X-ray GID data obtained after the electrochemical pretreatments provided direct information and evidence of changes in electrode surface crystalline structure and composition and indicated the specific changes for the surface as a function of E_{ulp}. As shown in Figure 3.5 (b), a relatively broad diffraction peak at 36.5 deg was ascribed to the polypropylene film since it was not present when no film was used to seal the electrochemical cell. The polypropylene film only presented this one diffraction peak within the angular region of interest and did not interfere with regions of the Pt(111) and Pt(002) diffraction peaks. The sharp peak around 34.8 deg corresponds to PtBi($1\bar{2}0$). The survey scan ranged from 31 deg to 42 deg, which covered the Pt diffraction peaks which would provide information about the changes in surface composition and structure. For an E_{ulp} value of +0.40V, the GID pattern did not exhibit any significant changes. However, upon close inspection and in comparison to *ex-situ* GID results, there were actually small changes inducing a very small bump at the Pt(111) angular position. When the E_{ulp} was increased to +0.80V, as shown in Figure 3.5 (b), a shoulder peak at Pt(111) angular position provided direct evidence that Pt crystalline domains had formed at the electrode surface. This is the consequence of the Bi leaching-out process due to surface oxidation at high positive E_{ulp} values. We believe that Bi was oxidized to Bi_2O_3 (or other oxidized species) when the PtBi electrode was subjected to relatively high positive E_{ulp} values (+0.80V or beyond), and these oxidized species readily dissolved into solution. Since Pt-Bi bonds are broken during this procedure and the resulting Pt atoms bond together to form both nanoscale crystalline domains and amorphous species on the intermetallic surface. The *in-situ* GID data provides compelling evidence of the formation of these nanoscale

crystalline domains. The Bi leaching-out process and Pt domain formation procedure is schematically shown in Figure 3.6. For the highest E_{ulp} value of +1.20V, a distinct and clearly resolved Pt(111) diffraction peak was evident in Figure 3.5(b). Even around the Pt(002) angular position, there was a clearly defined diffraction peak. In this case, a large amount of Bi was dissolved into solution and the Pt crystalline domain size increased to considerable values. Based on the Scherrer Equation, the Pt crystalline domain size was estimated to be ca. 5~7 nm. However, diffraction signals only arise from crystalline structures and amorphous species do not give rise to a detectable scattering peak. The estimated Pt domain size obtained from diffraction refers only to the crystalline part. The actual morphology and domain size of the Pt islands on the PtBi intermetallic substrate could be much larger than this value. This case was supported by AFM experiments described below. Pseudo-2D-mapping patterns (Figure 3.7) for this series of in-situ X-ray GID measurements showed clear signals of Pt crystalline domains. According to the uniform partial powder ring at the Pt(111) angular position, these Pt domains were “perfect” powder polycrystalline and had no preferential orientations.

3.3.4 Ex-situ atomic force microscopy

The *in-situ* X-ray GID data provided valuable insights of the intermetallic PtBi electrode surface crystalline structure and composition and particularly the changes arising from electrode polarization over a wide potential range. However, GID is essentially insensitive to short-range ordered structure (non-crystalline species) and amorphous materials. AFM, on the other hand, can provide a great deal of information regarding surface roughness and morphology. As shown in Figure 3.8, for a freshly polished PtBi electrode, although a very shining mirror-like electrode surface was

Figure 3.6 Schematic of Bi leaching-out and Pt domain formation procedures.

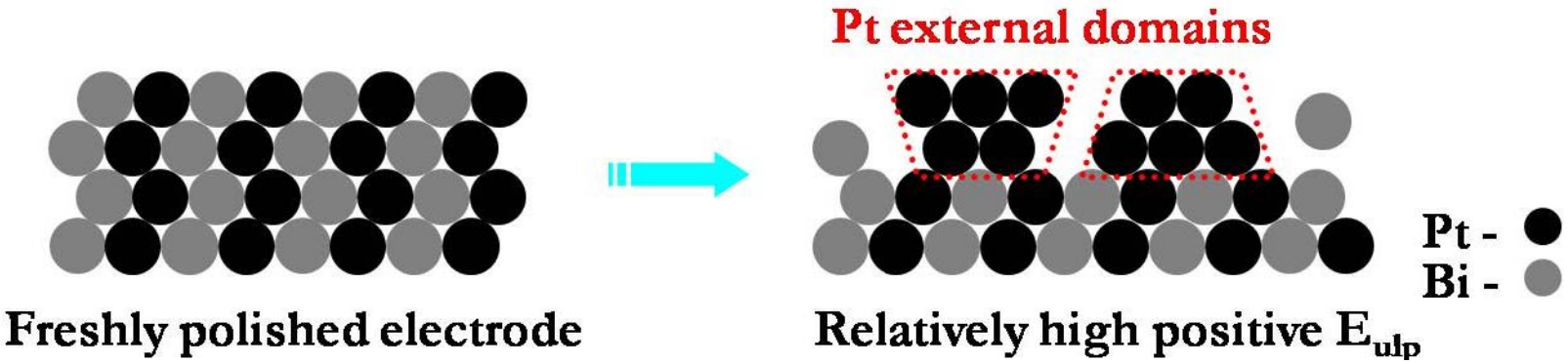
Pt external domains
Pt -
Bi -
Freshly polished electrode
Relatively high positive E_{ulp}

Figure 3.7 Pseudo-2D-Mapping images for in-situ X-ray GID investigations as a function of E_{ulp}.

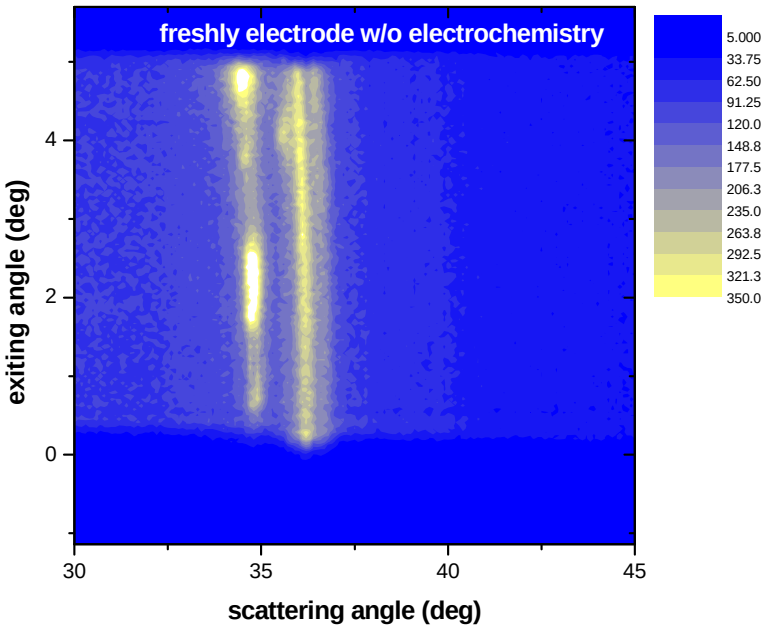
freshly electrode w/o electrochemistry
exiting angle (deg)
scattering angle (deg)
5.000
33.75
62.50
91.25
120.0
148.8
177.5
206.3
235.0
263.8
292.5
321.3
350.0

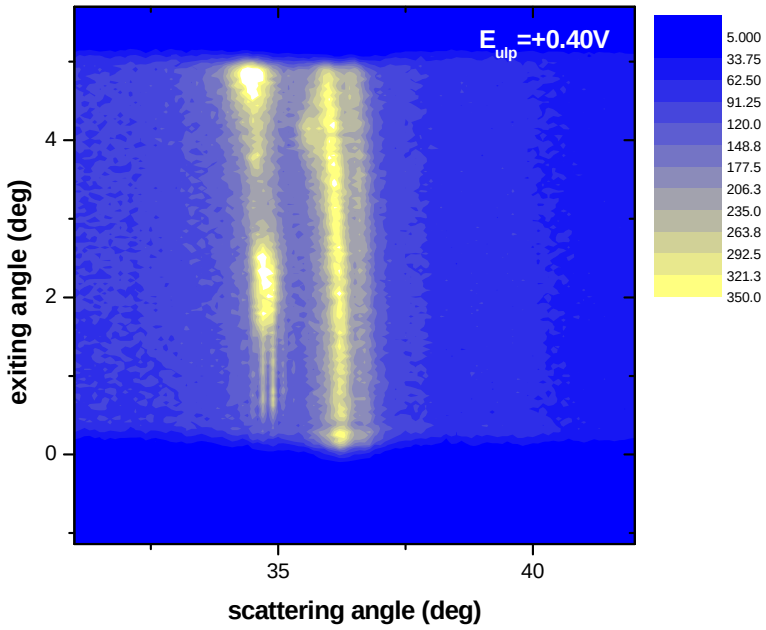
E ulp =+0.40V
exiting angle (deg)
scattering angle (deg)
5.000
33.75
62.50
91.25
120.0
148.8
177.5
206.3
235.0
263.8
292.5
321.3
350.0

Figure 3.7 (Continued)

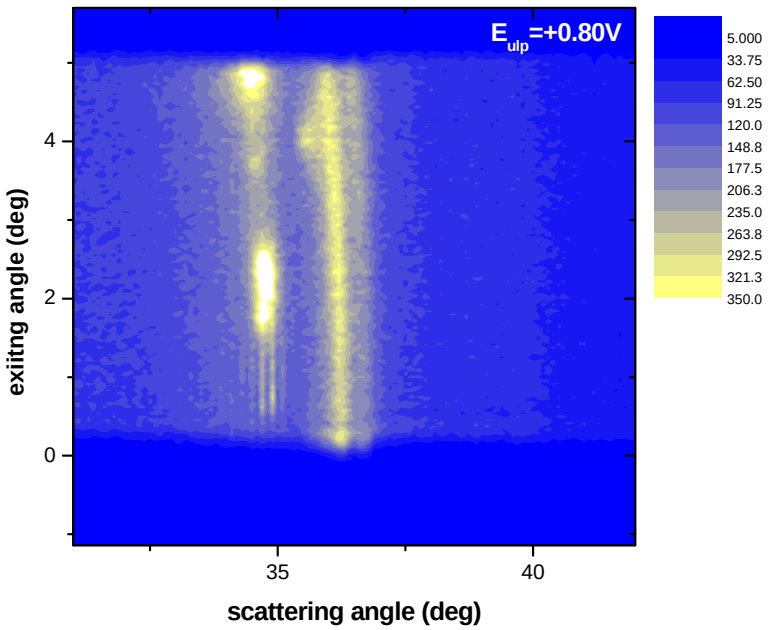

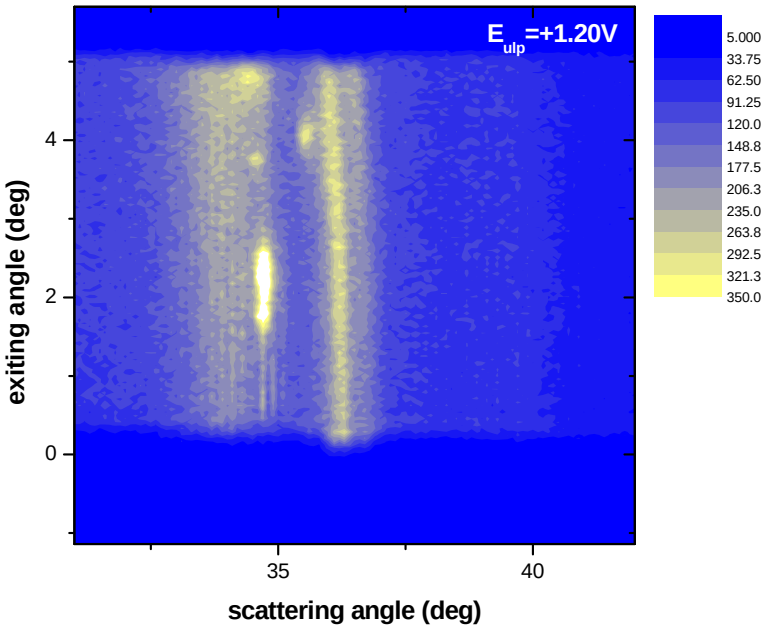

Figure 3.8 *Ex-situ* AFM images corresponding to different E_{ulp} polarizations.

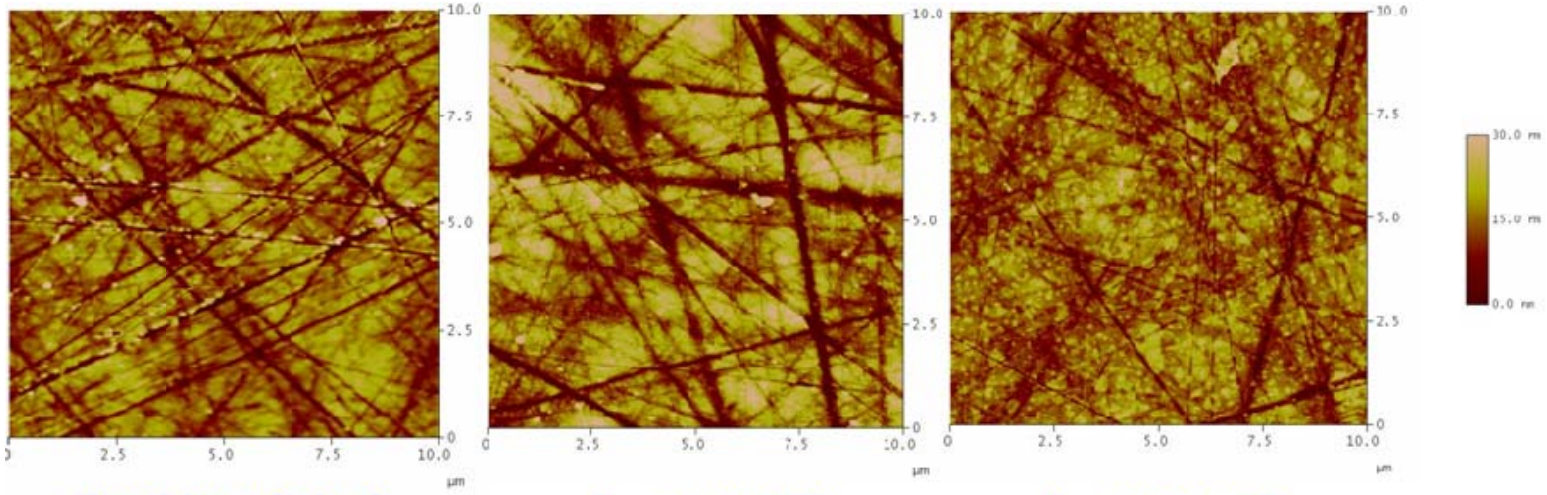

Freshly polished **E_{ulp}=400mV** **E_{ulp}=1200mV**

achieved, there were distinct and abundant deep scratches on the surface. The RMS value of the surface roughness, based on software calculation, was ~5-7 nm. When the electrode was polarized to an E_{ulp} value of +0.40 V and after sweeping for 10 cycles, the surface roughness and morphology did not present significant difference to a freshly polished electrode. This result was consistent with previous *in-situ* X-ray GID data, which did not exhibit distinctive Pt diffraction peaks since surface degradation had not taken place at this relatively low positive E_{ulp} value. On the other hand, abundant large islands (typical size was ~100-200 nm) were formed on the electrode surface when it was subjected to E_{ulp} of +1.20 V. As shown earlier, at this potential, the Bi leaching-out process is very vigorous and Pt crystalline domains form on the intermetallic surface. Changes in the surface crystalline structure and morphology were quite distinct in comparison to a freshly polished electrode. This apparent inconsistency can be readily reconciled by considering the difference between physical size and crystalline domain. The 100 nm domain size obtained from AFM images relative to physical size, which likely includes amorphous species on the surface. The crystalline domain size, calculated from GID data, was ~5-7 nm which is much smaller than 100 nm. Besides the presence of amorphous species on the surface, the Pt islands in the AFM image could also be due to the aggregation and agglomeration of small crystalline domains. This explanation is depicted in Figure 3.9.

3.4 Conclusion and summary

In order to establish the relationships between surface structure/composition and catalytic reactivity and obtain valuable insights to understand surface reaction mechanism and guide the design of new electrocatalysts, the synchrotron-based *in-situ* X-ray GID technique has been employed to investigate the surface structure and

Figure 3.9 Schematic of aggregation of nanosize Pt crystalline domains.

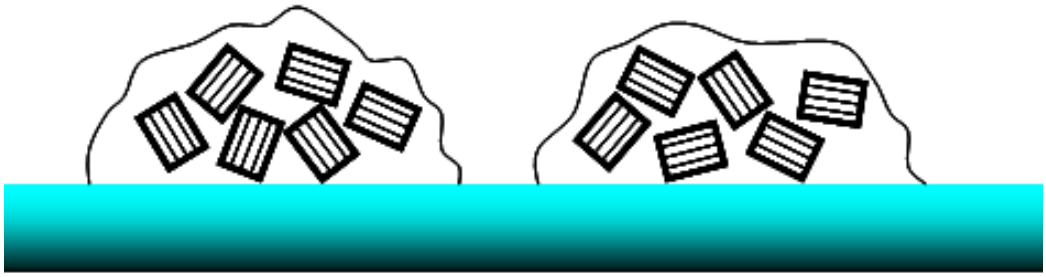

Pt nanoscale crystalline domain -

composition of the ordered intermetallic phase PtBi (a promising candidate for SOMs electrooxidation) especially the changes in surface crystalline structure and composition arising from electrode polarization over a wide potential range. First of all, a general purpose *in-situ* electrochemical cell was designed and built up to conduct surface X-ray scattering studies in combination with electrochemical characterization. While in this study we only carried out diffraction studies, the cell can be utilized for X-ray fluorescence and absorption studies. The effects of pretreatments for these ordered intermetallic phases including chemical and mechanical polishing procedures and electrochemical pretreatments were thoroughly investigated. In term of polishing procedures, we established the conditions that would reproducibly yield stoichiometric and mirror-like surfaces. We also established the effects of applied potentials to surface structure, morphology and composition. In general, surface composition was altered during surface oxidation process, especially at relatively high positive E_{ulp} values. The less noble element, Bi, was leached out from the surface and dissolved into the 0.1 M sulfuric acid electrolyte solution which served as the supporting electrolyte. This process was initiated at an E_{ulp} value of +0.40V and was much more evident for E_{ulp} values of +0.80V and beyond. The leached out Bi likely generated Bi_2O_3 or other bismuth oxidized species which were subsequently dissolved. The remaining Pt atoms sintered together to form nanoscale crystalline domains on the PtBi intermetallic substrate and *in-situ* X-ray GID data provided direct and compelling evidence for this process. Analysis of the diffraction peaks yielded Pt crystalline domains of ~5-7 nm. *Ex-situ* AFM experiments provided additional insights on the physical size distribution of the Pt islands on the surface after very aggressive electrode polarization (e.g. +1.20V). The size, based on AFM images, was over 100 nm which is much larger than the radii obtained from the GID data. We ascribe this apparent inconsistency to the aggregation and agglomeration of 5 nm Pt crystalline

domains into larger overall structures. The influence of this Pt domain forming process on the electrocatalytical activity could be rationally and reasonably explained by our previous studies.[18] For many of these ordered intermetallic phases (e.g. PtBi and PtPb), electrocatalytical activity could be enhanced by potential excursions to relatively high E_{ulp} values. From the results presented here, this phenomenon could correspond the formation of to a Pt_{surf}/PtBi electrode surface. That is, it appears that active form of the catalyst is one that is slightly Pt rich.

Besides the influence of electrochemical pretreatment to electrode presented here, we also believe that the presence of different fuel molecules and the nature of the supporting electrolytic solution can affect electrocatalytic activity and electrochemical stability. Such work is ongoing and will be reported elsewhere.

REFERENCES

1. M. Winter and R.J. Broad, *Chem. Rev.* 104, 4245, **2004**
2. H.D. Abruña *et al.*, *Bulletin of Chemical Society of Japan* 80, 1843, **2007**
3. N.S. Lewis and D.G. Nocera, *Proceeding of the National Academy of Sciences* 103, 15729, **2006**
4. E.S. Smotkin and R.B. Diaz-Morales, *Annual Review of Materials Research* 33, 557, **2003**
5. J.K. Nørskov, T. Bligaard, J. Rossmeisl and C.H. Christensen, *Nature Chemistry* 1, 37, **2009**
6. X. Yu and P.G. Pickup, *J. of Power Sources* 182, 124, **2008**
7. H. Liu, C. Song, L. Zhang, J. Zhang, H. Wang and D.P. Wilkinson, *J. of Power Sources* 155, 95, **2006**
8. M. Watanabe and S. Motoo, *J. of Electroanal. Chem.* 60, 267, **1975**
9. M. Watanabe and S. Motoo, *J. of Electroanal. Chem.* 60, 275, **1975**
10. J.S. Spendelow and A. Weickowski, *Phys. Chem. Chem. Phys.* 21, 2654, **2007**
11. E. Casado-Rivera, Z. Gál, A.C.D. Angelo, C. Lind, F.J. DiSalvo and H.D. Abruña, *Chem. Phys. Chem.* 4, 193, **2003**
12. E. Casado-Rivera, D.J. Volpe, L. Alden, C. Lind, C. Downie, T. Vázquez-Alvarez, A.C.D. Angelo, F.J. DiSalvo and H.D. Abruña, *J. Am. Chem. Soc.* 126, 4043, **2004**
13. R. Borup *et al.*, *Chem. Rev.* 107, 3904, **2007**
14. H. Cha, C. Chen and Y. Shiu, *J. of Power Sources* in press
15. D.R. Blasini, D. Rochefort, E. Fachini, L.R. Alden, F.J. DiSalvo, C.R. Cabrera and H.D. Abruña, *Surface Science* 600, 2670, **2006**
16. J. Als-Nielsen and D. McMorrow, *Elements of Modern X-ray Physics* (Wiley) **2001**

17. D.E. Nowak, D.R. Blasini, A.M. Vodnick, B. Blank, M.W. Tate, A. Deyhim, D.-M. Smilgies, H.D. Abruña, S.M. Gruner and S.P. Baker, *Rev. Sci. Instrum.* 77, 113301, **2006**

18. D.J. Volpe, E. Casado-Rivera, L. Alden, C. Lind, K. Haggerdon, K. Downie, C. Korzeniewski, H.D. Abruña and F.J. DiSalvo, *J. Electrochem. Soc.* 151, A971, **2004**

CHAPTER FOUR

KINETIC STABILIZATION OF THE ORDERED INTERMETALLIC PHASES AS FUEL CELL ANODE MATERIALS*

4.1 Introduction

Electrocatalysts of anode and cathode materials for direct fuel cells (DFC) have been extensively studied due to increasing demands for sustainable energy sources.[1-5] For electrooxidation of small organic molecules (SOMs) at room temperature, platinum has been plagued its high cost and susceptibility to poisoning by carbon monoxide which is a common intermediate during SOMs oxidation processes.[6-7] In order to lower the expense of electrocatalysts and preclude the diminution of catalytic activity due to CO poisoning phenomenon, the addition of a non-noble metal has been presented to form bimetallic alloys. The most successful example for methanol oxidation has been a PtRu alloy which is currently commercialized for industrial applications.[8-9] Based on the so-called "bifunctional mechanism" of methanol oxidation, occurring on such a bimetallic surface, it is widely accepted that Ru atoms promote the formation of weakly bonded oxygenated species in close proximity to methanolic residues adsorbed on Pt sites, facilitating their oxidation to carbon dioxide.[10] In addition, Pt d-band vacancies are increased by adding Ru atoms and this is behaved to facilitate this catalytic activity promotion.[11] PtRu alloys can be unstable due to their very small enthalpies of formation of the constituent elements. Both the bulk and surface chemistries of these materials have been extensively investigated.[12-15] The top layer of a PtRu alloy catalyst can be significantly altered in composition and

*Reproduced with permission from the manuscript in preparation, ready to be submitted.

structure under active electrochemical control. It is generally accepted that the activity of PtRu alloys towards methanol oxidation takes place at the boundary between the Pt and Ru nanoscale domains within the alloy matrix.[16] The normalized boundary line between different domains would be dramatically decreased to result in lowing catalytic activity after the phase segregation induced by specific electrochemical treatment.

In addition to PtRu alloys, as anode materials, many bimetallic materials, as anodes or cathodes, have attracted a great deal of research interest and have been broadly studied as bulk, surface or nanomaterials. Chen and co-workers[17] reported on the activity of PtFe nanoparticles, with varied molecular ratios, towards the electrooxidation of formic acid. They noted that electrocatalytic activity was strongly dependent on the composition of the PtFe nanoparticles. $Pt_{0.5}Fe_{0.5}$ exhibited the maximum activity towards the oxidation of formic acid and optimal tolerance to CO poisoning. For cathode materials, Strasser and co-workers[18-19] reported on novel core/shell PtCu alloy particles towards the oxygen reduction reaction (ORR). Core/shell PtCu nanoparticles with a Pt outmost skin layer were obtained via electrochemical dealloy from uniform PtCu alloy nanoparticles. They exhibited almost 4 times higher activity towards the ORR when compared to state-of-the-art Pt electrocatalyts. Wagner[20] demonstrated that Pt rich PtCo alloy material was a promising candidate for the ORR in terms of the Pt-mass-based performance. Their Pt-mass-based fuel cell activity showed an improvement of 2~3 times when compared to pure Pt. Mavrikakis and Adzic[21] reported on a new category of Pt or PtM (M=Ir, Ru, Os, Au, Re etc) monolayer modified Pd single-crystal-surface-supported materials exhibited almost double digit Pt-mass-based activity gains. Stamenkovic and Markovic[22] reported on a nickel modified Pt(111) surface prepared in ultra high vacuum (UHV) that exhibited improved activity towards the ORR which was 10-fold

higher than that of Pt(111) or 90-fold more active than current commercial Pt/C catalysts in fuel cell tests.

Unlike alloy materials, ordered intermetallic phases have well-defined crystalline structures and generally high enthalpies of formation which render them much more stable relative to alloys. The case of ordered intermetallic phases allows for the deliberate control of electronic and geometric structure at the atomic scale. In terms of electrocatalytic applications, DiSalvo and Abruña[23-24] demonstrated that PtBi and PtPb are promising candidates as anode materials towards formic acid (PtBi and PtPb) and methanol (PtPb) oxidation reactions, and also exhibited excellent tolerance to carbon monoxide poisoning. In previous experiments[25-26], the ordered intermeatllic phases were not stable to the application of moderate to high positive potentials. The less noble metals (Bi or Pb) would leach out from the matrix and dissolve into the solution when the electrode was subjected to cycling to +0.80V or beyond. During this process, Pt crystalline domains, of ~5 nm diameter, were formed on the surface due to the sintering/aggregation of Pt atoms. The physical size of these Pt islands (based on morphological characterization) was up to 200 nm suggesting that nanocrystalline Pt domains agglomerated and could also be covered by some amorphous Pt atoms. Unstable oxidized surface species, Bi_2O_3 for PtBi and $PbCO_3$ for PtPb, were also formed on the electrode surface at +0.60V or lower and then dissolved into the solution at +1.00V or beyond.[27]

Beyond the surface characterization of the ordered intermetallic phases in absence of fuel molecules, it is also of great importance to investigate changes in the surface composition and structure of these intermetallic electrodes during the oxidation process of SOMs under real electrochemical conditions. We have employed synchrotron-based *in-situ* X-ray grazing incidence diffraction (GID) techniques to investigate changes in the surface crystalline structure of these materials in the

presence of fuel molecules in the supporting electrolyte. Active and non-active fuel molecules were employed in a series of control experiments to rationalize the surface reaction mechanism. The electrodes were deliberately subjected to different electrochemical treatments by either cycling or holding the applied potential. These studies were used to explore the surface composition/structure/property/activity relationships of these intermetallic phases and to provide valuable insights to guide the design of new electrocatalyts.

4.2 Materials and Experimental Section

4.2.1 Ordered Intermetallic PtBi and PtPb Phases Synthesis

The synthesis procedure of the polycrystalline ordered intermetallic phase PtBi is briefly described here. Platinum powder (Johnson Matthey, 99.999%) and bismuth powder (Alfa Aesar, 99.9999%) from pellets were thoroughly mixed in the appropriate molar ratios in an agate mortar. Pellets (6 mm OD, 4 mm length) were pressed in a hydraulic press. The pellets were sealed in evacuated fused silica tubes (10 mm ID, 100 mm length) and heated, oriented vertically, in a box furnace to 800 ℃ for 24 hours and annealed at 650 ℃ for 48 hours. The pellets were ground and the above procedure was repeated twice. The procedure to synthesize the polycrystalline PtPb intermetallic phase was similar to that of PtBi. More detailed information on the synthesis and characterization of the materials has been previously reported.[23-24]

4.2.2 Electrochemistry

All electrochemical characterizations were carried out, in an *in-situ* three-electrode electrochemical cell, which was purposely designed and built for combining X-ray

surface scattering and electrochemical characterization.[25] The ordered polycrystalline intermetallic electrodes were placed in the center of this *in-situ* cell. Cyclic votalmmetry (CV) was carried out on a BAS CV-27 potentiostat/golvanostat (Bioanalytical System) and recorded on a computer through a PCI-DAQ card (National Instruments). All potentials are referenced to a Ag/AgCl (saturated NaCl) electrode without regard for the liquid junction potential. All chemicals were A.R. level or higher (Sigma Aldrich) and were used as received. 18.2 MΩ DI water (Millipore-Milli Q) was used for all electrochemical experiments. The typical CV characterization consisted of cycling the potential at 10mV/s from -0.20V to different upper limit potentials, labeled as E_{ulp}, ranging from +0.40V to +1.20V, in the presence (or absence) of specific fuel molecules in solution. Chronoampetric characterization was also carried out on a BAS CV-27 potentiostat/golvanostat (Bioanalytical System) and recorded on a computer through a PCI-DAQ card (National Instruments). After holding initial potential at -0.20V for 5 min, the applied potential was stepped to a specific value and held constant for over 30 min.

4.2.3 In-situ X-ray Surface Grazing Incidence Diffraction

After electrochemical pretreatment, part of the electrolytic solution was withdrawn from the cell so that a polypropylene film covering the whole cell was recessed, generating a thin film of electrolyte. The electrolyte film, however, was sufficiently thick to ensure good potential control in all cases. We employed two different kinds of scans for X-ray scattering characterization. Surface X-ray grazing incidence partial survey diffraction was carried out over the three different angular ranges: 18~ 28 deg which covered some of the strongest PtM (M=Bi or Pb) and oxidized lead species diffraction peaks; 30~40 deg which covered the major Pt, PtM and bismuth oxidized

species diffraction peaks respectively; and 42~50 deg which covered some of the weak PtM diffraction peaks. A horizontal in-pane X-ray scattering geometry was employed. In this case, the electrode surface normal was perpendicular to the ground, and the detector moved within the plane which was almost parallel to the electrode surface. Particular attention was given to changes in the emergence and intensity of platinum and bismuth or lead surface oxidized species, and also the disappearance and intensity of PtM diffraction peaks as a function of applied E_{ulp}. The critical angle for PtM ordered intermetallic phases is ~0.5 deg. The typical incidence angle employed in the partial survey or azimuthal GID experiments was ~0.25 deg which is well below the critical angle. All X-ray scattering experiments were carried out at the G-line station of the Cornell High Energy Synchrotron Source (CHESS). All diffraction experiments were carried out on a home-made six-circle *kappa* diffractometer. The experimental X-ray incidence energy was 9.374 KeV (1.323 Å). The beam size was 2 mm horizontal by 200 μm vertical. This asymmetry beam shape was deliberately chosen so as to optimize surface sensitivity. The typical photon flux intensity at the center of rotation (COR) of the diffractometer was ~10^{13} photons/sec/mm^2. A position sensitive detector (also known as linear gas detector) was utilized to collect the scattered photons. The detector angular resolution was ~0.18 deg. More detailed information about the diffractometer and experimental geometry can be found elsewhere.[25, 28]

4.2.4 Ex-situ atomic force microscopy

In order to complement the *in-situ* GID measurements, and to obtain a general idea about surface roughness and morphology, a series of *ex-situ* atomic force microscopy (AFM) experiments were conducted on a Veeco Dimension 3100 SPM/AFM system. Cyclic voltammetry and/or chronoamprometry experiments were carried out in a

conventional three-electrode electrochemical cell under similar conditions as described above. The hanging meniscus method was utilized and double-side copper tape was used for affixing the working electrode to a holder. After specific electrochemical treatment, the working electrode was removed from the cell and carefully extensively rinsed with Millipore water. After drying in air or under a nitrogen stream, the working electrode was transferred to the AFM instrument for investigation. The typical scan range was 10 μm × 10 μm.

4.3 Results and Discussions

4.3.1 Influence of different fuel molecules on a polycrystalline PtBi electrode

4.3.1.1 Stabilization effects induced by formic acid oxidation

In order to ascertain the effects induced by the presence of fuel molecules, the polycrystalline PtBi electrode was studied in different solutions in the presence of formic acid, or methanol or in 0.1M sulfuric acid supporting electrolyte only. PtBi intermetallic phases are known to exhibite high electrocatalytic activity towards the oxidation of formic acid but little activity towards methanol oxidation. The onset potential for formic acid oxidation on PtBi electrodes was ~0.00V. Figure 4.1 presents *ex-situ* X-ray GID partial survey scans over the 29~38 deg range carried out after cycling the potential at 10mV/s from -0.20V to an E_{ulp} value of +0.80V for at least 10 cycles in different solutions. Particular attention was paid to the Pt(111) diffraction peak position at 31.3 deg. In the absence of any fuel molecules in the 0.1M H_2SO_4 solution, Pt crystalline domains were formed on the PtBi electrode surface due to Bi leaching from the matrix and subsequent dissolution. On the other hand, when the PtBi electrode was subjected to a similar procedure but in the presence of 0.2M formic acid, there was no sign of formation of Pt nanocrystalline domains on the electrode surface.

Figure 4.1 GID data at +0.80V for a polycrystalline PtBi electrode subjected to different fuel molecules or only supporting electrolytic solution.

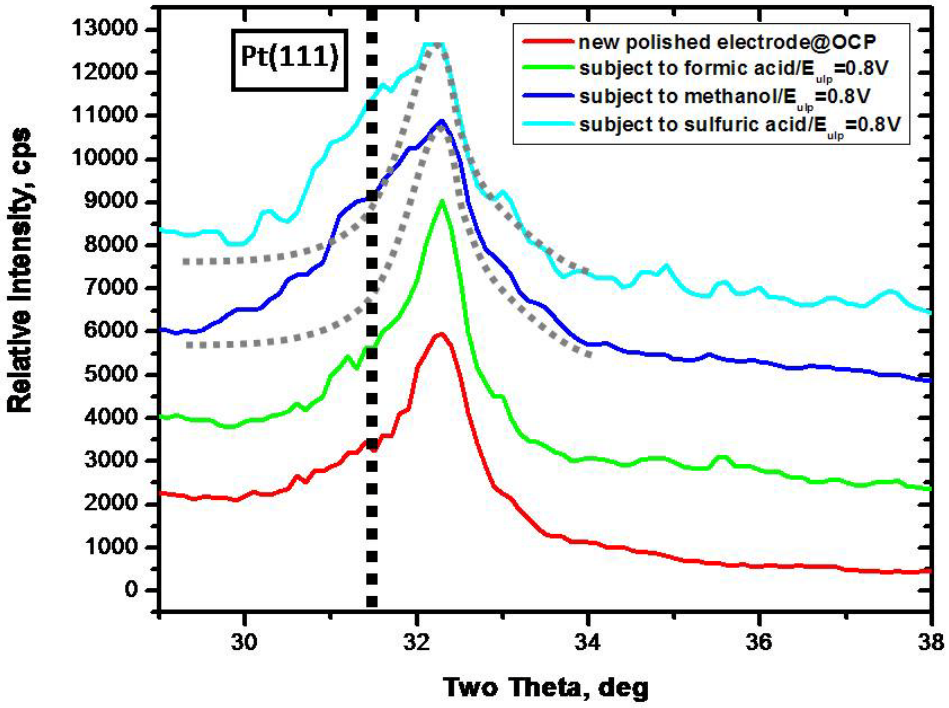
Pt(111)
new polished electrode@OCP
subject to formic acid/E ulp =0.8V
subject to methanol/E ulp =0.8V
subject to sulfuric acid/E ulp =0.8V
Relative Intensity, cps
Two Theta, deg
13000
12000
11000
10000
9000
8000
7000
6000
5000
4000
3000
2000
1000
0
30
32
34
36
38

Ex-situ AFM characterization also showed little change in morphology and surface roughness after electrochemical treatment in the presence of formic acid. This indicates that the Bi leaching out process was essentially eliminated and that no unsaturated Pt atoms were generated on the electrode surface. In order to ascertain the effects of other fuel molecules on the stability of ordered intermeatllic phases, 0.2M methanol was used in place of formic acid in the supporting electrolyte. As mentioned earlier, PtBi electrode does not exhibit any catalytic activity towards the oxidation of methanol. As a result, when similar experiments were carried out, we observed diffraction peaks in the GID data corresponding to Pt(111) domains. The nanocrystlline domain diameter of the Pt islands was ~5 nm which is relatively the same as for the Pt domains induced by cycling the potential in only supporting electrolyte. From the above discussion, it is evident that the stabilization effect induced by fuel molecules is not universal. Such molecules for which the electrode exhibited no catalytic activity did not provide any degree of stabilization.

In-situ X-ray GID characterization was used to explore the stabilization effects induced by the oxidation of formic acid on the PtBi electrode as a function of the applied E_{ulp}. *In-situ* X-ray GID scans over the 28~37 deg range were carried out to investigate the changes in appearance and intensity of Pt and PtBi diffraction peaks after cycling to E_{ulp} values of +0.80V, +0.85V, +0.90V, +0.95V and +1.00V. For each E_{ulp} value, the PtBi electrode was subjected to 10 cycles between -0.20 V and E_{ulp}. After each potential cycling process, the electrode surface was submitted to investigation via *in-situ* X-ray grazing incidence diffraction under active electrochemical control. Figure 4.2 presents diffraction peaks at 31.6 deg and 33 deg which correspond to PtBi (-120) and polypropylene, respectively. There was lno sign of Pt(111) shoulder or peak at 31.3 deg even for E_{ulp} values of +0.90V. Pt(111) diffraction peaks started to emerge at an E_{ulp} value of +0.95V and approached a similar

Figure 4.2 *In-situ* GID data of polycrystalline PtBi electrode in 0.2M HCOOH/0.1M H_2SO_4 solution after cycling to different E_{ulp} values.

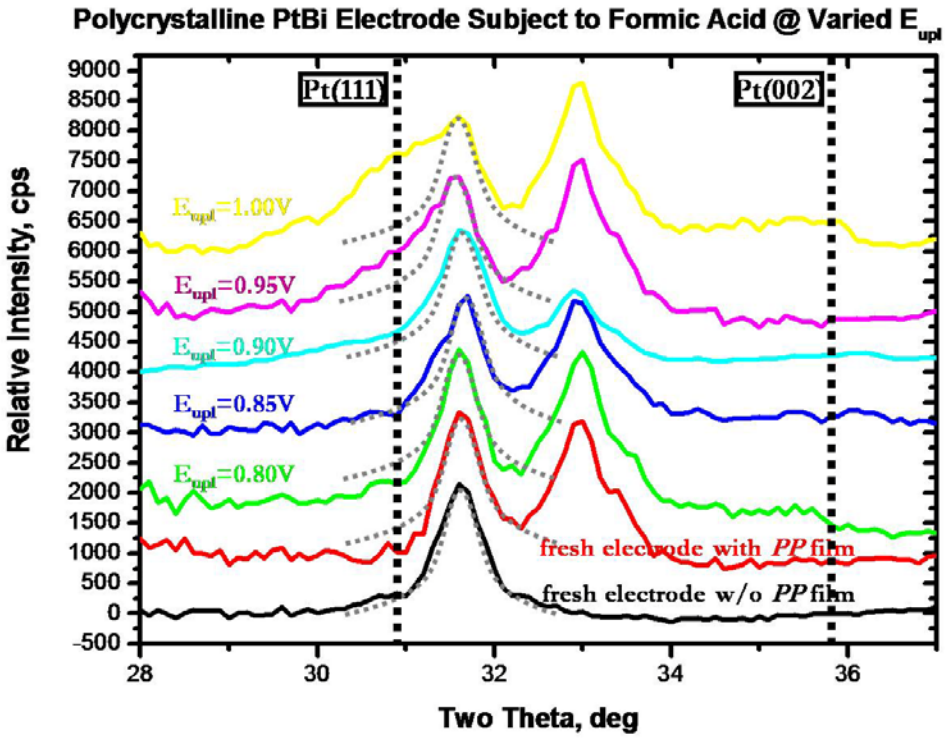
Polycrystalline PtBi Electrode Subject to Formic Acid @ Varied E upl
Pt(111)
Pt(002)
E upl=1.00V
E upl=0.95V
E upl=0.90V
E upl=0.85V
E upl=0.80V
fresh electrode with PP film
fresh electrode w/o PP film
Relative Intensity, cps
Two Theta, deg
9000
8500
8000
7500
7000
6500
6000
5500
5000
4500
4000
3500
3000
2500
2000
1500
1000
500
0
-500
28
30
32
34
36

full width at half maxim (FWHM) at an E_{ulp} value of +1.00V in comparison to the case of a 0.1M H_2SO_4 solution where such behavior was obtained for an E_{ulp} value of +0.80V. The stabilization effect of formic acid oxidation towards the PtBi electrode, as a function of applied E_{ulp}, could be rationalized based on the CV characterization (not shown here). The peak of anodic current wave for formic acid oxidation on the PtBi electrode was around +0.60V and formic acid would be fully oxidized (transport limit) around +0.90V. The stabilization effect (from formic acid oxidation) and the subsequent preclusion of the Bi leaching-out process is thus ascribed to the effective competition of fuel oxidation vs. electrode surface decomposition (leaching) effects.

4.3.1.2 Surface adsorption protection or kinetic stabilization

The stabilization effect of the PtBi electrode surface induced by the oxidation of formic acid could be rationalized in terms of the competition between the oxidation of formic acid at the electrode interface and corrosion/oxidation of the electrode surface itself which could be also described as the leaching out/dissolution process of surface bismuth species from the PtBi electrode. This assertion is consistent with the observation that no stabilization was induced by non-active fuel molecules (methanol) for the PtBi electrode. In addition to the surface/interface oxidation competition process described above, adsorbed species on the electrode surface could lower the surface energy, inhibiting the electron transfer process and thus protecting the electrode surface from the decomposition. In order to differentiate between these two stabilization mechanisms, we carried out a control experiment in the presence of non-active molecule with high absorbability. In such a purpose, malonic acid ($HOOCCH_2COOH$) was deliberately selected since it could not be catalytic oxidized by the PtBi electrode yet it is strongly adsorbed onto the electrode surface especially at

positive potentials due to its negative charge. As shown in the Figure 4.3 (a), CV profiles of the PtBi electrode in 0.2M $CH_2(COOH)_2$/0.1M H_2SO_4 were very similar to those in supporting electrolyte only. The cathodic wave around +0.45V was ascribed to the reduction of surface Pt-O species. The intensity of the Pt(111) diffraction peak at 32.3 deg increased as a function of applied E_{ulp} and nanocrystalline Pt domains were formed on the PtBi electrode surface after electrochemical treatment in presence of malonic acid in a manner analogous to results in 0.1M sulfuric acid alone. Figure 4.4 shows uniform powder partial diffraction rings in the pseudo 2D-mapping images of the *in-situ* X-ray GID characterization after cycling the potential to an E_{ulp} value of +1.20V for 10 cycles. Similar to the case with just supporting electrolyte or in the presence of non-active fuel molecules (e.g. methanol), “perfect” polycrystalline Pt islands with ~5 nm crystalline domain size were formed on the PtBi electrode surface as a result of the Bi leaching-out/dissolution process. All of these observations suggest that the stabilization effect was not due to the adsorption of species capable of protecting the surface.

Thus, for PtBi intermeatllic phases, the observed stabilization is ascribed to a competition process for oxidizing equivalents in the presence of active fuel molecules, such as formic acid in the supporting electrolyte. Formic acid molecules could be catalytically oxidized at relatively negative potentials relative to the oxidation/ corrosion of the electrode itself which occurred at relatively positive potentials. Thus at such positive values, the surface was rendered kinetically stabilized.

Figure 4.3 Control experiment to differentiate between mechanisms for stabilization of the PtBi electrode. (a) Cyclic voltammetry profiles of the PtBi electrode in 0.2M $CH_2(COOH)_2$/0.1M H_2SO_4 solution at 10mV/s between -0.20V and varied E_{ulp} values; (b) *In-situ* X-ray GID data of the PtBi electrode after electrochemical treatments in 0.2M $CH_2(COOH)_2$/0.1M H_2SO_4 solution.

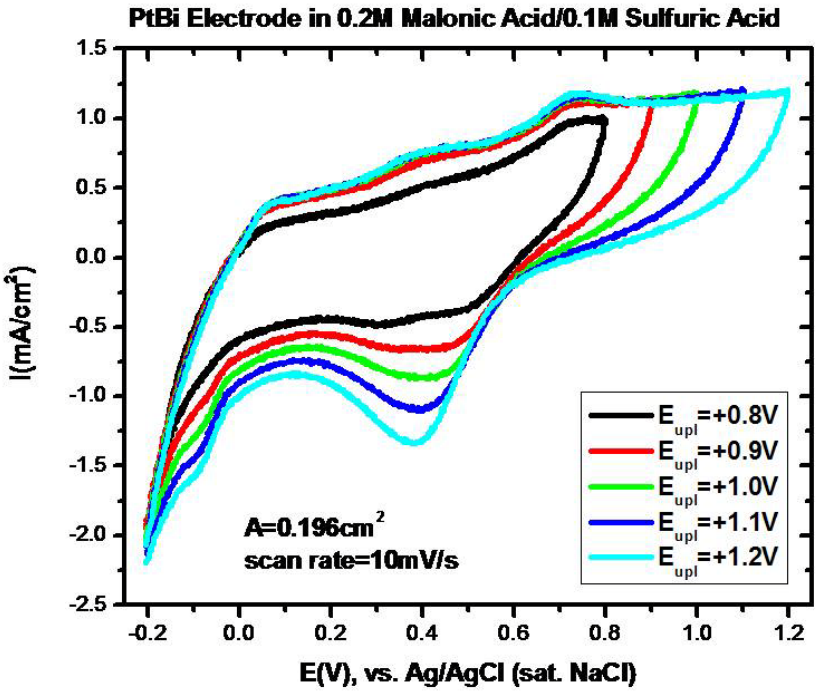
PtBi Electrode in 0.2M Malonic Acid/0.1M Sulfuric Acid
I(mA/cm²)
E(V), vs. Ag/AgCl (sat. NaCl)
A=0.196cm²
scan rate=10mV/s
E upl =+0.8V
E upl =+0.9V
E upl =+1.0V
E upl =+1.1V
E upl =+1.2V

(a)

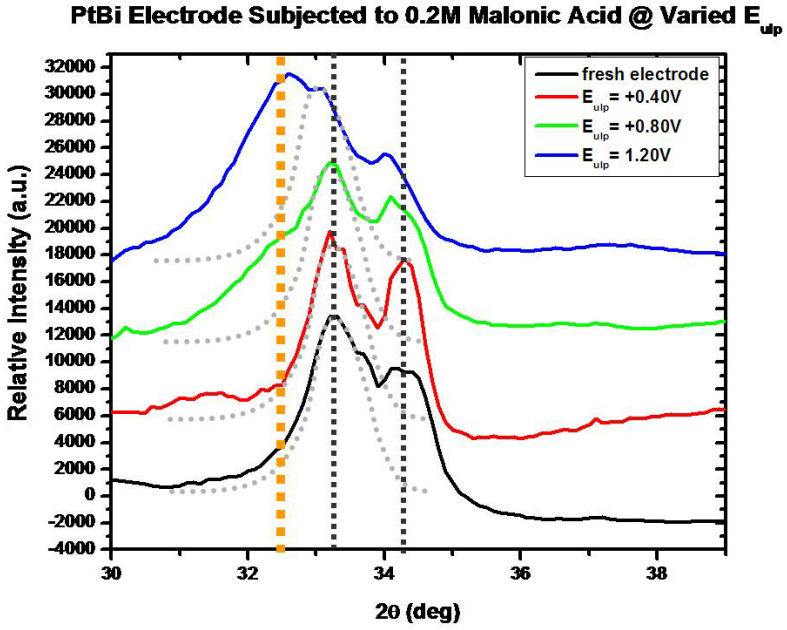
PtBi Electrode Subjected to 0.2M Malonic Acid @ Varied E ulp
Relative Intensity (a.u.)
2θ (deg)
fresh electrode
E ulp = +0.40V
E ulp = +0.80V
E ulp = 1.20V

(b)

Figure 4.4 Pseudo 2D-mapping images of *in-situ* X-ray GID data of the PtBi electrode in 0.2M $CH_2(COOH)_2$/0.1M H_2SO_4 after cycling potentials to E_{ulp} of +0.80V (b) and +1.20V (c) in comparison to the fresh polished electrode (a).

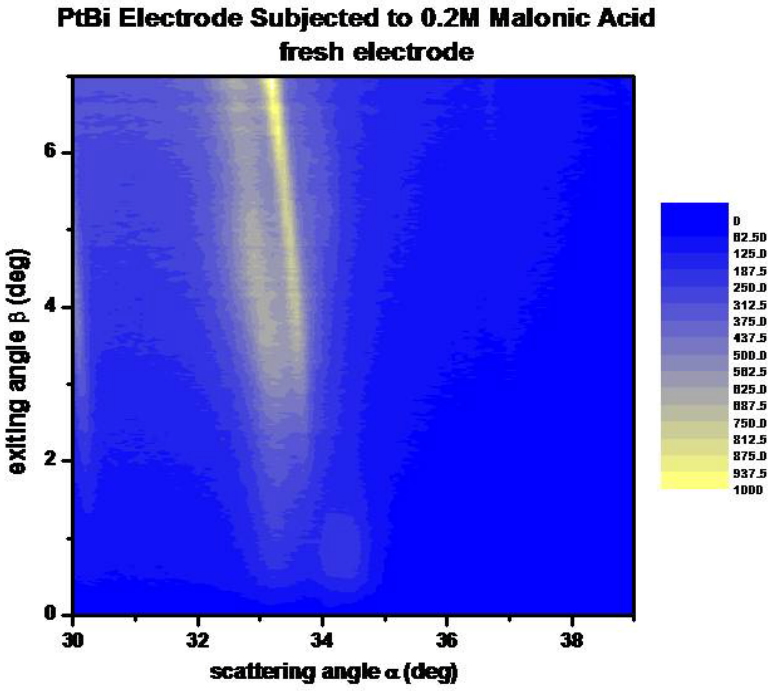
PtBi Electrode Subjected to 0.2M Malonic Acid
fresh electrode
exiting angle β (deg)
scattering angle α (deg)
0
2
4
6
30
32
34
36
38
0
62.5
125.0
187.5
250.0
312.5
375.0
437.5
500.0
562.5
625.0
687.5
750.0
812.5
875.0
937.5
1000

(a)

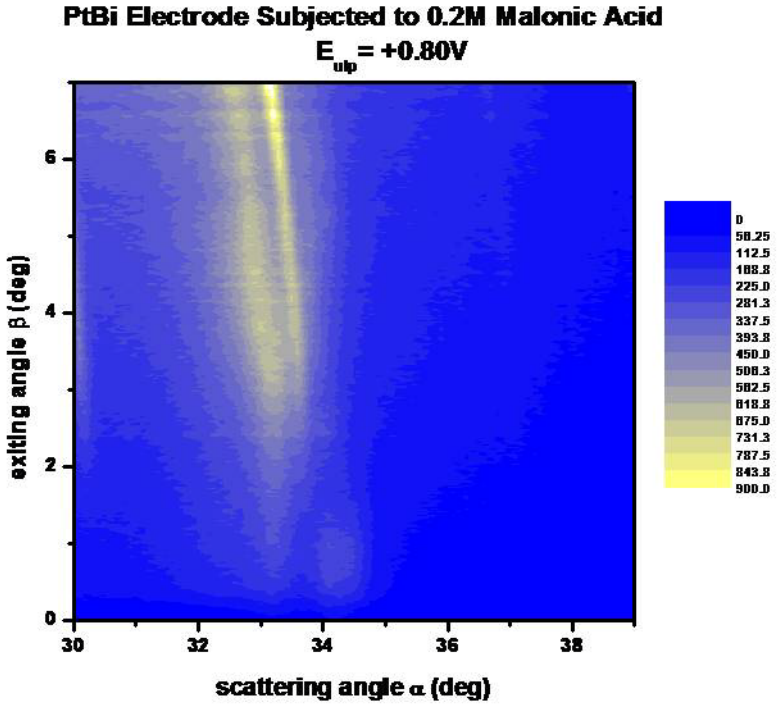
PtBi Electrode Subjected to 0.2M Malonic Acid
E_ulp = +0.80V
exiting angle β (deg)
scattering angle α (deg)
0
2
4
6
30
32
34
36
38
0
56.25
112.5
168.8
225.0
281.3
337.5
393.8
450.0
506.3
562.5
618.8
675.0
731.3
787.5
843.8
900.0

(b)

Figure 4.4 (Continued)

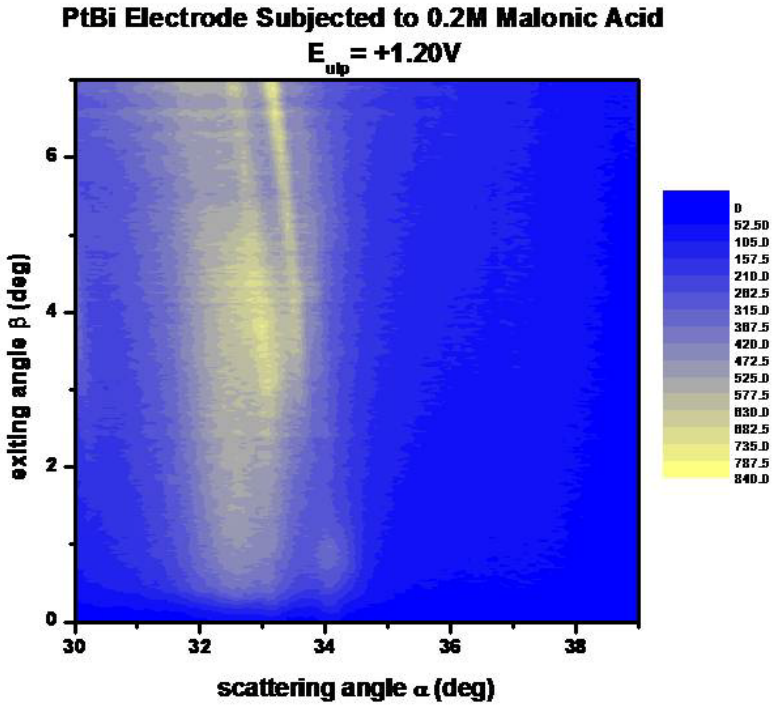

(c)

4.3.2 Influence of different fuel molecules on the stability of polycrystalline PtPb electrodes

4.3.2.1 Sulfuric acid solution as supporting electrolyte

Change in the surface composition and structure of polycrystalline PtPb electrodes as a function of applied E_{ulp} were investigated in 0.1M H_2SO_4 in the absence of fuel molecules via X-ray GID. Data were obtained after cycling the potential from -0.20V to various E_{ulp} values of +0.80V and +1.20V at 10mV/s for 10 cycles and compared to a freshly polished PtPb electrode. For a freshly polished PtPb electrode, diffraction signals of PtPb and Pt_3Pb intermetallic phases were presented in Figure 4.5. This PtPb working electrode was not pure phase and had a fraction of Pt_3Pb phase. This arises from the fact that PtPb is not a congruently melting phase. Several diffraction peaks due to $PbSO_4$ emerged at an E_{ulp} value of +0.80V instead of diffraction signals from Pt(111) at 32.3 deg. Similar to the PtBi electrode, the less noble element, Pb, leached out from the matrix and Pt atoms were left on the top surface layer of the intermeatllic electrode. In the presence of 0.1M sulfuric acid, these Pb ions formed $PbSO_4$ crystals which precipitated on the electrode surface. While the absolute amount of Pb leaching out from the surface was small, its local concentration at the electrode/solution interface was relatively high due to the special design of our *in-situ* electrochemical cell and we were especially sensitive to such processes. On the other hand, possible Pt(111) diffraction peaks overlapped with diffraction signals corresponding to $PbSO_4$ which were very strong and sharp. The surface $PbSO_4$ species either made the diffraction signals due to Pt crystalline domains difficult to detect or they inhibited the sintering/aggregation of remaining Pt atoms and the subsequent formation of Pt nanocrystalline domains. The pseudo 2D-mapping images (Figure 4.6) exhibited continuous and uniform partial powder diffraction rings due to $PbSO_4$ formation after

Figure 4.5 X-ray GID data of a PtPb/Pt_3Pb electrode in 0.1M H_2SO_4 solution after cycling potentials at 10mV/s to E_{ulp} values of +0.80V and +1.20V.

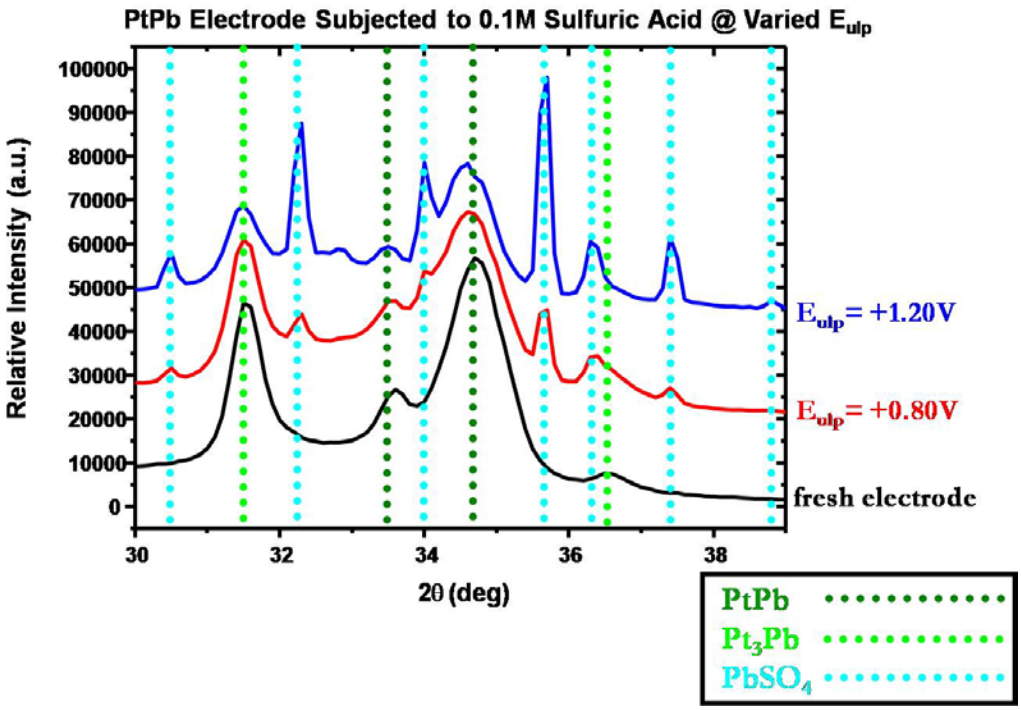
PtPb Electrode Subjected to 0.1M Sulfuric Acid @ Varied E$_{ulp}$
Relative Intensity (a.u.)
100000
90000
80000
70000
60000
50000
40000
30000
20000
10000
0
30
32
34
36
38
2θ (deg)
E$_{ulp}$ = +1.20V
E$_{ulp}$ = +0.80V
fresh electrode
PtPb
Pt$_3$Pb
PbSO$_4$

Figure 4.6 Pseudo 2D-mapping images of *in-situ* X-ray GID data of the PtPb electrode in 0.1M H_2SO_4 after cycling potentials to E_{ulp} values of +0.80V (b) and +1.20V (c) in comparison to the fresh polished electrode (a).

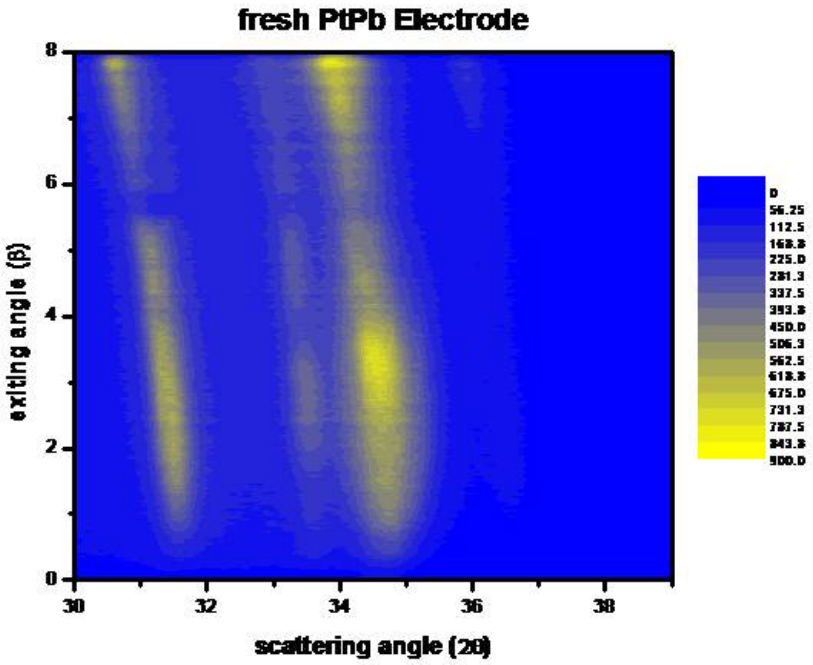
fresh PtPb Electrode
exiting angle (β)
scattering angle (2θ)
0
2
4
6
8
30
32
34
36
38
0
56.25
112.5
168.8
225.0
281.3
337.5
393.8
450.0
506.3
562.5
618.8
675.0
731.3
787.5
843.8
900.0

(a)

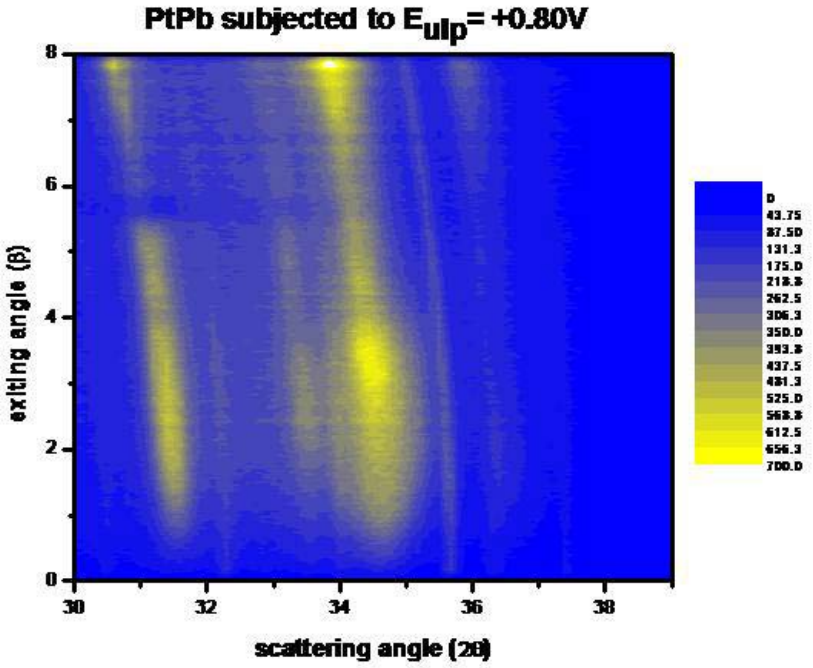
PtPb subjected to E$_{ulp}$= +0.80V
exiting angle (β)
scattering angle (2θ)
0
2
4
6
8
30
32
34
36
38
0
43.75
87.50
131.3
175.0
218.8
262.5
306.3
350.0
393.8
437.5
481.3
525.0
568.8
612.5
656.3
700.0

(b)

Figure 4.6 (Continued)

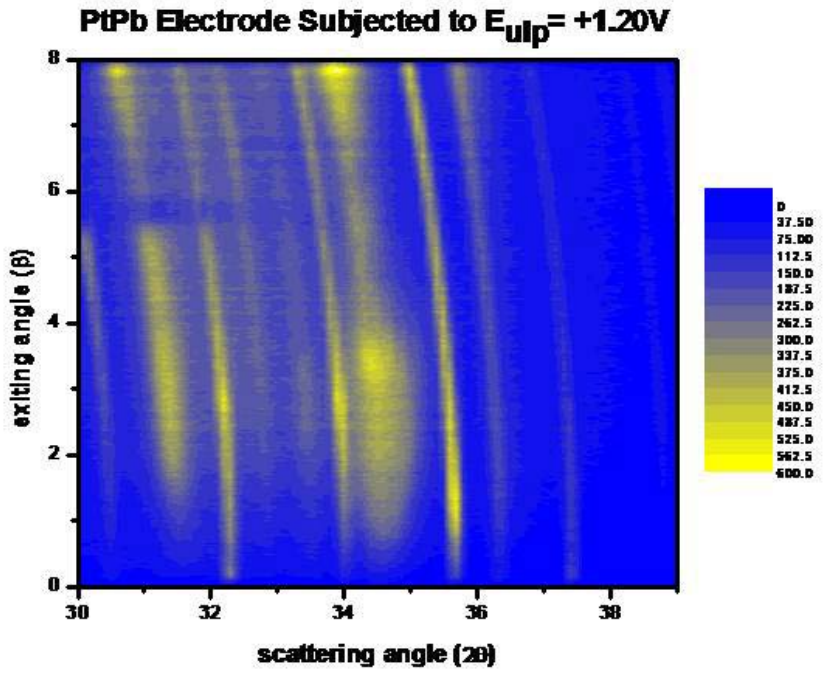

(c)

electrochemical pretreatment to an E_{ulp} value of +1.20V. We could not find evidence of Pt crystalline domain formation on the electrode surface in the pseudo 2D-mapping image of GID data focusing on the Pt(111) diffraction position of 32.3 deg. *Ex-situ* AFM characterization was utilized to investigate changes in the surface morphology and roughness as a function of the applied E_{ulp}. Large crystals of $PbSO_4$ with ~400 nm diameter were evident on the images of the PtPb electrode surface after cycling to an E_{ulp} value of +1.20V.

Because the diffraction signals corresponding to $PbSO_4$ were very strong and sharp, they could be utilized to monitor the lead leaching out/dissolution process as a function of the applied E_{ulp}. Because PtPb electrodes exhibit excellent electrocatalytic activity towards the oxidation of formic acid and methanol, both of them could stabilize the PtPb intermetallic phase based on the mechanism of competition of oxidations previously described. In Figures 4.7 and 4.8, the kinetic stabilization effect of the PtPb electrodes induced by oxidation of methanol was investigated via X-ray GID. There were no detectable diffraction signals ascribable to a $PbSO_4$ phase after cycling to E_{ulp} value of +1.00V in the presence of methanol. However, the electrochemical pretreatment in supporting electrolyte only, gave rise to Pb leaching out process and resulted in the formation of $PbSO_4$ at detectable levels. When comparing the diffraction signals of $PbSO_4$ from the PtPb electrode after cycling to E_{ulp} values of +0.80V in 0.1M H_2SO_4 (Figure 4.5) and E_{ulp} values of +1.20V in 0.2M CH_3OH/0.1M H_2SO_4 (Figure 4.7), the amount of surface $PbSO_4$ species on the PtPb after these two cases were very similar. This suggests that the lead leaching out process was largely precluded by the oxidation of methanol molecules. This was also qualitatively shown by the pseudo 2D-mapping images of X-ray GID data after different electrochemical treatments (Figure 4.8). As can be ascertained, there was little difference in the partial powder diffraction patterns as a function of applied

Figure 4.7 X-ray GID data of a PtPb/Pt_3Pb electrode in 0.2M CH_3OH/0.1M H_2SO_4 solution after cycling at 10mV/s to E_{ulp} values of +0.80V, +1.00V and +1.20V.

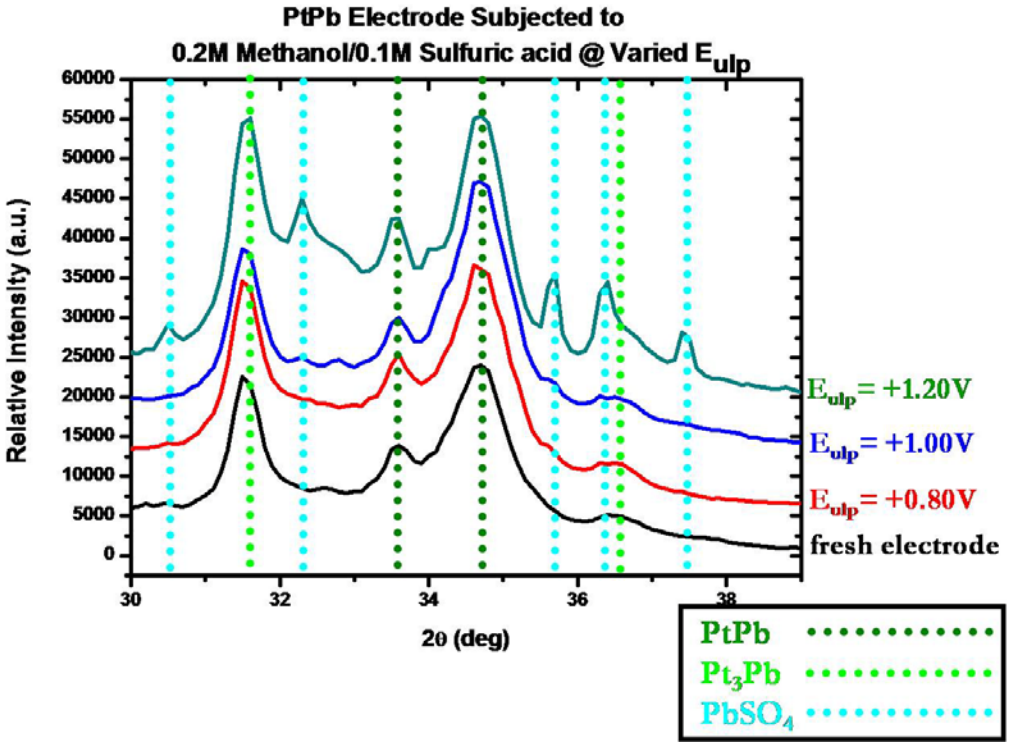
PtPb Electrode Subjected to
0.2M Methanol/0.1M Sulfuric acid @ Varied E_ulp
Relative Intensity (a.u.)
2θ (deg)
E_ulp = +1.20V
E_ulp = +1.00V
E_ulp = +0.80V
fresh electrode
PtPb
Pt3Pb
PbSO4

Figure 4.8 Pseudo 2D-mapping images of *in-situ* X-ray GID data of the PtPb electrode in 0.2M CH_3OH/0.1M H_2SO_4 after cycling to E_{ulp} values of +0.80V (b) and +1.20V (c) in comparison to the fresh polished electrode (a).

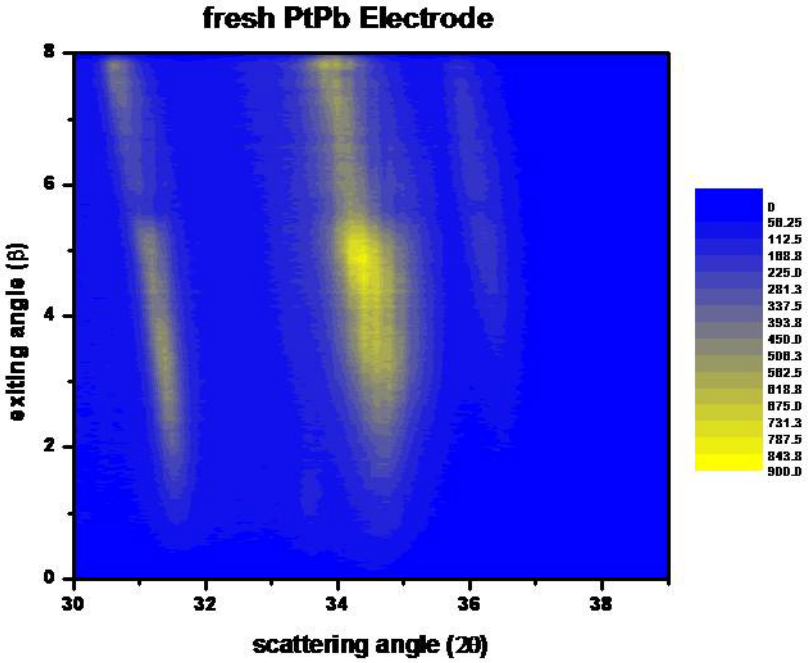
fresh PtPb Electrode
exiting angle (β)
scattering angle (2θ)
0
2
4
6
8
30
32
34
36
38
0
50.25
112.5
168.8
225.0
281.3
337.5
393.8
450.0
506.3
562.5
618.8
675.0
731.3
787.5
843.8
900.0

(a)

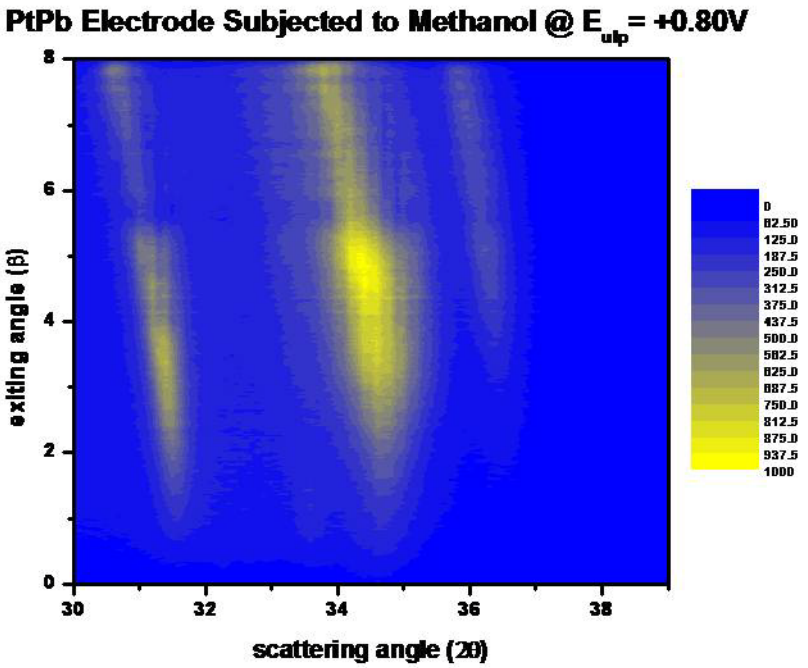
PtPb Electrode Subjected to Methanol @ E$_{ulp}$ = +0.80V
exiting angle (β)
scattering angle (2θ)
0
2
4
6
8
30
32
34
36
38
0
62.50
125.0
187.5
250.0
312.5
375.0
437.5
500.0
562.5
625.0
687.5
750.0
812.5
875.0
937.5
1000

(b)

Figure 4.8 (Continued)

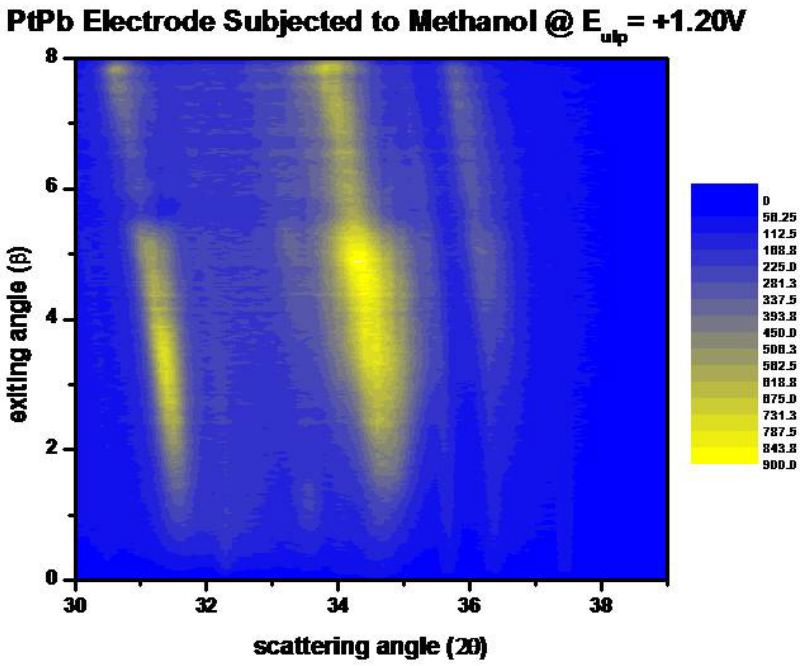

(c)

potential even for E_{ulp} values as high as +1.20V.

4.3.2.2 Perchloric acid solution as supporting electrolyte

The studies intended to investigate the change in surface composition and structure of the PtPb electrode in sulfuric acid solution could not be utilized to characterize the formation of platinum crystalline domains due to the strong interference of the $PbSO_4$ species precipitated on the PtPb electrode. In order to overcome this, perchloric acid was used as the supporting electrolyte in place of the sulfuric acid to investigate the stabilization effects induced by different fuel molecules. Surface X-ray GID scans of the polycrystalline PtPb electrode over the 30~39 deg range were recorded after cycling potentials between -0.20V and +1.20V at 10mV/s for 10 cycles in different solutions. Figure 4.9 (a) presents diffraction signals corresponding to Pt(111) for a freshly polished PtPb electrode. We believe that they are due to a Pt crystalline phase impurity incorporated into PtPb intermetallic phase during the synthesis process. This likely also arises as a result of the fact that PtPb is not a congruently melting phase. There were two significant changes in the surface composition and structure for the PtPb electrode after electrochemical pretreatment in 0.1M $HClO_4$: 1) apparent increase in the diffraction intensity of the Pt(111) peak; 2) shifting to lower two theta values of the PtPb(110) diffraction peak. The increase in the Pt(111) diffraction intensity likely resulted the formation of external Pt crystalline domains with ~5 nm diameter, as estimated from the Scherrer equation, as a consequence of the lead leaching out process induced by the electrochemical pretreatment to relatively positive E_{ulp} values. Shifting of the PtPb(110) diffraction peak reflected a small lattice expansion (less than 1%) for outmost layer of PtPb intermetallic crystal lattice. These two signs could be utilized to monitor the stabilization effect induced by different fuel molecules. As seen

Figure 4.9 X-ray GID data of a PtPb electrode in different solutions after cycling at 10mV/s to an E_{ulp} value of +1.20V: (a) in 0.1M $HClO_4$; (b) in 0.2M HCOOH/0.1M $HClO_4$; (c) in 0.2M CH_3OH/0.1M $HClO_4$.

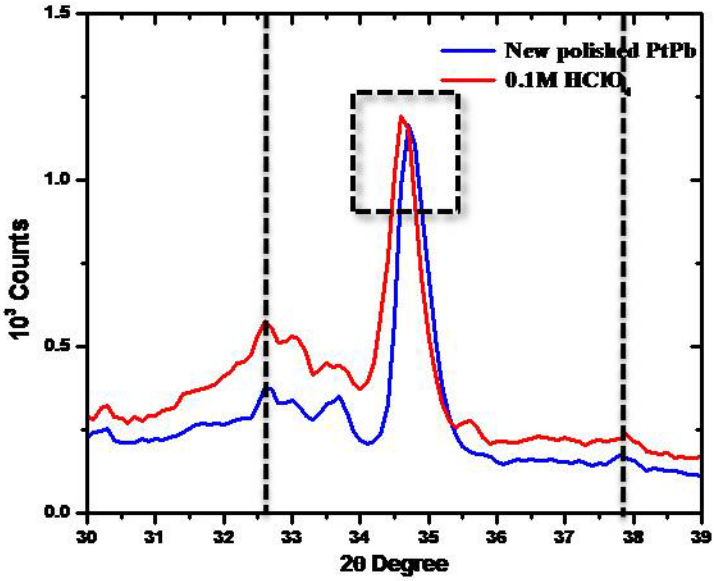
New polished PtPb
0.1M HClO4
10^3 Counts
2θ Degree

(a)

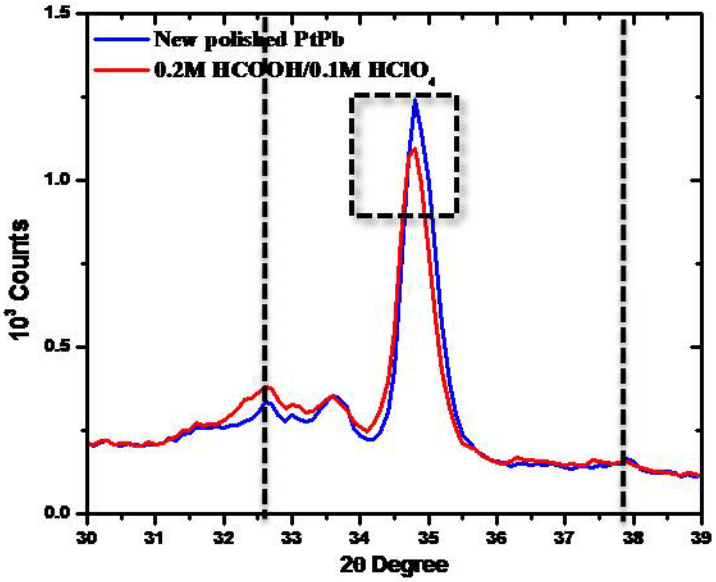
New polished PtPb
0.2M HCOOH/0.1M HClO4
10^3 Counts
2θ Degree

(b)

Figure 4.9 (Continued)

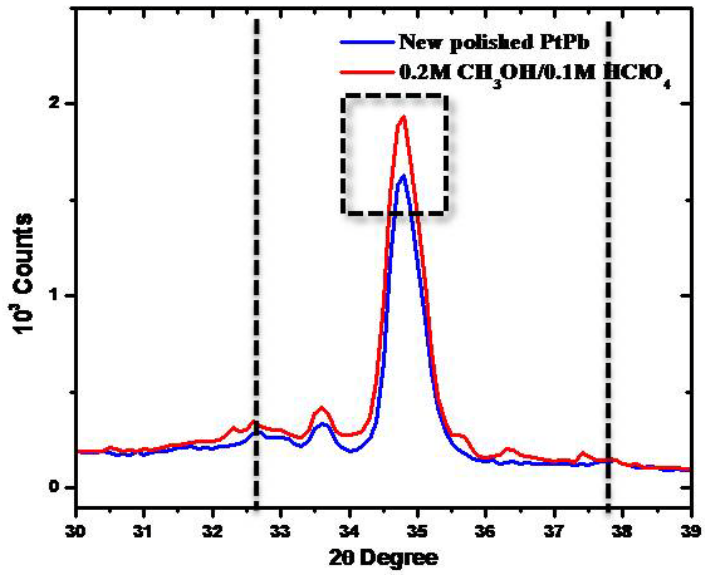

(c)

in Figure 4.9 (c), there was no detectable enhancement in the intensity of the Pt(111) diffraction peak and the PtPb(110) diffraction peak position remained unchanged during the oxidation of methanol at the PtPb electrode surface when cycling potential to an E_{ulp} value of +1.20V. It is evident that the lead leaching out /dissolution process was completely precluded by methanol. In Figure 4.9 (b), the kinetic stabilization effect induced by formic acid oxidation on the PtPb electrode was clearly observed with a much lower amplitude enhancement of the Pt(111) peak and shifting of PtPb(110) diffraction peak location when compared to those in 0.1M $HClO_4$ only. However, the lead leaching out/dissolution process was not completely precluded in this case based on a detectable enhancement in the intensity of Pt(111) diffraction peak when compared to the 0.2M CH_3OH/0.1M $HClO_4$ case. This phenomenon is consistent with the lower onset potential of formic acid oxidation relative to methanol oxidation.

4.3.3 The effects of holding potentials on polycrystalline PtM electrodes

4.3.3.1 Formation of Bi_2O_3 nanocrystalline domains

Previous X-ray photonelectron spectroscopy (XPS) characterization had shown that Bi_2O_3 and $PbCO_3$ species are formed on PtBi and PtPb electrodes, respectively, when cycling to E_{ulp} values of +0.80V. However, no crystalline bismuth or lead oxidized species were detected via in-situ X-ray GID technique for this kind of electrochemical pretreatment in only supporting electrolyte. The effects on the surface composition and structure of holding the potential, instead of cycling, were systematically investigated for both polycrystalline PtBi and PtPb electrodes. In Figure 4.10, same PtBi electrode was used for experiments in sulfuric acid and perchloric acid solutions. The diffractions peak at 33.2 and 34.3 deg were ascribed to PtBi(-120) and PtBi(110) respectively. Since the bulk PtBi electrode was not a perfect powder polycrystalline

Figure 4.10 Formation of surface bismuth oxidized species on a PtBi electrode after holding the potential at +1.20V for 30 min in 0.1M H_2SO_4 (left) or 0.1M $HClO_4$ (right) solutions.

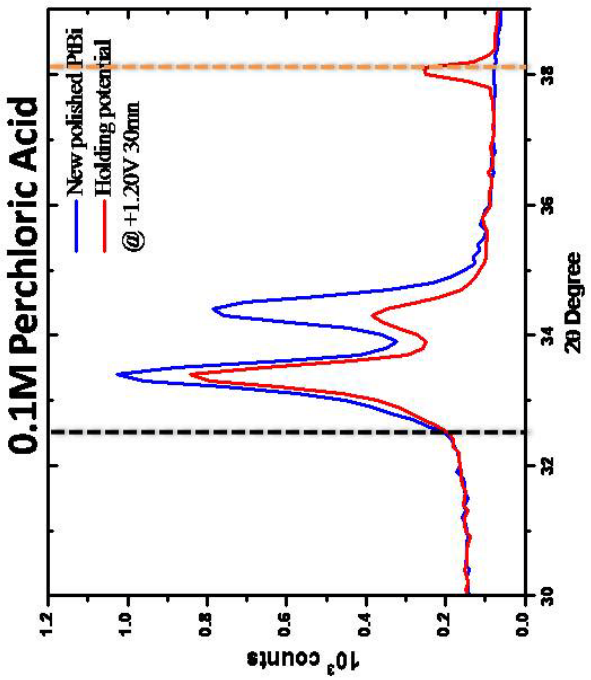
0.1M Perchloric Acid
New polished PtBi
Holding potential
@ +1.20V 30mn
10³ counts
2θ Degree

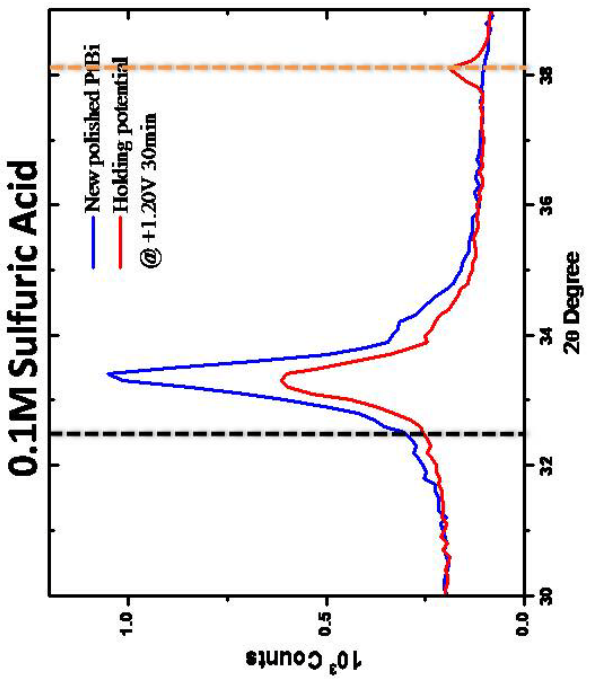
0.1M Sulfuric Acid
New polished PtBi
Holding potential
@ +1.20V 30min
10³ Counts
2θ Degree

smple, slightly different surface terminated crystalline structures would be obtained by ostensibly similar polishing procedures. This was a property observed for all intermetallic phases used in our experiments and which was illustrated by the non-uniform and discontinuous powder rings with unexpected spots in the pseudo 2D-mapping images. As mentioned earlier, no crystalline bismuth oxidized species had been detected and Pt nanocrystalline domains were formed as a consequence of bismuth leaching out from the matrix and dissolving into the solution after cycling potentials to relatively positive E_{ulp} values in the supporting electrolyte. In Figure 4.10, Surface X-ray GID data over the 30~39 deg range were obtained in 0.1M H_2SO_4 and 0.1M $HClO_4$, respectively, after holding the potentials at +1.20V for at least 30 min. There was no signal form Pt crystalline domains on the PtBi electrode to indicate that either bismuth was leached out from the matrix, or those Pt atoms remained as an amorphous phase after electrochemical pretreatment in 0.1M H_2SO_4 or $HClO_4$ solutions. A strong diffraction peak at 38.3 deg due to Bi_2O_3 suggested that well-defined crystalline bismuth oxidized species were generated on the surface while holding the potentials instead of forming unstable bismuth species that would leach into solution. The estimated crystalline domains of the Bi_2O_3 were ~50 nm, which is much larger than the size of Pt nanocrystalline domains induced by cycling potentials.

Well-defined PtBi electrode surfaces with different composition and structures could be reproducibly and deliberately produced by electrochemical pretreatments, with PtBi electrode surfaces decorated with a Pt skin induced by cycling potentials or with a top layer decorated with bismuth oxide nanocrystals induced by holding potentials. It was of great importance and interest to explore the electrocatalytic activities of differently terminated electrode surfaces. In Figure 4.11, the current density for formic acid oxidation increased after either potential cycling or holding potential pretreatments but it was surprising that the onset potentials and current

Figure 4.11 CV profiles for formic acid oxidation of differently terminated PtBi electrodes from electrochemical treatment of either holding or cycling the potential.

Pt crystalline structure ~5nm

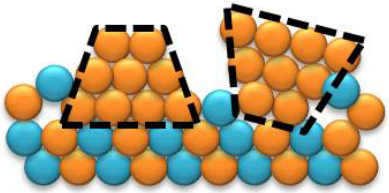

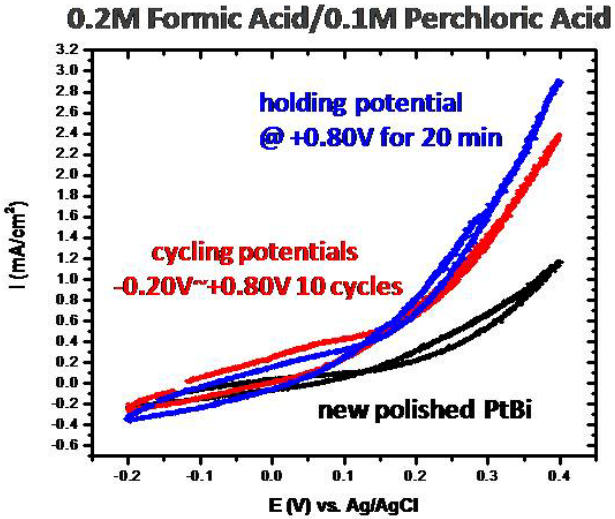

Bi_2O_3 crystalline structure ~50nm

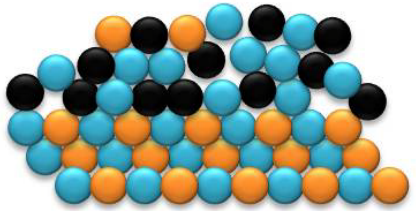

densities were very similar for both of these two electrode surfaces with different terminations. In comparison to a freshly polished electrode surface, the current density increase is likely due to more exposure of surface Pt atoms for pretreatment involving the cycling potential. The activity improvement for the Bi_2O_3 decorated electrode surface could be rationalized in terms of an increase in the boundary line between the PtBi intermeatllic domains and bismuth oxidized species, akin to PtRu alloys.

4.3.3.2 Instability of outmost layer of PtPb intermetallics

Previous *ex-situ* XPS experiment showed that $PbCO_3$ species are formed on the PtPb electrode surface after certain CV characterization in supporting electrolyte. However, no evidence of any crystalline lead oxidized species was detected via *in-situ* X-ray GID for similar electrochemical pretreatment. Surface X-ray GID scans over the 18~28 deg, 30~39 deg and 42~51 deg ranges, which included all major diffraction peaks corresponding to PbO, PbO_2 and $PbCO_3$ phases, were carried out after holding the potential at +1.20V for a series of time periods. Figure 4.12 presents data for a freshly polished PtPb electrode, with diffraction peaks at 32.2 and 37.3 deg corresponding to the Pt_3Pb intermetallic phase. This suggests the presence of Pt_3Pb domains in the I PtPb electrode. Unlike the formation of surface crystalline bismuth oxidized species on the PtBi electrode, no diffraction signals due to any type of lead oxidized species were obtained while holding the potential. On the contrary, the intensity of the Pt(111) diffraction peak gradually increased as a function of holding time at +1.00V in 0.1M $HClO_4$ solution while for the PtBi electrode, under similar electrochemical conditions, no Pt crystalline domains were formed on the electrode surface. Moreover, the PtPb diffraction peaks at 34.2 and 35.6 deg diminished, and at the same time, shifted to lower two theta values as a function of time. This suggests

Figure 4.12 Surface X-ray GID characterization to investigate the stability of the outmost layer of PtPb intermetallic phase and formation of Pt nanocrystalline domains.

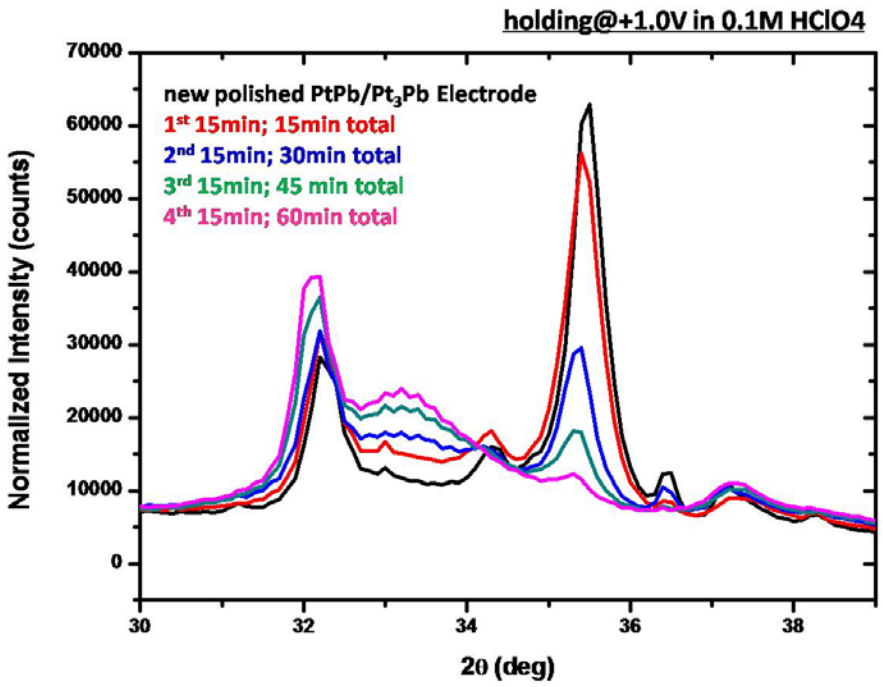
holding@+1.0V in 0.1M HClO4
new polished PtPb/Pt3Pb Electrode
1st 15min; 15min total
2nd 15min; 30min total
3rd 15min; 45 min total
4th 15min; 60min total
Normallized Intensity (counts)
70000
60000
50000
40000
30000
20000
10000
0
30
32
34
36
38
2θ (deg)

that the outmost PtPb layer was etched away and the crystal lattice was slightly expanded. The Pt nanocrsyalline domains formed by holding the potential were the consequence of lead leaching out into the solution which is similar to the PtPb electrode subjected to CV treatments. Special attention was paid to the diffraction peaks corresponding to the Pt_3Pb intermetallic phase. Those diffraction signals kept almost constant but also gradually shifted to lower two theta values as a function of holding time indicating slight expansion of the Pt_3Pb top layer.

4.4 Conclusion and Summary

Kinetic stabilization effects induced by the presence of active fuel molecules (formic acid and methanol) were observed and extensively investigated for both PtBi and PtPb intermetallic phases. Leaching of the less noble element (Bi or Pb) was completely precluded and no Pt nanocrystalline domains were formed on the electrode surface while in presence of active fuel molecules (formic acid for PtBi, formic acid and methanol for PtPb) in the supporting electrolyte. This phenomenon could be explained as the competition between the oxidation of active fuel molecules at the electrode/solution interface and the corrosion/oxidation process of the electrode surface itself. The active fuel molecules were catalytically oxidized at potentials negative of the corrosion/oxidation processes of the electrode surface. In the PtBi electrode case, monitoring the changes of Pt diffraction signals could be used to demonstrate the Bi leaching out and Pt domain forming processes. In the case of PtPb, $PbSO_4$ precipitation, arising from the lead leaching out process could be utilized to investigate these phenomena. Formation of surface $PbSO_4$ species appears to inhibit the formation of Pt crystalline domains on the electrode surface. On the other hand, in 0.1M $HClO_4$ solution, GID data indicated the formation of Pt crystalline domains as

well as a slight expansion of the surface crystal lattice for the PtPb intermetallic phase. The effects on the surface termination of the intermetallic phases, induced by different electrochemical treatments of cycling and potential holding were characterized via surface X-ray GID. When holding the potential, crystalline Bi_2O_3 domains, with ~50 nm diameter, were formed on the electrode surface and no Pt crystalline islands were generated as a consequence of the preclusion of the bismuth leaching out process. On the other hand, no lead oxidized species were detected, and at the same time, Pt nanocrystalline domains were formed on the PtPb electrode surface when holding the potential. In this study, we employed synchrotron based X-ray surface characterization to explore the change in electrode surface composition and structure of ordered intermetallic phases under active electrochemical control. Not only is the information obtained from such studies valuable to understand the electrocatalytic activity of intermetallic phases, but also, it is of great importance to provide a general fundamental research approach to explore, in-depth, more promising candidates in-depth as catalysts for fuel cell applications.

REFERENCES

1. J. Zhang, K. Sasaki, E. Sutter and R.R. Adzic, *Science* 315, 220, **2007**
2. N. Tian, Z. Zhou, S. Sun, Y. Ding and Z. Wang *Science* 316, 732, **2007**
3. J.K. Nørskov, T. Bligaard, J. Rossmeisl and C.H. Christensen, *Nature Chemistry* 1, 37, **2009**
4. B.S. Mun, M. Arenz, K.J.J. Mayrhofer, C.A. Lucas, G. Wang, P.N. Ross, V.R. Stamenkovic and N.M. Markovic, *Nature Materials* 6, 241, **2007**
5. M. Li, K. Sasaki, M.B. Vukmirovic, N.S. Marinkovic, P. Liu, A.I. Frenkel, A. Kowal, M. Shao, J. Zhang, R.R. Adzic, *Nature Materials* 8, 325, **2009**
6. H.D. Abruña *et al.*, *Bulletin of Chemical Society of Japan* 80, 1843, **2007**
7. N.M. Markovic and P.N. Ross, *Surface Science Reports* 45, 117, **2002**
8. M. Watanabe and S. Motoo, *J. of Electroanal. Chem.* 60, 267, **1975**
9. *"Catalysis and Electrocatalysis at Nanoparticle Surface"* edited by A. Wieckowski, E.R. Sovinova and C.G. Vaynenas (CRC, **2003**) Chapter 22 *"Design of Electrocatalysts for Fuel Cells"* by M. Watanabe, p827
10. M. Watanabe and S. Motoo, *J. of Electroanal. Chem.* 60, 275, **1975**
11. J. McBreen and S. Mukerjee, *J. of Electrochem.Soc.* 143, 1685, **1996**
12. A.S. Aricó, P.L. Antonucci, E. Modica, V. Baglio, H. Kim and V. Antonucci, *Electro. Acta.* 47, 3723, **2002**
13. V. Radmilovic, H.A. Gasteiger and P.N. Ross, *J. Catal.* 154, 98, **1995**
14. R. Liu, H. Iddir, Q. Fan, G. Hou, A. Bo, K.L. Ley, E.S. Smotkin, Y.-E. Sung, H. Kim, S. Thomas, and A. Wieckowski, *J. Phys. Chem. B* 104, 3518, **2000**
15. S. Stoupin, E. Chung, S. Chattopadhyay, C. U. Segre and E.S. Smotkin, *J. Phys. Chem. B* 110, 9932, **2006**
16. J.S. Spendelow and A. Wieckowski, *Phys. Chem. Chem. Phys.* 21, 2654, **2007**

17. W. Chen, J. Kim, S. Sun and S. Chen, *Langmuir* 23, 11303, **2007**

18. S. Koh and P. Strasser, *J. Am. Chem. Soc.* 129, 12624, **2007**

19. R. Srivastava, P. Mani, N. Hahn and P. Strasser, *Angew. Chem. Int. Ed.* 46, 8988, **2007**

20. H.A. Gasteiger, S.S. Kocha, B. Sompalli and F.T. Wagner, *Appl. Catal. B: Environ.* 56, 9, **2005**

21. J. Zhang, M.B. Vukmirovic, K. Sasaki, A.U. Nilekar, M. Mavrikakis and R.R. Adzic, *J. Am. Chem. Soc.* 127, 12480, **2005**

22. V.R. Stamenkovic, B. Fowler, B.S. Mun, G. Wang, P.N. Ross, C.A. Lucas and N.M. Markovic *Science* 315, 493, **2007**

23. E. Casado-Rivera, Z. Gál, A.C.D. Angelo, C. Lind, F.J. DiSalvo and H.D. Abruña, *Chem. Phys. Chem.* 4, 193, **2003**

24. E. Casado-Rivera, D.J. Volpe, L. Alden, C. Lind, C. Downie, T. Vázquez-Alvarez, A.C.D. Angelo, F.J. DiSalvo and H.D. Abruña, *J. Am. Chem. Soc.* 126, 4043, **2004**

25. Y. Liu, D.R. Blasini, F.J. DiSalvo and H.D. Abruña, *submitted*

26. Y. Liu, H. Abe, H.M. Edvenson, F.J. DiSalvo and H.D. Abruña, *submitted*

27. D.R. Blasini, D. Rochefort, E. Fachini, L.R. Alden, F.J. DiSalvo, C.R. Cabrera and H.D. Abruña, *Surface Science* 600, 2670, **2006**

28. D.E. Nowak, D.R. Blasini, A.M. Vodnick, B. Blank, M.W. Tate, A. Deyhim, D.-M. Smilgies, H.D. Abruña, S.M. Gruner and S.P. Baker, *Rev. Sci. Instrum.* 77, 113301, **2006**

CHAPTER FIVE

FABRICATION AND SURFACE CHARACTERIZATION OF SINGLE CRYSTAL PtBi AND PtPb (100) AND (001) ELECTRODES*

5.1 Introduction

The catalytic activity of material is generally dependent on composition or constitute, which in turn mediate electronic structures and properties,[1-2] or atomic structure or arrangement,[3-4] which are correlated to geometric parameters and coordination symmetry. Recently there has been a great deal of research on the development and design of new electrocatalysts as anodes and cathodes for fuel cell applications due to globally increasing demand for environmentally friendly power and energy sources.[5-6] Exploring and understanding structure-property-activity relationships of specific catalysts is of great importance to clarify reaction mechanisms and provide valuable information for design new catalysts. The case of single crystal surfaces, with well-defined and controllable electronic properties and atomic geometric structure, offer model reaction platforms for such work.[7]

In recent years, scientists have focused on the synthesis of well-defined nanomaterials which are capped by different single crystal facets and their application as fuel cell catalysts. Shouheng Sun and co-workers[8-9] have reported on the controlled synthesis of well-defined single crystal Pt nanoparticles capped with low-index facets either {100} or {111} and showed enhanced electrocatalytic activity towards oxygen reduction reaction (ORR) in comparison to conventional Pt nanospheres. Shigang Sun and co-workers[4,10] reported on high-index facets capped tetrahexahedral platinum

*Reproduced with permission from the manuscript in preparation, ready to be submitted.

nanocrystals synthesized by a square-wave voltammetric method. These Pt nanocrystals capped by {710}, {520} and {210} facets showed greatly enhanced electrocatalytic activity for the electrooxidation of formic acid and ethanol. Zhuang, Abruña and co-workers[11] demonstrated morphology-dependent activity of palladium nanomaterials from normal galvanic deposition. Pd nanorods which were capped by {110} facets had much higher catalytic activity towards the ORR than Pd nanoparticles which were capped by either {111} or {100} facets.

On the other hand, in order to reduce the amount of platinum employed thus lowering cost and mitigate carbon monoxide poison, bimetallic or mutlimetallic materials have attracted special attention in the fuel cell research community for some time.[12-13] Yang and co-workers[14] synthesized well-defined Pt-Pd cubic nanostructures which were capped by single crystal {100} facets. These Pt-Pd nanocubes showed great activity for the electrooxidation of formic acid consistent with results obtained on solid state single crystal surfaces.[15] A major drawback of nanocrystals capped with single crystal facets is a lack of characterization and analysis of structure and composition of single facets under active electrochemical control. Experimentally, it is also very difficult to manipulate such surfaces and facets.

Traditional solid state single crystals represent an ideal reaction platform and are amenable to surface characterization methods either *in-situ* or *ex-situ*. Abruña and co-workers[16-19] reported that bismuth-modified platinum high-index single crystal surfaces, which were prepared via the under potential deposition (UPD) process, exhibited extraordinary enhancements in reactivity towards formic acid oxidation. Stamenkovic and Markovic[2] reported that nickel modified Pt(111) surfaces prepared in an ultra high vacuum (UHV) system, showed improved activity towards the ORR. There were 10-fold more active than Pt(111) itself or 90-fold more active than the current commercial Pt/C catalyst used in fuel cells. They also reported on the catalytic

activity trend towards the ORR of a series of $Pt_3M(111)$ (M=Ni, Co, Fe, Ti, V) surfaces prepared under UHV system by sputtering and annealing.[20] To our knowledge, current research to explore the structure-property-activity based on experimental approach either uses well-defined nanocrystal as model or is based on modified noble single crystal surfaces. There are few literatures about direct fabrication of bimetallic or multimetallic single crystal surfaces from solid state intermetallic bulk materials.[21]

Ordered intermetallic phases have several advantages as potential electrocatalysts when compared to alloys. Intermetallic phases have high enthalpies of formation which result in more stable and ordered structure. They also have well-defined crystalline structure and their electronic and geometric structures can be controllably tuned through composition and phase. For electrocatalytic applications, DiSalvo and Abruña demonstrated that PtBi[22] and PtPb[23] exhibited high electrocatalytic activity towards formic acid (PtBi and PtPb) and methanol (PtPb) oxidation reactions as well as excellent tolerance to carbon monoxide poisoning. As nanomaterials, these intermetallic phases also exhibited high electrocatalytic activities for SOMs electrooxidation.[24-27]

In order to obtain a more in-depth understanding of the changes in structure and composition of the intermetallic phases under electrochemical control and explore structure-property-activity relationships, the surface characterization of well-defined single crystal intermetallic surfaces can provide the most valuable information. *In-situ* surface characterization studies will allow a better understanding, at the atomic level, of electrocatalytic activity.

5.2 Materials and Experimental Section

5.2.1 Synthesis of PtBi ad PtPb single crystal bulk materials

In order to obtain polycrystalline PtBi as starting material, platinum powder (John Matthey, 99.999%) and bismuth powder (Alfa Asear, 99.999%) from pellets were thoroughly mixed in the appropriate molar ratios in an agate mortar. Pellets (6 mm OD, 4 mm length) were pressed in a hydraulic press. The pellets were sealed in evacuated fused silica tubes (10 mm ID, 100 mm length) and heated, oriented vertically, in a box furnace to 800 ℃ for 24 hours and annealed at 650 ℃ for 48 hours. The pellets were ground and the above procedure was repeated twice. The polycrystalline PtBi sample was crushed and conventional powder X-ray diffraction confirmed phase purity. The crushed sample was loaded into a point fused silica tube (10 mm ID, 150 mm length), which was sealed under vacuum and then heated to 850 ℃. After cooling down to room temperature, the tube was held vertically on the pedestal of a Stockbarger crystal growth system. The furnace was slowly raised at a rate of 2 mm per hour, and the melting sample was cooled from 900 ℃ to 200 ℃ over a period of 154 hours, resulting in a high quality single crystal PtBi bulk material.

Synthesis of single crystal PtPb bulk materials is similar but more complicated than PtBi because PtPb is not a congruently melting phase. Platinum powder and lead powder (Alfa Asear, 99.9%) were mixed as 45 at% Pt and 55 at% Pb, placed in an alumina crucible and sealed in an evacuated silica tube. This tube was heated at 800 °C in a box furnace overnight. The $Pt_{.45}Pb_{.55}$ sample was crushed and loaded into a point fused silica tube (10 mm ID, 150 mm length) and sealed under vacuum. The sample was heated to 800°C and the molten sample was agitated to ensure that the melt completely filled the tip of the tube. After cooling to room temperature, the single crystal was grown in the same way as PtBi. The results in single crystal PtPb bulk

material in the tip of the silica and other platinum lead phases at the top of the tube. The multiphase material was removed from the single crystal PtPb during polishing steps.

5.2.2 Fabrication of different single crystal facets of PtM: (100) and (001)

The single crystal PtM bulk sample was placed on the sample holder at the top of a standard Huber goniometer head and then completely concreted with epoxy which was allowed to use overnight. The sample was polished via 1200 Grit sandpaper (Buehler) to expose a spot of 3~5 mm diameter. X-ray Laue Back-Reflection (BLR) was utilized to determine the precise orientation of single crystal facets by using MWL 110 Real-Time Back Reflection Laue Camera System (Multiwire Laoratories). All BLR patterns were recorded under following conditions: 150 mm film-to-specimen distance, 40 seconds recording time, background subtraction level 4 and 1 mm X-ray beam size. The BLR method was used to not only determine the precise orientations of different single crystal surfaces, but also confirm crystalline quality of single crystal PtM bulk materials. Clear BLR patterns with hexagonal symmetry and rectangular symmetry were for PtM (001) and (100) orientations, respectively. After determining its specific orientation, the sample on the Huber goniometer head was placed back to the polishing system and polished starting with 600 Grit sandpaper for 30 min and then, step by step, down to 800 Grit sandpaper for 60 min and 1200 Grit sandpaper for 60 min, lubricating the entire polishing procedure with deionized (DI) water. The final polishing was carried out with 1 μm diamond paste (Buehler) for 20 min and 200 nm diamond paste for 20 min with a suitable extender (Metadi-Buehler) to obtain a mirror-like surface. The BLR method was utilized to once again check the orientation after polishing in case of any misorienting or shifting of the facets. After dissolving the

epoxy, well-defined single crystal surfaces with precise orientation were obtained. The single crystal surfaces were annealed in a quartz tube at 400 ℃ for 12 hours under flowing 5% hydrogen/95% high purity nitrogen forming gas (Airgas) to remove any organic containments due to the orienting/polishing procedure and to decrease surface roughness.

5.2.3 In-situ X-ray grazing incidence diffraction measurement

The single crystal PtM electrodes with specific orientation were placed at the center of *in-situ* electrochemical cell, which was deliberately designed and built for combing X-ray surface scattering and electrochemical characterization.[28] Cyclic votalmmetry was carried out on a BAS CV-27 potentiostat/golvanostat (Bioanalytical Systems) and recorded on a computer through a PCI-DAQ card (National Instruments). All potentials are referenced to a Ag/AgCl (saturated NaCl) electrode without regard for the liquid junction potential. All chemicals were of at least A.R. purity or higher (Sigma Aldrich) and were used as received. 18.2 MΩ DI water (Millipore) was used for all electrochemical characterizations. The typical electrochemical treatment consisted of cycling the potential at 10mV/s from -0.20V to different upper limit potentials, labeled as E_{ulp}, ranging from +0.40V to +0.80V. After the electrochemical pretreatment, part of the supporting electrolyte was withdrawn so that the polypropylene film was recessed, generating a thin film of electrolyte. The electrolyte film, however, was sufficiently thick (we estimate the thickness to be of the order of 20 μm) to ensure good potential control in all cases. Two different scans for X-ray scattering characterization were employed. Surface X-ray grazing incidence partial survey diffraction was carried out over the range of 30~40 deg which covered the major Pt and PtM diffraction peaks. A horizontal in-pane X-ray scattering geometry

was employed. In this case, the electrode surface normal was perpendicular to the ground, and the detector moved within the plane which was almost parallel to the electrode surface. Particular attention was given to changes in the appearance and intensity of the platinum and disappearance and intensity of PtM diffraction peaks as a function of the applied E_{ulp}. Azimuthal scans, which were utilized to investigate the surface symmetry and pattern, were carried out at Pt(111), Pt(002) and PtM (110) diffraction peaks by rotating the single crystal sample. The critical angle for the PtM ordered intermetallic pahses is ~0.5 deg. The typical incidence angle employed in partial survey or azimuthal GID scan experiments was ~0.25 deg which is well below the critical angle. All X-ray scattering experiments were carried out at the G-line station at the Cornell High Energy Synchrotron Source (CHESS). All diffraction experiments were carried out on a home-made six-circle *kappa* diffractometer.[29] The experimental X-ray incidence energy was 9.374 KeV (1.323 Å). The beam size was 2 mm horizontal by 200 μm vertical. This asymmetric beam shape was deliberately chosen so as to optimize surface sensitivity. The typical photon flux intensity at the center of rotation (COR) of the diffractometer was ~10^{13} photons/sec/mm^2. A position sensitive detector (also known as linear gas detector) was utilized to collect the scattered photons. The detector angular resolution was ~0.18 deg. More detailed information about the diffractometer and experimental geometry can be found elsewhere.[28-29]

5.3 Results and discussions

5.3.1 BLR characterization for determination of specific facet orientation

PtBi and PtPb have the same crystal lattice structure (NiAs structure) and symmetry with slightly different lattice parameters. Figure 5.1 presents the crystal lattice

Figure 5.1 Crystallography basics of PtM intermetallic phases: (a) unit crystal lattice of PtM, lattice parameter for PtBi: a=b=4.324 Å, c=5.501Å; lattice parameter for PtPb: a=b=4.250 Å, c=5.456 Å; for both of them: $\alpha=\beta=90^{\circ}$, $\gamma=120^{\circ}$; (b) and (c) show a PtM(100) facet with 2 fold symmetry and a PtM(001) facet with 6 fold symmetry, respectively.

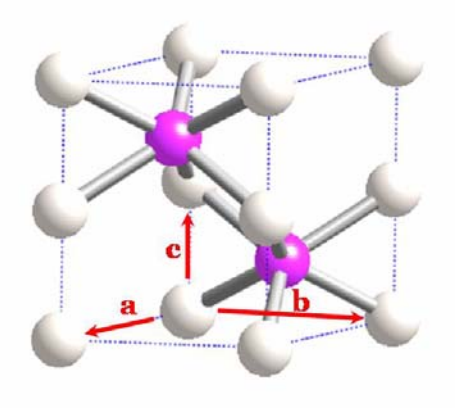

(a)

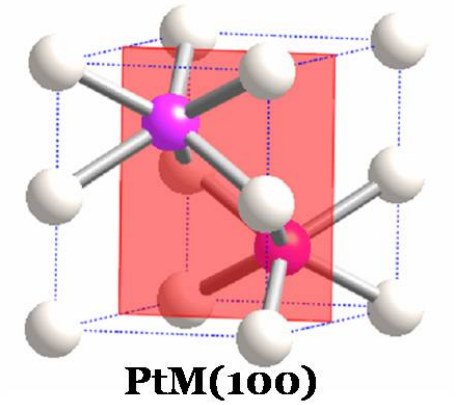

(b)

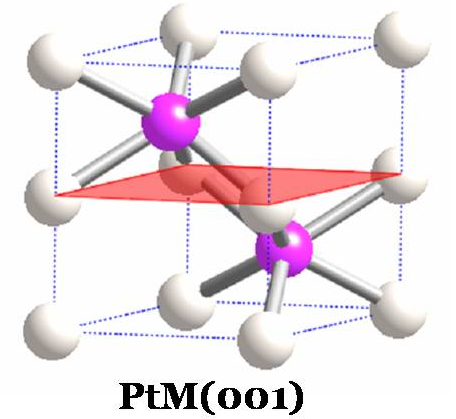

(c)

structure of these intermetallic phases. Platinum atoms, labeled as white balls, occupy the corner positions and bismuth or lead atoms are labeled as pink balls. More detailed information for PtM (100) and (001) facets is presented in Figure 5.2. PtM (100) facets have 2-fold rectangular symmetry. From the side view of a PtM(100) surface, there are two kinds of terminations for this facet. In the case of PtBi, there is a platinum termination with a Pt-Pt distance of 4.324Å and 2.75Å, respectively. The other one is a bismuth termination with zigzag shaped double bismuth layers. The PtM (001) facet has 6-fold hexagonal symmetry. Besides the platinum termination with a Pt-Pt distance of 4.324Å, this facet can be terminated by bismuth single layer. BLR was utilized to precisely determine the specific orientation and check the quality of the single crystal samples. As shown in Figure 5.3, clear BLR images of hexagonal and rectangular patterns for PtBi(001) and (100), respectively, were obtained by adjusting the arcs of the standard Huber goniometer head. Lack of phase purity of single crystal intermetallics would give images which had either twin BLR patterns or some minor reflection pattern incorporating with major symmetry. The miscut angle of the single crystal surfaces prepared by this method was measured to be ~0.25 deg, which is consistent with the 0.20 deg of instrumental resolution. While a annealing procedure under the flow of forming gas at 400℃ for over 12 hours improved surface roughness and removed organic contaminants, an atomically flat surface could not be obtained unless Argon sputtering and thermo-annealing process under UHV system were employed.[30]

5.3.2 Cyclic Voltammetric Characterization of PtM single crystal electrodes

Cyclic voltammetric characterization was carried out in 0.1M sulfuric acid at a scan rate of 10mV/s in the *in-situ* X-ray electrochemical cell. As shown in Figure 5.4 (a),

Figure 5.2 Different views of PtM (100) and (001) facets showing detailed information of surface symmetries and atomic arrangements, respectively.

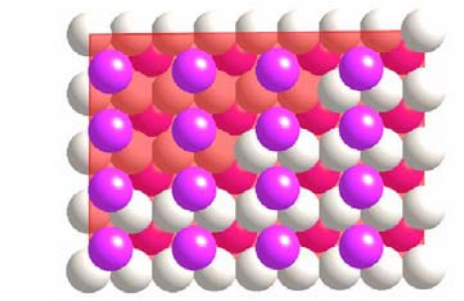

top view

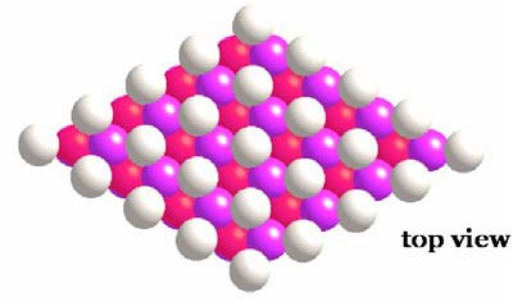

top view

PtM(100)

PtM(001)

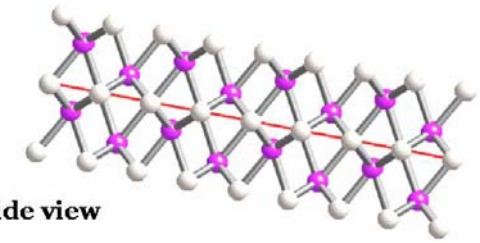

side view

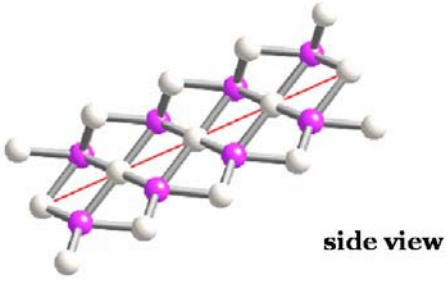

side view

Figure 5.3 BLR images of high quality single crystal PtBi(001) orientation (left) and PtBi(100) orientation (right).

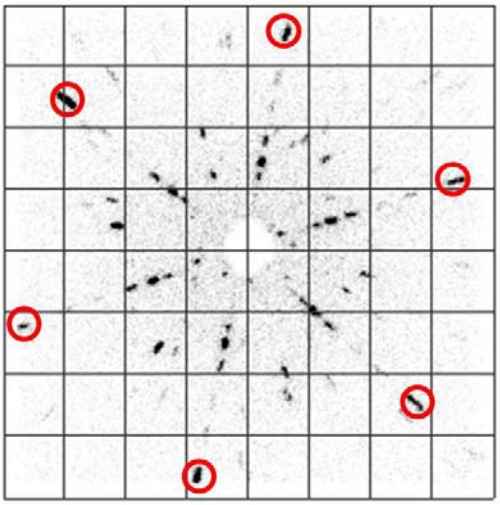

PtBi(001)

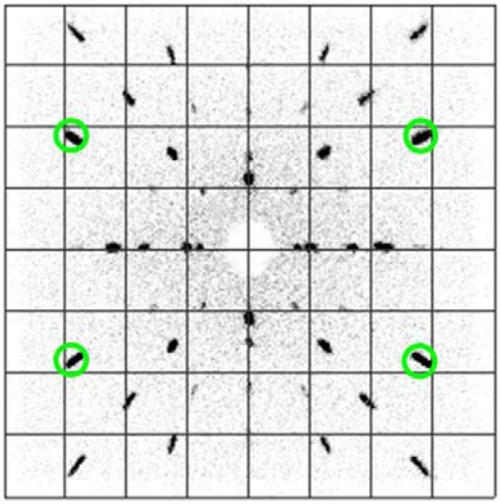

PtBi(100)

Figure 5.4 Cyclic voltammetric characterization of single crystal PtBi(001) surface in 0.1M sulfuric acid solution at a scan rate of 10mV/s. (a) Comparison of CV profiles of normal polycrystalline PtBi and single crystal PtBi(001) electrodes; (b) CV profiles of single crystal PtBi(001) electrode cycling up to different E_{ulp} values.

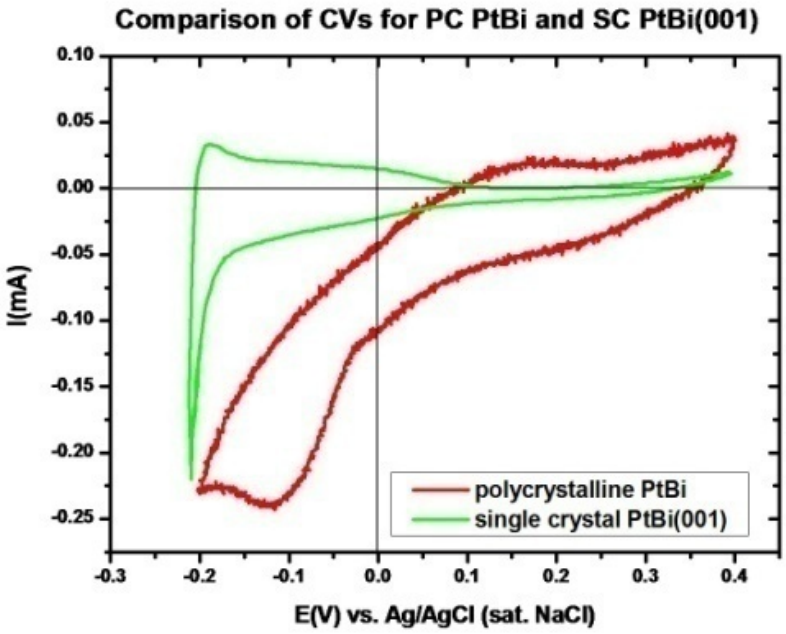
Comparison of CVs for PC PtBi and SC PtBi(001)
I(mA)
E(V) vs. Ag/AgCl (sat. NaCl)
polycrystalline PtBi
single crystal PtBi(001)

(a)

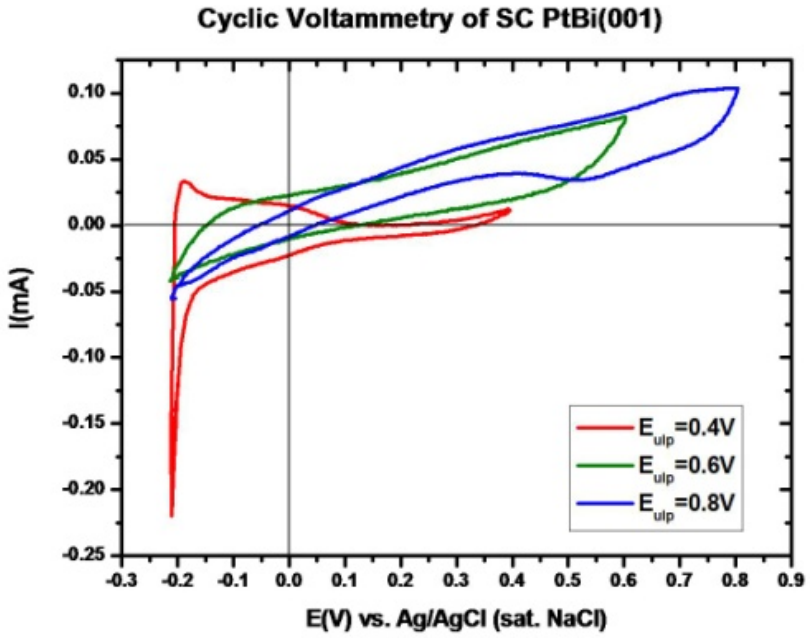
Cyclic Voltammetry of SC PtBi(001)
I(mA)
E(V) vs. Ag/AgCl (sat. NaCl)
E_ulp=0.4V
E_ulp=0.6V
E_ulp=0.8V

(b)

the CV profile of the single crystal PtBi(001) electrode had well-defined hydrogen adsorption/desorption waves around -0.20V and no evidence for oxidation/reduction process for surface bismuth species which were clearly present as a cathodic wave around -0.10V and an anodic wave around 0.15V in the CV profile of a polycrystalline PtBi electrode. There are two observations that suggest that PtBi(001) surface was Pt rather than Bi terminated: 1) the CV profile of PtBi(001) in the low potential region is very similar to that of a Pt(111) electrode. This is not surprising since both PtBi(001) and Pt(111) have the same 6-fold symmetry. The only difference is Pt-Pt distance for these two single crystal electrodes, 4.324Å for PtBi(001) and 2.780Å for Pt(111), respectively. For the PtBi(001) electrode, there were no waves around +0.40V associated with adsorption/desorption process of sulfate/bisulfate ions and which are characteristic of a Pt(111) surface. This phenomenon was rationalized by the larger Pt-Pt distance in PtBi(001) so that sulfate/bisulfate ions could not adsorb on the surface via a bridge mode; 2) as mentioned previously, there is no sign for oxidation/reduction of surface bismuth species in the CV profile of the PtBi(001) electrode. The results for the Pt-terminated PtBi(001) surface are consistent with general thermodynamic data and other surface characterization methods. This well-defined Pt-terminated PtBi(001) surface could be disrupted by cycling the potential to relatively positive values. In figure 5.4 (b), the characteristic waves corresponding to hydrogen evolution were absent in the CV profile after the electrode had been cycled to the E_{ulp} values of +0.60V and +0.80V. This irreversible process resulted in the oxidation and subsequent leaching of Bi atoms from the PtBi(001) surface. These aspects will be discussed in great detail below.

5.3.3 Formation of hexagonally patterned platinum nanosize domains on PtM(001) surfaces

For polycrystalline PtBi and PtPb electrodes, random polycrystalline platinum nanoparticle aggregates will be formed on the surface during electrochemical pretreatment to high potentials due to leaching of the less noble element. The changes in surface composition and structure of PtM single crystal electrodes as a function of cycling E_{ulp} values were investigated via *in-situ* synchrotron based X-ray grazing incidence scattering combined with electrochemical characterization. Where the discussions will center on the PtBi(001) surface, PtPb(001) electrode behaved in a similar fashion. Figure 5.5 (a) presents GID diffraction data obtained after different electrochemical pretreatments which consisted of a series potential cycles at 10mV/s from -0.20V to different E_{ulp} in 0.1M sulfuric acid supporting electrolytic solution. The E_{ulp} values included the open circuit potential (OCP), +0.40V, +0.60V and +0.80V respectively. For each E_{ulp} value, the PtBi(001) electrode was subjected to 10 cycles between -0.20V and E_{ulp}. After each potential cycling process, the electrode surface was investigated via X-ray GID technique. In order to determine the specific surface texture resulting from the electrochemical pretreatments, all GID experiments were conducted at an offset angle aligning to the diffraction peak of the single crystal PtBi(001) surface. Figure 5.5 (a) presents GID patterns obtained by scanning 2θ values along PtBi(110) direction. For a freshly polished electrode at OCP, only the PtBi(110) diffraction peak was presented over the angular range investigated, consistent with the high quality single crystal PtBi(001) surface, since GID in-plane surface diffraction could only detect the crystal lattice planes which are perpendicular to the electrode surface. Along with the diminution of the intensity of the PtBi(110) diffraction peak, the intensities of Pt(111) and Pt(002) diffraction peaks increased as

Figure 5.5 GID partial survey scans of the PtBi(001) surface. (a) GID patterns of the PtBi(001) surface along the PtBi(110) direction as a function of E_{ulp} values (new polished electrode at OCP, +0.40V, +0.60V, and +0.80V respectively); (b) GID patterns of the PtBi(001) surface along the (110) direction and with a 22 deg offset.

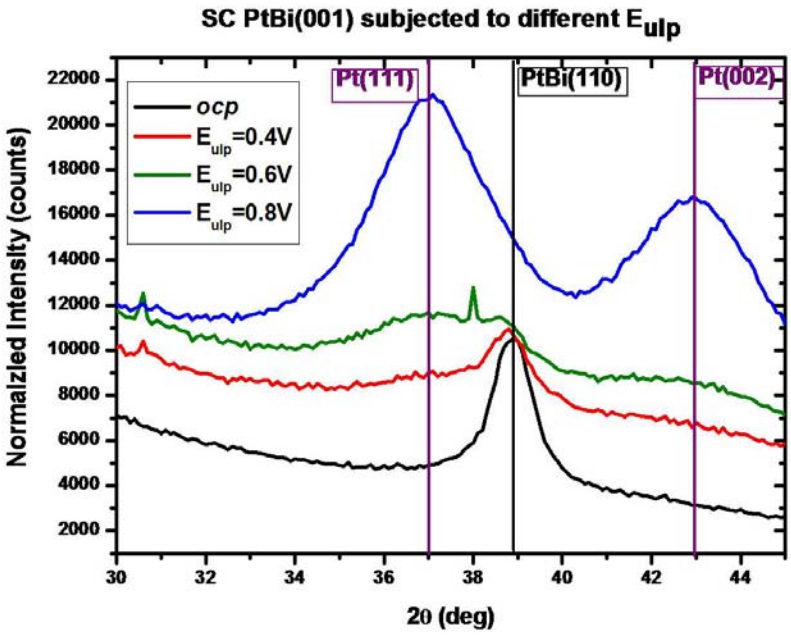
SC PtBi(001) subjected to different E_{ulp}
Pt(111)
PtBi(110)
Pt(002)
ocp
E_{ulp}=0.4V
E_{ulp}=0.6V
E_{ulp}=0.8V
Normalzled Intensity (counts)
2θ (deg)

(a)

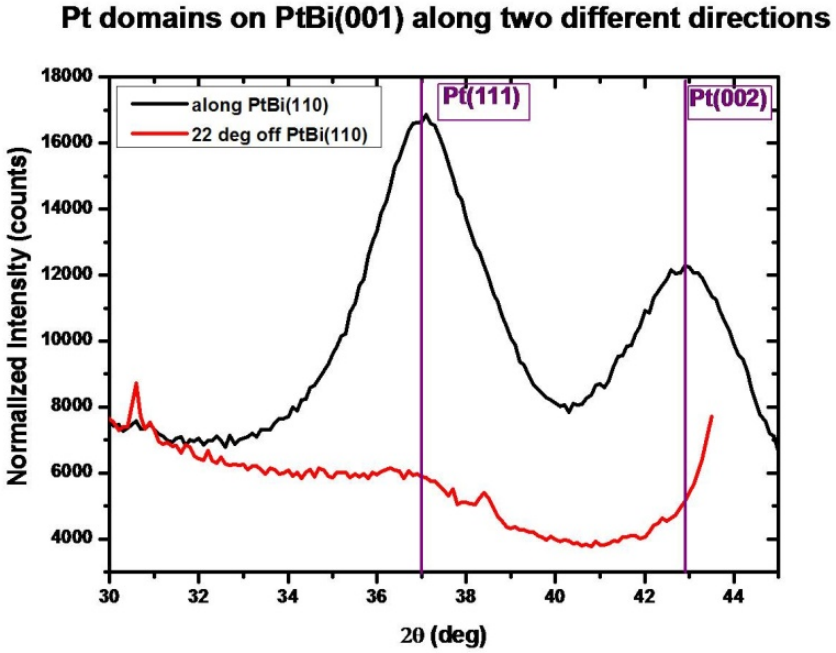
Pt domains on PtBi(001) along two different directions
along PtBi(110)
22 deg off PtBi(110)
Pt(111)
Pt(002)
Normallzed Intensity (counts)
2θ (deg)

(b)

function of applied E_{ulp} values. Since the typical sampling depth of the GID technique for our sample surface roughness is ~100Å, all variations in diffraction patterns and intensities are due to changes in the surface composition and structure. The increase in intensity of the Pt reflecting and the diminution of the PtBi(110) intensity suggest the leaching of Bi from the top layers of the PtBi surface. During the Bi leaching process which was controlled by the E_{ulp} values, the uncoordinated Pt atoms on the surface sintered together to form crystalline domains and islands which gave rise to the diffraction signals of Pt(111) and Pt(002). The Pt domains formed on the PtBi(001) surface are polycrystalline since two diffraction peaks, with different crystal lattice symmetries (6-fold hexagonal and 4-fold square respectively), were evident in the diffraction data after electrochemical pretreatment. Figure 5.5 (b) shows that the diffraction signals from Pt(111) and Pt(002) almost disappeared when the GID experiment was conducted along a direction that was offset 22 deg from PtBi(110) direction. Unlike the polycrystalline Pt domains with ~5 nm diameter formed on polycrystalline PtBi electrode after similar electrochemical pretreatment, crystalline Pt islands with a specific pattern and preferred direction were formed on the single crystal PtBi(001) surface. A series of GID azimuthal scans were conducted to obtain more detailed information about the symmetry and texture of these top layer Pt domains. A typical azimuthal scan was carried out by rotating the sample electrode while the detector was fixed at a specified 2θ value corresponding to given diffraction peak. GID azimuthal scans provide detailed information of either crystal lattice symmetry of targeted lattice planes, if the sample is a single crystal, or information on symmetry and texture of preferred polycrystalline domains if the sample is not a single crystal. Figure 5.6 (a) presents that both GID azimuthal scans of Pt(111) and Pt(002) presented 6-fold hexagonal symmetry. This suggests that polycrystalline Pt domains, with a hexagonal texture, were formed on the PtBi(001) surface which also has

Figure 5.6 GID azimuthal scans used to obtain the detailed information of Pt domains formed on the PtBi(001) single crystal surface.

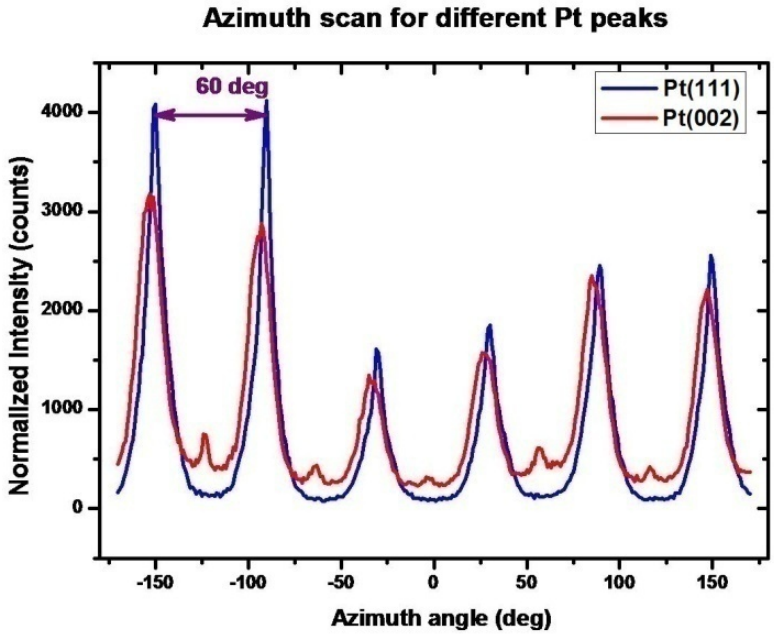
Azimuth scan for different Pt peaks
60 deg
Pt(111)
Pt(002)
Normallzed Intensity (counts)
4000
3000
2000
1000
0
-150
-100
-50
0
50
100
150
Azimuth angle (deg)

(a)

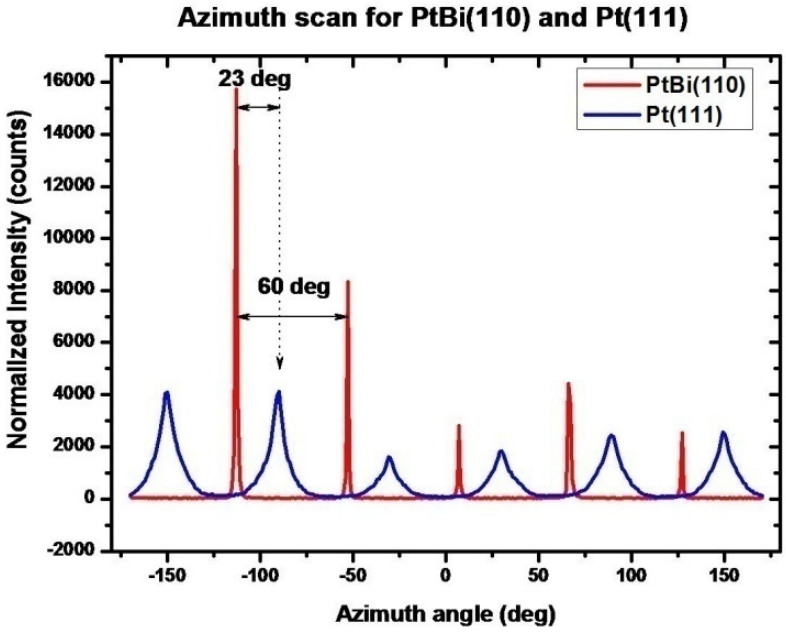
Azimuth scan for PtBi(110) and Pt(111)
23 deg
60 deg
PtBi(110)
Pt(111)
Normallzed Intensity (counts)
16000
14000
12000
10000
8000
6000
4000
2000
0
-2000
-150
-100
-50
0
50
100
150
Azimuth angle (deg)

(b)

hexagonal symmetry. It is interesting that the external Pt domains did not sit directly on the substrate PtBi(001) surface. GID azimuthal scans of PtBi(110) and Pt(111) in Figure 5.6 (b) suggest that the hexagonal texture structure of the external Pt domains had a 23 deg offset angle to the PtBi(001) electrode. The full width at half maxim (FWHM) of the Pt(111) diffraction peak was ca. 5 deg when a partial survey scan was carried out along a direction that was 23 deg offset to the PtBi(001) substrate. Using the Scherrer equation we estimate the crystalline domain size of these Pt islands to be ~15 nm. Figure 5.7 presents in schematic fashion the formation process of external Pt nanosize domains on a single crystal PtBi(001) surface. After the single crystal PtBi(001) electrode was subjected to potentials where Bi leached out, the three adjacent coplanar Pt atoms which bond directly to the Bi atoms would become unstable due to unsaturated coordination. These Pt atoms would sinter together to form a Pt domain which is 30 deg offset from the original direction. The experimentally measured value of 23 deg could be due to the miscut angle of the single crystal sample electrode. However, the qualitative picture presented is consistent with all of our experimental observations.

5.3.4 Formation of highly oriented Pt domains on PtM(100) surfaces

GID azimuthal scans were carried out to obtain detailed information regarding the formation process of Pt domains on the single crystal PtM(100) surfaces. Here we discuss the PtBi(100) case in detail noting that similar phenomena were also observed for the PtPb(100) surface. Figure 5.8 (a) presents GID azimuthal scans for the PtBi(100) surface along the long and short d-spacings. As can be ascertained, there were almost exactly peaks 180 deg apart for different d-spacing directions. In addition, there is almost 90 deg separation between azimuthal scans along the long and short

Figure 5.7 Schematic of formation of external Pt nanosized domains on a single crystal PtBi(001) surface. Pink shaded plane is the PtBi(001) surface. White spheres represent Pt atoms while spheres in red represent Bi atoms.

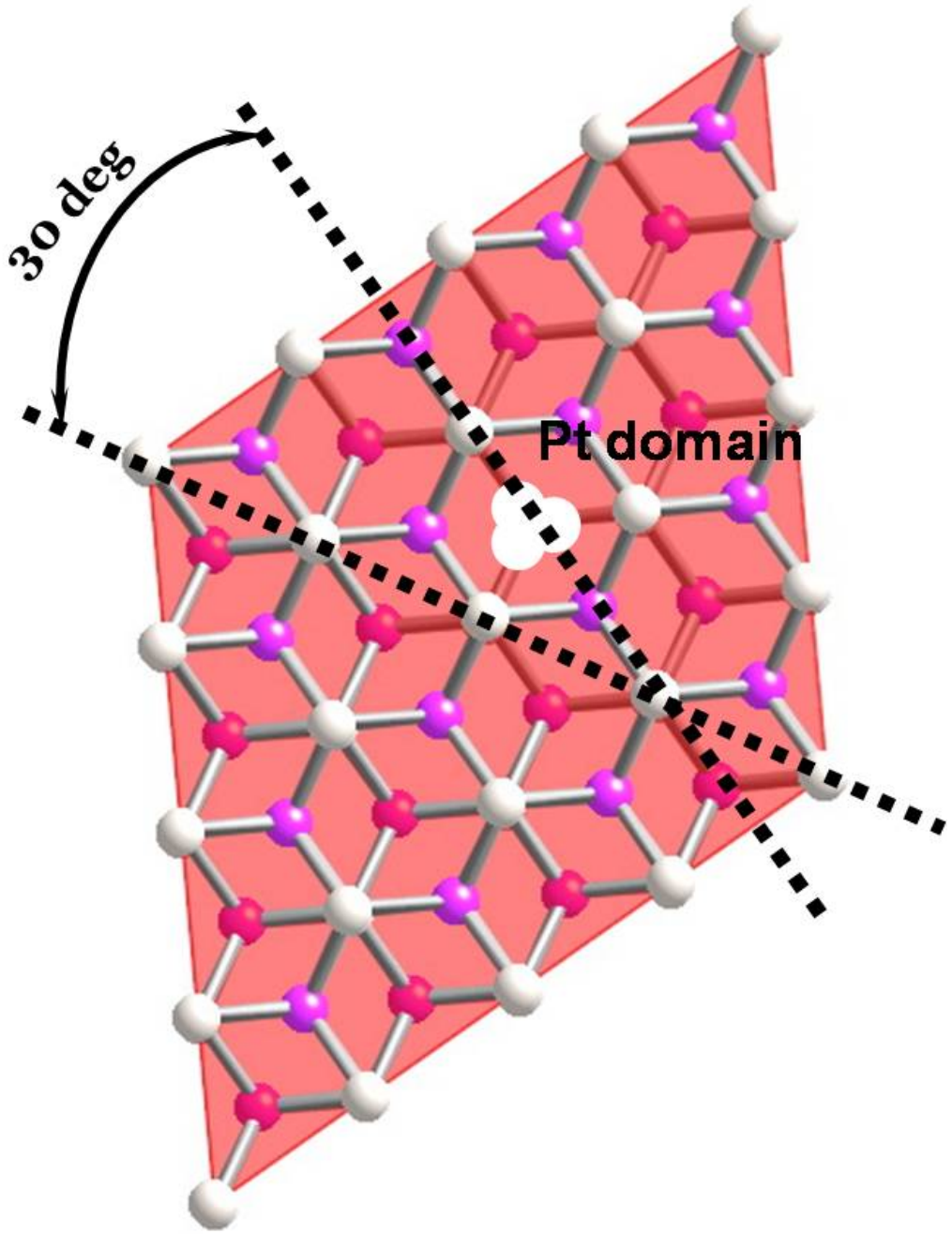
30 deg
Pt domain

Figure 5.8 GID azimuthal scans of single crystal PtBi(100) surfaces. (a) Azimuthal scans along long and short d-spacings for the PtBi(100) surface. (b) Azimuthal scans for Pt domains on a freshly polished single crystal PtBi(100) surface.

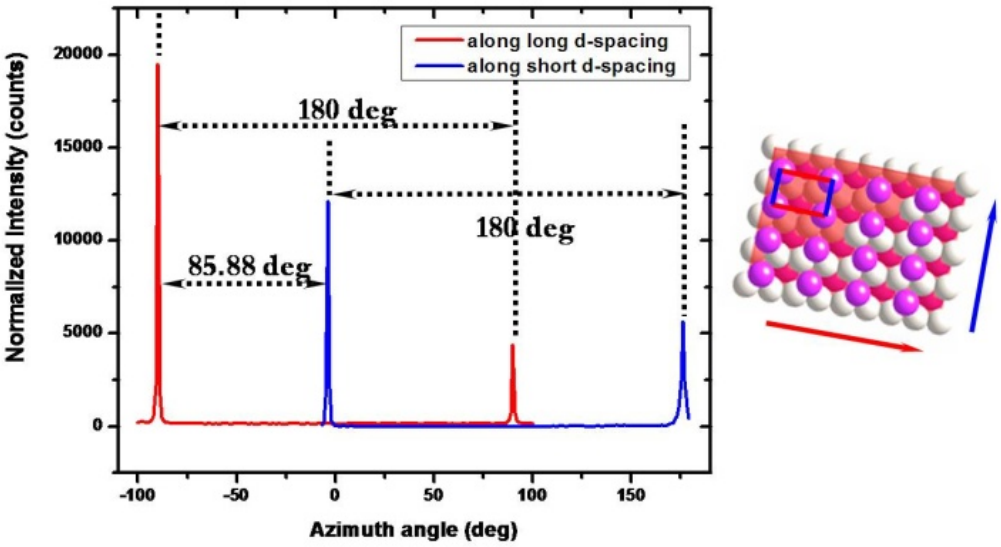
along long d-spacing
along short d-spacing
180 deg
180 deg
85.88 deg
Normalized Intensity (counts)
20000
15000
10000
5000
0
-100
-50
0
50
100
150
Azimuth angle (deg)

(a)

Figure 5.8 (Continued)

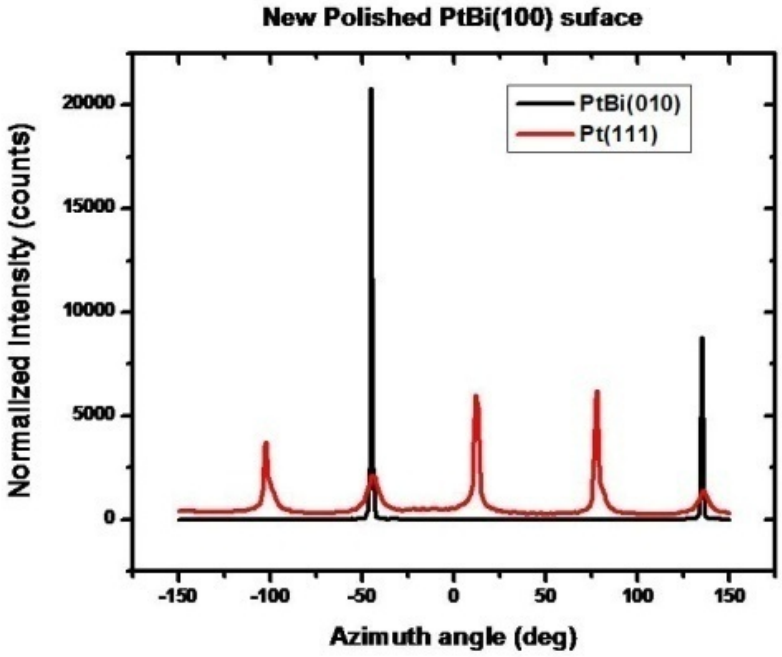

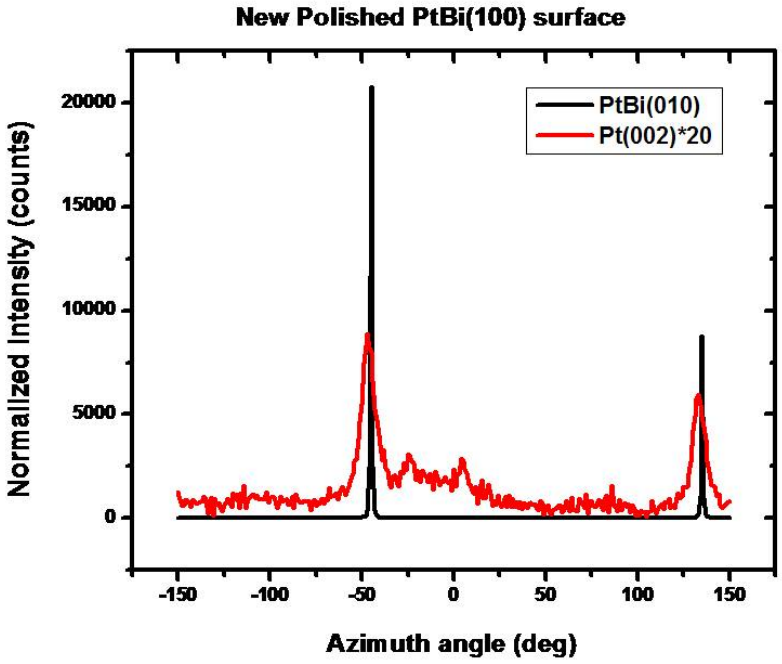

(b)

d-spacing directions. These results point to a high quality PtBi(100) surface with 2-fold rectangular symmetry; consistent with BLR results presented above. For a freshly polished single crystal PtBi(100) surface, there were Pt domains already present on the surface. As shown in Figure 5.8 (b), both diffraction signals corresponding to Pt(111) and Pt(002) reflections were detected. The presence of these peaks suggest that the initial Pt domains, on a freshly polished PtBi(100) electrode, were polycrystalline. If these initial domains were polycrystalline, with specific surface texture, the symmetries for Pt(111) and Pt(002) should be same. In azimuthal scans data, the Pt(111) diffraction peaks presented 6-fold hexagonal symmetry and Pt(002) diffraction peak presented 2-fold rectangular symmetry and neither of them had an offset angle relative to the substrate PtBi(100) surface. Both of the symmetries from azimuthal scans were also consistent with the crystal lattice symmetries for Pt(111) and (002) diffraction peaks, respectively. From the foregoing, it appears that the initial Pt domains have properties of single crystals. It should be noted that the intensity of the Pt(002) diffraction peak was very weak and about 5% (1/20) of that due to Pt(111). Based on this analysis, the initial Pt domains on a freshly polished PtBi(100) electrode are in a highly oriented polycrystalline form which can be described as a partial single crystal form in which the exposure surface is perpendicular to Pt(111) lattice plane. The intensities of the Pt(111) and Pt(002) diffraction peaks were also dependent on the E_{ulp} values but the symmetries of these two diffraction peaks in azimuthal scans remained unchanged during electrochemical pretreatments.

5.3.5 Anisotropic electrocatalytic activities of PtM (100) and (001) surfaces

Anisotropic (structure dependent) electrocatalytic activities of noble metal single

crystal facets (such as Pt) have been extensively studied from experimental and computational points of view.[31-34] It is also interesting and important to study the anisotropic activities for different single crystal facets of intermetallic phases. Both polycrystalline PtBi and PtPb electrodes show much better activity towards formic acid oxidation than Pt. As shown in Figure 5.9, PtBi(100) and (001) surfaces had similar onset potentials for the oxidation of formic acid with the latter having a slightly higher activity. On the other hand, the PtPb(100) surface had much higher activity, relative to PtPb(001), towards the oxidation of formic acid with a negative shift in the onset potential of over 100mV and over a 50% improvement in current density. The surface cleavage energies (labeled as E_{sc}), a computation parameter representing surface activity, of PtBi and PtPb (100) and (001) facets had similar trends with the E_{sc} of PtM(001) facet being much higher than that of PtM(100) facet.[35] The experimental activities derived from CV profiles were not consistent with these computational results. The discrepancy could be due to the fact that the computation study is under vacuum conditions and does not take into account specific experimental parameters, such as solution environment, surface oxide formation and adsorption of fuel molecules. In order to explore the relationship between electrocatalytic activity and E_{ulp} values for different single crystal facets, peak values of current density for anodic (i_{pa}) and cathodic (i_{pc}) waves were plotted versus cycling number for electrochemical treatment. In Figure 5.10 (a), global maxima of i_{pa} and i_{pc} for a PtBi(001) surface were at an E_{ulp} value of +0.60V, but for PtPb(100) and PtPb(001) surfaces, they were at an E_{ulp} value of +1.20V. Based on previous data,[36] the highest activity of the PtBi electrode could be due to the formation of Bi_2O_3 species on the electrode surface which could facilitate the oxidation process of formic acid by providing surface oxygen. The activity decreased as a function of cycle number and E_{ulp}. This was ascribed to oxidized surface species that were not stable and dissolved

Figure 5.9 Cyclic voltammetric profiles of the electrooxidation of formic acid on PtBi single crystal surfaces (left) and PtPb single crystal surfaces in 0.2M formic acid in 0.1M sulfuric acid solution at 25mV/s scan rate.

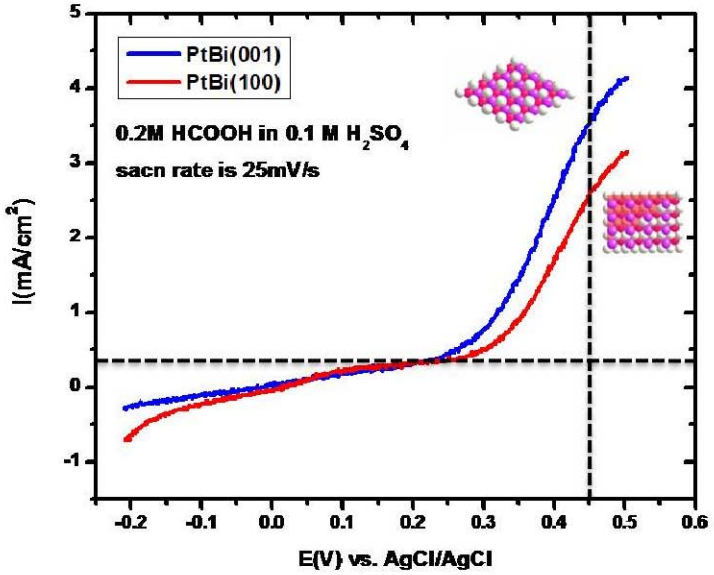
PtBi(001)
PtBi(100)
0.2M HCOOH in 0.1 M H2SO4
sacn rate is 25mV/s
I(mA/cm2)
E(V) vs. AgCl/AgCl

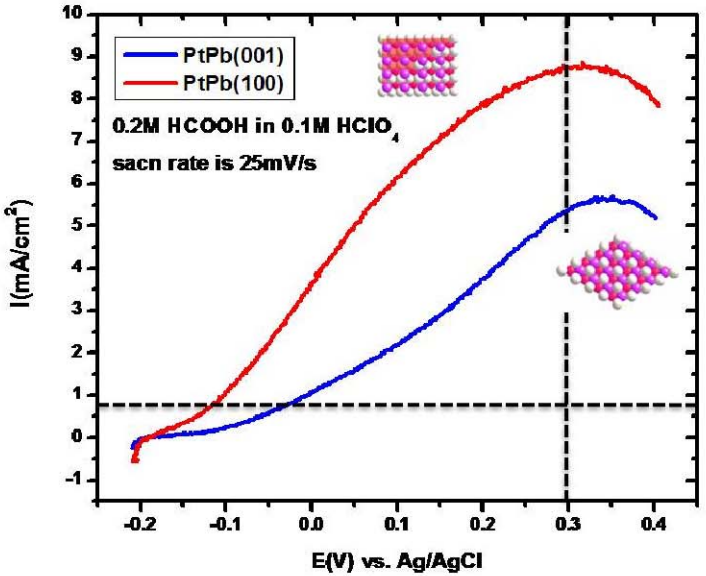
PtPb(001)
PtPb(100)
0.2M HCOOH in 0.1M HClO4
sacn rate is 25mV/s
I(mA/cm2)
E(V) vs. Ag/AgCl

Figure 5.10 Electrocatalytic activities of PtBi (001) and PtPb (001) and (100) electrodes towards electro-oxidation of formic acid as a function of cycling numbers during electrochemical characterization.

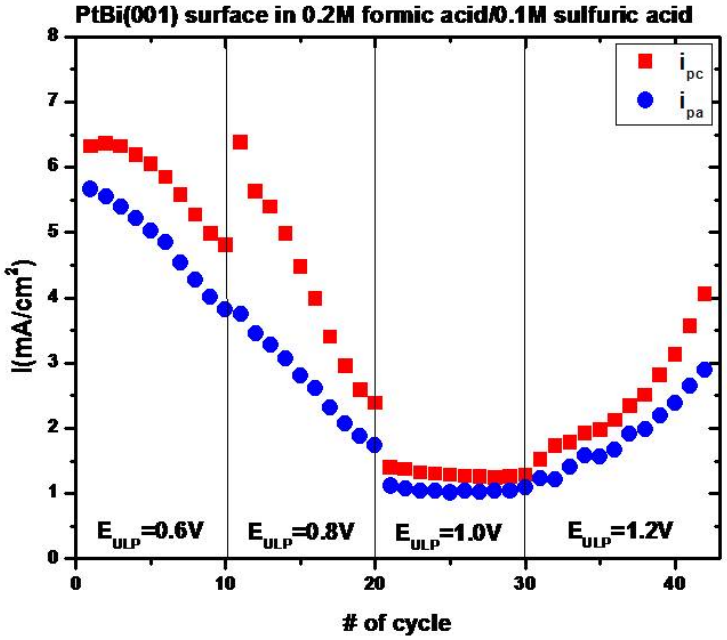
PtBi(001) surface in 0.2M formic acid/0.1M sulfuric acid
i_pc
i_pa
I(mA/cm²)
E_ULP=0.6V
E_ULP=0.8V
E_ULP=1.0V
E_ULP=1.2V
# of cycle

(a)

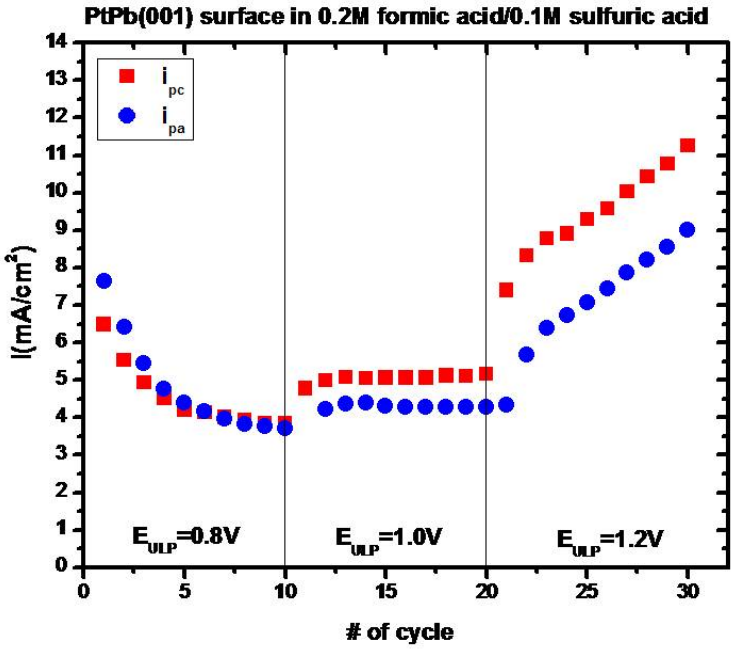
PtPb(001) surface in 0.2M formic acid/0.1M sulfuric acid
i_pc
i_pa
I(mA/cm²)
E_ULP=0.8V
E_ULP=1.0V
E_ULP=1.2V
# of cycle

(b)

Figure 5.10 (Continued)

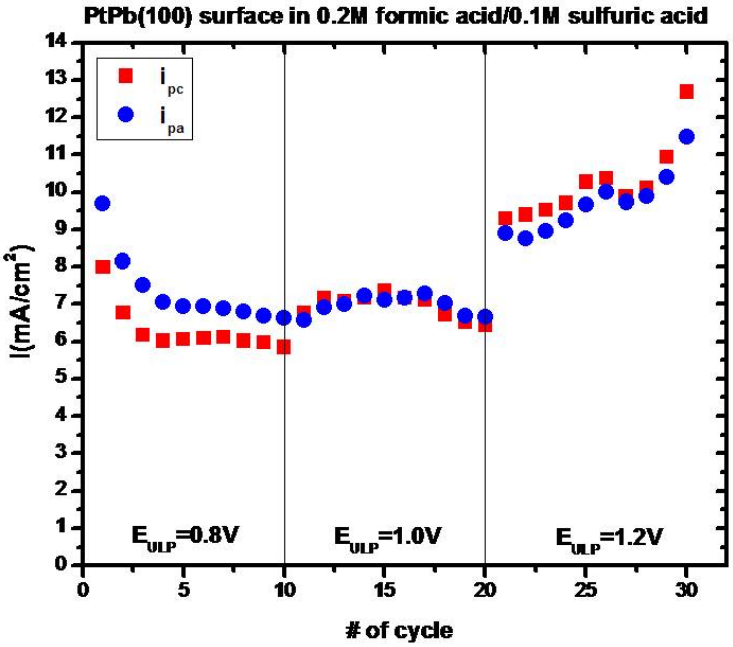

(c)

when E_{ulp} was up to +0.80V. The highest activity for PtPb electrodes at an E_{ulp} value of +1.20V could be due to formation of a Pt-rich surface and increase of boundary lines of Pt and PtPb grains. When the E_{ulp} value was up to +1.20V, lead atoms leached out (dissolving into solution) and Pt-rich terminated surface was formed for both PtPb(100) and (001) facets. At the same time, the boundary lines between Pt and PtPb grains were greatly enhanced. This could be rationalized in a manner analogous to previous studies for PtRu alloys where activity was ascribed to the interface between Pt and Ru domains. For both of PtBi and PtPb single crystal facets, the electroactivity at an E_{ulp} value of +1.00V was the global minimum and remained quite stable, suggesting that the surface composition remained constant.

5.4 Conclusion and summary

High quality single crystal PtM (M=Bi, Pb) (100) and (001) surfaces were prepared via orientating and cutting using single crystal ordered intermetallic bulk phases as starting materials. The BLR method was utilized to obtain the precise orientation and the miscut angle was less than 0.3 deg which was limited by instrumental resolution. This procedure represents a general method for preparing high quality single crystal intermeatllic surfaces from bulk materials synthesized by solid state chemistry. The surface structure and composition of different single crystal PtM facets were thoroughly characterized by GID partial survey scans and azimuthal scans which were utilized to determine the surface texture and crystal lattice symmetry. Freshly polished PtM(001) facets, with 6-fold hexagonal symmetry, were Pt terminated. Similar to polycrystalline PtM intermetallics, Pt rich surfaces were formed due to leaching of the less noble metal following electrochemical pretreatment to high positive potential values (high E_{ulp}). Furthermore, well-defined Pt domains with 6-fold hexagonal

symmetry, which was 23 deg offset to the PtM(001) substrate, were formed when cycling the PtM(001) electrode to an E_{ulp} value of +0.80V. On the other hand, partially single crystal, or described as highly orientated polycrystalline Pt structures, were formed on freshly polished PtM(100) electrodes. Anisotropic electrocatalytic activities towards formic acid oxidation were observed on different single crystal intermetallic facets. For PtBi single crystal electrodes, the (100) and (001) surfaces had little difference in either current density or onset potentials. On the other hand, for PtPb single crystal electrodes, the (100) surface had a significant (over 100mV) more negative onset potential and a 50% enhancement in current density when compared to the (001) surface.

The extensive investigations on single crystal intermetallic phases are providing an in-depth understanding of this new category of materials which are promising candidates as anode materials for SOMs oxidation in fuel cell applications. Addition studies, such as the influence of fuel molecules on the intermetallic phases under active electrochemical control and characterization of intermeatllic nanoparticles, are in progress and will be reported elsewhere.

REFERENCES

1. J. Zhang, K. Sasaki, E. Sutter and R.R. Adzic, *Science* 315, 220, **2007**
2. V.R. Stamenkovic, B. Fowler, B.S. Mun, G. Wang, P.N. Ross, C.A. Lucas and N.M. Markovic *Science* 315, 493, **2007**
3. R. Narayanan and M.A. El-Sayed, *Nano Letters* 4, 1343, **2004**
4. N. Tian, Z. Zhou, S. Sun, Y. Ding and Z. Wang *Science* 316, 732, **2007**
5. H.D. Abruña *et al.*, *Bulletin of Chemical Society of Japan* 80, 1843, **2007**
6. N.S. Lewis and D.G. Nocera, *Proceeding of the National Academy of Sciences* 103, 15729, **2006**
7. N.M. Markovic and P.N. Ross, *Surface Science Reports* 45, 117, **2002**
8. C. Wang, H. Daimon, T. Onodera, T. Koda and S. Sun, *Angew. Chem. Int. Ed.* 47, 3588, **2008**
9. C. Wang, H. Daimon, Y. Lee, J. Kim and S. Sun, *J. Am. Chem. Soc.* 129, 6974, **2007**
10. Z. Zhou, N. Tian, Z. Huang, D. Chen and S. Sun, *Faraday Discuss.* 140, 81, **2009**
11. L. Xiao, L. Zhuang, Y. Liu, J. Lu and H.D. Abruña, *J. Am. Chem. Soc.* 131, 602, **2009**
12. M. Watanabe and S. Motoo, *J. of Electroanal. Chem.* 60, 267, **1975**
13. M. Watanabe and S. Motoo, *J. of Electroanal. Chem.* 60, 275, **1975**
14. H. Lee, S.E. Habas, G.A. Somorjai and P. Yang, *J. Am. Chem. Soc.* 130, 5406, **2008**
15. M.J. Lloca, J.M. Feliu, A. Aldaz and J. Clavilier, *J. of Electroanal. Chem.* 376, 151, **1994**
16. S.P.E. Smith and H.D. Abruña, *J. Phys. Chem.* 103, 6764, **1999**
17. S.P.E. Smith and H.D. Abruña, *J. of Electroanal. Chem.* 467, 43, **1999**

18. S.P.E. Smith, K.F. Ben-Dor and H.D. Abruña, *Langmuir* 15, 7325, **1999**

19. S.P.E. Smith, K.F. Ben-Dor and H.D. Abruña, *Langmuir* 16, 787, **2000**

20. B.S. Mun, M. Arenz, K.J.J. Mayrhofer, C.A. Lucas, G. Wang, P.N. Ross, V.R. Stamenkovic and N.M. Markovic, *Nature Materials* 6, 241, **2007**

21. H.A. Gasteiger, N.M. Markovic and P.N. Ross, *J. Phys. Chem.* 99, 8945, **1995**

22. E. Casado-Rivera, Z. Gál, A.C.D. Angelo, C. Lind, F.J. DiSalvo and H.D. Abruña, *Chem. Phys. Chem.* 4, 193, **2003**

23. E. Casado-Rivera, D.J. Volpe, L. Alden, C. Lind, C. Downie, T. Vázquez-Alvarez, A.C.D. Angelo, F.J. DiSalvo and H.D. Abruña, *J. Am. Chem. Soc.* 126, 4043, **2004**

24. C. Roychowdhury, F. Matsumoto, P. Mutolo, H.D. Abruña and F.J. DiSalvo, *Chem. Mater.* 17, 5871, **2005**

25. C. Roychowdhury, F. Matsumoto, V.B. Zeldovich, S.C. Warren, P. Mutolo, M.J. Ballesteros, U. Wiesner, H.D. Abruña and F.J. DiSalvo, *Chem. Mater.* 18, 3365, **2006**

26. L.R. Alden, C. Roychowdhury, F. Matsumoto, D.K. Han, V.B. Zeldovich, H.D. Abruña and F.J. DiSalvo, *Langmuir* 22, 10465, **2006**

27. L.R. Alden, D.K. Han, V.B. Zeldovich, F. Matsumoto, H.D. Abruña and F.J. DiSalvo, *Chem. Mater.* 18, 5591, **2006**

28. Y. Liu, D.R. Blasini, F.J. DiSalvo and H.D. Abruña, *submitted*

29. D.E. Nowak, D.R. Blasini, A.M. Vodnick, B. Blank, M.W. Tate, A. Deyhim, D.-M. Smilgies, H.D. Abruña, S.M. Gruner and S.P. Baker, *Rev. Sci. Instrum.* 77, 113301, **2006**

30. J. Sanabria-Chinchilla, H. Abe, F.J. DiSalvo and H.D. Abruña, *Surface Science* 602, 1830, **2008**

31. A. Berna, J.M. Delgado, J.M. Orts, A. Rodes and J.M. Feliu, Langmuir 22, 7192, **2006**

32. M. Baldauf and D.M. Kolb, *J. Phys. Chem.* 100, 11375, **1996**

33. V.R. Stamenkovic, B.S. Mun, K.J.J. Mayrhofer, P.N. Ross, N.M. Markovic, J. Rossmensl, J. Greeley and J.K. Nørskov, *Angew. Chem. Int. Ed.* 45, 2897, **2006**

34. J.K. Nørskov, T. Bligaard, J. Rossmeisl and C.H. Christensen, *Nature Chemistry* 1, 37, **2009**

35. L.-L. Wang and D.D. Johnson, *J. Phys. Chem. C* 112, 8266, **2008**

36. D.R. Blasini, D. Rochefort, E. Fachini, L.R. Alden, F.J. DiSalvo, C.R. Cabrera and H.D. Abruña, *Surface Science* 600, 2670, **2006**

CHAPTER SIX

X-RAY FLUORESCENCE INVESTIGATION OF ORDERED INTERMETALLIC PHASES AS ELECTROCATALYSTS TOWARDS THE OXIDATION OF SMALL ORGANIC MOLECULES*

6.1 Introduction

In the general area of heterogeneous catalysts,[1-2] it is of great importance to characterize nanomaterial catalysts under operating conditions as such studies can provide an in-depth atomic-level understanding of the reaction mechtaanism or interfacial processes. Recent advances in functional catalytic materials and spectroscopic methods that can operate under ambient pressures now enable us to investigate a catalyst in its active state. Particularly for electrode materials for fuel cell applications, various surface/interface/nanomaterial characterization techniques, in combination with electrochemical characterization, allow monitoring of the transformation of electrocatalysts from the "as-prepared" to the "active-state", which may involve pronounced changes in the composition and structure of the catalysts.[3-6] X-ray Diffraction (XRD) has been widely utilized to characterize the crystalline composition and structure of condensed matter at surfaces/interfaces (also known as grazing incidence diffraction, GID) where electrochemical reactions occur. However, it is very difficult for XRD to yield the appropriate information for short-range structures or amorphous phases of catalysts. For nanomaterial catalysts, one argument in favor of the utilization of XRD has been that the number of surface atoms is significant with respect to the number of atoms in the bulk, so that XRD data of such

*Reproduced with permission from the manuscript in preparation, ready to be submitted.

nanomaterial samples would be directly relevant to catalysis. While this argument might be valid for other bulk-sensitive techniques, it does not work for XRD, because the structural uniformity of the bulk of a material does not pertain to the surfaces of nanoparticles. For example, surface reconstructions have major consequences on the average arrangement of surface atoms.[7-8] X-ray photoelectron spectroscopy (XPS) is a powerful method with great surface sensitivity, and can offer qualitative or semi-quantitative composition and oxidation state information, but its requirement of strict ultra high vacuum (UHV) does not permit active electrochemical control.[9] X-ray absorption spectroscopy (XAS), including X-ray absorption near edge structure (XANES) and extended X-ray absorption fine structure (EXAFS), has attracted a great deal of research attention, especially for analysis and characterization of catalysts.[6, 10-12] XAS provides element-specific information about the local chemistry and physical structure of the element under investigation. XANES offers information about the chemical state of the element, including oxidation state and local geometry, and EXAFS offers quantitative information about interatomic distances, coordination numbers, and the types of neighboring atoms. XAS is a valuable method to investigate short-range order and is especially suitable for nanomaterials. A disadvantage of XAS (or EXAFS) is that sophisticated and complicated data analysis and simulation is required.

X-ray fluorescence (XRF) is a widely used analytical technique employed in fields,[13-15] such as environmental studies,[16] medicine,[17] polymers,[18] biology,[19] botany,[20] archeology,[21] pharmacology[22] and planetary studies.[23] Attention tests of the XRF technique include the fact that it is nondestructive, has high elemental selectivity, simplicity of quantification and low detection limits. There have been such studies on the application of XRF in combination with electrochemistry for the characterization of surface species, nanoparticles and nanowires or indirectly in catalyst research. For

example: De Wael and co-workers[24] reported on a study in which they used scanning synchrotron radiation X-ray fluorescence (SR-XRF), on the microscopic scale, to characterize the immobilization of cobalt(Ⅱ) tetrasulfonated phthalocyanie tetrasodium salt (Co(Ⅱ)TSPc) on gold electrodes via different electrochemical surface modification techniques. Electrochemical and SR-XRF analysis were performed in order to compare the amount of adsorbed CoTSPc onto the gold electrode and to determine the level of uniformity of the deposited layer. Van Meel and co-workers[25] developed a fast and direct determination procedure for precious metals (such as Pt, Pd, Rh) in spent automotive catalysts by using the novel high-energy polarized-beam XRF technique. Wang and co-workers[26] developed a barcoding procedure for alloy nanowires based on nondestructive X-ray fluorescence readout. Ternary Co-Ni-Cu alloy nanowires were generated via one-step template-guided electrodeposition with distinct XRF barcode patterns. The resulting fluorescence barcodes correlated well with the composition of the metal mixture plating solution, indicating a reproducible plating process. To our knowledge, there is no report on methodology development or application of nondestructive XRF directly to characterize nanomaterials electrocatalyts for fuel cell applications especially under active electrochemical control.

In the past decades, interest in the direct conversion of chemical energy to electricity via fuel cells has received increasing attention. The use of fuel cells can circumvent Carnot cycle limitations and can, in principle, supply energy with conversion efficiencies in excess of 80%, depending on the fuel used.[27] Due to increasing demands of power sources for small portable electronic devices, the development and utilization of direct alcohol fuel cells (DAFCs) has continuously attracted a great deal of research interest.[28-30] Some of the major obstacles, however, are the performance and their cost of anode and cathode electrode catalysts.[31] It is of

great importance to discover advanced functional materials as anode catalysts for oxidations of small organic molecules (SOMs). Pt is an excellent catalyst for dehydrogenation of fuels which is one of the key steps in the complete oxidation reaction pathways of SOMs. However, Pt is easily poisoned by carbon monoxide which is the most common intermediate during SOM oxidation. In order to mitigate the poisoning effects induced by CO and decrease the cost of electrode materials, a secondary metallic element is often introduced into the matrix to form bimetallic electrocatalyts. PtRu alloys are the most successful case and widely used in the fuel cell industry especially for direct methanol fuel cells. Its success has been rationalized by a bifunctional mechanism and/or third body effect.[32-33] Unfortunately, as with all alloys, or more accurately solid solutions, PtRu electrodes have no well-defined surface crystalline structure, with its surface sites occupied by Pt or Ru atoms in a totally random mode. Moreover, the very small enthalpy of formation of PtRu alloys leads to a thermodynamic stability problem: during extended periods of operation, particularly under high temperature or high current density conditions, the alloy electrode surface is depleted of Ru atoms, loses electrocatalytic activity and is prone to poisoning by CO.

Ordered intermetallic phases exhibit inherent properties which overcome many of the shortcomings of alloy materials. Intermetallics are binary or multi-elemental metallic compounds which have well-defined crystalline structures. In principle, the electronic and atomic structures, can be deliberately controlled; both of which are widely acknowledged to be important parameters in electrocatalytic activity. DiSalvo and Abruña[34-35] reported that ordered intermetallic PtBi and PtPb phases were promising candidates towards the oxidation of formic acid and methanol in comparison to commercial Pt and PtRu materials. Not only do they exhibit electrocatalytic activity, but they could also serve as model systems to explore

structure/composition/property/activity relationships. Control of surface termination, composition, and structure of the intermetallic phases provide alteration to fabrication of modified single crystal metal surfaces via electrodepostion or bimetallic single crystal surfaces generated by chemical vapor deposition or sputtering methods.[36] Previous research has demonstrated that polycrystalline PtBi intermetallic electrodes can be reproducibly terminated with Pt nanocrystal domains decorating the surface after cycling the potential or as Bi_2O_3 2D nanocrystalline film decorating the surface after holding the potential at specified value. In the case of PtPb, Pt nanocrystal domains were formed on the surface via both treatments (cycling and holding the potential) but later treatment could induce aggressive corrosion of the top PtPb layers.[37-38] On single crystal electrodes, Pt nano islands with 6-fold hexagonal or 2-fold rectangular symmetries were formed on the PtM (M=Bi or Pb) (001) and (100) surfaces, respectively, instead of formation of random Pt nanocrystal domains/islands as on the polycrystalline intermetallic phases.[36] While the work on single crystal intermetallic surfaces has been important to reveal structure-activity relationships, it is of more praticalimportance to characterize intermetallic nanomaterial samples since they are directly used in industrial applications.

In this paper, XRF was utilized to quantitatively investigate and characterize intermetallic nanoparticles. X-ray diffraction (XRD), though powerful, has some limitations in the characterization of these materials, because of: 1) low diffraction intensities of nanoparticles immobilized on electrode surfaces, such as glassy carbon, even when using a high flux synchrotron beam; 2) strong back scattering from the GC electrode surface at grazing incidence; 3) unability of obtaining information of the surface atoms instead of the bulk. XRF data showed that there were significant changes in the composition of PtBi and PtPb nanoparticles, as a function of applied potential, in absence or presence of fuel molecules in the supporting electrolyte.

PtM/Pt core/shell nanoparticles were formed as a consequence of the less noble elements (Bi or Pb) leaching out from the nanoparticle matrix and dissolving into the solution. Similar to bulk electrodes[38], kinetic stabilization effects, induced by the presence of active fuel molecules, were also observed for the intermetallic nanoparticles. More importantly, a universal simplified nondestructive multifunctional characterization method was developed to investigate bimetallic electrocatalysts, especially under active electrochemical control.

6.2 Materials and Experimental Section

6.2.1 Synthesis of ordered intermetallic PtBi and PtPb nanoparticles

With the exception of Bi and Pb precursors, all materials used were reagent grade. $Bi(MOEEAA)_3$, as Bi precursor, was prepared by reacting stoichiometric amounts of bismuth acetate (99.999%, Alfa Aesar) and (2-[2-{2-methoxyl}ethoxy]ethoxy) acetic acid (MOEEAA) (Aldrich). The final product was purified and collected as a colorless, viscous liquid and stored in an argon-filled glovebox. $Pb(MOEEAA)_2$, as lead precursor, was prepared in the same way, using lead acetate (Aldrich) as the starting material. Anhydrous methanol was degassed with argon for over 2 hr. To synthesize intermetallic PtBi nanoparticles, 0.25 g of $Bi(MOEAA)_3$ was dissolved into the degassed methanol. A stoichiometric amount, relative to bismuth precursor, of the $H_2PtCl_6 \cdot 6H_2O$ (as platinum precursor), was dissolved in 10 mL of degassed anhydrous methanol and added to the bismuth precursor solution. 0.3 g of $NaBH_4$ was added into 15 mL degassed anhydrous methanol. This solution was immediately added to the metal precursor solution. There was instant bubbling, and a black product formed, which precipitated out of the solution within 10 min. The clear solution and the black product were stirred under argon for 12 hr. The solid product was then separated from

the supernatant liquid by decantation and centrifugation; it was subsequently rinsed three times each with distilled water and acetone in order to remove the side products. Afterward, the powders were dried under vacuum at room temperature. PtPb intermetallic nanoparticles were prepared in the same way as described above, with the exception of using lead precursor. More detailed information about synthesis and standard characterizations of these intermetallic nanoparticles can be found elsewhere.[39]

6.2.2 Electrochemistry

To obtain nanoparticles modified electrodes, a suspension of the nanoparticle catalysts (refered to as nanoparticle ink) was firstly prepared as follows: 4 mg of the dried PtBi or PtPb nanoparticle sample were added to 3980 μL of Millipore water (18.2 $M\Omega \cdot cm^{-1}$, Millipore Milli-Q) and 1000 μL of isopropyl alcohol (Aldrich). Additionally, 20μL of a 5% w/w Nafion solution in alcohols (Aldrich) was then added to this mixture. The resulting mixture was sonicated in a bath type ultrasonicator for at least 30 min. Each nanoparticle ink describe above was coated onto a 5 mm diameter GC electrode via simple drop casting method. The GC electrode that served as the supporting substrate electrode was previously polished with 800 and 1200 Grit sandpapers (Buehler) for 15 min respectively. The final polishing procedure was carried out by using 1 μm diamond paste suspended in a suitable extender (Metadi-Buehler) for 15 min. The smooth GC electrode was then rinsed with Millipore water and allowed to dry in air. The modified working electrode was obtained by coating 80 $\mu m \cdot cm^{-2}$ of the intermetallic nanoparticles (20 μL of nanoparticle ink) and then dried under nitrogen atmosphere. All electrochemical characterizations were carried out in the *in-situ* electrochemical cell designed purposely for *in-situ* synchrotron radiation X-ray

techniques and which was sealed by 5μm polypropylene film in order to minimize X-ray absorption and back scattering effects.[37] Cyclic voltammetry was carried out on a BAS CV-27 potentiostat/galvanostat (Bioanalytical Systems) and recorded on a computer through a PCI-DAQ card (National Instruments). All potentials are referenced to a Ag/AgCl (saturated NaCl) electrode without regard for the liquid junction potential. The electrochemical pretreatment was done by cycling the electrodes between -0.20V and E_{ulp} (upper limit potential) values of +0.40V to +1.20V for 10 cycles at 10 mV/s in 0.1M $HClO_4$ (Aldrich, ultrapure reagent). SOMs oxidations at the nanoparticle modified GC electrodes were examined in a mixture of 0.2M formic acid (Mallinckrodt, 88% analytical reagent) or 0.2M methanol (Aldrich) in 0.1M $HClO_4$ at a sweep rate of 10 mV/s for 10 cycles. All solution were prepared with Millipore water and deaerated with high purity nitrogen for at least 15 min before each experiment.

6.2.3 Synchrotron radiation XRF

SR-XRF experiments were performed at the C1 station of the Cornell High Energy Synchrotron Source (CHESS). This beamline is dedicated to X-ray absorption/fluorescence experiments using either "white" or monochromatic radiation with photon energies ranging from 5 to 50 KeV. Figure 6.1 shows the experimental geometry used for our SR-XRF experiments, which also allowed for XANES and/or EXAFS investigations in grazing incidence surface fluorescence mode for solid state samples or conventional transmission mode for nanoparticle samples. The white beam from CESR was monochromatized by a Si(111) single crystal. The incident beam was 1 mm × 1 mm in size after the upper stream Huber slits and monitored by an upper stream ion chamber. The X-ray beam impinged on the electrode surface with incidence

Figure 6.1 Schematic of the experimental geometry of X-ray fluorescence experiments at the C1 station at CHESS.

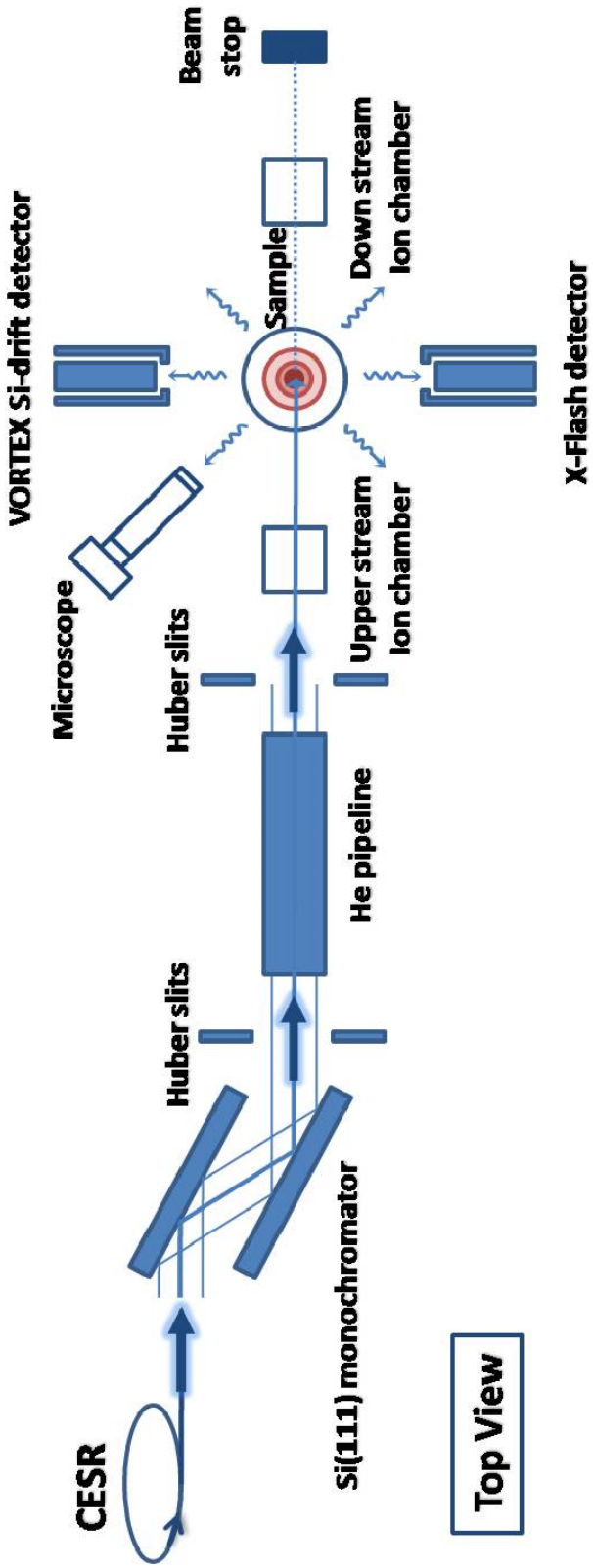
Beam stop
Down stream Ion chamber
Sample
VORTEX Si-drift detector
X-Flash detector
Microscope
Upper stream Ion chamber
Huber slits
He pipeline
Huber slits
Si(111) monochromator
CESR
Top View

angle of 1 deg. This small glancing angle was purposely chosen to maximize the electrode area under the beam and minimize the background scatter from the GC electrode substrate. Two detectors, a VORTEX Si-drift detector and an X-Flash detector, were set up to record the fluorescent photons from the intermetallic nanoparticles. For the PtBi nanopaticle case, a single channel analyzer (SCA) was set up on the X-Flash detector to monitor mainly the Bi Lα fluorescent photons at 10.84 KeV and distinguish them from the Pt Lβ fluorescent photons at 11.07 KeV. Table 6.1 presents the binding energies and emission lines for Pt, Bi and Pb used in the experiments. Due to the small energy difference between the Bi Lα and Pt Lβ emissions, the SCA detector could not completely discriminate between them and only provided a qualitative analysis of the Bi fluorescence. This SCA detector, based on the X-Flash detector, was set up not only for experimental convenience, to directly monitor the progress of the energy scan, but also to obtain EXAFS and XANES information over the Bi L_3 edge. On the other hand, the entire multi channel analyzer (MCA) spectrum was recorded via the VORTEX detector including the dispersive energy range for all fluorescent, scattered and incident photons, to give accurate and specific photon counts for XRF investigations for post-experimental data analysis using XPaXs software.[40] For PtPb nanoparticles, the only difference was the set-up condition of the SCA covering the Pb L_α emission.

For combing X-ray characterization with electrochemistry, electrodes were pretreated by cycling 10 times between -0.20V and E_{ulp} values , and subsequently part of the supporting electrolyte solution was withdrawn so that the polypropylene film was recessed, generating a thin film of electrolyte as described above. The electrolyte film, however, was sufficiently thick to ensure good potential control in all cases. For PtBi nanopaticle modified electrodes, the energy scan was carried out from 13.3 KeV, which is 120 eV lower than the binding energy of Bi L_1, to 14.0 KeV, which is 580 eV

Table 6.1 Binding energies, emission lines of Pt, Bi and Pb elements.*

	Binding Energy (KeV)			Emission Lines (KeV)			
	L_1	**L_2**	**L_3**	**Lα1**	**Lα2**	**Lβ1**	**Lβ2**
Pt	13.88	13.27	11.56	9.44	9.36	11.07	11.25
Bi	16.39	15.71	13.42	10.84	10.73	13.02	12.98
Pb	15.86	15.20	13.04	10.55	10.45	12.61	12.62

* The data was adapted from "*X-ray data booklet"* edited by A. Thompson *et al.* Lawrence Berkeley National Laboratory, University of California, Berkeley CA 94720

above the binding energy of Bi L_3 and also higher than the binding energy of Pt L_1. The photon energy range was selected to obtain quantitative X-ray fluorescence emission from both bismuth and platinum and, at the same time, EXAFS and XANES information across the bismuth L_3 adsorption edge. For PtPb nanoparticle modified electrodes, the energy scan was from 12.95 KeV, which is 80 eV below the binding energy of Pb L_3, to 13.30 KeV, which is 350 eV above the binding energy of Bi L_1 and also higher than binding energy of Pt L_2. Each energy scan took about 15 min and 10 scans were average to minimize noise and obtain appropriate statistics.

6.3 Results and discussions

6.3.1 XRF MCA spectra of PtBi and PtPb nanoparticles

The energy resolutions of the VORTEX and X-Flash detectors were not sufficient to completely separate the X-ray emission lines from Pt Lβ and Bi Lα when the incident beam energy was higher than 13.42 KeV. In order to get accurate fluorescent emission intensities of specific elements in the nanoparticles, under active electrochemical control, the entire MCA spectrum was recorded via the VORTEX detector. Table 6.2 presents the detailed information of the X-ray transitions which give rise to the X-ray emission lines for Pt, Bi and Pb used in the experiments and data analysis.

As mentioned earlier, for PtBi nanoparticles, the energy scan started from 13.30 KeV, which is below the binding energy of the Bi L_3 edge. The fluorescent signals were coming from Pt emission lines and were dominated by the 9.44 KeV Pt Lα and 11.07 KeV Pt Lβ emission lines. Bismuth fluorescence signals increased after scanning the energy past 13.42 KeV; the Bi L_3 absorption edge. For PtPb nanoparticles, the energy scan started from 12.95 KeV, which is below the binding energy of the Pb L_3 edge. At this point, the fluorescent signals were dominated by Pt

Table 6.2 Transitions that give rise to the emission lines.

Labels	Transition	Binding Energy (KeV)		Emission Energy (KeV)	Relative Intensity
Lα1	$M_5 \rightarrow L_3$	**Pt**	11.56	9.44	100
		Bi	13.42	10.84	100
		Pb	13.04	10.55	100
Lα2	$M_4 \rightarrow L_3$	**Pt**	11.56	9.36	11
		Bi	13.42	10.73	11
		Pb	13.04	10.45	11
Lβ1	$M_4 \rightarrow L_2$	**Pt**	13.27	11.07	67
Lβ2	$N_5 \rightarrow L_3$	**Pt**	11.56	11.25	23
		Bi	13.42	12.98	25
		Pb	13.04	12.62	25
Ll	$M_1 \rightarrow L_3$	**Pt**	11.56	8.27	5

Ll and Lα. Pb fluorescent signals were evident after scanning the energy past 13.04 KeV; the Pb L_3 absorption edge. Figure 6.2 presents a typical Bi Lα fluorescence spectrum recorded by the SCA detector which was deliberately set up to cover the range of Bi Lα fluorescent photons. There were two steps in XRF intensities at 13.42 KeV and 13.88 KeV, respectively, corresponding to the energies of Bi L_3 and Pt L_1 absorption edges. There was also a small step at 13.88 KeV ascribed to the Pt L_1 absorption edge. This was unexpected and surprising since only Pt Lβ emissions, with binding energy of 13.27 (Pt L_2 edge) or 11.56 (Pt L_1 edge) KeV, could be detected by the SCA detector based on the energy window. There are two possible reasons for this phenomenon: 1) there is an unknown Pt fluorescence emission directly associated with Pt L_1 edge at 13.88 KeV; 2) there is a complicated process involving non-radiative energy dissipation to give Pt Lβ emissions associated with the initial excitation of 13.88 keV. In order to figure out the origin of this fluorescence process ascribed to the Pt L_1 edge in Figure 6.2, the MCA spectrum was recorded and post-experimental simulation and fitting data analysis based on XPaXs software carried out. If the first assertion were correct, a new fluorescence peak would appear in the MCA spectrum once the energy passed by 13.88 KeV. If the non-radiative process is the correct explanation, in place of appearance of a new emission peak, the intensity of Pt Lβ emission should increase at the energy scanned past 13.88 KeV. As seen in Figure 6.3, the MCA spectrum obtained before and after the binding energy of the Pt L_1 edge strongly suggest that the second explanation is likely responsible for the observed phenomenon. In essence, there was no new peak detected in the MCA spectrum after scanning the energy past 13.88 keV. Instead, the intensity of the Pt Lβ fluorescence peak increased. Although a bit speculation on our put, we believe that Pt L_1 electrons were ejected by the 13.88 keV incident photons and the generated holes were left on the L_1 level. Electrons from the Pt L_2 and L_3 levels filled the holes (on Pt L_1 level) by

Figure 6.2 A typical energy scan recorded by the SCA detector for a PtBi nanoparticle modified electrode. The marks of A, B, C, D correspond to MCA scans in Figure 6.3.

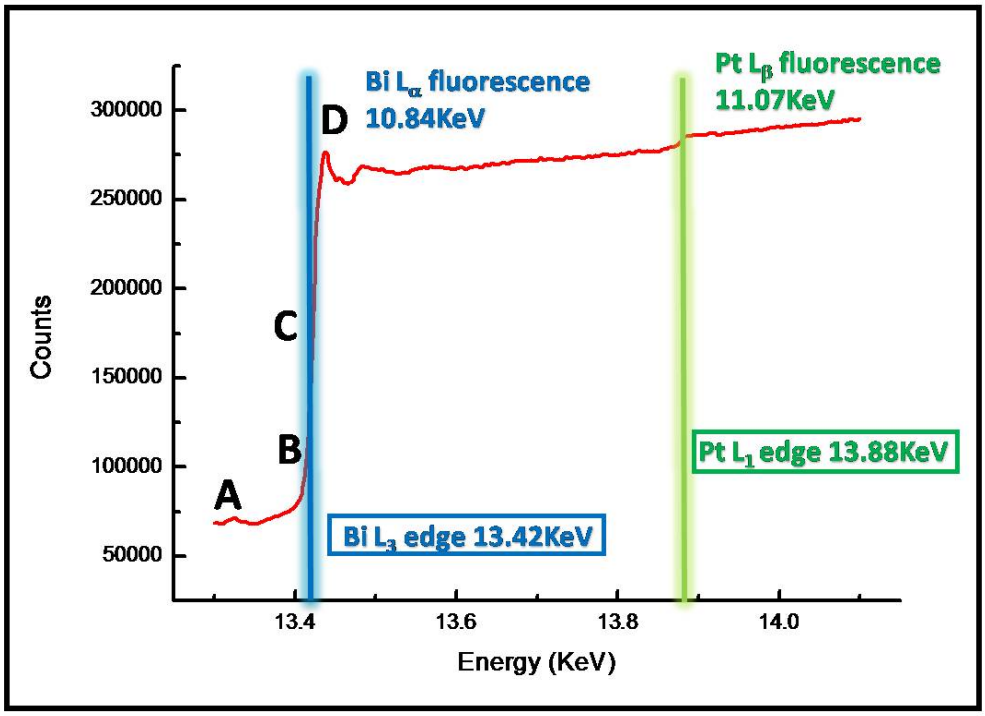
Bi L_α fluorescence
10.84KeV
Pt L_β fluorescence
11.07KeV
D
C
B
A
Pt L_1 edge 13.88KeV
Bi L_3 edge 13.42KeV
Counts
300000
250000
200000
150000
100000
50000
13.4
13.6
13.8
14.0
Energy (KeV)

Figure 6.3 MCA scans for a PtBi nanoparticle modified electrode recorded by VORTEX detector. The panels A, B, C, D correspond to different incident energy as pointed in Figure 6.2.

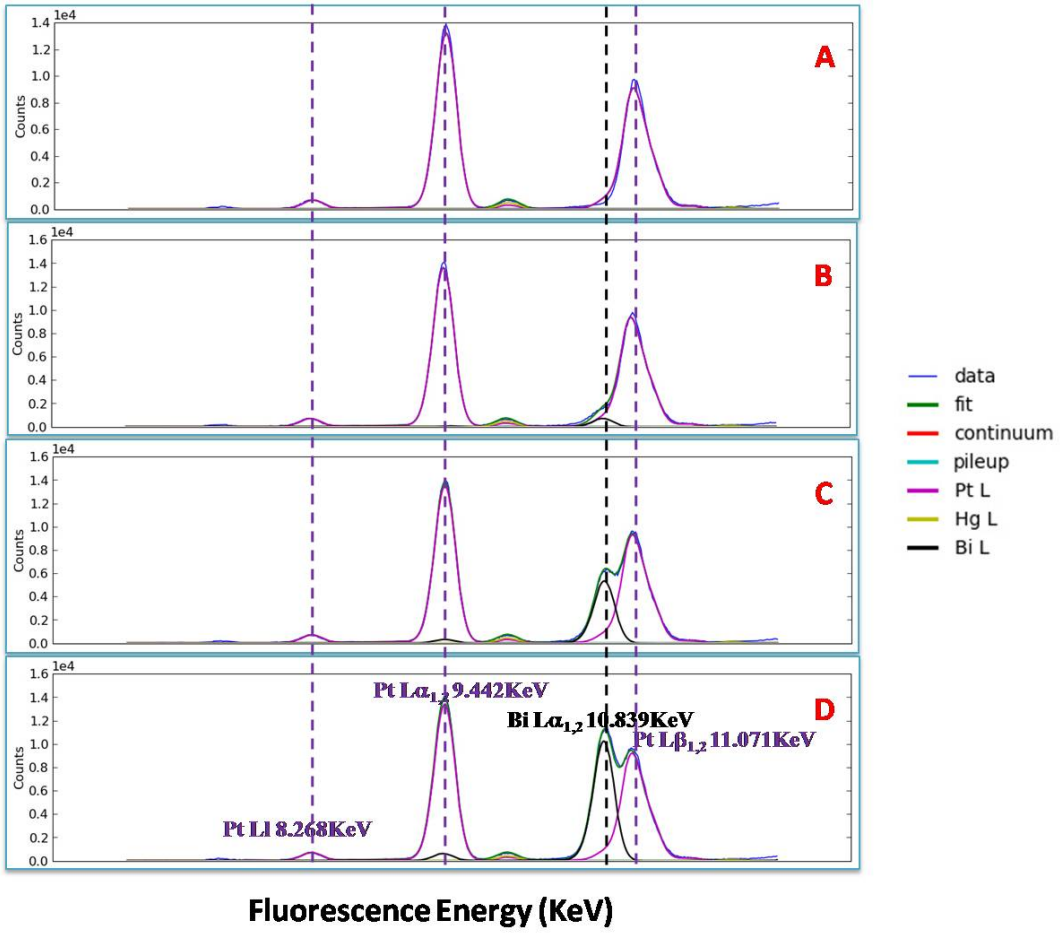
A
B
C
D
Counts
1e4
data
fit
continuum
pileup
Pt L
Hg L
Bi L
Pt Lα1,2 9.442KeV
Bi Lα1,2 10.839KeV
Pt Lβ1,2 11.071KeV
Pt Ll 8.268KeV
Fluorescence Energy (KeV)

intra-atomic relaxation and the extra energy was dissipated via a non-radiative process. Then the electrons at higher levels, like Pt M_4 or N_5, jumped into the holes left on Pt L_2 and L_3 to generate more Pt Lβ fluorescent photons.

Figure 6.3 shows four images (A, B, C, D) of MCA scans corresponding to four different representative positions in a typical energy scan, such as in Figure 6.2. Scan A was recorded at an energy well below the Bi L_3 absorption edge; scan B was at the foot of the rising Bi Lα fluorescence emission; scan C was at the middle of the Bi L_3 absorption edge; and scan D was at just over the Bi L_3 absorption edge. In Figure 6.3, the x axis represents energies of photons which went into the VORTEX detector and were recorded by a MCA with 1200 channels. The experimental data were fitted with the XPaXs software follwoing the optimization of many parameters, such as detector calibration, thickness of the nanoparticle sample, substrate properties, distance between the detector and sample, attenuation factor in front of the detector and others. The simulations of possible emission peaks, corresponding to different elements, are presented in different colors. The Pt Ll, Lα and Lβ emissions were consistently presented in the A, B, C scans because all of these peaks were excited at the beginning of the energy scan. From B, C, and D scans, the increasing trend of the Bi Lα emission is clearly evident as the energy passed over the Bi L_3 absorption edge at 13.42 KeV. Based on the simulations of fluorescence peaks from the different elements, precise XRF intensities corresponding to each element and each specific emission could be obtained without interference.

6.3.2 Quantitative characterization for the leaching out process of the less noble metals based on XRF data

It is of great importance to characterize the changes in composition and structure of

intermetallic nanoparticles, since these are the actual phases for commercial and industrial applications. As stated previously, X-ray diffraction, a conventional characterization method for the bulk or the surfaces of electrocatalysts under active potential control, is not suitable for *in-situ* measurement of nanoparticles. The amount of immobilized nanoparticles (80 μg/cm^2) on the substrate of the GC electrode, which was optimized for electrocatalytic activity, did not give detectable diffraction signals, even when using the well-established grazing incidence diffraction method which focuses surface characterization. Moreover, the substrate GC electrode gave strong and broad backscattering peaks which covered the two theta range corresponding to the major diffraction peaks of PtBi and PtPb intermeatllic phases. Thus, XRD nor GID methods could be utilized to characterize these nanoparticles under active electrochemical control. In previous studies we have known that the composition and structure of intermetallic surfaces, in either polycrystalline or single crystal forms, dramatically changed as a function of applied potentials. Different electrochemical pretreating methods, such as cycling vs. holding the potential, gave rise to differently terminated surfaces. The results from *in-situ* GID or XRD investigations were qualitative or, at best, semi-quantitative. Here, changes in the nanoparticles were characterized via the XRF method in a more quantitative way. Specific energy scans to acquire XRF data were carried out for a freshly prepared nanoparticle modified electrode or after cycling the electrode to potentials between -0.20V and E_{ulp} for 10 cycles in 0.1M $HClO_4$. As mentioned above, in order to obtain precise intensities of each emission peak of specific elements, XRF data were extracted from simulations of experimental records via MCA spectra. At the same time, pseudo SCA detector recorded mainly the Bi Lα fluorescence with some contribution from the Lβ fluorescence. In Figure 6.4, we made use of XRF data obtained via the SCA detector to get quantitative information about molar ratios of Pt to Bi in the nanoparticles.

Figure 6.4 Scans depicting changes in the molar ratios of Pt to Bi from nanoparticles as a function of applied E_{ulp} values of +0.40V (a), +0.80V (b) and +1.20V (c) in supporting electrolyte only based on quantitative XRF data.

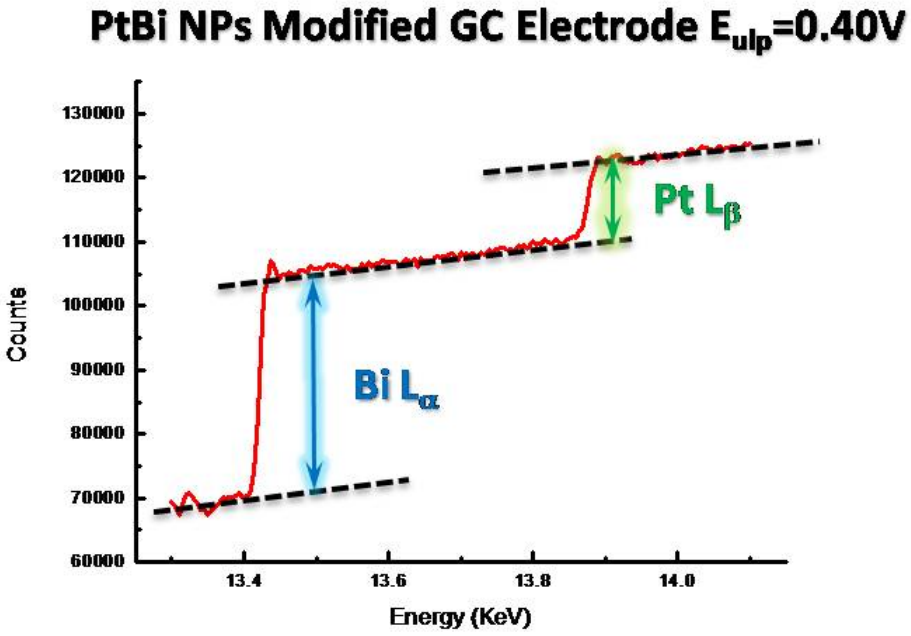
PtBi NPs Modified GC Electrode E_{ulp}=0.40V
Counts
130000
120000
110000
100000
90000
80000
70000
60000
13.4
13.6
13.8
14.0
Energy (KeV)
Pt L_β
Bi L_α

(a)

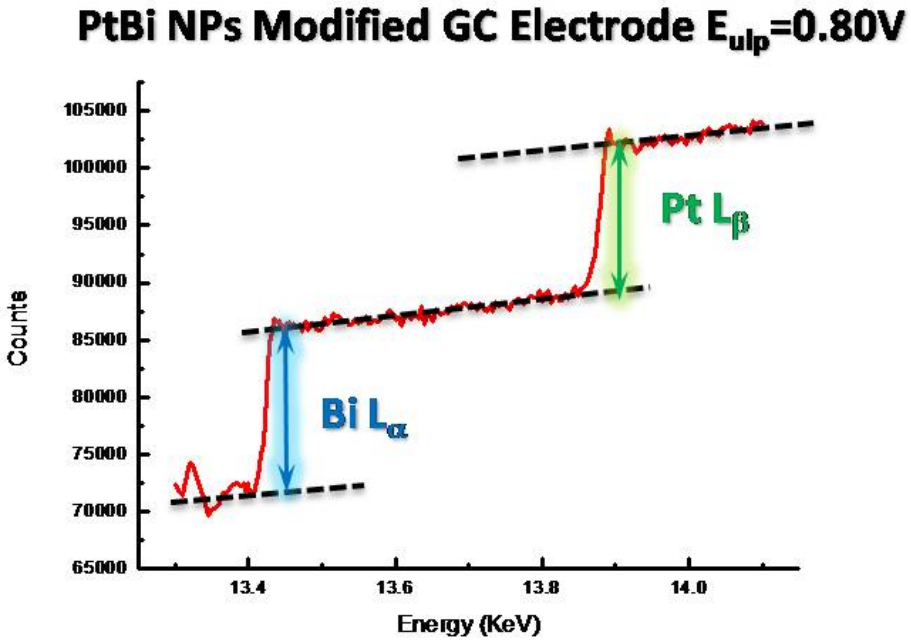
PtBi NPs Modified GC Electrode E_{ulp}=0.80V
Counts
105000
100000
95000
90000
85000
80000
75000
70000
65000
13.4
13.6
13.8
14.0
Energy (KeV)
Pt L_β
Bi L_α

(b)

Figure 6.4 (Continued)

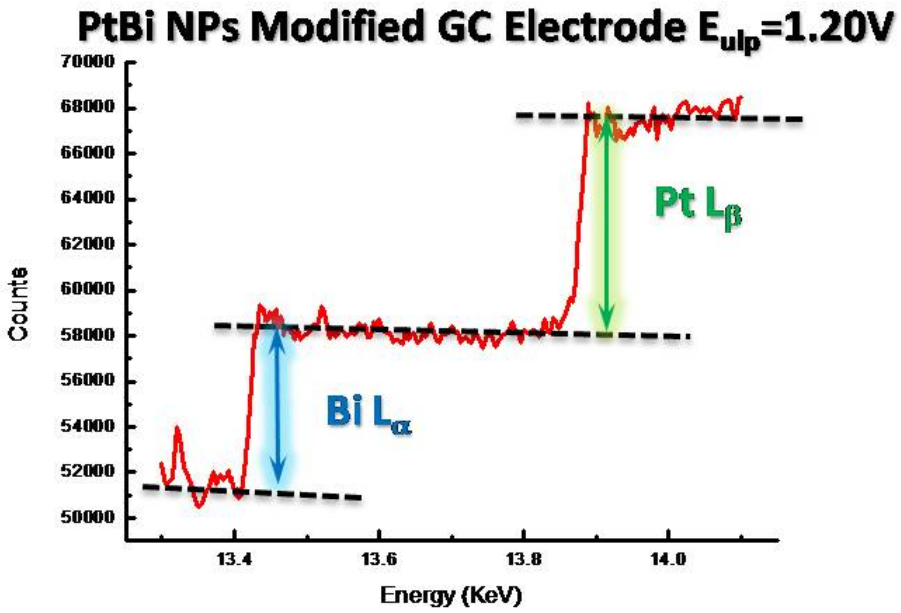

(c)

From Figure 6.4, we could derive the ratios of fluorescence intensities of Pt to Bi which were 0.42, 0.96 and 1.36, respectively, for the E_{ulp} values of +0.40V, +0.80V and +1.20V. These results suggest that the Bi leaching out process from the nanoparticles occurred at more negative E_{ulp} values than for bulk intermetallic phases. Since the XRF experiment was carried out at incidence angle of 1~2 deg, and the thickness of the nanoparticle modified layer on the GC electrode was ~50 μm, almost the entire layer of nanoparticles on the working electrode was sampled under this experimental condition. It should be kept in mind that the fluorescence signals favored the information about the surface composition of the nanoparticles instead of that of entire nanoparticles. The molar ratios of Pt to Bi of the intermetallic PtBi nanoparticles increased as a function of applied E_{ulp} in 0.1M H_2SO_4, indicating that the bismuth atoms gradually leached out from the surfaces of the nanoparticles while cycling potentials to increasingly positive values in supporting electrolyte. As a result, the surfaces became enriched in Pt after these electrochemical pretreatments. The nanoparticles were essentially changed from uniform composition intermetallic nanoparticle to a core/shell nanostructure with an intact intermetallic PtBi phase at the core and a Pt rich outmost layer of PtBi phase as the shell. Similar behavior was observed for intermetallic PtPb nanoparticle-modified electrodes also, with the only difference being that the working electrode was subjected to electrochemical pretreatment by holding (not scanning) the potential. Figure 6.5 shows pseudo 2D-mapping images of XRF data for PtPb nanoparticles while holding the potential at +0.40V and +0.80V in 0.1M $HClO_4$ solution. The 2D-mapping images provide more detailed information of intensities for each emission peak of a specific element in a quantitative way. Each line in a 2D-mapping image represents an individual emission line from a specific element. While there was little change in fluorescence intensities emissions from Pt atoms, the intensity of the Pb Lα emission decreased dramatically.

Figure 6.5 Pseudo 2D-mapping image of XRF data of PtPb nanoparticles as a function of applied E_{ulp} of +0.40V (left) and +0.80V (right) in supporting electrolyte only.

PtPb NPs in 0.1M HClO4 holding @+0.40V 10min

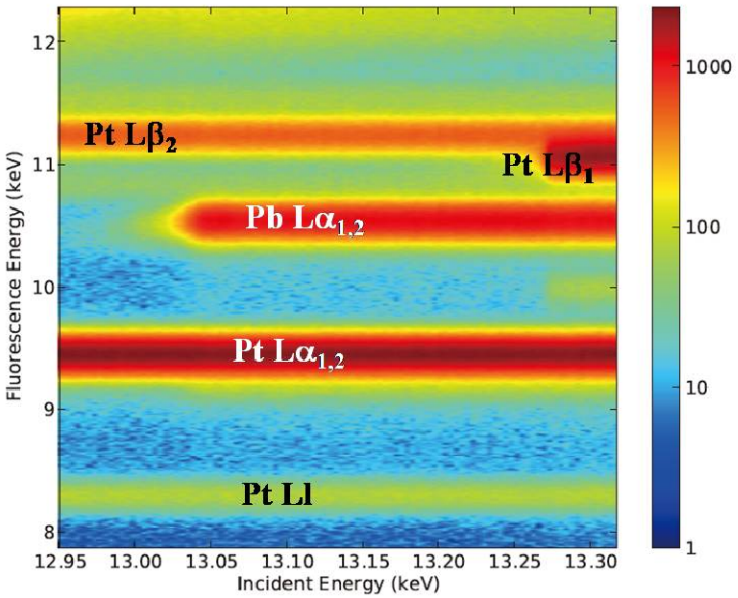

PtPb NPs in 0.1M HClO4 holding @+0.80V 10min

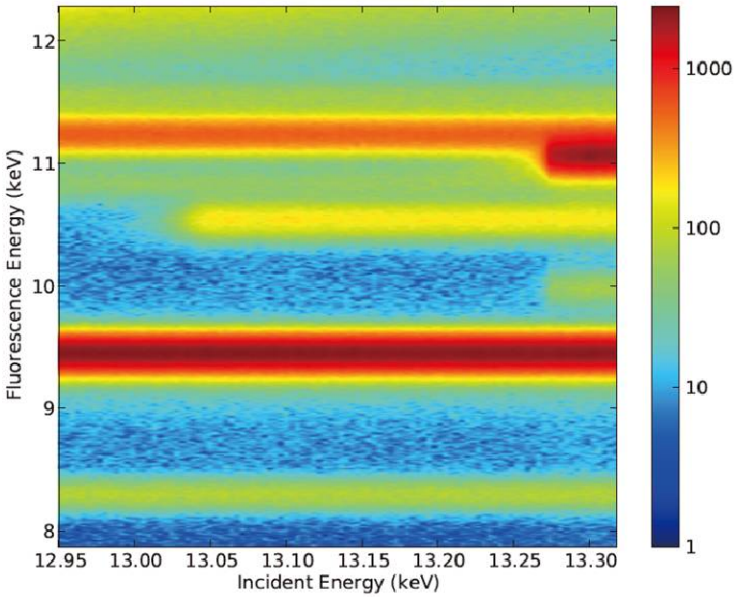

Thus, Pb was clearly leached out from the nanoparticle sample by increasing the applied potential and ostensibly gave rise to Pt shell/PtPb core nanoparticles. Since the absolute intensities of the Pt fluorescence changed little for applied potentials of +0.40V and +0.80V, one would expect that the diameter of the nanoparticles likely decreased extensively as a consequence of the leaching out process of Pb. More discussion about XRF data extracted from MCA spectra will be extensively discussed elsewhere in future.

6.3.3 Kinetic stabilization of intermetallic nanoparticles phases

We have previously documented kinetic stabilization effects induced by active fuel molecules present in solution for bulk electrodes of PtBi and PtPb intermetallic phases. XRF experiments were carried out to determine of such kinetic stabilization effects were also present for intermetallic nanoparticle phases. Figure 6.6 presents XRF data for a PtBi nanoparticle-modified electrode while cycling the E_{ulp} to +0.80 V in the absence or presence of formic acid in supporting electrolyte. The Pt to Bi fluorescence intensity ratios were 0.19 and 0.96, respectively, in 0.2M HCOOH/0.1M H_2SO_4 and in 0.1M H_2SO_4 only. In the former case, the Bi leaching out process was precluded by the PtBi-catalyzed oxidation of formic acid, while the latter involved the corrosion/oxidation of the nanoparticles themselves. These results are very similar to those for bulk electrodes but in this case, we could obtain more quantitative data. The fluorescence intensity ratio of Pt to Bi of 0.19 for cycling the E_{ulp} to +0.80V in 0.2M HCOOH/0.1M H_2SO_4 was much lower than that, 0.42, for cycling the E_{ulp} to +0.40V in 0.1M H_2SO_4 only. Two main conclusion could be derived: 1) aggressive leaching out of Bi occurred even for an E_{ulp} value of +0.40V, which is 400 mV negative of the results obtained from qualitative GID/XRD characterizations; and 2) the leaching out

Figure 6.6 Scans depicting changes in the molar ratios of Pt to Bi from PtBi nanoparticles after cycling to an E_{ulp} value of +0.80V in the absence (a) and presence (b) of formic acid in the supporting electrolytes based on quantitative XRF data.

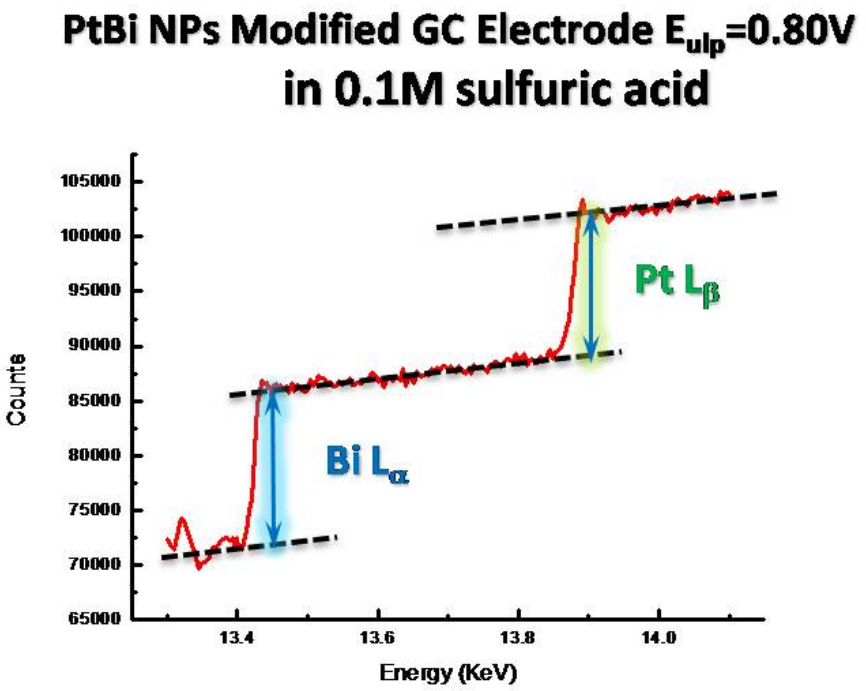
PtBi NPs Modified GC Electrode E_{ulp}=0.80V
in 0.1M sulfuric acid
Counts
105000
100000
95000
90000
85000
80000
75000
70000
65000
13.4
13.6
13.8
14.0
Energy (KeV)
Pt L_β
Bi L_α

(a)

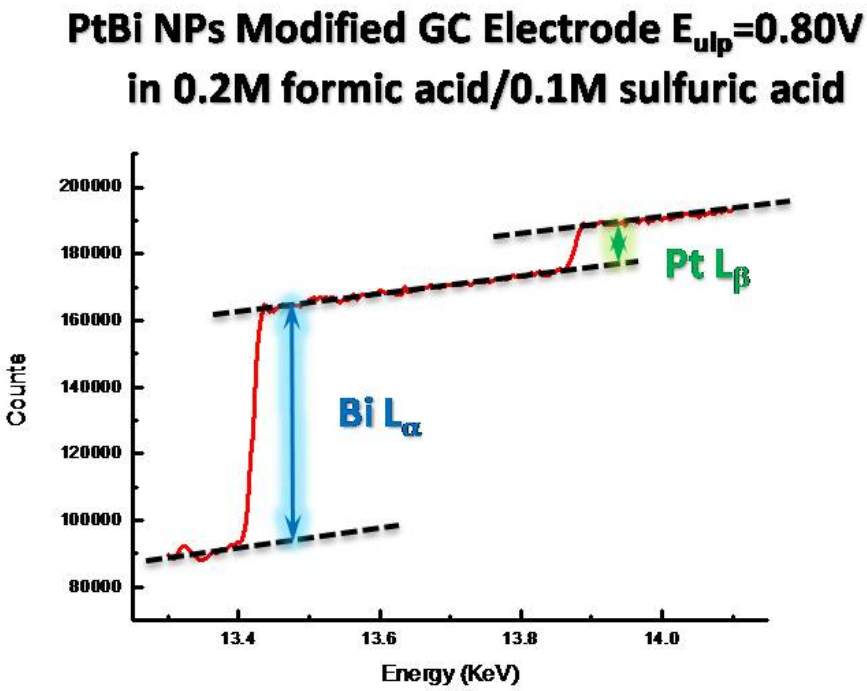
PtBi NPs Modified GC Electrode E_{ulp}=0.80V
in 0.2M formic acid/0.1M sulfuric acid
Counts
200000
180000
160000
140000
120000
100000
80000
13.4
13.6
13.8
14.0
Energy (KeV)
Pt L_β
Bi L_α

(b)

process of Bi from PtBi nanoparticles was completely precluded at an E_{ulp} value of +0.80V in presence of formic acid molecules in the supporting electrolyte. Figure 6.7 presents pseudo 2D-mapping images of XRF data for PtBi nanoparticles for holding potentials at +0.40V and +1.20V for 10 min in 0.2M HCOOH/0.1M H_2SO_4 solution. Special attention was paid to the changes in the fluorescence intensities of Pt and Bi emissions and the ratios of Pt to Bi at different E_{ulp} values. The intensity of the Bi Lα emission decreased slightly (less than 10%) while increasing the holding potential from +0.40V to +1.20V and there were very small changes in the intensities of the Pt emission lines during electrochemical treatments. This suggests that while kinetic stabilization effects are observed for PtBi nanoparticles under these conditions at the same time bismuth starts to leach out from the matrix while the E_{ulp} value is +1.20V. This potential is well positive of the potential at which the formic acid molecules are fully oxidized and the surface corrosion of the nanoparticles is enabled.

6.3.4 EXAFS and XANES characterization of Bi L_3 edge from PtBi nanoparticles

There were two ways to obtain EXAFS and XANES spectra from this our XRF experimental geometry: 1) directly recorded via the SCA detector; 2) recompile the spectrum from the XRF data extracted from the MCA scan after special data analysis by XPaXs software. Figure 6.8 presents the EXAFS and XANES spectra obtained via the SCA detector while cycling to different E_{ulp} values of +0.40V, +0.60V, +0.80V, +1.00V and +1.20V in 0.1M H_2SO_4. As is evident, the EXAFS spectra exhibited little change during electrochemical pretreatments. In the XANES spectra, the Bi L_3 edge absorption edge shifted to higher energy while cycling of the potentials to any positive values when compared to a freshly prepared electrode. This indicates that bismuth atoms on the surfaces of the nanoparticles are oxidized as the binding energy

Figure 6.7 Pseudo 2D-mapping image of XRF data of PtBi nanoparticles as a function of applied E_{ulp} of +0.40V (left) and +1.20V (right) in the presence of formic acid in supporting electrolyte.

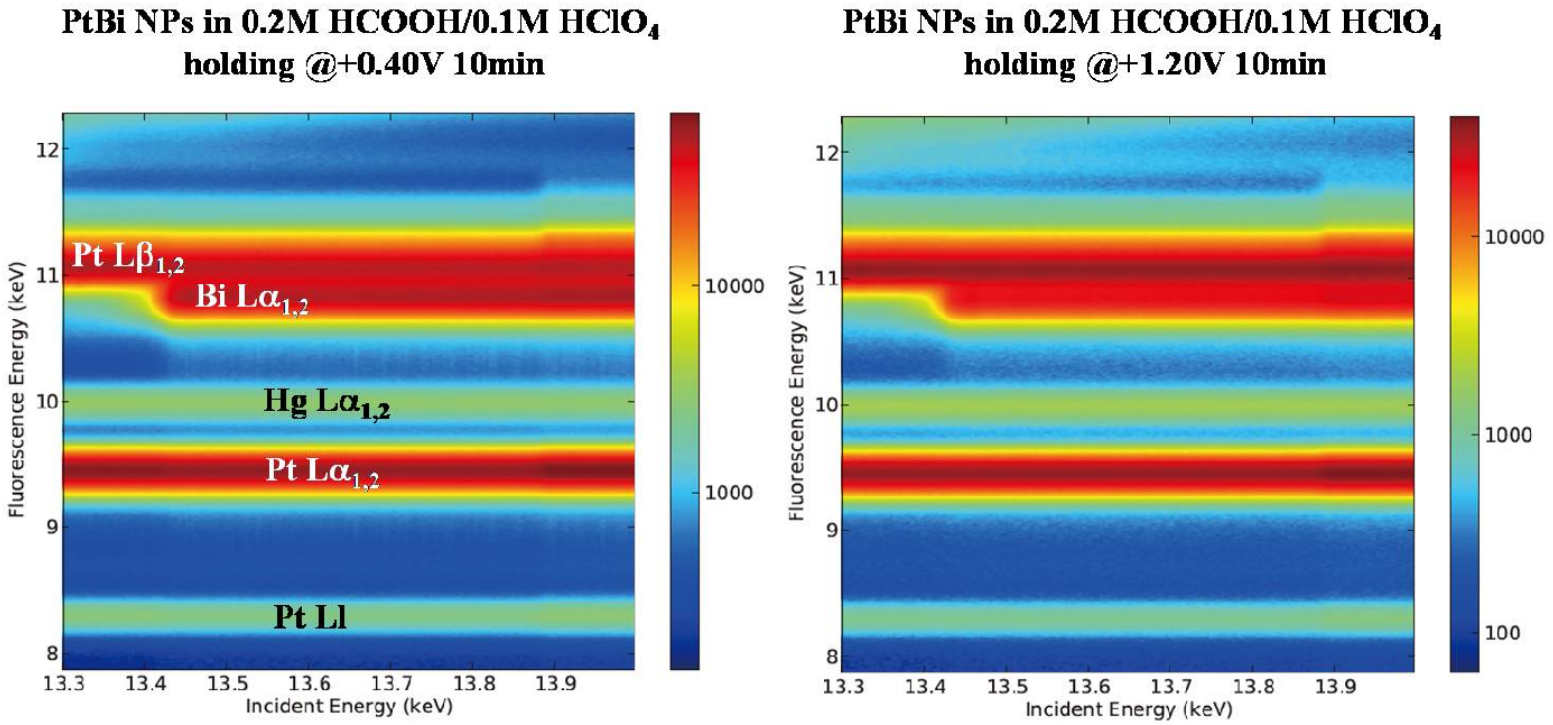
PtBi NPs in 0.2M HCOOH/0.1M HClO4
holding @+0.40V 10min
Pt Lβ1,2
Bi Lα1,2
Hg Lα1,2
Pt Lα1,2
Pt Ll
Fluorescence Energy (keV)
Incident Energy (keV)
10000
1000
PtBi NPs in 0.2M HCOOH/0.1M HClO4
holding @+1.20V 10min
Fluorescence Energy (keV)
Incident Energy (keV)
10000
1000
100

Figure 6.8 EXAFS (a) and XANES (b) spectra of Bi L_3 edge from PtBi nanoparticles directly recorded via the SCA detector while cycling the E_{ulp} to different values in 0.1M H_2SO_4.

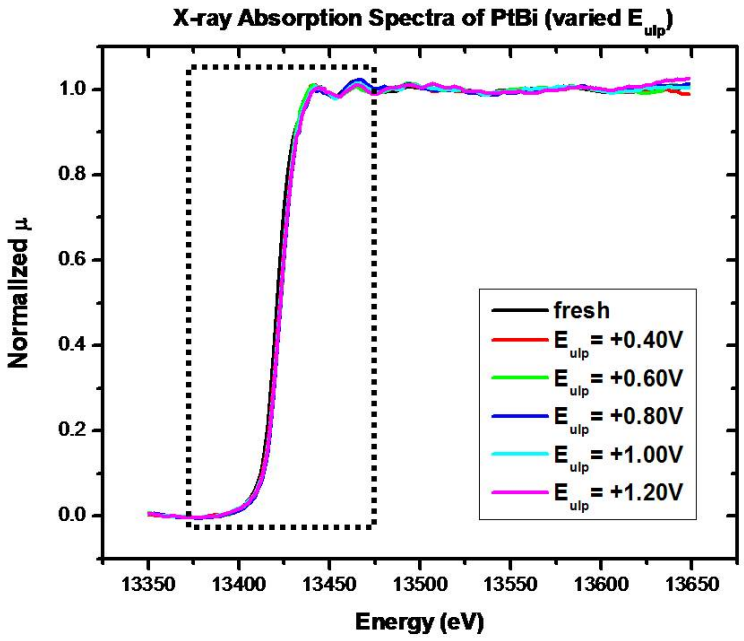
X-ray Absorption Spectra of PtBi (varied E_ulp)
Normallized μ
Energy (eV)
fresh
E_ulp = +0.40V
E_ulp = +0.60V
E_ulp = +0.80V
E_ulp = +1.00V
E_ulp = +1.20V

(a)

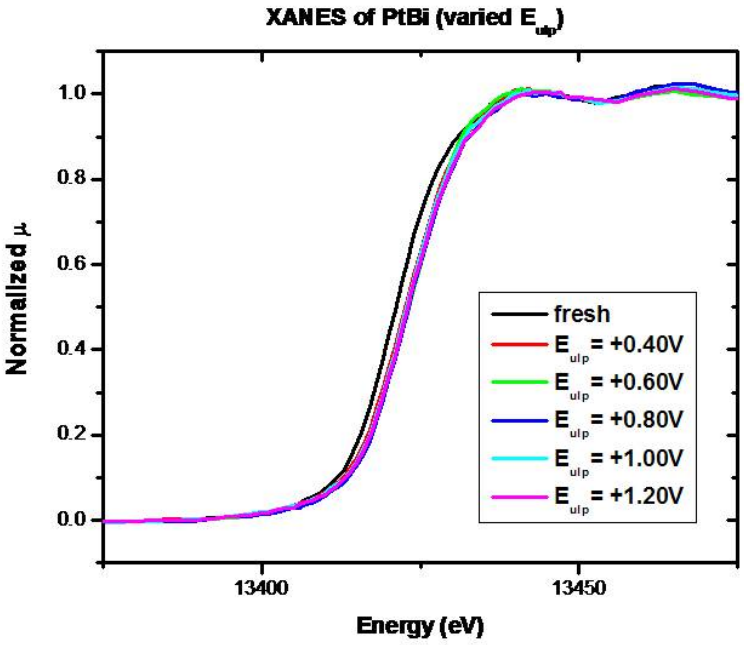
XANES of PtBi (varied E_ulp)
Normallized μ
Energy (eV)
fresh
E_ulp = +0.40V
E_ulp = +0.60V
E_ulp = +0.80V
E_ulp = +1.00V
E_ulp = +1.20V

(b)

(absorption edge) shifts to higher value. Besides the sudden change in adsorption edge from freshly prepared electrodes to electrodes cycled to the E_{ulp} of +0.40V, there was little change in the XANES spectra. It should be kept in mind that XRF data from pseudo SCA detector got interference from Pt Lβ emissions. A more complete analysis of EXAFS and XANES data as a function of applied potential will be presented elsewhere.

6.4 Conclusion and Summary

In this paper, a simple, universal, multi-functional and nondestructive XRF method was developed to characterize the composition and structure of intermetallic PtBi and PtPb nanoparticles as electrocatalysts under active electrochemical control. SCA data derived from conventional X-Flash detector and MCA spectra recorded via VORTEX detector were utilized to yield either quantitative XRF information or EXAFS and XANES spectra. Similar to solid state electrodes investigated by qualitative or semi-quantitative XRD or GID methods, the less noble elements (Bi or Pb) were leached out from the intermetallic nanoparticles while cycling or holding the potential to positive values in supporting electrolyte only. The leaching out process was initially detected at an E_{ulp} value of +0.40V which is much more negative than expected based on previous studies on bulk samples. The core/shell structures were formed after certain electrochemical pretreatments and the diameters of the nanoparticles significantly decreased. Kinetic stabilization effects induced by active fuel molecules present in solution were observed for these nanoparticles in a way analogous to observation on bulk samples of these materials. EXAFS and XANES data showed that surface bismuth atoms in the nanoparticles were oxidized once the electrode was subjected to applied E_{ulp} as low as +0.40V and the oxidation state of Bi changed little

as function of applied potential to more positive values. While our studies conducted on PtBi nanoparticles, this method could be generally utilized to characterize any bimetallic or multi-elemental electrocatalytic nanoparticles especially for samples in which there could be interference from the fluorescence emission from different elements.

REFERENCES

1. G. Rupprechter and C. Weilach, *Nnao Today* 2, 20, **2007**
2. N.M. Markovic and P.N. Ross, *Surface Science Reports* 45, 117, **2002**
3. G. Ertl *et al.*, *Handbook of Heterogeneous Catalysis* Wiley-VCH, Weinheim, **1997**
4. G.A. Somorjai, *Introduction to Surface Chemistry and Catalysis* John Wiley & Sons, Inc., New York, **1994**
5. R. Schlögl, *Advances in Catalysis (Chapter 5)* 52, 273, **2009**
6. S.R. Bare and T. Ressler, *Advances in Catalysis (Chapter 6)* 52, 339, **2009**
7. E.H. Conrad, *Prog. Surf. Sci.* 39, 65, **1992**
8. M.E. Gallagher, C.A. Lucas, V. Stamenkovic, N.M. Markovic and P.N. Ross, *Surf. Sci.* 544, L729, **2003**
9. A.M. Venezia, *Catalysis Today* 77, 359, **2003**
10. Y. Iwasawa, *X-ray Absorption Fine Structure for Catalysts and Surfaces* World Scientific, Singapore, **1996**
11. B.M. Weckhuysen, *In-situ Spectroscopy of Catalysts* American Scientific Publishers, Stevenson Ranch, **2004**
12. S. Mukerjee, J. Ziegelbauer, T. Arruda, D. Rmaker and B. Shyam, *The Electrochem. Soc. Interface* 17, 46, **2008**
13. K. Tsuji, K. Nakano, H. Hayashi, K. Hayashi and C. Ro, *Anal. Chem.* 80, 4421, **2008**
14. P. Wobrauschek, *X-ray Spectrom.* 36, 289, **2007**
15. C. Streli, *Appl. Spectro. Rev.* 41, 473, **2006**
16. M. Mages, M. Óvári, W. Von Tümpling and K. Kröpfl, *Anal. Bioanal. Chem.* 378, 1095, **2004**
17. E. Hernandez-Caraballo and L.M. Macro-Parra, *Spectrochim. Acta* 58B, 2205,

2003

18. S. Bouykens and C. Vazquez, *Spectrochim. Acta* 59B, 1189, **2004**
19. M.L. Carvalho, A.F. Marques, M.T. Lima and U. Reus, *Spectrochim. Acta* 59B, 1251, **2004**
20. C.L. Pearson, D.S. Dale, P.W. Brewer, P.I. Kuniholm, J. Lipton and S.W. Manning, *J. Arch. Sci.* 36,1206, **2009**
21. A.R. Woll, J. Mass, C. Bisulca, R. Huang, D.H. Bilderback, S. Gruner and N. Gao, *Appl. Phys.* A83, 235, **2006**
22. E. Marguí, K.V. Meel, R.V. Grieken, A. Buendía, C. Fontà, M. Hidalgo and I. Queralt, *Anal. Chem.* 81, 1404, 2009
23. E. Gebel, *Anal. Chem.* 80, 8862, **2008**
24. K. Peeters, K. De Wael, L Vincze and A. Adriaens, *Anal. Chem.* 77, 5512, **2005**
25. K. Van Meel, A. Smekens, M. Behets, P. Kazandjian and R. Van Grieken, *Anal. Chem.* 79, 6383, **2007**
26. S. Sattayasamitsathit, J. Burdick, R. Bash, P. Kanatharana, P. Thavarungkul and J. Wang, *Anal. Chem.* 79, 7571, **2007**
27. J. Larminie and A. Dicks, *Fuel Cell Systems Explained (Second Ed.)* Wiley, England, **2003**
28. C.L. Lamy, J.-M. Leger and S. Srinivasan, *Direct Methanol Fuel Cell: From a Twentieth Century Electrochemist's Dream to a Twenty-First Century Emerging Technology,* Kluwer Academic/Plenum Publishers, New York, Vol.24, **2001**
29. E. Reddington, A. Sapienza, B. Gurau, R. Viswanathan, S. Sarangapani, E.S. Smotkin and T.E. Mallouk, *Science* 280, 1735, **1998**
30. K. Scott and A. Shukla, *Direct Methanol Fuel Cells: Fundamentals, Problems, and Perspectives* in *Modern Aspects of Electrochemistry*, Springer, New York, Vol.40, **2007**

31. J. Lipkowski and P.N. Ross, *Electrocatalysis* Wiley-VCH, New York, **1992**
32. M. Watanabe and S. Motoo, *J. of Electroanal. Chem.* 60, 267, **1975**
33. M. Watanabe and S. Motoo, *J. of Electroanal. Chem.* 60, 275, **1975**
34. E. Casado-Rivera, Z. Gál, A.C.D. Angelo, C. Lind, F.J. DiSalvo and H.D. Abruña, *Chem. Phys. Chem.* 4, 193, **2003**
35. E. Casado-Rivera, D.J. Volpe, L. Alden, C. Lind, C. Downie, T. Vázquez-Alvarez, A.C.D. Angelo, F.J. DiSalvo and H.D. Abruña, *J. Am. Chem. Soc.* 126, 4043, **2004**
36. Y. Liu, H. Abe, H.M. Edvenson, F.J. DiSalvo and H.D. Abruña, *submitted*
37. Y. Liu, D.R. Blasini, F.J. DiSalvo and H.D. Abruña, *submitted*
38. Y Liu, M.A. Lowe, F.J. DiSalvo and H.D. Abruña, *submitted*
39. C. Roychowdhury, F. Matsumoto, V.B. Zeldovich, S.C. Warren, P.F. Mutolo, M. Ballesteros, U. Wiesner, H.D. Abruña and F.J. DiSalvo, *Chem. Mater.* 18, 3365, **2006**
40. XPaXs software: XPaXS is a collection of python packages and libraries for X-ray Science. This software is developed with the goal of providing useful real-time feedback and analysis of scanning XRF experiments. See website http://dale.chess.cornell.edu/~darren/xpaxs/.

CHAPTER SEVEN

EXAFS INVESTIGATION OF PtBi INTERMETALLIC NANOPARTICLES

7.1 Introduction

X-ray absorption spectroscopy (XAS) is a powerful method for probing the average local electronic and geometric structure of catalysts in the working state or catalytically active state, and has attracted increasing research interests in the interdisciplinary research communities of sustainable energy, catalysts, nanomaterials and photochemistry. XAS includes two major sub-categories: extended X-ray absorption fine structure (EXAFS) and X-ray absorption near-edge structure (XANES), also referred as near-edge X-ray absorption fine structure (NEXAFS).

EXAFS refers to modulations in the absorption coefficient for energies up to 1000 eV beyond the absorption edge in an X-ray absorption spectrum.[1] This effect was first discovered in 1923 by Kronig[2] and successfully rationalized with a short-range order theory by Sayers, Stern and Lytle in 1971,[3] who proposed that a Fourier transform of the EXAFS spectrum with respect to the photoelectron wave number, would have peaks corresponding to the nearest-neighbor interatomic distance. Theories of EXAFS have been extensively developed for the last three decades, and instruments, experimental designs and software for data analysis and processing of EXAFS, especially for synchrotron radiation as the X-ray source, have also been extensively advanced.[4-6] The information extracted from the EXAFS data is not easily converted into an unambiguous three-dimensional structure and detailed quantitative information is not routinely obtained especially for multiphasic systems. Nevertheless, the EXAFS technique can information about interatomic distances and the coordination numbers

around metal atoms in catalytic materials.

XANES is associated with the excitation process of a core electron to bound and quasi-bound states.[7-8] Since the excitation process involves multi-electron and multi-scattering effects, the interpretation of the XANES data is much more complex. In spite of the limitations of the interpretation, XANES spectra offer information about both the electronic state of the target atom and the local chemical environment around it.

EAXFS and XANES techniques have a number of attributes that make them especially well suited for the application to catalysis research: 1) sensitivity to the local structure only and thus independent of the crystalline phase; hence, the ability to probe the nanoscale phenomena that often results in non-bulk properties and which cannot be investigated by conventional scattering techniques; 2) element specificity, which is ideal to characterize bimetallic or multi-metallic catalysts or in resolving complex interactions among the catalyst, adsorbates and support materials; 3) the long penetration length of hard X-rays providing the possibility to conduct in-situ characterization in combination with other instrumental techniques; 4) the high brightness of synchrotron radiation sources, which allows applications to low concentrations of real catalysts.

The potential of X-ray absorption spectroscopy in the field of heterogeneous catalysis was first demonstrated by Lytle in 1974.[9] The applications of XAS/EXAFS/XANES techniques in catalysis science have been aggressively developed and studied for more than twenty years.[10-15] XAS can now be used in several different ways to determine local structural information about catalysts under active atmospheres and operating conditions. The type of information that could be obtained from *in-situ* EXAFS/XANES investigations of catalysts under such conditions includes: 1) structures of samples in reactive atmospheres; 2)

transformation of one species to another; 3) oxidation state determination; 4) determination of supported metal cluster size and shape; and 5) electronic structure. *In-situ* XAS studies in catalysis[16-19] are now a well-established discipline with newly emerging applications in many sub-category fields in catalysis research, such as liquid phase and high pressure reactions,[20] biomass conversion,[21] fuel cell technology,[22-23] catalyst deactivation[24] and exhaust gas treatment.[25] Another experimental advantage for the application of EXAFS/XANES techniques to catalysis research is that there are no special requirements for sample preparation. These characterization methods have been widely and successfully employed to investigate solid state bulk materials, surfaces, nanomaterials or gas and liquid samples. Walsh *et al.*[26] and McBreen *et al.*[27] reported on the use of *in-situ* XAS characterization was utilized to determine average coordination number (N), particle size and shape of platinum nanoparticles as a function of applied potential. Pt oxide growth was measured by fitting EXAFS data taken at potential intervals from +0.1V up to +1.2V vs. a saturated calomel electrode (SCE). The amplitude of the Pt-Pt peak near 2.8 Å in the FT-EXAFS decreased while that of the Pt-O signal at ~1.8 Å increased. This was readily explained as an increase in Pt-O interactions at the expense of the Pt-Pt bonds. Bimetallic electrocatalysts, as fuel cell anodes or cathodes, have also been extensively explored by EXAFS/XANES methods. One of the most important bimetallic catalysts is PtRu which is known for possessing superior methanol/CO tolerance in comparison to pure Pt.[28] Russell and co-workers[29] recently reported on an EXAFS study of carbon-supported PtRu alloy catalysts with varying Pt:Ru ratio were characterized via EXAFS method, which was supplemented with X-ray diffraction (XRD), X-ray photoelectron spectroscopy (XPS) and cyclic voltammetry (CV) techniques. Results from XRD and XANES gave a clear indication that the particles were well mixed/alloyed. The bulk compositions of the particles were determined by EXAFS and XRD. Both techniques showed that the

surfaces of the particles were enriched with Pt when compared to the nominal bulk composition. Smotkin and co-workers[30] conducted *in-situ* XAS measurements (complimented with *ex-situ* XRD) of PtRu anode electrodes in an operating direct methanol fuel cell (DMFC). No changes in the core structures of the phase segregated catalyst was observed as the potential traversed the current onset potential of the DMFC. During DMFC operation, the catalyst was essentially metallic with half of the Ru incorporated into a face centered cubic (FCC) Pt alloy lattice and the remaining half in an amorphous phase. EXAFS analysis suggested that the FCC lattice was not fully disordered. The EXAFS indicates that the Ru-O bond lengths were significantly shorter than those reported for ruthenium oxides, suggesting that the phases in which the Ru resided in the catalysts were different from oxides.

PtRu alloys, which exhibit excellent catalytic activity towards the oxidation of methanol and carbon monoxide, lack a well-defined crystalline structure, and have a random occupation of surface sites. Moreover, extensive phase segregation occurs in PtRu alloy during electrochemical treatment which can dramatically decrease their electrocatalytic activity.[31] Ordered intermetallic phases exhibit inherent properties which overcome many of the shortcomings from alloy materials presented above. Intermetallics are binary or multi-elemental metallic compounds which have well-defined crystalline structures. Electronic structures and atomic geometries which are widely accepted to be important parameters to control electrocatalytic activity, can also be deliberately adjusted and controlled. DiSalvo and Abruña[32-33] reported that ordered intermetallic PtBi and PtPb phases are promising electrocatalyst candidates towards the oxidations of formic acid and methanol in comparison to commercialized Pt or PtRu materials. Not only are these materials of great interest by themselves, but also they could serve as model systems, especially as bimetallic surfaces with terminations of controllable composition and structure to explore

structure/composition/property/ activity relationships. They would also complement single crystal metal surfaces, modified via electrodeposition or bimetallic single crystal surfaces generated by chemical vapor deposition or sputtering.[34] It is of particular interest and importance to characterize intermetallic nanoparticles because catalysts in nanophases are directly used in industrial applications.[35]

Here we report on *in-situ* and *ex-situ* EXAFS/XANES investigations of PtBi intermetallic nanoparticles. In previous studies[36] we have shown that amorphous oxidized species were generated upon cycling the potential to relatively positive values. While we had made great efforts to characterize the ordered intermetallic nanoparticles via *in-situ* X-ray grazing incidence diffraction (GID),[37] the inherent limitation of the technique when applied to nanoparticles precluded such studies. Specially GID is not suitable to detect short-range order in phases instead of long-range ordered crystalline structure; and the amount of nanoparticles used to prepare the working electrode was too small to provide sufficient diffraction signals; even though GID has great surface sensitivity. The properties of EXAFS/XANES make these techniques ideal to characterize the local structure and chemical environment of nanoparticles. The aim of this work is to obtain information on the chemical oxidation states, types and number of coordination neighboring atoms and local geometry while under operating conditions.

7.2 Materials and Experimental Section

7.2.1 Synthesis of PtBi intermetallic nanoparticles

With the exception of Bi precursors, all materials used were reagent grade which were used as obtained without further purification. $Bi(MOEEAA)_3$, as Bi precursor, was prepared by reacting stoichiometric amounts of bismuth acetate (99.999%, Alfa Aesar)

and (2-[2-{2-methoxyl}ethoxy]ethoxy) acetic acid (MOEEAA) (Aldrich). The final product was purified and collected as a colorless, viscous liquid and stored in an argon-filled glovebox. To synthesize intermetallic PtBi nanoparticles, 0.25 g of $Bi(MOEAA)_3$ were dissolved into degassed methanol. A stoichiometric amount, relative to the bismuth precursor, of the $H_2PtCl_6 \cdot 6H_2O$ (as platinum precursor), was dissolved in 10 mL of degassed anhydrous methanol and added to the bismuth precursor solution. 0.3 g of $NaBH_4$ were added into 15 mL of degassed anhydrous methanol. This solution was immediately added to the metal precursor solution. There was instant bubbling, and a black product formed, which precipitated out of the solution within 10 min. The clear solution and the black product were stirred under argon for 12 hr. The solid product was then separated from the supernatant liquid by decantation and centrifugation; it was subsequently rinsed three times each with distilled water and acetone in order to remove side products. Afterwards, the powders were dried under vacuum at room temperature. More detailed information about the synthesis and standard characterizations of these intermetallic nanoparticles can be found elsewhere.[38]

7.2.2 Electrochemistry

Nanoparticle modified glassy carbon (GC) electrodes were prepared via the following procedure (more detailed procedures are described elsewhere[35]): A mixture, containing 4 mg dried PtBi nanoparticles sample, 3980 μL of Millipore water (18.2 $M\Omega \cdot cm^{-1}$, Millipore Milli-Q), 1000 μL of isopropyl alcohol (Aldrich) and 20μL of a 5% w/w Nafion solution in alcohols (Aldrich), was sonicated in a bath type ultrasonicator for at least 30 min, then it was coated onto a 5 mm diameter GC electrode via a simple drop casting method. The modified working electrode was obtained by coating 80 $\mu m \cdot cm^{-2}$

of the intermetallic nanoparticles (20 μL of nanoparticle mixture) and then drying under a nitrogen atmosphere. All electrochemical characterizations were carried out in an electrochemical cell designed purposely for *in-situ* surface characterizations using synchrotron radiation X-ray techniques. The cell was sealed by a 5μm polypropylene film to minimize X-ray absorption and back scattering effects.[37] Cyclic voltammetry (CV) was carried out with a BAS CV-27 potentiostat/galvanostat (Bioanalytical Systems) and recorded on a computer through a PCI-DAQ card (National Instruments). All potentials are referenced to a Ag/AgCl (saturated NaCl) electrode without regard for the liquid junction potential. The electrochemical pretreatment was done by cycling the electrodes between -0.20V and E_{ulp} (upper limit potential) values from +0.40V to +1.20V for 10 cycles at 10 mV/s in 0.1M $HClO_4$ (Aldrich, ultrapure reagent). All solutions were prepared with Millipore water and deaerated with high purity nitrogen for at least 15 min before each experiment.

7.2.3 EXAFS/XANES experiments

The *in-situ* and *ex-situ* EXAFS/XANES data were acquired at the Materials Research Collaborative Access Team (MRCAT) beamline, Sector 10-ID, of the Advanced Photon Source (APS) at Argonne National Laboratory (ANL), IL. Figure 7.1 shows the experimental set up and geometry of this XAS experiment. All *in-situ* EXAFS/XANES data were obtained in fluorescence mode from the PtBi intermetallic nanoparticle modified electrode under active electrochemical control, and the fluorescent photons were recorded by a 10-cm-long ionization chamber operated with flowing N_2. For this case, the XAS data were recorded over the Pt L_3 and Bi L_3absorption edges. Multiple quick scans were taken at the Pt L_3 edge (11564 eV) and Bi L_3 edge (13419 eV) for every freshly modified GC electrode and after each

Figure 7.1 Schematic of the EXAFS/XANES experimental and X-ray optical set up.

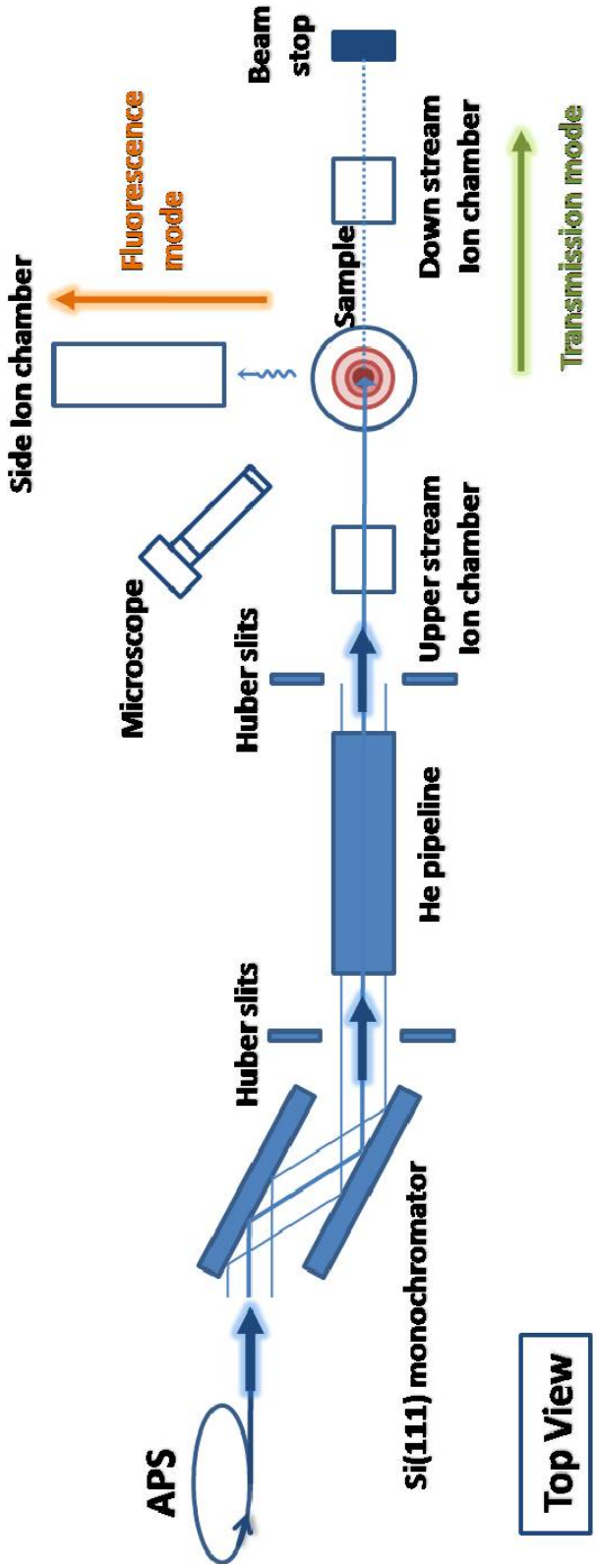
Beam stop
Fluorescence mode
Down stream Ion chamber
Side Ion chamber
Sample
Transmission mode
Microscope
Huber slits
Upper stream Ion chamber
He pipeline
Huber slits
APS
Si(111) monochromator
Top View

electrochemical pretreatment described above. On the other hand, the *ex-situ* XAS data for reference materials or for energy calibration were obtained in transmission mode from Bi metallic powder (Aldrich), Bi_2O_3 powder (Aldrich) and Pt foil (EXAFS Materials). The transmitted photons were recorded by a 30-cm-long ionization chamber operated with flowing N_2. All of the reference materials, except for the Pt foil, were ground to a fine powder and dusted onto scotch tape. Sufficient layers of tape were used to obtain $\Delta\mu\chi \approx 1$ at each absorption edge for the reference spectra.

Multiple scans obtained for each experimental condition were rebinned, summed, deglitched, and normalized using Athena software.[39] Athena employs the AUTOBK algorithm for background minimization below the *R*bkg value, which in our case was set to 1.0.

7.3 Results and Discussions

7.3.1 XANES data analysis of Pt and Bi L_3 edges of PtBi nanoparticles

Figure 7.2 (a) presents XANES spectra obtained at the Pt L_3 edge (11564 eV) from a Pt foil via transmission mode, and a freshly prepared PtBi nanoparticle modified GC electrode via fluorescence mode. Both of them were recorded with Lytle detectors (ionization chamber with flowing N_2 gas). The large edge intensity of the Pt foil indicates extensive oxidation of the as-used Pt foil. The lower edge intensity for PtBi nanoparticles at the Pt L_3 edge was consistent with the Bi L_3 edge data which showed that bismuth species were extensively oxidized in the as-synthesized PtBi nanoparticles which had been exposed to air for a long time. Figure 7.2 (b) shows the derivative XANES spectra at the Pt L_3 edge. The precise shift in the absorption edge from Pt foil to PtBi nanoparticles was -1.1 eV. This negative shift in the Pt L_3 absorption edge suggests that platinum atoms in the intermetallic crystal lattice were

Figure 7.2 XANES spectra at Pt L_3 edge of freshly prepared PtBi intermetallic nanoparticle modified electrode and Pt foil in conventional mode (a) and derivative mode (b).

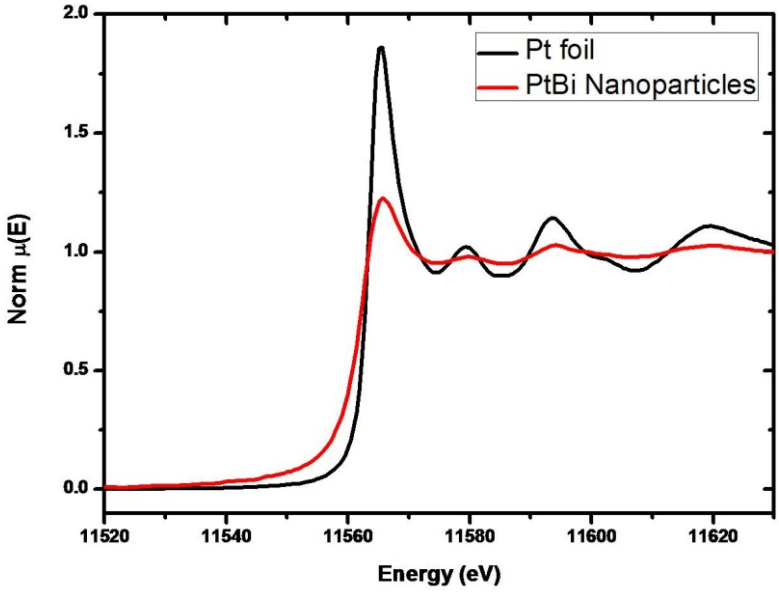
Pt foil
PtBi Nanoparticles
Norm μ(E)
Energy (eV)
2.0
1.5
1.0
0.5
0.0
11520
11540
11560
11580
11600
11620

(a)

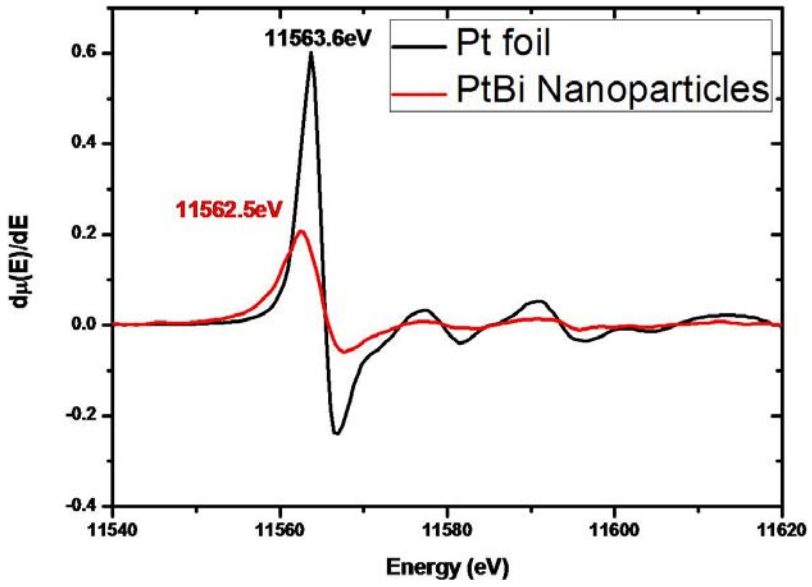
11563.6eV
11562.5eV
Pt foil
PtBi Nanoparticles
dμ(E)/dE
Energy (eV)
0.6
0.4
0.2
0.0
-0.2
-0.4
11540
11560
11580
11600
11620

(b)

largely metallic in cluster and gained small partial electron density.

Figure 7.3 (a) presents XANES spectra obtained at the Bi L_3 edge (13419 eV) from bismuth powder and bismuth oxide powder (Bi_2O_3), used as reference materials, via transmission mode, and a freshly prepared PtBi nanoparticle modified GC electrode via fluorescence mode. The increased "white line" intensity of the intermetallic Bi versus pure metallic Bi is likely due to "alloy-induced" d-band vacancies.[40] The large edge intensity of PtBi nanoparticles signified extensive oxidation of the prepared PtBi nanoparticles. Moreover, the energy of the Bi L_3 absorption edge in PtBi was between those of pure metallic bismuth and Bi_2O_3 phase. This also suggests that the bismuth species in the nanoparticles were initially partially oxidized and that the oxidation level was less than that of Bi in Bi_2O_3. Figure 7.3 (b) presents the derivative XANES spectra at the Bi L_3 edge for PtBi nanoparticles and the reference materials. The energy of the Bi L_3 absorption edge in PtBi nanoparticles was 1.2 eV higher than that of pure metallic bismuth and 2.2 eV lower than that of the Bi_2O_3 phase. The above XANES data suggests that bismuth species, in fresh PtBi nanoparticles, are partially oxidized to BiO_x where x is smaller than 1.5, but that platinum species were only partially oxidized. Moreover, and a bit surprising, platinum atoms presented a slightly positive valence charge in the PtBi intermetallic crystal lattice. Figure 7.4 presents *in-situ* XANES spectra recorded via fluorescence mode after each electrochemical pretreatment which included cycling the potential 10 times from -0.20V to increasingly E_{ulp} values of +0.40V, +0.80V and +1.20V for 10 cycles. The decreased white line intensity for an E_{ulp} value of +0.40V versus fresh nanoparticles indicates that less bismuth oxide is present on the nanopaticle modified electrode after cycling the potential to +0.40V. This phenomenon can be rationalized by dissolution of the bismuth oxide on the nanoparticle surface during the potential cycling process. A similar behavior has been previously observed for bulk PtBi electrodes. For example,

Figure 7.3 XANES spectra at the Bi L_3 edge for freshly prepared PtBi intermetallic nanoparticle modified electrode, bismuth and bismuth oxide powder in conventional mode (a) and derivative mode (b).

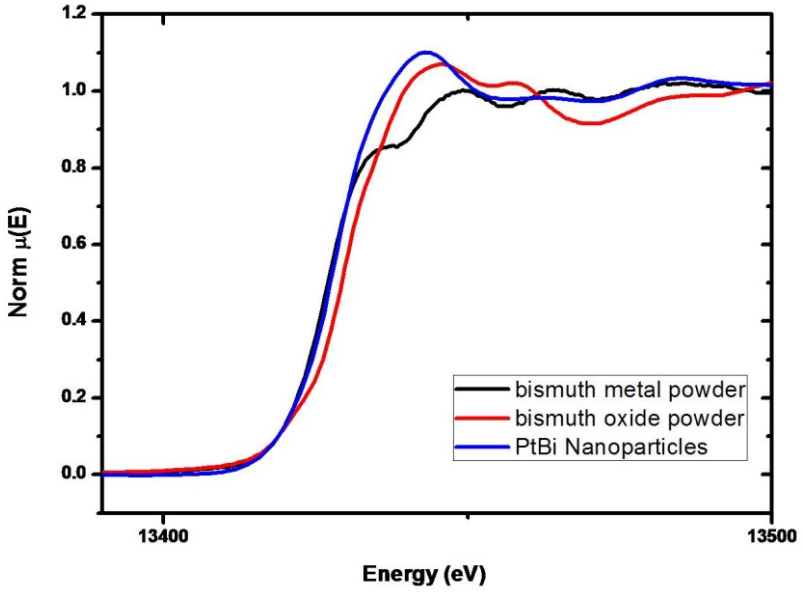
Norm μ(E)
Energy (eV)
bismuth metal powder
bismuth oxide powder
PtBi Nanoparticles

(a)

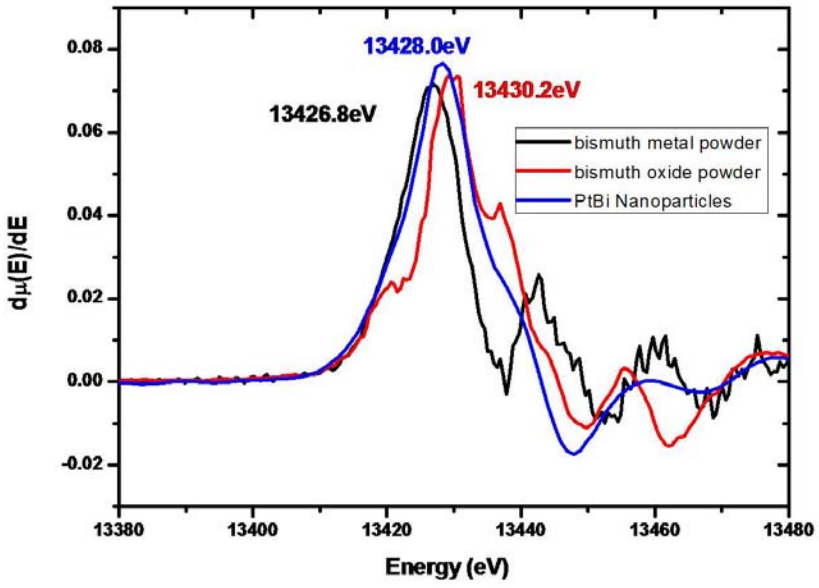
13428.0eV
13430.2eV
13426.8eV
dμ(E)/dE
Energy (eV)
bismuth metal powder
bismuth oxide powder
PtBi Nanoparticles

(b)

Figure 7.4 XANES spectra at the Bi L_3 edge of PtBi nanoparticle modified electrode as a function of applied E_{ulp} in 0.1M H_2SO_4.

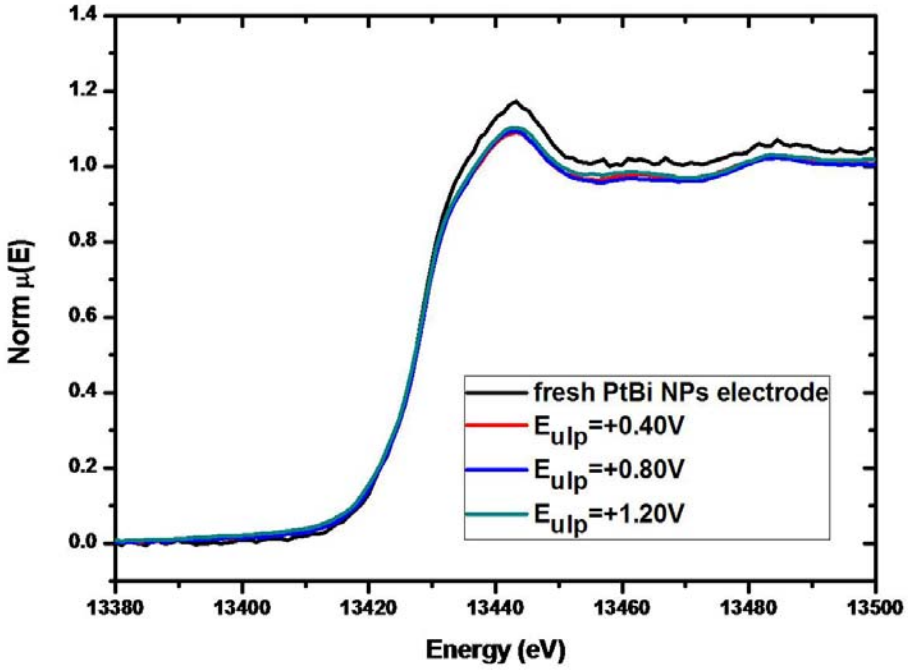
1.4
1.2
1.0
0.8
0.6
0.4
0.2
0.0
Norm μ(E)
13380
13400
13420
13440
13460
13480
13500
Energy (eV)
fresh PtBi NPs electrode
E_ulp=+0.40V
E_ulp=+0.80V
E_ulp=+1.20V

previous *ex-situ* XPS data suggested that Bi_2O_3 species were formed on the surface of a polycrystalline PtBi intermetallic bulk electrode for an E_{ulp} value of +0.40V and subsequently dissolved at increasing E_{ulp} values.[36] The absorption edges in the XANES spectra presented in Figure 4 remained virtually unchanged as a function of the applied potential, suggesting that the oxidation states of bismuth species in the nanoparticle were insensitive to the applied E_{ulp} values. We interpret this as indicating that bismuth species in the interior of the PtBi intermetallic nanoparticles were partially oxidized to BiO_x ($x < 1.5$) during the electrode preparation process and could not be further oxidized to higher oxidation states while cycling the potential to increasingly values. On the other hand, the oxidized bismuth species on the surfaces of PtBi nanoparticles were essentially dissolved into solution even at the beginning of the series of electrochemical pretreatments in 0.1M H_2SO_4, so they would not contribute to the signal in a detectable fashion.

7.3.2 EXAFS data analysis of Pt and Bi L_3 edges of PtBi nanoparticles

Figure 7.5 (a) presents EXAFS spectra obtained at the Pt L_3 edge (11564 eV) from Pt foil, via transmission mode, and a freshly prepared PtBi nanoparticle modified GC electrode, via fluorescence mode.

From sample inspection, it is clear that the oscillations in the EXAFS spectrum for the PtBi nanoparticles had significant smaller amplitude than those for Pt foil and that the "white line" intensity for the Pt foil was much more intense than that for the PtBi nanoparticles. Figure 6 presents the Fourier-Transformed (FT) EXAFS data of the Pt L_3 edge from the different materials. There is a peak at 2.60Å corresponding to the first coordination shell and is consistent with the known FCC structure of Pt. The peaks below 2.60 Å were treated as noise since the shortest distance between atoms in

Figure 7.5 EXAFS spectra at the Pt L_3 edge for a Pt foil and freshly prepared PtBi nanoparticle modified electrode (a) and Bi L_3 edge from bismuth, bismuth oxide powder and a freshly prepared PtBi nanoparticle modified electrode (b).

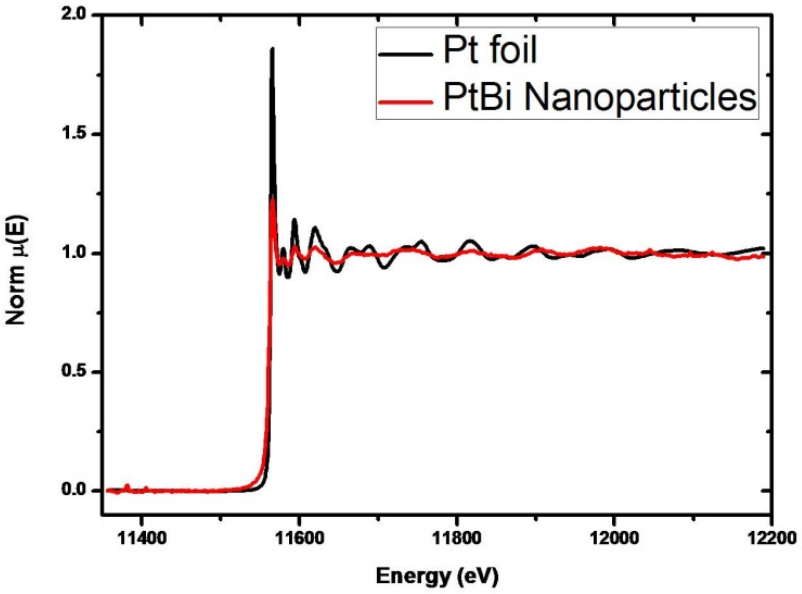
Pt foil
PtBi Nanoparticles
Norm μ(E)
Energy (eV)
2.0
1.5
1.0
0.5
0.0
11400
11600
11800
12000
12200

(a)

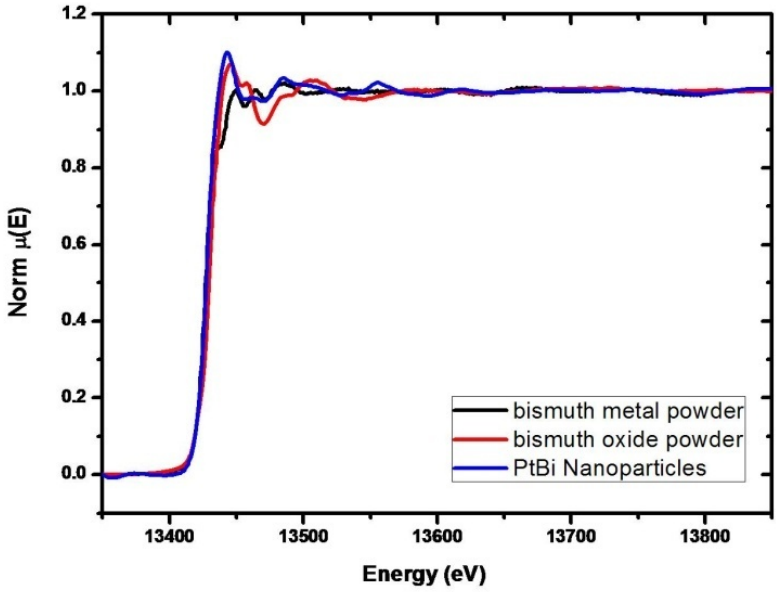
bismuth metal powder
bismuth oxide powder
PtBi Nanoparticles
Norm μ(E)
Energy (eV)
1.2
1.0
0.8
0.6
0.4
0.2
0.0
13400
13500
13600
13700
13800

(b)

Figure 7.6 Fourier-Transformed EXAFS spectra at the Pt L_3 edge for Pt foil (a) and freshly prepared PtBi nanoparticle modified electrode (b).

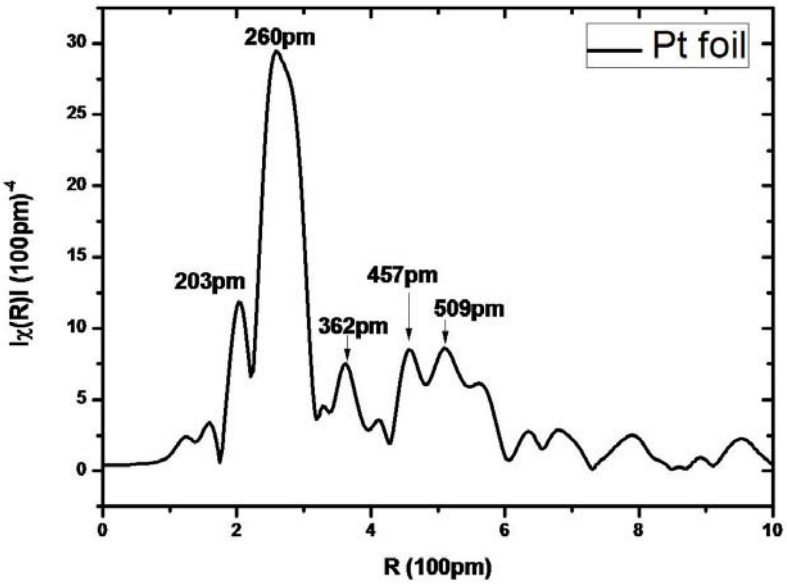
Pt foil
260pm
203pm
362pm
457pm
509pm
|χ(R)| (100pm)^-4
R (100pm)

(a)

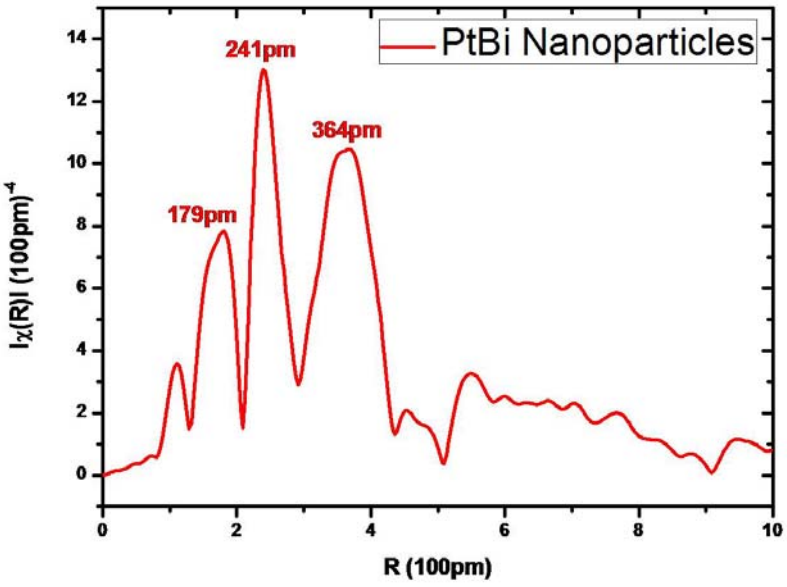
PtBi Nanoparticles
241pm
364pm
179pm
|χ(R)| (100pm)^-4
R (100pm)

(b)

a Pt crystal is above this value. Peaks at 3.62 Å and 4.57 Å were ascribed to the second and third layers of near neighbors. FT-EXAFS data at the Bi L_3 edge suggests that the first layer of Pt near neighbors in PtBi nanoparticles was at distance of 2.41 Å. This is consistent with the closest Pt-Pt distance in the PtBi intermetallic crystal structure. These results indicate that the PtBi nanoparticles retain the intermetallic crystalline structure at the nanoscale level although the outmost layer surface atoms were substantially oxidized and lost the intermetallic structure. The second layer of near neighbors in PtBi nanoparticles was at a distance of 3.64 Å, which is consistent with the Pt-Bi distance in PtBi intermetallic phase.

Figure 7.5 (b) presents the EXAFS spectra obtained at the Bi L_3 edge (13419 eV) for reference materials indicating bismuth powder and bismuth oxide powder (Bi_2O_3) (obtained via transmission mode) and a freshly prepared PtBi nanoparticle modified GC electrode (obtained via fluorescence mode). Relative to the EXAFS signals at the Pt L_3 edge, the oscillatory features in the Bi absorption coefficient were small in amplitude and quickly decayed for energies 250 eV above the adsorption edge. We believe that the small amplitude and rapid dampening arise, at least in part, from a large Debye-Waller factor. FT-EXAFS data at the Bi L_3 edge for different species are presented in Figure 7.7. The first layer of near neighbor atoms for pure metallic Bi, Bi_2O_3 and PtBi were 2.31, 1.50, 1.82 Å, respectively. While these values are somewhat shorter than the values derived from the corresponding crystal structures, the trend is in the anticipated direction. *In-situ* EXAFS and FT-EXAFS data at the Bi L_3 edge from PtBi nanoparticles (not shown here) exhibited virtually no changes as a function of the applied potential except for a sudden decrease in the absorption edge intensity after the electrode was subjected to the electrochemical pretreatment described above.

Figure 7.7 Fourier-Transformed EXAFS spectra at the Bi L_3 edge of Bi vs. Bi_2O_3 (a) and Bi_2O_3 vs. PtBi nanoparticles (b).

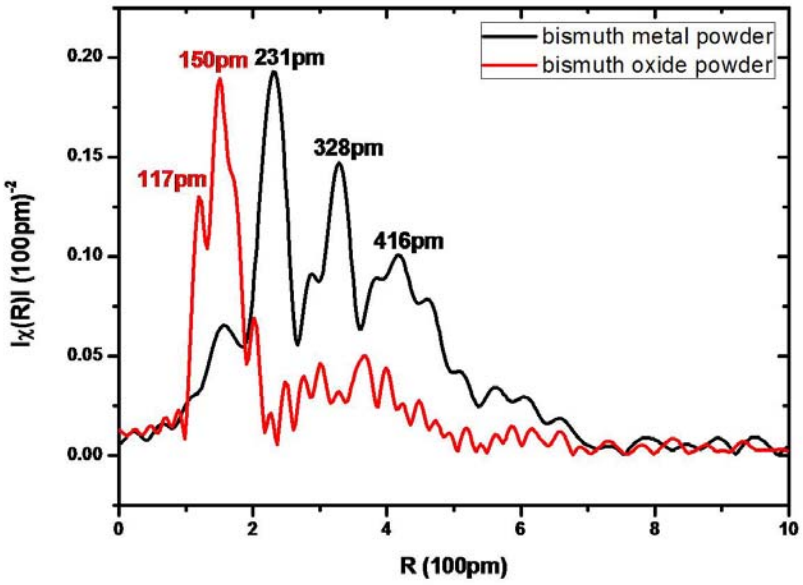
bismuth metal powder
bismuth oxide powder
150pm
231pm
328pm
117pm
416pm
|χ(R)| (100pm)^-2
R (100pm)
0.00
0.05
0.10
0.15
0.20
0
2
4
6
8
10

(a)

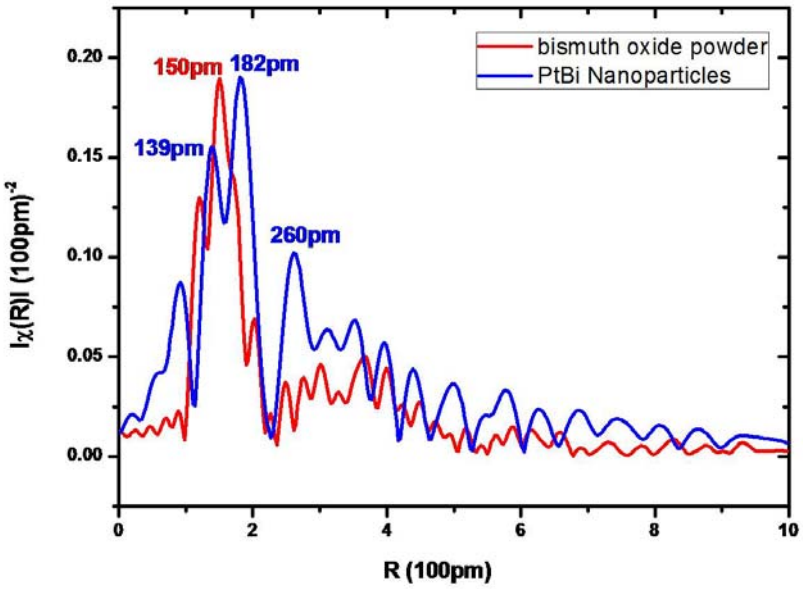
bismuth oxide powder
PtBi Nanoparticles
150pm
182pm
139pm
260pm
|χ(R)| (100pm)^-2
R (100pm)
0.00
0.05
0.10
0.15
0.20
0
2
4
6
8
10

(b)

7.4 Conclusion and Summary

In-situ and *ex-situ* EXAFS/XANES techniques were utilized to characterize PtBi intermetallic nanoparticles. For a freshly prepared PtBi nanoparticle-modified electrode, bismuth atoms on the surface were partially oxidized to BiO_x ($x < 1.5$) during the preparation procedure while the nanoparticles were exposed to air. FT-EXAFS data at the Pt L_3 edge suggested that the intermetallic crystalline structure was maintained at the nanoscale level although the outmost layer atoms of the nanoparticles were substantially oxidized. Although XANES data at the Bi L_3 edge of PtBi nanoparticles changed very little with cycling potentials, suggesting that the chemical state of bismuth species were insensitive to the applied potentials, a sudden decrease in the white line intensity of PtBi after electrochemical pretreatment at an E_{ulp} value of +0.40V versus freshly prepared electrode, was observed. This could be ascribed to dissolution of bismuth oxidized species on the surfaces of the PtBi nanoparticles when subjected to the CV treatments. More detailed work using the XAS method to study different intermetallic nanomaterials under electrochemically active control will be presented in the future.

REFERENCES

1. D.C. Kongingsberger and R. Prins, *X-ray Absorption: Principles, Applications, Techniques of EXAFS, SEXAFS and XANES*, Wiley, New York, **1988**
2. R.D. Kronig, *Z Phys.* 70, 317, **1931**
3. D.E. Sayers, E.A. Stern, and F.W. Lytle, *Phys. Rev. Lett.* 27, 1204, **1971**
4. E.A. Stern, D.E. Sayers and F.W. Lytle, *Phys. Rev. B* 11, 4836, **1975**
5. B.K. Teo, *EXAFS: Basic Principles and Data Analysis*, Springer, Berlin, **1986**
6. Y. Iwasawa, *X-ray Absorption Fine Structure for Catalysts and Surfaces*, World Scientific, Singapore, **1996**
7. J. Stöhr, *NEXAFS Spectroscopy*, Springer, Berlin, **1992**
8. A. Bianconi, in *X-ray Absorption: Principles, Applications, Techniques of EXAFS, SEXAFS and XANES,* D.C. Kongingsberger and R. Prins eds., Wiley, New York, p573, **1988**
9. F.W. Lytle, D.E. Sayers and E.B. Moore, *Appl. Phys. Lett.* 24, 45, **1974**
10. H.D. Abruña, G.M. Bommarito and H.S. Yee, *Acc. Chem. Res.* 28, 273, **1995**
11. B.-K. Teo, *Acc. Chem. Res.* 13, 412, **1980**
12. L.R. Sharpe, W.R. Heineman and R.C. Elder, *Chem. Rev.* 90, 705, **1990**
13. S. Mukerjee, J. Ziegelbauer, T. Arruda, D. Rmaker and B. Shyam, *The Electrochem. Soc. Interface* 17, 46, **2008**
14. J.-D. Grunwaldt and A.I. Frenkel, *Synchrotron Radiation News* 22, 2, **2009**
15. S.R. Bare and T. Ressler, *Advances in Catalysis (Chapter 6)* 52, 339, **2009**
16. J.-D. Grunwaldt, M. Caravati, S. Hannemann and A. Baiker, *Phys. Chem. Chem. Phys.* 6, 3037, **2004**
17. B.M. Weckhuysen, *Chem. Commun.* 97, **2002**
18. H. Topsøe, *J. Catal.* 216, 155, **2003**

19. M.A. Bañares, *Catal. Today* 100, 71, **2005**
20. J.D. Grunwaldt and A. Baiker, *Phys. Chem. Chem. Phys.* 7, 3526, **2005**
21. J.G. Parsons, K.J. Tiemann, J.R. Peralta-Videa and J.L. Gardea-Torresdey, *Environ. Sci. Technol.* 40, 4181, **2006**
22. J. Zhang, K. Sasaki, E. Sutter and R.R. Adzic, *Science* 315, 220, **2007**
23. M. Li, K. Sasaki, M.B. Vukmirovic, N.S. Marinkovic, P. Liu, A.I. Frenkel, A. Kowal, M. Shao, J. Zhang and R.R. Adzic, *Nature Materials* 8, 325, **2009**
24. T. Ressler, M. Hagelstein, U. Hatje and W. Metz, *J. Phys. Chem. B* 101, 6680, **1997**
25. A. Iglesias-Juez, A. Martínez-Arias, M.A. Newton, S.G. Fiddy and M. Fernández-García, *Chem. Commun.* 4092, **2005**
26. M.E. Herron, S.E. Doyle, S. Pizzini, K.J. Roberts, J. Robinson, G. Hards and E.C. Walsh, *J. Electroanal. Chem.* 324, 243, **1992**
27. S. Murkerjee and J. McBreen, *J. Electroanal. Chem.* 448, 243, **1998**
28. H.A. Gasteiger, N.M. Markovic and P.N. Ross, *J. Phys. Chem.* 99, 8920, **1995**
29. R.J.K. Wiltshire, C.R. King, A. Rose, P.P. Wells, H. Davies, M.P. Hogarth, D. Thompsett, B. Theobald, F.W. Mosselmans, M. Roberts and A.E. Russell, *Phys. Chem. Chem. Phys.* 11, 2305, **2009**
30. S. Stoupin, E.-H. Chung, S. Chattopadhyay, C.U. Segre and E.S. Smotkin, *J. Phys. Chem. B* 110, 9932, **2006**
31. N.M. Markovic and P.N. Ross, *Surface Science Reports* 45, 117, **2002**
32. E. Casado-Rivera, Z. Gál, A.C.D. Angelo, C. Lind, F.J. DiSalvo and H.D. Abruña, *Chem. Phys. Chem.* 4, 193, **2003**
33. E. Casado-Rivera, D.J. Volpe, L. Alden, C. Lind, C. Downie, T. Vázquez-Alvarez, A.C.D. Angelo, F.J. DiSalvo and H.D. Abruña, *J. Am. Chem. Soc.* 126, 4043, **2004**
34. Y. Liu, H. Abe, H.M. Edvenson, F.J. DiSalvo and H.D. Abruña, *submitted*

35. Y. Liu, M.A. Lowe, K.D. Finkelstein, D.S. Dale, F.J. DiSalvo and H.D. Abruña, *submitted*
36. D.R. Blasini, D. Rochefort, E. Fachini, L.R. Alden, F.J. DiSalvo, C.R. Cabrera and H.D. Abruña, *Surface Science* 600, 2670, **2006**
37. Y. Liu, D.R. Blasini, F.J. DiSalvo and H.D. Abruña, *submitted*
38. C. Roychowdhury, F. Matsumoto, V.B. Zeldovich, S.C. Warren, P.F. Mutolo, M. Ballesteros, U. Wiesner, H.D. Abruña and F.J. DiSalvo, *Chem. Mater.* 18, 3365, **2006**
39. B. Ravel and M. Newville, *Phys. Scr.* T115, 1007, **2005**
40. R. Viswanathan, G. Hou, R. Liu, S.R. Bare, F. Modica, G. Mickelson, C.U. Segre, N. Leyarovska and E.S. Smotkin, *J. Phys. Chem. B* 106, 3458, **2002**

CHAPTER EIGHT

CONCLUSION AND OUTLOOK

8.1 Concluding Remarks

In this dissertation, I have extensively discussed various X-ray studies in combination with electrochemistry of novel ordered intermetallic compounds, in polycrystalline, single crystal or nanoscale forms, as promising anode materials for fuel cell applications. *In-situ* grazing incidence diffraction characterization was initially done for polycrystalline PtBi and PtPb intermetallic electrodes. The surface composition and structure were dramatically changed as a function of applied upper limit potentials (E_{ulp}) while cycling the E_{ulp} to increasingly positive values (from +0.40V to +1.20V) in the supporting electrolyte only. The less noble elemetns (Bi or Pb) gradually leached out from the intermetallic electrode surface and dissolved into the solution. Pt islands with physical diameters of ca. 200 nm were formed, but crystalline domains within these islands were ~ 5 nm. The major experimental obstacle for these *in-situ* measurements came from the surface roughness of the electrodes. It was difficult to approach the minimum sampling depth of 10 Å, which is theoretically achievable for ideal atomically flat surfaces. Nevertheless the capability of GID characterization for these PtBi and PtPb electrodes was demonstrated by adjusting experimental parameters so as to reach a compromise between the sampling depth and surface roughness.[1]

The effects on the structure and composition of PtM (M=Bi and Pb) electrodes of holding the potential, as opposed to scanning, have also been extensively studied. Bismuth oxides nanocrystal domains, with diameters of ca. 50 nm were controllably

produced on the electrode surface after holding the potential at +1.20V for 30 min in different supporting electrolytes. In addition, there was no evidence of the formation of Pt nanocrystal domains on the electrode surface. The electrocatalytic activity towards formic acid oxidation following the two different pretreatments was quite similar. It was suggested that the activity of PtBi might come from the boundary lines between bismuth oxide and PtBi intermetallic domains which is similar to proposed activity of PtRu alloys. On the other hand, there was no evidence of the formation of any kind of oxidized lead species on the surface of PtPb electrodes subjected to a similar treatment. However, Pt nanocrystal domains were formed and the outmost layers of the intermetallic crystals were etched away at the same time.

The presence of active fuel molecules in the solution largely precluded the leaching out process of less noble element. A kinetic stabilization mechanism was used to rationalize this observation. In detail, a competition process between the oxidation of fuel molecules and the oxidation/corrosion of the electrode surface itself was established at the electrode/solution interface. The ready oxidation of active fuel molecules kinetically limited the oxidation/corrosion of the electrode surface.

As mentioned earlier, intermetallic phases can serve as model systems for catalytic research to supplement current models, such as alloy materials and deposited bimetallic single crystal facets.[2] To achieve this goal, high quality single crystal facets of intermetalllic PtBi and PtPb (100) and (001) were prepared using the Laue back reflection method (BRL) to assist with crystal orientation. Well-defined Pt domains with a 6-fold symmetry but offset 23 deg to the (001) facet substrate were produced while cycling the potential to +1.00V. In this experiment, azimuthal scans proved to be a very useful tool to explore the surface texturing of single crystal facets. Furthermore, bulk surfaces were shown to serve as an excellent platform for obtaining information about the relationships among structure/ composition/property/activity of the

materials.

It is also of great importance to characterize nanocatalysts which are widely used for industrial applications. For such materials, methods that are sensitive to short-range order are better suited for these investigations. X-ray fluorescence (XRF) and X-ray absorption spectroscopic (XAS) methods were utilized to characterize intermetallic nanoparticles. Two major advantages of the XRF and XAS investigations were: 1) quantitative characterization; 2) local element-specific chemical information. Neither of them could be obtained from diffraction data.

8.2 Future Directions on X-ray Studies of Intermetallic Phases

Even though polycrystalline and single crystal intermetallic phases have been extensively characterized by various complementary X-ray techniques, there are some important and interesting issues which have not yet been addressed.

It is clear that the stability of the different facets is varied. It is of great interest to correlate the activities from different facets to their thermodynamic or dynamic stabilities both via computational and experimental approaches. Preliminary results were obtained by GID. Polycrystalline intermetallic phases could serve as model systems but there were two obstacles which could not be easily overcome: 1) although GID mehod has excellent surface sensitivity, the diffraction technique is not good at quantitative studies; 2) polycrystalline intermetallic phases employed here had no “perfect” polycrystalline structure, or in other words, had discontinuous and sharp spots on the powder ring patterns. Equivalent terminations could not be guaranteed after each polishing procedure for the surface characterization. As a result, several compromises had to be made to perform this investigation. Instead of recording and analyzing the absolute intensities of diffraction peaks, ratios of targeted diffraction

peaks to a selected internal calibration peak (which had no significant change during electrochemical treatments) were used to interpret the observed phenomena. Since an in-plane diffraction geometry was employed, the changing trends of intensities of diffraction peaks reflected the stabilities of the crystal planes which were perpendicular to the planes giving rise to the diffraction signals. From this first step, the results suggest that the stabilities of facets could be correlated to the ratios of platinum atoms on the exposed facets. This work was in collaboration with Michael A. Lowe (a graduate student in the Abruña group).

Crystal truncation rod (CTR) measurements from single crystal surfaces have excellent surface sensitivity and can offer information about the atoms of the outmost layer of the surface.[3-6] While high quality intermetallic single crystal facets were fabricated in the previous experiments, the surface roughness was too high for these crystals to be employed in CTR measurement. Another experimental obstacle was the limited dynamic range of the detector used for the CTR experiment. Initial attempts were carried out to measure CTR from a PtBi(001) facet at G2 station. Figure 8.1 (a) shows the preliminary results of this experiment. The intensity of the diffracted signal was recorded at discrete *l* values from 4.01 to 4.50 (anti-Bragg position) and from 3.99 to 3.50 with appropriate attenuation parameters. A calibration measurement correlated the intensity factors to the attenuation parameters, and all data were appropriately scaled in intensity and plotted in Figure 8.1 (a). The diffracted intensity dropped very quickly while the crystal was moved away from the Bragg peak position, but some features around l values of 3.65 and 4.35 were clearly evident in the CTR plot. In order to successfully use CTR measurements for intermetallic single crystals, it is of great importance to reduce the surface roughness. One possible approach is to deposit PtBi an dPtPb in a layer-by-layer way along specific crystal orientations to a substrate which has similar crystal lattice parameters while in an ultra high vacuum system.

Figure 8.1 Preliminary CTR measurement along the PtBi(004) direction (a). Stimulated X-ray reflectivity from a PtBi surface with various surface roughness values (b).

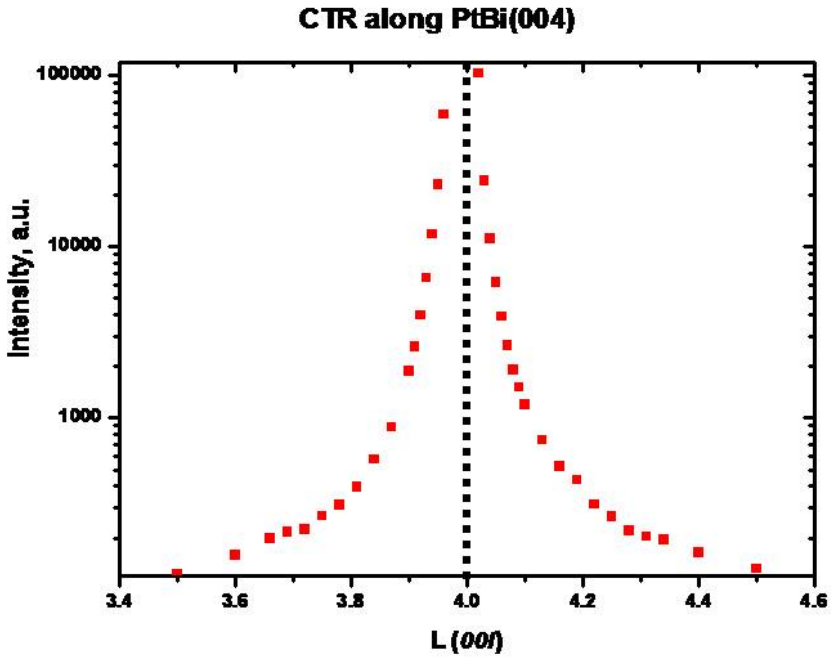
CTR along PtBi(004)
Intensity, a.u.
100000
10000
1000
3.4
3.6
3.8
4.0
4.2
4.4
4.6
L (00l)

(a)

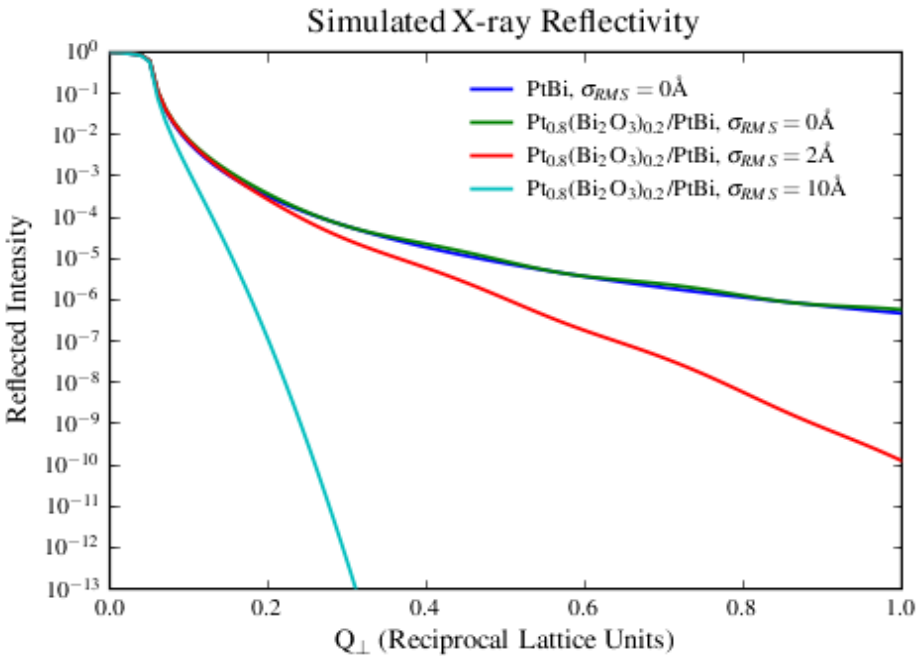
Simulated X-ray Reflectivity
Reflected Intensity
PtBi, $\sigma_{RMS} = 0$Å
$Pt_{0.8}(Bi_2O_3)_{0.2}$/PtBi, $\sigma_{RMS} = 0$Å
$Pt_{0.8}(Bi_2O_3)_{0.2}$/PtBi, $\sigma_{RMS} = 2$Å
$Pt_{0.8}(Bi_2O_3)_{0.2}$/PtBi, $\sigma_{RMS} = 10$Å
$Q_\perp$ (Reciprocal Lattice Units)

(b)

On the other hand, new diode-array linear detector with an enormously expanded dynamic range is available at G2 station and might offer new opportunity for CTR measurement.

8.3 New Opportunities in Other Energy Technologies

Besides the characterization of electrocatalysts for fuel cell applications, X-ray techniques employed and developed in this dissertation offer great research opportunities to investigate and improve other systems for energy storage and conversion.

X-ray techniques have been extensively employed to *in-situ* characterize Li-Ion batteries. [7-15] Initial attempts of *in-situ* measurement for $LiCoO_2$ cathode materials in a Li-ion battery were carried out at the F3 and C1 stations. A transmission type *in-situ* cell designed by Michael A. Lowe was employed for diffraction (F3 station) and EXAFS (C1 and F3) measurements (Figure 8.2). A 2D area detector was utilized to record the diffraction powder rings from the *in-situ* battery cell during the charging/discharging processes. EXAFS data of the Co K edge were recorded in transmission mode at the C1 station by a Lytle detector (ionization chamber) and via both transmission and fluorescence modes at the F3 station by VORTEX and Lytle detectors, respectively. These studies demonstrated the capability of *in-situ* measurements of Li-ion batteries.

Solar cells have attracted enormous research interests in the last decade.[16-18] X-ray techniques have been widely applied to characterize the catalysts for solar cells.[19-22] Due to the continuous discovery and development of new catalysts with unknown structures, *in-situ* X-ray characterization methods provide great opportunities to accelerate the research related to solar cell catalysts. Dau and co-workers[23] reported on

Figure 8.2 Schematic of *in-situ* electrochemical cell for Li-ion battery investigation.

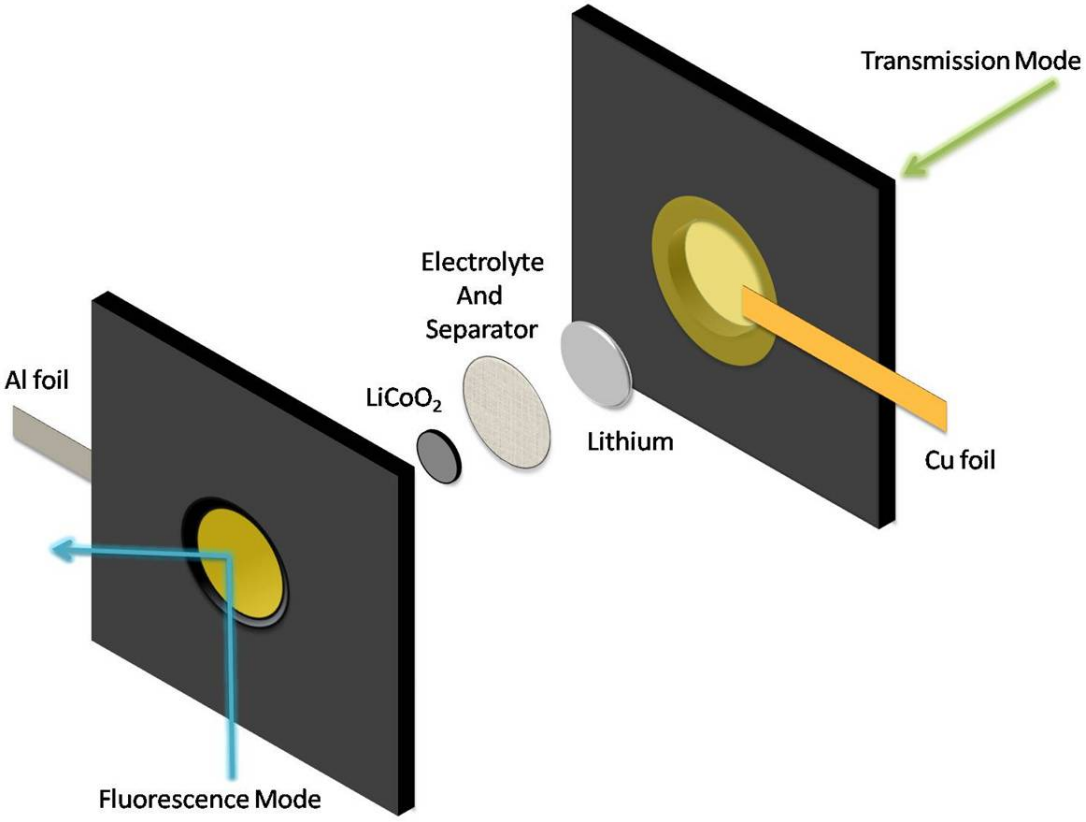
Transmission Mode
Electrolyte
And
Separator
Al foil
$LiCoO_2$
Lithium
Cu foil
Fluorescence Mode

the use of XAS/EXAFS methods to reveal the structure of recently discovered amorphous cobalt catalysts[24] to produce oxygen from water with high efficiency. They proposed that the central structural unit found in the bulk of the novel water-oxidation catalyst is a cluster of interconnected complete or incomplete Co^{III}-oxo cubanes. Unfortunately this experiment was carried out in *ex-situ* fashion. One would generally expect that the structure and composition of the catalyst film may change under working conditions. A possible improvement to the work would be to do *in-situ* surface sensitive diffraction to reveal crystal structure information.

Clearly there are numerous opportunities for the use of *in-situ* X-ray based techniques in energy investigations.

REFERENCES

1. D.R. Blasini, *Characterization of thin films and the thin film phenomena in electrochemically active systems via X-ray methods*, dissertation, **2006**
2. N.M. Markovic and P.N. Ross, *Surface Science Reports* 45, 117, **2002**
3. R. Feidenhans'l, *Surface Science Reports* 10, 105, **1989**
4. I.K. Robinson, *Phys. Rev. Lett.* 50, 1145, **1983**
5. V.M. Kaganer, *Phys. Rev. B* 75, 245425, **2007**
6. J. Als-Nielsen and D. McMorrow, *Elements of Modern X-ray Physics*, Wiley, England, **2001**
7. M. Okubo, E. Hosono, J. Kim, M. Enomoto, N. Kojima, T. Kudo, H. Zhou and I. Honma, *J. Am. Chem. Soc.* 129, 7444, **2007**
8. J. Hu, Z. Wen, Q. Wang, X. Yao, Q. Zhang, J. Zhou and J. Li, *J. Phys. Chem. B* 110, 24305, **2006**
9. A. Rong, X.P. Gao, G.R. Li, T.Y. Yan, H.Y. Zhu, J.Q. Qu and D.Y. Song, *J. Phys. Chem. B* 110, 14754, **2006**
10. J. Bréger, N. Dupré, P.J. Chupas, P.L. Lee, T. Proffen, J.B. Parise and C.P. Grey, *J. Am. Chem. Soc.* 127, 7529, **2005**
11. A. Deb, U. Bergmann, E.J. Cairns and S.P. Cramer, *J. Phys. Chem. B* 108, 7046, **2004**
12. Y. Sharma, N. Sharma, G.V. Subba Rao and B.V.R. Chowdari, *Adv. Funct. Mater.* 17, 2855, **2007**
13. M.V. Reddy, T. Yu, C.H. Sow, Z.X. Shen, C.T. Lim, G.V. Subba Rao and B.V.R. Chowdari, *Adv. Funct. Mater.* 17, 2792, **2007**
14. D. Ensling, M. Stjerndahl, A. Nytén, T. Gustafsson and J.O. Thomas, *J. Mater. Chem.* 82, **2009**

15. A. Nytén, M. Stjerndahl, H. Rensmo, H. Siegbahn, M. Armand, T. Gustafsson, K. Edström and J.O. Thomas, *J. Mater. Chem.* 3483, **2006**
16. J. Chen, J.Z. Wang, A.I. Minett, Y. Liu, C. Lynam, H. Liu and G.G. Wallace, *Energy Environ. Sci.* 393, **2009**
17. H.B. Gray, *Nature Chemistry* 1, 7, **2009**
18. S. Günes, H. Neugebauer and N.S. Sariciftci, *Chem. Rev.* 107, 1324, **2007**
19. W. John Albery *Acc. Chem. Res.*, **1982**, *15* (5), pp 142–148
20. Y. Hu, Z. Zheng, H. Jia, Y. Tang and L. Zhang, *J. Phys. Chem. C* 112, 13037, **2008**
21. J. Xia, N. Masaki, K. Jiang and S. Yanagida, *J. Phys. Chem. C* 111, 8092, **2007**
22. H.-Y. Chen, H. Yang, G. Yang, S. Sista, R. Zadoyan, G. Li and Y. Yang, *J. Phys. Chem. C* 113, 7946, **2009**
23. M. Risch, V. Khare, I. Zaharieva, L. Gerencser, P. Chernev and H. Dau, *J. Am. Chem. Soc.* 131, 6936, **2009**
24. M.W. Kanan and D.G. Nocera, Science *321*, 1072, **2008**